Modeling of Gas Radiation Heat Transfer for the CFD Analysis of Containment Atmosphere Mixing

Modellierung des Wärmetransports mittels Gasstrahlung für die CFD-Analyse der Mischungsvorgänge im Sicherheitseinschluss

Von der Fakultät für Maschinenwesen der Rheinisch-Westfälischen Technischen Hochschule Aachen zur Erlangung des akademischen Grades eines Doktors der Naturwissenschaften genehmigte Dissertation

vorgelegt von

Xiongguo Liu

Berichter: Univ.-Prof. Dr. rer. nat. Hans-Josef Allelein
Univ.-Prof. Dr.-Ing. Reinhold Kneer
Univ.-Prof. Dr.-Ing. Xu Cheng

Tag der mündlichen Prüfung: 17. März 2023

Diese Dissertation ist auf den Internetseiten der Universitätsbibliothek online verfügbar.

Statutory Declaration

I hereby declare that I have created this work completely on my own and used no other sources or tools than the ones listed, and that I have marked any citations accordingly.

Hiermit versichere ich, dass ich die vorliegende Arbeit selbständig verfasst und keine anderen als die angegebenen Quellen und Hilfsmittel benutzt sowie Zitate kenntlich gemacht habe.

Xiongguo Liu
Germany, April, 2023

Abstract

During a severe nuclear accident, considerable amounts of steam, non-condensable gases, e.g., H_2, CO or CO_2, and radioactive aerosols are released into the containment building along with progressing core damage and molten corium concrete interaction. It is necessary to predict the flammable gas transport within the containment building to design measures that prevent their accumulation and potentially resulting combustion events challenging containment integrity. During prior model validation, it was found that the gas radiation heat transfer in humid gas mixtures can affect the hydrogen mixing process in slow buoyancy-driven flows, while there is a strong sensitivity to the model coefficients. Consequently, the objective of this thesis is to develop a reliable and efficient radiative transfer equation solver for complex 3D geometries, to formulate and assess suitable spectral properties of multi-component gas mixtures, and to investigate the impact of thermal radiation on the gas mixing process in buoyancy-driven flows. As basis for the investigation of thermal radiation in containment flows, a robust and reliable Monte Carlo solver is implemented in *containmentFoam*, a tailored CFD package for containment safety analysis developed at Forschungszentrum Jülich. Two non-gray gas models, the statistical narrow band correlated-k model (SNBCK) and as reference the line-by-line model (LBL) are tailored to the expected thermo-fluid dynamic conditions of a severe accident based on the HITRAN2016 database. In particular the numerically efficient formulation and implementation of the Monte Carlo method and the non-gray gas models are considered to ensure and optimize their practical applicability. Based on a thorough verification against reference solutions, the validation against two sets of application-oriented experiments in the PANDA facility (Paul Scherrer Institute) is conducted: The OECD/NEA HYMERES-2 H2P2 experiments were designed as a separate effect test to evaluate radiation heat transfer, whereas the complex interaction with gas mixing can be assessed in the OECD/NEA SETH-2 ST1 experiments. The analysis of the H2P2 series confirms that the gas temperatures are significantly over predicted when radiation is neglected in humid gas mixtures. There is a substantial accuracy improvement in simulation results for the tailored models in comparison with other models. Within the ST1 series, this effect is superposed by convective gas mixing, i.e., the erosion of a stratified light gas layer by a steam jet with different momenta. This detailed analysis reveals that the observed effect on gas temperatures, induces a local change of buoyancy forces and thus influences the helium-steam mixing process. The relevance of this effect increases with decreasing flow momentum. These results clearly indicate that gas radiation must not be neglected in containment model validation and applications despite of the modest gas temperature differences ($\Delta T < 50$ K). The developed radiation transport library demonstrated to be applicable to technical scale analysis at moderate additional numerical cost. Furthermore, it can also serve as a basis to develop and verify more efficient models in the future.

Kurzfassung

Während eines schweren Reaktorunfalls werden mit fortschreitender Kernschädigung und der Beton-Schmelze-Wechselwirkung erhebliche Mengen Dampf, nicht kondensierbarer Gase (z. B. H_2, CO oder CO_2) und radioaktiver Aerosole in den Sicherheitsbehälter freigesetzt. Der Transport brennbarer Gase wird simuliert, um Maßnahmen zur Verhinderung von Ansammlungen und möglicher Verbrennungsvorgänge, die die Integrität des Sicherheitsbehälters gefährden können, zu entwickeln. Vorangegangene Modellvalidierungen zeigten, dass Gasstrahlung in dampfhaltigen Gasgemischen den H_2-Transport in Auftriebsströmungen beeinflussen kann, wobei eine starke Sensitivität gegenüber den Modellkoeffizienten besteht. Ziel dieser Arbeit ist es, einen zuverlässigen und effizienten Strahlungstransportlöser für komplexe 3D-Geometrien zu entwickeln, ein geeignetes Spektralmodell für das Gasgemisch zu formulieren und zu bewerten sowie den Einfluss der Wärmestrahlung auf den Mischungsprozess in Auftriebsströmungen zu untersuchen. Zur Untersuchung des Wärmestrahlungstransports im Sicherheitsbehälter wird ein robuster und belastbarer Monte-Carlo-Löser in *containmentFoam*, ein am Forschungszentrum Jülich entwickeltes CFD-Paket für den Sicherheitseinschluss, implementiert. Zwei Spektralmodelle, das Statistical Narrow Band Correlated-K (SNBCK) und als Referenz das Line-by-Line (LBL) Modell, werden mittels der HITRAN2016-Datenbank auf die erwarteten thermo-fluiddynamischen Bedingungen zugeschnitten. Die numerisch effiziente Formulierung und Implementierung des Monte-Carlo-Verfahrens und der Spektralmodelle wird berücksichtigt, um ihre praktische Anwendbarkeit zu gewährleisten. Nach sorgfältiger Verifikation erfolgt die Validierung anhand zweier anwendungsorientierter Versuche an der PANDA-Anlage (Paul Scherrer Institut): Die OECD/NEA HYMERES-2 H2P2 Einzeleffekt-Versuche ermöglichen die Untersuchung des Strahlungswärmetransports, während die komplexe Wechselwirkung mit Mischungsvorgängen anhand der OECD/NEA SETH-2 ST1 Experimente bewertet wird. Die Analyse der H2P2-Versuchsreihe bestätigt, dass die Gastemperaturen bei Vernachlässigung der Strahlung in feuchten Gasgemischen deutlich überschätzt werden. Die maßgeschneiderten Spektralmodelle weisen verglichen mit bestehenden Modellen eine sichtbar bessere Vorhersagegüte auf. In den ST1-Versuchen wird dieser Effekt mit konvektiver Gasmischung, d.h. der Erosion einer Leichtgasschichtung mittels eines Dampfstrahls, überlagert. Die detaillierte Analyse zeigt, dass die Änderung der Gastemperaturen die lokalen Auftriebskräfte und somit mit abnehmender Strömungsgeschwindigkeit zunehmend den Mischungsprozess beeinflusst. Die Ergebnisse zeigen deutlich, dass die Gasstrahlung bei der Validierung und Anwendung von CFD-Modellen für den Sicherheitseinschluss nicht vernachlässigt werden darf. Die Strahlungstransportbibliothek erwies sich bei moderaten zusätzlichen numerischen Kosten als anwendbar für Analysen im technischen Maßstab. Zukünftig kann sie auch der Entwicklung und Verifizierung effizienterer Modelle dienen.

Contents

Abstract v

Kurzfassung vi

Abbreviation and Nomenclature xv

1 Introduction 1

2 Background and Motivation 5

2.1 Severe Accident Scenario in Pressurized Water Reactors 5

2.2 Numerical Analysis for Containment Safety 9

2.2.1 Lumped Parameter Code 9

2.2.2 Computational Fluid Dynamics 11

2.3 Thermal Radiation Modeling in Containment Flows 17

2.4 Open Issues and Objectives 22

3 Theory of Thermal Radiation Transfer 24

3.1 Fundamental Concepts and Equations 24

3.2 Spectral Gas Properties 33

3.2.1 Line-by-Line Model 36

3.2.2 Narrow Band Model 43

3.2.3 Wide Band Model 46

3.2.4 Weighted-Sum-of-Gray-Gases Model 49

3.2.5 Gray Gas Model 50

3.2.6 Assessment of Different Spectral Gas Property Models 52

3.3 Numerical Methods for Radiative Transfer Equation 59

3.3.1 P_1 method 61

3.3.2 Finite Volume Discrete Ordinate Method 62
3.3.3 Discrete Transfer Method 67
3.3.4 Monte Carlo Method 70
3.3.5 Assessment of Different Numerical Solution Methods 72
3.4 Summary of Thermal Radiation Modeling in Containment Flows . . . 75

4 Modeling Gas Radiation Transport for Application to Containment Flows 77

4.1 Development of Tailored Non-gray Gas Model for Containment Flows 78
4.1.1 Line-by-Line Model 78
4.1.2 Statistical Narrow Band Correlated-k Model 83
4.2 Monte Carlo Algorithm within Participating Media 91
4.2.1 Monte Carlo Sampling 95
4.2.2 Monte Carlo Ray Tracing 102
4.2.3 Estimation of Statistical Error 109
4.2.4 First Verification of the Monte Carlo Solver 110
4.3 Monte Carlo Variance Reduction Technique 111
4.3.1 Shifted Monte Carlo Method 112
4.3.2 Emission Reciprocity Monte Carlo Method 113
4.3.3 Comparison of Different Monte Carlo Algorithms 116
4.3.4 Efficient Parallelization Implementation Using Global Mesh . 118
4.4 Monte Carlo Solver Coupled into CFD 122
4.5 Summary of Model Development 124

5 First Validation and Discussion 126

5.1 Validation Strategy 127
5.2 PANDA H2P2 Test Series 129
5.2.1 H2P2 experimental setup 129
5.2.2 H2P2 CFD Setup 132
5.2.3 H2P2 Results and Discussion 135
5.2.4 Summary of H2P2 Test Series 146
5.3 PANDA ST1 Test Series 148
5.3.1 ST1 Experimental Setup 148

5.3.2 ST1 CFD Setup 150
5.3.3 ST1 Results and Discussion 154
5.3.4 Summary of ST1 Test Series 171

6 Conclusion and Outlook **174**

6.1 Summary and Conclusions 174

6.2 Outlook and Perspective 176

Acknowledgement **178**

Bibliography **179**

Appendix A Barycentric Tracking Algorithm **196**

Appendix B Thermal Radiation Library Source Code **198**

List of Figures

1.1 Number of operational nuclear reactors and net operating capacity in the world from 1954 to 2020 [SCH20] 1

2.1 Schematic diagram of a pressurized water reactor 6
2.2 Physical phenomena during a PWR severe accident 7
2.3 Containment modeling, detailed CAD model (left), simplified CAD model (middle) and GOTHIC nodalization (right) [BOC16] 10
2.4 Generic containment geometry in *containmentFoam* [KEL23] 12
2.5 Surface interpolation in FVM 16
2.6 Numerical algorithm for the coupling of CFD and thermal radiation 19
2.7 H_2O, CO_2, and CO LBL absorption coefficients at 300 K 20

3.1 Spectral radiation intensity, modifed from [HOW20] 26
3.2 Blackbody radiation intensity $I_{b,\eta}(T)$ at different temperatures 27
3.3 Thermal radiation energy balance within a short distance 29
3.4 Diffusive reflection on boundary surfaces: (a) rough surface, (b) condensation surface 31
3.5 Three transitions between two energy states [LOU00] 33
3.7 Potential well curve for a diatomic molecule, modified from [KUL18] 35
3.8 H_2O absorption coefficient in 2.7 μm bands at p = 1 atm, x_{H_2O} = 1: T = 1000 K (top), 600 K (middle), and 400 K (bottom), modified from [TAI99] 40
3.9 CO_2 absorption coefficient in 4.3 μm bands at p = 1 atm, x_{CO_2} = 1: T = 1000 K (top), 600 K (middle), and 400 K (bottom), modified from [TAI99] 41
3.10 H_2O absorption coefficient in 400 K and 1 atm at different molar fractions: x_{H_2O} = 0.01, 0.1, and 1.0 42
3.11 CO_2 absorption coefficient in 400 K and 1 atm at different molar fractions: x_{CO_2} = 0.01, 0.1, and 1.0 42

3.12 Narrow band models: (a) Elsasser narrow band model and (b) statistical narrow band model [MOD13] 44

3.13 LBL and EM2C/SNB [RIV95] narrow band transmissivity comparison: T = 800 K, p = 1 atm, x_{H_2O}=0.3, x_{CO_2}=0.2, x_{N_2}=0.5, and L = 1.0 m 45

3.14 LBL and EWBM band transmissivity comparison: T = 600 K, p = 1 atm, x_{H_2O}=0.1, x_{CO_2}=0.1, x_{N_2}=0.8 and L = 1.0 m 47

3.15 Comparison of the total emissivity between WSGG [LIU21] and LBL for p_{H_2O} = 0.8 atm 50

3.16 Planck mean absorption coefficient for CO_2 and H_2O 51

3.17 One-dimensional RTE discretization 54

3.18 Radiative source term for different non-gray gas models in test case 1: $T = 1000\,K$, $p = 1.0\,atm$, $x_{N_2} = 0.7$, $x_{H_2O} = 0.2$, $x_{CO_2} = 0.1$ and $L = 1.0\,m$ 55

3.19 Radiative source term for different non-gray gas models in test case 2: $T = 800 + 200\sin^2(\pi x)\ K$, $p = 1\,atm$, $x_{H_2O} = 0.2 + 0.2\sin^2(2\pi x)$, $x_{CO_2} = 0.1\cos^2(2\pi x)$ and $L = 1.0\,m$ 57

3.20 Radiative energy balance within a small control volume 60

3.21 Discretization of solid angle Ω, modified from [CHA93] 63

3.22 Finite volume discrete ordinates method 65

3.23 Solid angle overlapping effect in the fvDOM model 66

3.25 Ray tracking procedure in the discrete transfer method 69

3.26 2D rectangular test case [GOU00] 72

3.27 Radiative source term $-\nabla \cdot q_r$ at the $x - th$ central line 73

3.28 Radiative wall heat flux q_r at the bottom wall 74

4.1 LBL absorption coefficient illustration 82

4.2 Comparison of absorption coefficients calculated by the SNBCK and LBL models for H_2O 84

4.3 Evaluation of k-distribution function from the LBL absorption coefficient for H_2O ($p = 1.0\,atm$, $x_{H_2O} = 0.1$ and $T = 400\,K$), modified from [MOD13] 85

4.4 Evaluation of cumulative function from the LBL absorption coefficient for the SNBCK model [MOD13] 88

4.5 H_2O cumulative distribution function with different molar fractions x_{H_2O} = 0.01, 0.1, 0.4, and 1.0 under p_{tot} = 1.0 atm 89

4.6 LBL and SNBCK-FZJ band transmissivity comparison: T = 400 K, p = 1 atm, x_{H_2O} = 0.2, x_{CO_2} = 0.1, x_{N_2} = 0.7 and L = 1.0 m 90
4.7 Comparison of Monte Carlo and conventional techniques for thermal radiation analyses [MOD13] 91
4.8 Monte Carlo computational flow chart 94
4.9 Monte Carlo wavenumber sampling algorithm (T= 400 K, x_{H_2O} = 0.1 and P_{tot} = 1 atm), modified from [SOU13] 98
4.10 Diffusive emission from the gray surface 101
4.11 Initial fluid conditions for the Monte Carlo simulation 102
4.12 Monte Carlo energy bundle sampling procedure 103
4.13 Monte Carlo tracking process over the computational domain 105
4.14 Monte Carlo diffusive wall reflection 106
4.16 ERM reverse path, modified from [TES02] 115
4.17 Radiative source term evaluation using different Monte Carlo methods: T = 500 K, p = 1.0 atm, x_{H_2O} = 0.2 , x_{N_2} = 0.8 and L = 0.1 m 117
4.18 Relative error evaluation using different Monte Carlo methods: T = 500 K, p = 1.0 atm, x_{H_2O} = 0.2, x_{N_2} = 0.8 and L = 0.1 m 117
4.19 Master-slave parallel computing architecture 118
4.20 Monte Carlo global mesh algorithm 119
4.21 Monte Carlo and CFD coupling algorithm 123

5.1 PANDA facility for H2P2 test series (dimensions in mm) [OEC21, KAP23] 130
5.2 Sensor locations for H2P2 experiment, thermocouples are indicated by × and Helium mass spectrometer measurements by ○ 131
5.3 PANDA H2P2 2D wedge mesh with 15 degree angle 132
5.4 H2P2_2_2 test scenario: Time=400s (left), Time=1200s (right) 134
5.5 H2P2_2_2 evolution of the pressure history 135
5.6 H2P2_2_2 2D temperature profile at the end of injection phase 137
5.7 H2P2_2_2 evolution of temperature at the central line 138
5.8 H2P2_2_2 evolution of helium concentration at the central line 140
5.9 H2P2_5 evolution of the pressure history 141
5.10 H2P2_5 2D temperature profile at the end of injection phase 143
5.11 H2P2_5 evolution of temperature at the central line 144
5.12 H2P2_5 evolution of helium concentration at the central line 145

5.13 PANDA ST1 experiment, modified from [OEC13] 148
5.14 PANDA ST1 experiment precondition, modified from [OEC13] 149
5.15 PANDA ST1 mesh 151
5.16 PANDA ST1 numerical model in OpenFOAM [LIU22b] 153
5.17 Vertical temperature profile above 4 m for the ST1_1_2 experiment . . 154
5.18 Comparison of the temperature field for the ST1_1_2 experiment . . . 155
5.19 ST1_1_2 temperature sensor C20 157
5.20 ST1_1_2 temperature sensor C14 158
5.21 ST1_1_2 transient helium dilution process 159
5.22 Comparison of the density distribution for the ST1_1_2 experiment . 161
5.23 Comparison of the velocity distribution for the ST1_1_2 experiment . 162
5.24 Vertical temperature profile above 4 m for the ST1_2_2 experiment . . 164
5.25 Comparison of the temperature field for the ST1_2_2 experiment . . . 165
5.26 ST1_2_2 temperature sensor C20 166
5.27 ST1_2_2 temperature sensor C14 167
5.28 ST1_2_2 transient helium dilution process 168
5.29 Comparison of the velocity distribution for the ST1_2_2 experiment . 170
5.30 Comparison of radiative source term and $cond.$ + $conv.$ term in the ST1_1_2 test at 600 s 173

A.1 Barycentric coordinate tracking algorithm 197

List of Tables

3.1 Types of infrared radiation [ISO07] 25
3.2 Limits of the spectral bands for methane in FDS [MCG00, MCG13] . . 48
3.3 Absorption coefficients for the gray gas model [CAS15] 52
3.4 Overview of spectral gas properties, modified from [BEC13] 53
3.5 Summary of relative errors and computational time for the one-dimensional test case with a homogeneous media 56
3.6 Summary of relative errors and computational time for the one-dimensional test case with a nonhomogeneous media 58
3.7 Summary of numerical errors and computational time for the Goutiere's 2D case 75

4.1 HITRAN LBL database parameters [ROT09, ROT05] 80
4.2 Gauss quadrature points and weights for the SNBCK model [RIV92] 87
4.3 Statistical error evaluation using the Monte Carlo method with LBL and SNBCK non-gray models for the Goutiere's 2D case [GOU00]: T = 1000 K, T_{wall} = 0 K, p = 1.0 atm, x_{H_2O} = 0.2 and x_{N_2} = 0.8 111
4.4 Efficiency comparison between the normal mesh and the global mesh for the PANDA ST1 experiment 121

5.1 Summary of the governing equations in *containmentFoam* simulations 128
5.2 Test matrix for the selected two H2P2 experiments 130
5.3 Mesh sensitivity study for the H2P2_2_2 experiment 133
5.4 Summary of simulation results for the H2P2_2_2 at 1200 s 136
5.5 Summary of simulation results for the H2P2_5 at 1200 s 142
5.6 Test matrix for the selected two ST1 experiments 149
5.7 Mesh sensitivity study for the ST1_2_2 experiment 152
5.8 Summary of different non-gray gas models for ST1_1_2 and ST1_2_2 test cases in the quasi-steady state 171

Abbreviations and Nomenclature

Abbreviations

BWR Boiling water reactor

CDSD Carbon dioxide spectroscopic databank

CFD Computational fluid dynamics

CFL Courant Friedrichs Lewy number

DTM Discrete transfer method

EWBM Exponential wide band model

FDS Fire dynamic simulator

fvDOM Finite volume discrete ordinate method

fvMCM Finite volume Monte Carlo method

FZJ Forschungszentrum Jülich

GWBM Gray wide band model

HITRAN High-resolution transmission molecular absorption database

HITEMP High-temperature molecular spectroscopic database

HYMERES Hydrogen Mitigation Experiments for Reactor Safety

IAEA International atomic energy agency

LBL Line-by-line model

LOCA Loss of coolant accident

MCCI Molten core concrete interaction

MPI Message passing interface

NEA Nuclear energy agency

OECD Organisation for economic co-operation and development

OpenFOAM Open source field operation and manipulation

PSI Paul Scherrer Institute

PWR Pressurized water reactor

POSIX Portable Operating System Interface

RANS Reynolds-averaged Navier-Stokes

RTE Radiative transfer equation

SNB Statistical narrow band model

SNBCK Statistical narrow-band correlated-k model

SST Shear stress transport turbulence model

TMI Three Mile Island

WSGG Weighted-sum-of-gray-gases model

Nomenclature

List of Latin Symbols

A Surface area [m^2]

c Speed of light [m/s]

G Incident radiation [W/m^2]

g Gravitational acceleration constant [m/s^2]

h Planck constant, $6.62607015 \times 10^{-34}$ [$m^2 \cdot kg/s$]

h_{tot} Total enthalpy [$kg \cdot m^2/s^2$]

h_i $i-th$ specie total enthalpy [$kg \cdot m^2/s^2$]

I Radiation intensity [$W/(m^2 \cdot sr)$]

I_η	Spectral radiation intensity $[W/(m^2 \cdot sr \cdot cm^{-1})]$
J_i	Mass diffusion flux of species i $[kg/(m^2 \cdot s)]$
k	Boltzmann constant, 1.380649×10^{-23} $[J/K]$
L	Path length $[m]$
p	Pressure $[kg/(m \cdot s^2)]$
q_r	Radiative wall heat flux $[W/m^2]$
$\nabla \cdot q_r$	Radiative source term $[W/m^3]$
S	Surface area $[m^2]$
$S(T)$	Spectral line intensity at T $[cm^{-1}/(molecule \cdot cm^{-2})]$
s	Path length $[m]$
T	Temperature $[K]$
U	Velocity vector $[m/s]$
x, y, z	Cartesian coordinates $[m]$
V	Volume $[m^3]$

List of Greek Symbols

Ω	Solid angle $[sr]$
ω	Specific rate of dissipation $[s^{-1}]$
σ	Stefan-Boltzmann constant, 5.6703×10^{-8} $[\ W/(m^2 \cdot K^4)]$
σ_η	Spectral scattering coefficient $[\ m^{-1}]$
γ	Line half-width $[\ cm^{-1}]$
ϵ	Surface emissivity [–]
θ	Polar angle from z axis [–]
$\tau_{\Delta\eta}$	Band transmittance [–]
τ	Transmittance [–]

τ	Reynolds shear stress [$kg/(m \cdot s^2)$]
η	Wavenumber [cm^{-1}]
κ	Absorption coefficient [m^{-1}]
ϕ	Azimuthal angle [–]
$\phi(\Omega', \Omega)$	Phase scattering function [–]
ρ	Density [kg/m^3]
ρ	Surface reflectivity [–]
δ	Dirac delta function [–]
μ	Viscosity [$kg/(m \cdot s)$]
μ_t	Turbulent viscosity [$kg/(m \cdot s)$]
ν	Kinematic viscosity [m^2/s]
ν	Frequency [s^{-1}]
ν_t	Turbulent kinematic viscosity [m^2/s]
λ	Thermal conductivity [$W/(m \cdot K)$]
λ_t	Turbulent thermal conductivity [$W/(m \cdot K)$]
λ	Wavelength [μm]

Dimensionless Number

Re	Reynolds number
Sc	Schmidt number
Pr	Prandtl number
Pr_t	Turbulent Prandtl number
Sc_t	Turbulent Schmidt number

Chapter 1

Introduction

Nuclear power plays an important role in the global energy economy. The contribution of nuclear energy to the global electricity generation is about 10.1% in 2020 [SCH20]. As shown in Fig. 1.1, there were 408 nuclear reactors in operation across the world in 2020, which provided a total capacity of 362 GW_e to the electricity system. There was exponential growth in nuclear power plants during the 1970s.

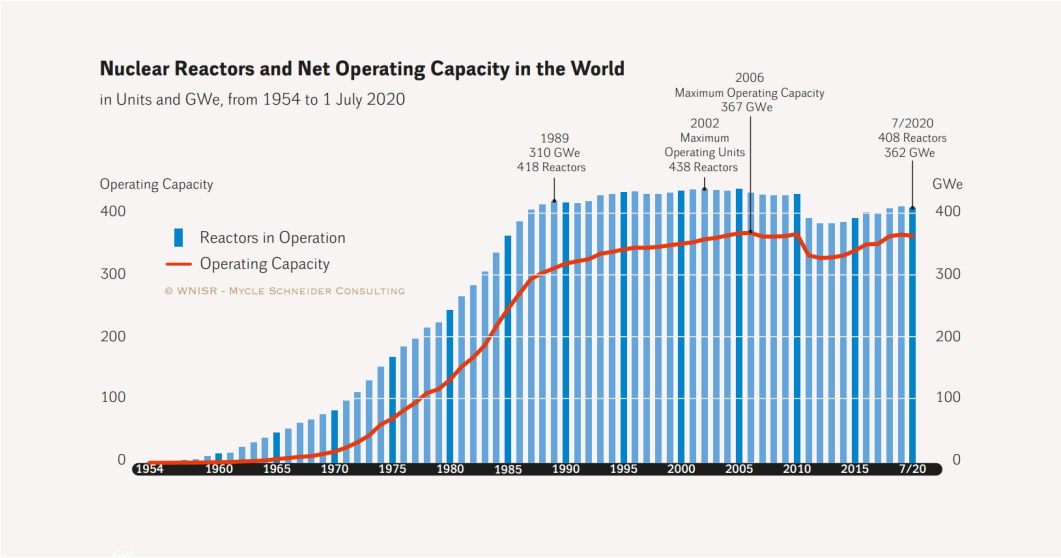

Figure 1.1: Number of operational nuclear reactors and net operating capacity in the world from 1954 to 2020 [SCH20]

After that, two severe accidents changed this trend. The first severe nuclear accident was the Three Mile Island (TMI) accident [TOT86] which occurred in the USA

on March 28th 1979. The second one was the Chernobyl accident [HOH86] on April 26th 1986 near the city of Pripyat in the Soviet Union. TMI and Chernobyl severe accidents were a wake-up call for the nuclear safety in the whole society [ZEB82]. An uncontrolled severe accident can cause the release of radioactive materials into atmosphere. Consequently, many nuclear reactor projects were suspended in the late 1990s. The main cause for the fall in nuclear operating capacity is nuclear safety. The situation became worse when the Fukushima Daiichi severe accident [IAE15] happened in 2011. Hydrogen released from the reactor core eventually resulted in explosions in the Fukushima containment building, which blew off the roof of the containment building [HIN13]. As the result of hydrogen explosion in containment buildings, radioactive materials were released directly into the atmosphere, resulting in a negative impact on human health and the natural environment. Therefore, it is vital to retain radioactive materials inside the containment building under any circumstances. The lessons learned from past severe accidents have significantly contributed to improving reactor safety. Overall, reactor safety is a top priority in the licensing and management of nuclear power plants.

Since most of the nuclear reactors worldwide are light water reactors, i.e., PWR and BWR, the background of this thesis is the numerical simulation of hydrogen mixing for the containment severe accident analysis in light water reactors. During a postulated severe nuclear accident, large quantities of steam, hydrogen, and radioactive products are released from the reactor coolant loop into the containment building. Hydrogen, as a very light gas, can accumulate in some regions in the containment building. The hydrogen mixing is related to the heat transfer between containment atmosphere and structures. If the hydrogen concentration is above the flammable limit of hydrogen–oxygen-steam mixtures, the potential of hydrogen explosion is the main challenge of containment integrity. The containment intensity is mandatory to maintain to prevent the release of radiative materials into atmosphere. It is crucial to have a detailed understanding of hydrogen transport in the containment during a postulated severe accident for effective mitigation of hydrogen in containment atmospheres [OEC99].

The accurate prediction of hydrogen distribution from its release point to the reactor containment atmosphere over a long time, such as several days, is still a challenging task considering the numerical efficiency and uncertainty in modeling. Numerical simulations play a crucial role in the containment safety assessment, particularly in some scenarios with limited experimental data. Due to the complexity and potential hazards in nuclear severe accidents, it is hard and expensive to perform large-scale experimental tests to gather comprehensive data. The thermal hydraulics phenomena during a severe accident in the containment building are complex. There are several physical phenomena related to the hydrogen distribution in containment buildings, e.g., the release of steam and hydrogen from the primary circuit, the stratification of hydrogen [KEL17], the wall condensation

on containment structures [KIM90], and the effect of spraying and passive recombiners. To prevent over-pressurization, an emergency venting system is installed to maintain the integrity of containment structures [GRO90]. The use of new technologies can help to ensure the integrity of containment; however, it is difficult to perform the reactor safety analysis.

Since the 1980s, a variety of lumped-parameter codes, e.g., RELAP [ALL10], COCOSYS [ALL08], ASTEC [DOR09], and GOTHIC [AND10], have been developed to predict the thermal-hydraulic behaviour under severe accident conditions in containment buildings as a basis for the reactor licensing and safety assessment. As the containment building is extremely large, e.g., 70000 m^3 for German 1300 MW_e PWR [HAS84], it is manageable to have an assumption of homogeneity in a large control volume ($0.01 \sim 10^2\, m^3$) to save computational time which is called the nodalization scheme [SHA10]. Most of the lumped-parameter codes utilize the nodalization scheme in the containment safety analysis. However, the resolved insights into the local phenomena in small regions are hard to obtain in lumped-parameter codes. Furthermore, it requires experimental data to generate empirical parameters for lumped-parameter codes. Nowadays, Computational Fluid Dynamics (CFD) methods are widely applied in nuclear safety analyses. The high-resolution temperature and hydrogen distributions can be obtained from CFD simulations, which is the main advantage of the CFD method. For example, the Ansys CFX [AND10] code solves fundamental conservation equations for multi-phase flows with mass, momentum, species and energy transport. However, it is difficult to add specific models for containment safety analysis in CFX, which requires in-depth knowledge of both the software and the specific physics involved in containment flows. Hence, the open source CFD package OpenFOAM [MOU16] is attracting considerable interest from the nuclear community for containment safety analysis. The *containmentFOAM* solver [KEL21], on the basis of open-source CFD toolkit OpenFOAM, is a tailored CFD package for the containment safety analysis developed at Forschungszentrum Jülich (FZJ).

The validation and verification of those computational codes are compulsory [OEC07b, MAL10]. An essential step in the development of specific CFD codes is validation against large scale experiments with the aid of advanced measurement techniques. The OECD-SETH project [PAL10] was carried out to understand the hydrogen behaviour in the reactor containment during a postulated severe accident. The Hydrogen Mitigation Experiments for Reactor Safety (HYMERES) project [AND19] was an international joint project, providing the validation database for CFD reactor safety analysis. Those projects were performed for understanding the heat transfer phenomena in containment flows. It is concluded that the impact of thermal radiation in a humid containment environment is significant [LIU22b]. Consequently, accurate modeling of thermal radiation heat transfer in combination with a well validated CFD model is pursued in the present work.

Many investigations on natural convection and buoyancy-driven flows using CFD codes were previously conducted [ROS09, OEC14b]. In the previous work, thermal radiation was unreasonably neglected due to modest temperature differences ($\Delta T < 100K$) in containment atmospheres. However, it depends on the relative strength of convective and conductive heat transfer to determine whether thermal radiation is of significance to the heat balance or not. The containment flows are mainly driven by buoyancy forces, which are closely linked to the temperature distribution. The radiation heat transfer affects the temperature and thereby changes the buoyancy forces and hydrogen mixing processes in containment flows. Additionally, under severe accident conditions the containment building is filled with a large amount of steam (> 60 vol.%) released from the cooling system. Hence, it must consider gas radiation in the hydrogen mixing process of containment atmosphere. The objective of this thesis is to investigate the radiative heat transfer within an absorbing and emitting medium and quantify its influence on the hydrogen mixing process under different humid conditions and impinging jets in containment atmospheres. This thesis focuses on developing a specific, reliable, and efficient thermal radiation solver with spectral gas properties for buoyancy flows in high humidity and low temperature atmospheres. Besides the reliable thermal radiation solver, the complex interaction between thermal radiation and buoyancy flows is also investigated. Thermal radiation can affect temperature distribution and thus change the density field. The interaction between thermal radiation and fluid is a complex nonlinear problem. In the presence of huge amounts of steam in the containment building, the bulk and wall condensations can change the spectral gas property and give rise to different radiative source terms in the energy equation. One task of this thesis is to quantify this complex effect.

The present thesis is divided into six chapters. Chapter 2 gives the background and motivation to clarify the nuclear severe accident and containment safety analysis. The following chapter, Chapter 3, is the description of the fundamental theory of thermal radiation modeling, clarifying the difficulties and challenges in the spectral gas properties and numerical efficiency with technical scale meshes. Different radiation solvers are presented to understand the difficulty of thermal radiation modeling. In Chapter 4, the tailored non-gray gas model and the Monte Carlo algorithm and its implementation are discussed. The verification and validation are given in Chapter 5, in which the PANDA H2P2 and ST1 experiments are selected to validate the Monte Carlo numerical solver. The last chapter, Chapter 6, summarizes the results of this thesis, recalls the major conclusions, and gives an outlook to future work.

Chapter 2

Background and Motivation

2.1 Severe Accident Scenario in Pressurized Water Reactors

The main advantage of nuclear power is the high energy density of uranium fuel [STA18]. Although nuclear power is considered a carbon-emission-free energy source [HOF02], there has been a strong awareness of the potential hazard of nuclear reactors after the TMI, Chernobyl and Fukushima severe accidents. Before discussing the numerical modeling, the severe accident scenario in PWRs is outlined in this section. The starting point of severe accidents in the pressurized water reactor is the loss of coolant event [UJI99], which may be caused by a number of reasons, e.g., the rupture of coolant pipes or the disconnection from electricity supply [OEC09a].

The coolant system in PWRs is illustrated in Fig. 2.1. The coolant system in PWRs consists of two separate circuits: the primary circle and the secondary circle. In the primary loop, water serves as both the coolant and neutron moderator which operates at a high pressure of around 160 atm to prevent boiling. The temperature of the coolant in the primary loop typically reaches around 600 K due to the fission heat. The primary loop is responsible for removing the nuclear fission heat generated in the reactor core. A pump is used in the primary loop to transfer the fission heat into the secondary loop. The functionality of the pump relies heavily on a continuous supply of electricity. The secondary loop has a steam generator to generate hot steam for turbines [TON79]. The nuclear fuel is located at the bottom part of the reactor vessel, and it is surrounded by zircaloy cladding, which provides structural support and corrosion resistance [ZIE13]. The fission energy can heat up the cooling water in the primary loop, and the thermal heat is transferred into the secondary coolant through the steam generator. During normal operation, the elec-

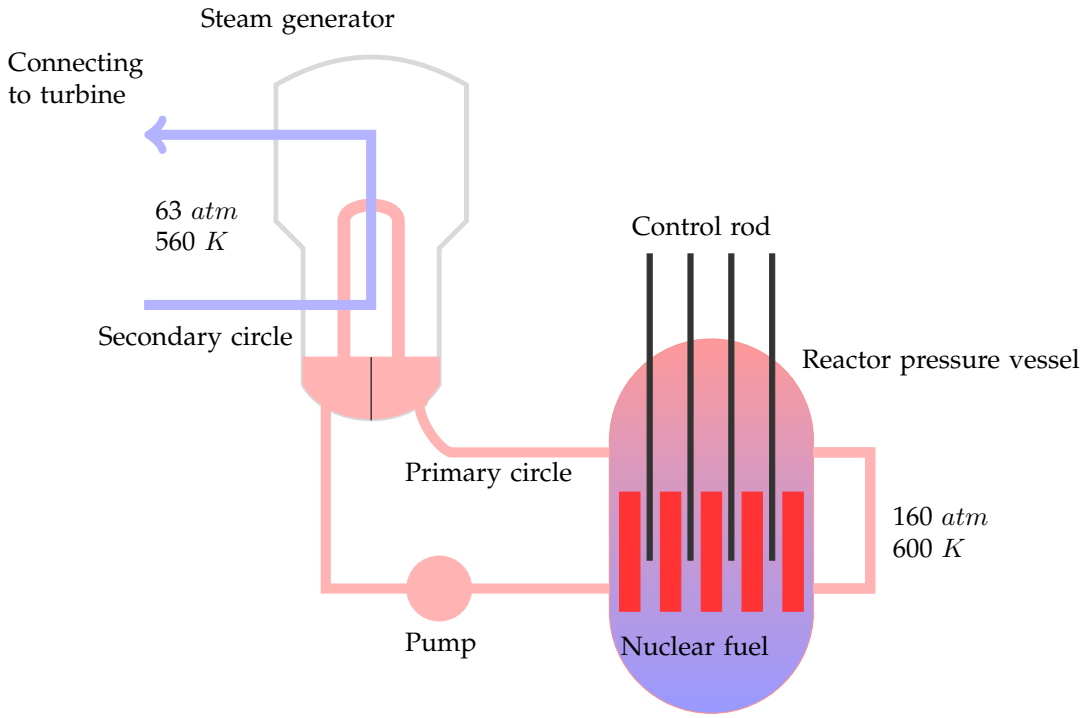

Figure 2.1: Schematic diagram of a pressurized water reactor

tricity supply network is mandatory for the primary pump. Without the supply of electricity in nuclear plants, an accident sequence may be initiated in pressurized water reactors, posing potential safety risks. After a loss of electrical power accident in the PWR, the reactor can immediately shut down through the injection of control rods. The fission reaction chain simultaneously stops; however, the decay heat from fission products must be removed from the core as quickly as possible. If the decay heat can not be effectively removed through the emergency core cooling system [HOF99], large amounts of hydrogen may be generated through the chemical reaction between the zircaloy cladding and steam [TAN11]. If the temperature of reactor core is above 1500 K, the chemical reaction between steam and zircaloy cladding is

$$Zr + 2H_2O \rightarrow ZrO_2 + 2H_2, \quad \Delta H_R = -586\,kJ/mol \tag{2.1}$$

The reaction heat released from the zircaloy-steam chemical reaction can further heat up the reactor core, leading to a core meltdown accident. It is reported that about 1300 kg of H_2 (15000 m^3) can be generated in the first 7 hours of the accident in a 1000 MW_e PWR [SAD17, SEH11]. The huge amounts of hydrogen may accumulate at the top of containment owing to its density. The hydrogen explosion can challenge the integrity of the containment building. The integrity of containment must be maintained to prevent the release of radioactive substances.

After the TMI and Fukushima severe accidents, the hydrogen explosion risk is a key consideration for the containment safety. The containment safety strategy is to keep the hydrogen concentration below the flammable limit. Various methods are employed to avoid the occurrence of flammable mixtures in a containment system: inert gas injection, passive auto-catalytic recombiner, and ignitor [IAE11]. The accurate prediction of hydrogen concentration is vital for the hydrogen removal system. Besides hydrogen, CO and CO_2 are also released into the containment atmosphere during the molten core concrete interaction (MCCI) phase [SEH11]. Carbon monoxide is a flammable gas; therefore, the potential risk of CO explosion is also important for ensuring nuclear safety.

There are many physical phenomena happening in the containment atmosphere, such as hydrogen stratification, bulk and wall condensation, hydrogen mixing, and aerosol release (see Fig. 2.2). If the decay heat is not effectively removed after a

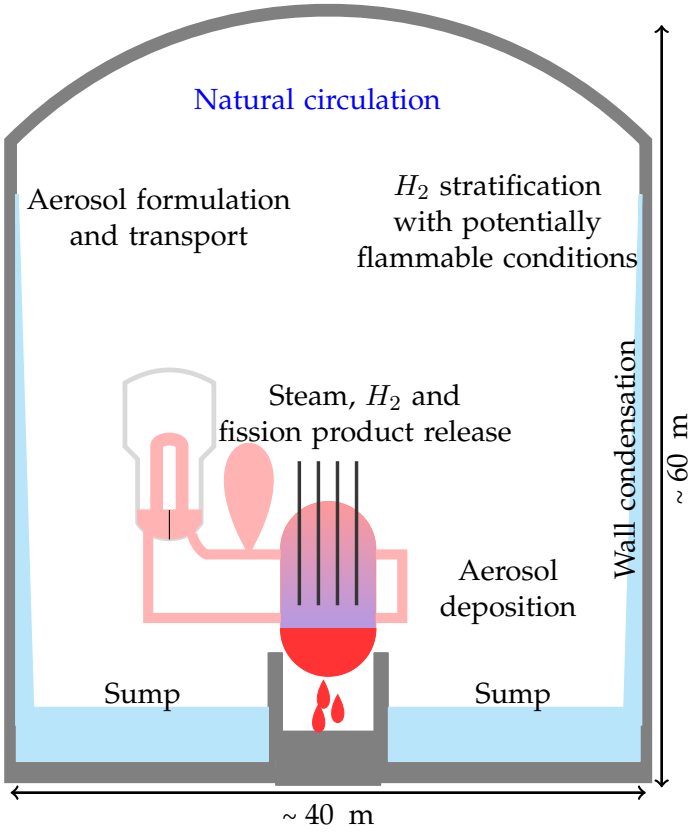

Figure 2.2: Physical phenomena during a PWR severe accident

LOCA accident, the molten core at around 2800 K impinges on the lower head of the reactor pressure vessel causing the failure of reactor pressure vessel. After the

hot steam-hydrogen-fission product jet is released from the reactor vessel, it becomes a plume in the containment building. The motion of gas in the containment atmosphere is mainly controlled by two forces: inertial force and buoyant force. Since the containment building is large enough (70000 m^3 for German 1300 MW_e PWR), the plume is mainly driven by the density difference in containment flows. The released hydrogen tends to accumulate at the top of the containment building owing to its density. If the concentration of hydrogen is above the flammable limit, the potential risk of hydrogen explosion is one of the main challenges for the integrity of containment. It is necessary to predict the local concentration of hydrogen in the containment atmosphere to implement the hydrogen mitigation method.

After the high-pressure hot steam and non-condensable gases are released from the primary coolant system, the hot steam and gases experience a rapid temperature drop leading to the formation of liquid water. The wall and bulk condensation processes can occur in the presence of large amounts of steam in containment flows. Consequently, the wall and bulk condensations can change the hydrogen mixing process. The condensation water can be collected in the sump containment, which is considered as a heat and mass source for the gas mixture composition in the containment atmosphere [MAL11]. Besides the hydrogen and steam, the fission products released from the primary cooling system are present in the form of aerosol. The aerosol formation and transport in containment atmosphere is vital to determine the source term in industrial safety studies. As depicted in Fig. 2.2, steam condensation on aerosols has a major impact on the overall deposition rate [FIS99]. The radiative aerosol deposition along with the bulk and wall condensation is another consideration in the reactor safety assessment [OEC09b].

If the integrity of the containment building is maintained, passive cooling systems [SEH11, CHE00], including natural circulation, condensation and spraying, can play a vital role in restoring and maintaining radioactive aerosols inside the containment to minimize the release of harmful substances into the environment following a nuclear accident. The main challenge of containment integrity is the potential for a hydrogen explosion in the presence of a large amount of hydrogen. When hydrogen releases from the primary cooling system, the phenomenon of hydrogen mixing in the containment building is a complex issue. Since the natural circulation plays an important role in the hydrogen mixing (see Fig. 2.2), the thermal hydraulics within the containment atmosphere may have a strong impact on the hydrogen mixing process. The difference in temperature can change the density field, which has a strong impact on the buoyant force. In order to ensure the functionality of hydrogen removal systems under different conditions, the accurate prediction of hydrogen distribution is vital in the containment design phase [OEC18]. The background of this thesis is the analysis of hydrogen distribution within the containment building.

2.2 Numerical Analysis for Containment Safety

The containment building is the last line of defense. After the failure of confinement in the Fukushima severe accident, radioactive materials were directly released into the atmosphere [SEH11]. Many efforts (theory, simulation, and experiment) have been conducted to clearly describe a timed sequence of the Fukushima accident, but none of them can successfully reproduce the process of a severe accident in detail for a number of reasons. First of all, there was no sufficient diagnostic information from the Fukushima accident, because most of the electronic sensor devices cannot work in a high dose radiation environment. On the other hand, the containment thermal-hydraulic modeling is still a challenging task. The containment safety analysis is related to a number of scenarios, from molecular scale to technical large scale over a long period of time (~ hours or days): aerosol transport, hydrogen stratification, wall and bulk condensation and turbulent mixing. An accurate and specific containment code is necessary to understand the sequence of severe accidents, to design new generation reactors, and to evaluate the containment safety. There are two kinds of numerical methods for the containment safety analysis: lumped parameter code and CFD [SEH11].

2.2.1 Lumped Parameter Code

After around 40 years development, a number of physical scenarios can be modeled in the lumped parameter codes [ALL10], e.g., condensation, aerosol, spraying and hydrogen deflagration. The lumped parameter codes (such as GOTHIC, GASFLOW, COCOSYS, CONTAM and ASTEC) are based on empirical equations to resolve the thermal-hydraulic behavior. Therefore, lumped parameter codes always require less computational time than CFD methods. The whole computation domain is divided into a number of coarse control nodes (~ m^3). For example, the GOTHIC [BOC16] 3D nodalization for the containment building is given in Fig. 2.3. The containment building is a complex facility with a number of complex compartments. Numerical simplification technique is required during the GOTHIC nodalization procedure to save the computational effort [OEC07b]. Since the control volume in the GOTHIC code is relatively large, the temperature and pressure spatial variations cannot be resolved within the control volume. Two control volumes in GOTHIC are linked to each other with a flow path [DOL15], which is used to calculate the mass and energy transfer between two control volumes. For example, the principle of mass conservation for the control volume i in CONTAM code [DOL15] is

$$\frac{\partial m_i}{\partial t} = \sum_j F_{i,j} + F_i \tag{2.2}$$

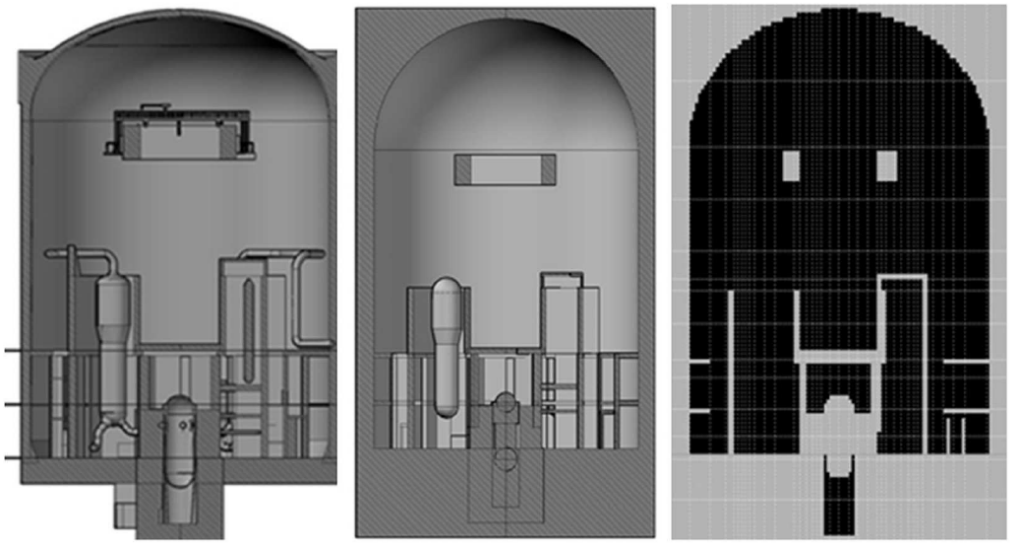

Figure 2.3: Containment modeling, detailed CAD model (left), simplified CAD model (middle) and GOTHIC nodalization (right) [BOC16]

where m_i is the mass of flow within the control volume i; $F_{i,j}$ is the mass flow rate between the control volume i and the control volume j; F_i is the mass source term. Since the flow path method is applied in lumped parameter codes, the coarse mesh simplification may underpredict the penetration of the hot jet in containment flows [OEC07b]. As the control volume is relatively large in lumped parameter codes, turbulent effects are not modeled in lumped parameter codes. The turbulent heat transfer is taken into account via empirical equations. There are many empirical parameters defined by the user to obtain reliable results, and those empirical parameters are generated from the experimental data.

For example, steam condensation is an important phenomenon to remove the decay heat from the reactor core under a postulated accident. The complex interaction between hot steam and wall on the boundary layer is difficult to resolve in numerical codes. To reduce the computational effort, lumped parameter codes apply the empirical equation to simulate the wall condensation in containment flows [OEC99]. The most used empirical equation for steam condensation, proposed by Uchida [UCH64] in 1965, was obtained from experimental data. The condensation heat flux $q''_{condensation}$ between hot steam and containment structures can be simplified as

$$q''_{condensation} = h_{condensation} \Delta T \qquad W/m^2 \tag{2.3}$$

where ΔT is the temperature difference between wall and media. The heat transfer

coefficient $h_{condensation}$ is given by

$$h_{condensation} = 380 \left(\frac{Y_{n/c}}{1 - Y_{n/c}} \right)^{-0.7} \qquad W/(K \cdot m^2) \tag{2.4}$$

where $Y_{n/c}$ is the mass fraction of non-condensable gases. This model is one of the condensation correlations implemented in GOTHIC code [PAP11]. In order to improve the numerical accuracy, more condensation experiments are required to modify the empirical parameters. Furthermore, more investigations about the accurate simulation of injection jets and associated mixing processes, sufficient refinement of nodalisation, and elimination of numerical disturbances are required in the lumped parameter codes.

In order to provide validation databases for the containment solver, a number of international projects, e.g., ERCOSAM [PAL03], SETH-1 [PAL10], SETH-2 [OEC12], have demonstrated the accumulation of hydrogen in containment buildings due to its density when there is no hydrogen mitigation system present. Even though having a high concentration of steam in the containment atmosphere, the hydrogen explosion is likely to happen when the hydrogen concentration exceeds the flammable limit for steam-air-hydrogen mixtures. After performing a number of experiments related to containment safety, the international standard problem ISP-47 [OEC07b] on containment thermal hydraulics is proposed to assess the capabilities of lumped parameter and CFD codes in the containment safety analysis. The previous investigation has concluded that lumped parameter codes can predict temperatures and steam concentrations well in comparison to the experimental data [ALL08]. However, the lumped parameter code can not capture the flow pattern by using the coarse nodalisation near the injection region [OEC07b]. The velocity field cannot be calculated in lumped parameter codes by using the large nodalization scheme. The numerical uncertainty may accumulate over a long simulation time leading to unreasonable predictions. Hence, it is necessary to develop a specific CFD code to provide code-to-code and code-to-experiment comparisons for the containment safety analysis. The importance of CFD modeling in the containment safety analysis is the inherent three-dimensional effect without numerical simplifications which can not be predicted by lumped parameter codes. Therefore, a tailored CFD containment solver, named *containmentFoam* [KEL21, KAM21, LIU22b], has been developed at Forschungszentrum Jülich for the containment safety assessment.

2.2.2 Computational Fluid Dynamics

Different from the lumped-parameter method, the computational domain is divided into a number of fine control volumes in the CFD method. The computa-

tional mesh is fine enough to capture boundary layers. In consequence, the number

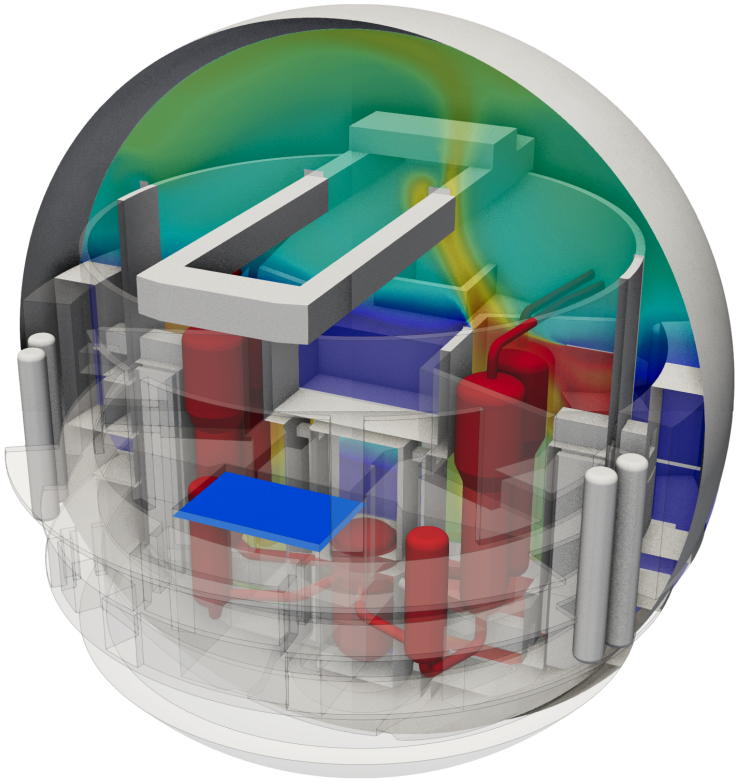

Figure 2.4: Generic containment geometry in *containmentFoam* [KEL23]

of control volumes for the containment safety analysis may be larger than 1 million in the CFD method [KEL21]. In order to resolve the shear stress on the boundary wall, it requires a huge amount of control volumes near the boundary layer in CFD simulations [SCH16]. When using a fine mesh in CFD simulations, the gradient of velocity and temperature can be calculated without using any empirical equation (see Fig. 2.4). The complex containment compartments are considered in Fig. 2.4 in respect to real reactor conditions. However, the numerical accuracy is sensitive to the CFD mesh [AND08]. The mesh uncertainty is mandatory to quantify in the containment safety analysis [JI23].

A number of papers have been published related to the CFD modeling in containment flows, e.g., condensation [ZSC14, KUM21], buoyancy turbulence [KAM21], passive autocatalytic recombiner [KEL21] and bubble modeling [LIA22]. The comparisons between the simulation and experiment have concluded that CFD modeling can be applied for the containment safety analysis [IAE03]. The containment flows are characterized as multi-phase, multi-species turbulent flows with low Mach numbers. Consequently, many numerical models and libraries are re-

quired in *containmentFoam* [KEL21]: the buoyancy turbulence model; the multi-component species transport model for non-premixed mixtures; the wall and bulk condensation model; and the thermal radiation model. The computationally efficient Unsteady Reynolds-Averaged Navier-Stokes (URANS) approach [WIL98] can describe the time averaged turbulence flows with high accuracy in engineering applications, and turbulence fluctuation is commonly modeled by the two equation models, e.g., $k-\omega$ and $k-\epsilon$ models [WIL98]. The CFD governing equations are the conservation of mass, momentum and total energy laws. In addition, the fluid status follows the ideal gas equation due to the relatively low pressure in containment safety analysis. The CFD governing equations are as follows.

$$\frac{\partial \rho}{\partial t} + \nabla \cdot (\rho U) = S_m''' \tag{2.5}$$

$$\frac{\partial (\rho Y_i)}{\partial t} + \nabla \cdot (\rho U Y_i) = \nabla \cdot \left[\rho \left(D + \frac{\nu_t}{Sc_t} \right) \nabla Y_i \right] + S_Y''' \tag{2.6}$$

$$\frac{\partial (\rho U)}{\partial t} + \nabla \cdot (\rho U U) = \nabla \cdot \tau - \nabla p + \rho g + S_U''' \tag{2.7}$$

$$\tau = \rho(\nu + \nu_t) \left[\nabla U + (\nabla U)^T - \frac{2}{3} \delta \nabla \cdot U \right] \tag{2.8}$$

$$\rho = \frac{pM}{RT} \tag{2.9}$$

where ρ is the fluid density; U is the velocity vector; S_m''' is the mass source term; Y_i is the i–th species mass fraction; D is the molecular diffusivity; Sc_t is the turbulent Schmidt number; S_Y''' is the species source term; S_U''' is the momentum source term; τ is the Reynolds shear stress; ν is the kinematic viscosity; ν_t is the turbulent kinematic viscosity; δ is the Dirac delta function; g is the gravitational acceleration; p is the total pressure; R is the universal gas constant; M is the molecular weight.

The numerical calculation of Navier-Stokes equations is a challenging task due to lack of the pressure equation. The most common procedure for CFD simulations is to derive a pressure equation from the momentum and continuity equations [FER02]. The SIMPLE algorithm is a common procedure to solve the pressure-velocity equations in CFD codes, which is an acronym for semi-implicit method for pressure linked equations in CFD [PAT18]. Since turbulence is important for the hydrogen mixing process in containment flows, the characterization of turbulence must be considered with a high accuracy. In this thesis the standard two equation $k-\omega$ SST model is employed to calculate the turbulent kinematic viscosity. Furthermore, the buoyancy turbulence source term is crucial in the prediction of hydrogen erosion in containment flows [KAM21]. The standard $k-\omega$ SST[1] model with the

[1] SST-2003, https://turbmodels.larc.nasa.gov/sst.html

buoyancy turbulence source term is

$$\frac{\partial(\rho k)}{\partial t} + \nabla \cdot (\rho U k) = P - \beta^* \omega k + \nabla \cdot [(\mu + \sigma_k \mu_t)\nabla k] + P_{k,b} \tag{2.10}$$

$$\frac{\partial(\rho\omega)}{\partial t} + \nabla \cdot (\rho U \omega) = \frac{\gamma}{\nu_t} P - \beta \rho \omega^2 + \nabla \cdot [(\mu + \sigma_\omega \mu_t)\nabla\omega] + 2(1 - F_1)\frac{\rho\sigma_{\omega 2}}{\omega}\nabla k \cdot \nabla\omega + P_{\omega,b} \tag{2.11}$$

where k is the turbulent energy; ω is the specific rate of dissipation; P is the turbulence production; $P_{k,b}$ is the turbulence production due to buoyancy; μ is the viscosity; μ_t is the turbulent viscosity; $P_{\omega,b}$ is the turbulence dissipation due to buoyancy; F_1 is the blending function; β^*, σ_k, β, γ, σ_ω, $\sigma_{\omega 2}$ and γ_1 are model constants. After the k and ω equations are solved in CFD codes, the turbulent viscosity ν_t is calculated as

$$\nu_t = \frac{k}{\omega} \tag{2.12}$$

The turbulence model has a strong effect on the hydrogen mixing in containment flows. Therefore, the best practice guideline for the nuclear safety analysis is applied in numerical simulations [AND08].

The hydrogen mixing in containment flows is not only related to the turbulence modeling but also the density field. In the past, a considerable number of investigations about containment thermal-hydraulics were conducted [OEC12, OEC16, SEH11]. It is concluded that the hydrogen mixing process is closely related to thermal-hydraulic phenomenon in the containment flow. In the transient phase, containment flows are mainly driven by the temperature difference or buoyancy force. The correct temperature predication is also vital to resolve the hydrogen mixing in containment flows over a long term. In *containmentFoam* the conservation of total enthalpy $h_{tot} = h + \frac{1}{2}U^2$ equation is given as follows

$$\frac{\partial(\rho h_{tot})}{\partial t} + \nabla \cdot (\rho U h_{tot}) = \rho U \cdot g + \frac{\partial p}{\partial t} + \nabla(\lambda + \lambda_t)\nabla T - \sum_i h_i \nabla \cdot J_i - \nabla \cdot q_r + S_h''' \tag{2.13}$$

where J_i is the mass diffusion flux of species i; h_i is the i–th species enthalpy; λ is the thermal conductivity; λ_t is the turbulent thermal conductivity; $\nabla \cdot q_r$ is the radiative source term; S_h''' is the energy source term. In multi-component flows, the diffusion of enthalpy $\nabla(c_p T)$ in the energy equation must be taken into account to obtain a consistent temperature predication in containment flows [KEL21]. In the energy equation Eq. 2.13, the radiation source term is one of the source term $\nabla \cdot q_r$ in containment flows.

After the definition of computational geometry in the containment safety analysis, the general conservation of flow variable ϕ is given in Eq. 2.14.

$$\frac{\partial(\rho\phi)}{\partial t} + \nabla \cdot (\rho U \phi) - \nabla \cdot (\rho\Gamma\nabla\phi) = S'''(\phi) \tag{2.14}$$

The integral conservation law is applied for each control volume in the finite volume method (FVM) [VER07]. There is no path flow between two control volumes in the CFD method. In the finite volume method, the fluxes, representing the mass, momentum or energy, are evaluated across the control surfaces where the fluid flow either enters or exits the control volume. Therefore, all numerical quantities have clear physical meaning in CFD simulations. Since the computational domain is divided into a number of fine control volumes in CFD simulations, the conservation equation for each control volume in integral form is

$$\int \frac{\partial(\rho\phi)}{\partial t} dV + \oint (\rho U \phi) \cdot \vec{n} dS - \oint (\rho \Gamma \nabla \phi) \cdot \vec{n} dS = \int S'''(\phi) dV \tag{2.15}$$

As shown in Eq. 2.15, the partial differential equation is converted into a surface integral problem after applying the Gauss law [PAT18]. For example, the discretisation of the convection term in Eq. 2.15 for the CFD method is

$$\begin{aligned} \int \nabla \cdot (\rho U \phi) dV &= \oint (\rho U \phi) \cdot \vec{n} dS \\ &\simeq \sum_{face} (\rho U \phi)_{face} \cdot S_{face} \end{aligned} \tag{2.16}$$

where S_{face} is the surface area for the control volume. To illustrate the idea of finite volume method, a simple example is shown in Fig. 2.5. The control volume P has five neighbouring control volumes. It is noted that the flow variable ϕ is not stored on the surface but on the volume center. In order to calculate the face flux between the control volume P and the control volume $Neighbour$ in Fig. 2.5, a numerical interpolation scheme is defined to reconstruct the surface value ϕ_{face} from the volume centres. The most common one is the linear upwind scheme [JAS96]. The linear upwind scheme is

$$\phi_{face} = \phi_P + \nabla\phi \cdot (\vec{x}_{face} - \vec{x}_P) \tag{2.17}$$

$$\simeq \phi_P + \frac{\phi_P - \phi_{Neighbour}}{|\vec{x}_P - \vec{x}_{Neighbour}|} |\vec{x}_{face} - \vec{x}_P| \tag{2.18}$$

where $\vec{x}_P$ is the position of point P.

As shown in Fig. 2.5 the surface center is not coincide with the center of line $P - Neighbour$, which is called the non-orthogonality error in CFD simulations. The OpenFOAM framework provides a number of interpolation schemes, e.g., linearUpwind, limitedLinear and LUST [MOU16], to minimize the numerical error. The accuracy of numerical interpolation is also related to the computational mesh. If the flow variable ϕ changes rapidly in the computational domain, it is necessary to refine the discretisation mesh to reduce the numerical error. The mesh sensitivity investigation is also recommended for CFD numerical simulations [JI23]. The detailed description about the finite volume method can be found in the literature

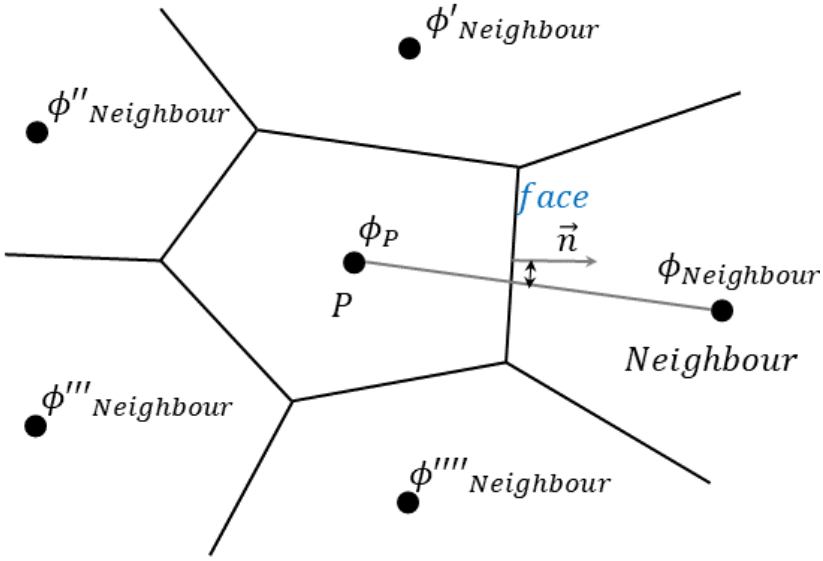

Figure 2.5: Surface interpolation in FVM

[JAS96, MOU16]. After the numerical discretisation and reconstruction, the algebraic equation for the flow variable ϕ is expressed as

$$a_p\phi_p + \sum_{l}^{neighbour} a_l\phi_l = b \tag{2.19}$$

where a_p is the linear coefficient for the point p; a_l is the linear coefficient for the neighbour point l; ϕ_l is the value at the neighbour point l; b is the linear source term.

After discretizing the partial differential equation and converting it into a system of algebraic equations $Ax = b$, there are several matrix algorithms can be employed to solve the resulting system [FER02]. The dimension of the computational matrix A may be larger than one million for CFD simulations in real containment buildings, capturing the high-resolution of fluid fluctuation in containment flows, which can not be obtained by lumped parameter codes. The CFD simulation becomes an important tool to predict the hydrogen mixing in containment flows with the development of computational capability [KEL21]. The tailored *containmentFOAM* code has already validated against several experiments, e.g., THAI [KEL21, KUM20] and PANDA [LIU22b]. The simulation results obtained from *containmentFoam* are in good agreement with experiment. In addition to the detailed CFD modeling in *containmentFoam*, another advantage is that *containmentFoam* can couple with the system code to model the passive auto-catalytic recombiner in containment flows.

However, more investigations are required to develop tailored numerical models for the reactor safety analysis. In the past, thermal radiation was neglected in the containment flow simulations for the reason of relatively low temperature levels. Recently many experiments have shown that gas radiation even at low temperature levels can play a significant role in low velocity or natural convection flows in large cavities [PAL10, OEC21]. A series of steam injection experiments has been conducted to understand the relationship between the buoyancy driven flow and the thermal radiation in the PANDA facility, which is designed for the containment safety analysis at PSI. Considering that the hydrogen transport and mixing processes are primarily driven by buoyancy forces, thermal radiation absorption within the non-gray media can have an effect on the flow and transport processes inside the containment. Furthermore, it was found that the non-gray gas model can affect the radiative source term in the thermal radiation solver, leading to a different temperature prediction [KEL21, LIU21].

2.3 Thermal Radiation Modeling in Containment Flows

In order to predict the hydrogen concentration accurately in containment atmospheres after a postulated severe accident, thermal radiation heat transfer phenomenon is necessary to be considered in the CFD energy equation. The radiative heat transfer plays an important role in the hydrogen mixing process as it can change the temperature distribution with large amounts of steam in the containment flow. But few investigations were performed to quantify the influence of thermal radiation within the containment flows [LIU22b]. Even though the temperature inside the containment is relatively low, the steam molar fraction may be 60 vol.% or larger during the severe accident [SEH11], which has a strong absorption effect over the infrared radiation spectrum. The strength of the radiative source term is comparable with that of conduction and convection terms in containment flows, especially in the low-velocity regions. Moreover, the radiation absorption effect is amplified when the infrared active gases, such as H_2O and CO_2, mix with the transparent gases, e.g., N_2. Theoretically, thermal radiation can transfer heat over a longer distance than conduction and convection, which makes the temperature field smooth in containment flows.

However, the numerical coupling of CFD and thermal radiation simulation over a long term (> days) in containment flows is still unclear due to the computational effort. Although the thermal radiation is not the dominant heat transfer mode for severe accident analyses, thermal radiation heat transfer is not a local phenomenon. In such a case, it has a significant effect on the temperature and density fields. Due to the fact that hydrogen has a wide flammability range, the hydrogen concentration must be precisely predicted to prevent an unexpected explosion. More investi-

gation is necessary to quantify this complex relationship between CFD and thermal radiation modelings. A more efficient and reliable radiation solver with spectral gas properties is mandatory to fill the gap in the containment safety analysis. In this thesis the effect of thermal radiation heat transfer is investigated, which plays a significant role in the balance of thermal energy. The spectral radiative transfer equation [MOD13] within a non-scattering medium is shown in Eq. 2.20. The radiative source term is equal to the difference between radiative absorption energy and emission energy.

$$\Omega \cdot \nabla I_\eta(r,\Omega) = -\kappa_\eta I_\eta(r,\Omega) + \kappa_\eta I_{b,\eta}(r,\Omega) \tag{2.20}$$

$$\nabla \cdot q_r = \int_\eta \int_{4\pi} \kappa_\eta I_{b,\eta}(r,\Omega) d\eta d\Omega - \int_\eta \int_{4\pi} \kappa_\eta I_\eta(r,\Omega) d\eta d\Omega \tag{2.21}$$

where η is the wavenumber; Ω is the solid angle; κ_η is the spectral absorption coefficient; I_η is the spectral intensity; $I_{b,\eta}$ is the black body emission spectral intensity. The absorption coefficient κ_η is the description of absorption effect for the non-gray gas species, which is wavenumber dependent. The detailed discussion about spectral gas properties can be found in Chapter 3. Thermal radiation simulations require fine spatial and angular resolutions with the spectral gas property to accurately capture the radiation transport behavior in containment atmospheres.

Thermal radiation is among one of the heat transfer mechanisms in the energy equation (see Eq. 2.13). The accuracy of heat transport modeling is also affected by the turbulent flow. Numerical modeling of radiative heat transfer within non-gray gas mixtures is extremely difficult. It is necessary to develop an efficient thermal radiation solver for the radiative transfer equation. In addition, the interaction between thermal radiation and CFD is complex to quantify. The CFD and thermal radiation coupling algorithm is presented in Fig. 2.6. When solving the radiative transfer equation, the transient temperature, total pressure, and partial pressure are obtained from the CFD module. The absorption coefficient κ_η is updated based on the given temperature and pressure fields before the radiative transfer equation is solved. After solving the radiative transfer equation, the radiative source term is coupled with other energy terms in the total enthalpy equation. The interaction between CFD and thermal radiation is described in section 4.4. There are numerous studies about the simulation of CFD and thermal radiation using segregated solvers, but not in the containment flows. In containment flows, the impact of nonlinear interaction is not completely understood over a long transient period. After a long transient period the numerical error generated from the thermal radiation and CFD solvers may accumulate leading to significant differences. However, modeling the radiative heat transfer is a difficult task even with the help of high-performance computers for the reason of spectral gas property κ_η, variation of temperature T and pressure p, and spatial distribution of radiative intensity $I(r,\Omega)$ in different solid angles Ω.

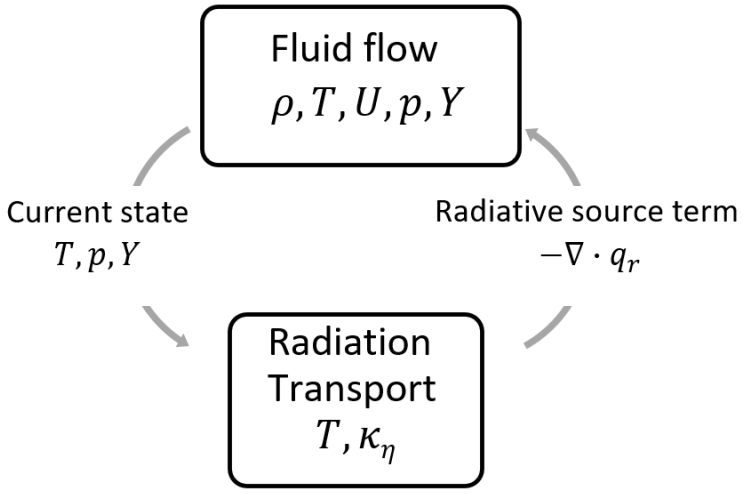

Figure 2.6: Numerical algorithm for the coupling of CFD and thermal radiation

Two kinds of thermal radiation heat transfer are considered in containment flows: surface-to-surface radiation and non-gray gas radiation [OEC14a]. Cheng et al. [CHE00] investigated the Westinghouse AP600 containment design for the decay heat removal by natural convection flows with the surface-to-surface radiation modeling. It has found that the high surface emissivity can improve the thermal radiation heat transfer between media and containment structures in containment flows. Therefore, the surface emissivity may have a strong impact on the hydrogen concentration profile on boundary walls. The small scale DIANA [DEH19] experiment demonstrated the impact of surface-to-surface radiation in natural convection flows within small cavities. Both RANS and LES methods were applied to simulate this experiment with and without considering the surface-to-surface radiation. It was concluded that the temperature distribution is consistent with the experiment when accounting for the surface-to-surface radiation in numerical simulations. After the direct containment heating phase [BOE93], the wall temperature is lower than the media temperature in containment flows. Consequently, only the surface-to-surface thermal radiation is not enough in the thermal radiation analysis for containment flows. The non-gray gas radiation heat transfer within the containment atmosphere cannot be neglected in the presence of large amounts of steam.

The challenges of gas radiation analysis are twofold: one is the modeling of spectral gas properties; the other is the efficiency and accuracy of radiation solvers. Although the computation capability has drastically increased in last decades, solving thermal radiation transport within a non-gray gas media is still an expensive task,

even for steam-air mixtures. The absorption coefficient varies significantly over the whole infrared radiation spectrum, making the radiative transfer equation more difficult to solve. There are three infrared active gases in containment atmospheres: steam, CO and CO_2. As shown in Fig. 2.7, the steam, CO and CO_2 absorption coefficients are strongly dependent on the wavenumber. The steam, CO and CO_2

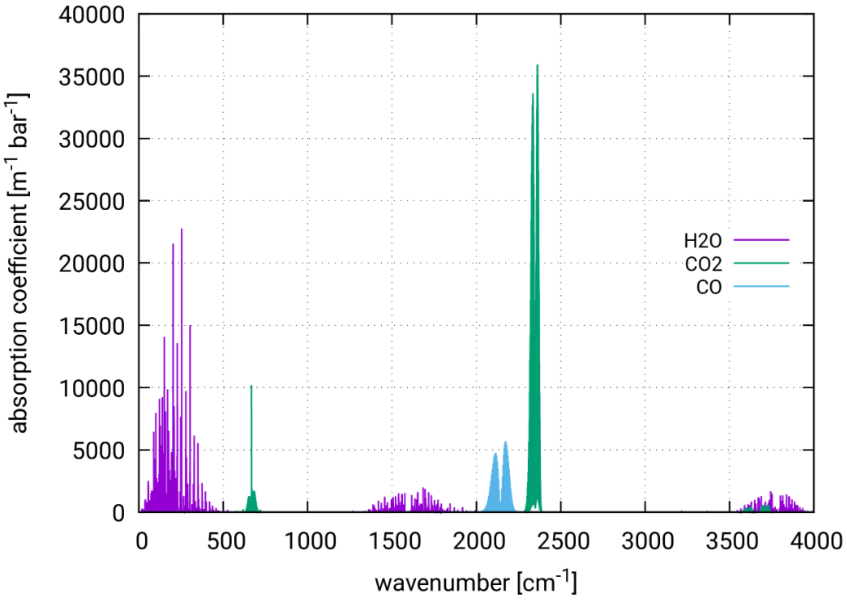

Figure 2.7: H_2O, CO_2, and CO LBL absorption coefficients at 300 K

absorption spectra have a number of discrete absorption bands. The absorption effect is not continuous over the whole infrared radiation spectrum, and there is a transparent gap between two absorption bands for non-gray gases. The non-gray gas analysis is more complex than the surface-to-surface radiation, considering the variance of absorption coefficients. According to the spectral resolution, there are four main types of non-gray gas model in thermal radiation analyses: gray gas model, wide band model, narrow band model, and Line-by-Line model.

The simplest gas property model is the gray gas model based on the Planck mean absorption coefficient [ZHA02]. The Planck mean absorption coefficient is only a function of temperature and partial pressure of species, i.e., H_2O, CO and CO_2. There is no spectrum interval for the gray gas model and the radiation intensity is resolved over the whole infrared spectrum. As a result, the gray gas model is an efficient way to obtain a rough estimation, and it is faster than other non-gray models. The gray gas model can be applied for different radiation solvers for the code-to-code verification. Under the gray gas assumption, the impact of spectral gas property can be eliminated to compare the numerical stability and ac-

curacy of different radiation solvers. The gray assumption is reasonable in flame simulations considering the formation of soot. In the past decades, the gray gas model was generally coupled with the P_1 radiation solver in combustion applications [MOD13, HOW20]. But it is not suitable for the containment safety analysis because of the numerical error over a long transient period.

The weighted-sum-of-gray-gases (WSGG) model is widely employed in engineering calculations. It represents the spectral gas property by using a few gray gases with different weighting factors according to the fluid temperature. The finite volume discrete ordinates method (fvDOM) with the WSGG model is a common choice for thermal radiation analysis in combustion applications. Unfortunately, most of the existing WSGG models are developed for the combustion chambers with a fixed p_{H_2O}/p_{CO_2} ratio, not specific for containment applications. The wide band model, e.g., Exponential Wide-Band model, has a band resolution around 500 cm^{-1} based on the main vibration-rotation bands. In other words, the wide band model only considers the strongest vibration-rotation bands within the whole spectrum (see Fig. 2.7). The exponential wide band model only provides the spectral gas property in terms of transmissivity, not the absorption coefficient which is required for the radiative transfer equation [STR02]. Therefore, this model is suitable to integrate with the discrete transfer method (DTM), which only requires the transmissivity. Yin et al. [YIN10] applied the exponential wide band model as the reference to derive the WSGGM model.

The statistical narrow band model (SNB) [RIV95] gives the band parameters with a spectral width 25 cm^{-1} from 150 - 9300 cm^{-1}. Similarly, the statistical narrow band model also gives the band transmissivity. In order to extract the absorption coefficient from the SNB model, the statistical narrow band correlated-k model was published from the EM2C laboratory [SOU97] in France. The fvDOM solver with the statistical narrow band correlated-k model requires a large amount of computational time. The most accurate model for spectral gas properties is the Line-by-Line model, which is based on quantum mechanics. The updated HITRAN2016 database [ROT09] is a compilation of molecular absorption parameters for low temperature applications (< 1000 K). It contains thousands of transition lines in the 10-9000 cm^{-1} region. However, it is rare to perform the Line-by-Line integration calculation in engineering applications due to the computational effort it requires [CHU12]. The Line-by-Line integration model is suitable for the benchmark test cases to verify/assess other non-gray gas models. The containment flow conditions are far from combustion regarding its temperature level ($\leq 1000\,K$), pressure level (1 ~ 8 bar) and optical thickness (high steam concentration). Nevertheless, there is no dedicated non-gray gas model for the reactor severe accident analysis. Besides, the volume of containment building is about 80000 m^3 for a 1000 MW_e commercial PWR. In such a case, the thermal radiation absorption effect is more significant than small scale facilities. A tailored non-gray gas model is necessary for containment

safety analysis. In order to verify and assess the accuracy of the new development, the LBL model is also required to provide the code-to-code verification. In addition to spectral gas properties, the second objective of this thesis is to develop a reliable and efficient thermal radiation solver for complex 3D engineering geometries.

For the thermal radiation numerical solvers, there are two in-built radiation models in OpenFOAM-6: P_1 and fvDOM. The P_1 model is the first-order spherical harmonics method, assuming the radiation intensity is isotropic in the solid angle Ω. In other words, the P_1 model cannot resolve the directional dependency of radiation intensity. Consequently, the P_1 model is only suitable for optically thick applications. The diffusion approximation is barely accurate in the optically thin media. The P_1 radiative transfer solver is a reasonable choice, but the numerical accuracy is compromised for the sake of computational resources. The fvDOM method is computationally expensive [COE14], which resolves angular radiation intensity $I(x, y, z, \Omega)$ at a set of quadrature directions Ω. Furthermore, the fvDOM solver suffers from false scattering and ray effect [CHA93]. When considering the spectral gas properties, it is required to solve a set of quadrature directions for each spectral band, making the SNBCK model consideration in fvDOM impractical. The other kind of radiation solver is the ray tracing method, e.g., Monte Carlo and the discrete transfer method. Although the Monte Carlo radiation solver is the most time-consuming among the existing radiation solvers, the computational effort does not significantly increase when considering non-gray gas models in the Monte Carlo method. This is because the Monte Carlo method solves the integral form of radiative transfer equation, not resolving the spectral radiation intensity. In the next chapter, Chapter 3, the existing radiation numerical solvers, e.g., P1, fvDOM and Monte Carlo method are investigated under the gray gas assumption to assess the numerical accuracy. The purpose is to select a reliable and suitable radiation solver for thermal radiation analysis in containment flows. With the gray gas assumption, the impact of the spectral gas property can be eliminated.

2.4 Open Issues and Objectives

While the previous work already identified the certain impact of gas radiation heat transfer on the prevailing flows and transport processes, they also confirmed a strong sensitivity to the chosen solver and approximation of the radiative transfer equation, the model for spectral gas properties and related numerical schemes and coefficients [LIU22a]. Mostly the P_1 approximation of the radiative transfer equation was employed along with a gray gas assumption without further justification. Existing radiation modeling experience originate from other applications, primarily combustion engineering, which cannot be directly transferred to containment analysis.

Thus, the overall objective of this thesis is to investigate the effect of thermal radiation heat transfer in containment flows, in particular with respect to the slow natural circulation processes occurring subsequent to the depressurization of the reactor cooling system. For this purpose, the first task is to develop a numerically accurate and efficient thermal radiation solver, which can be used to analyze radiation transport in complex 3D geometries. Secondly, suitable spectral gas property models for the non-gray gas mixture are identified and tailored for the expected range of thermo-fluid dynamic conditions in the containment atmosphere during a severe accident. However, the numerical analysis of thermal radiation is still a challenging task for a number of reasons:

- The mathematical description of equilibrium radiative transfer equation is a function of six independent variables: position, solid angle, and emission wavenumber. Even though assuming the gray gas property, solving the radiation intensity in large 3D geometries is still tedious and computationally expensive, especially for the containment building.
- Another issue related to thermal radiation analysis is the spectral gas property. Different from the gray assumption for the wall emissivity, the non-gray gas absorption coefficients (e.g., H_2O, CO_2 and CO) vary strongly along the wavenumber η, and the simplest gray gas assumption is far from satisfactory. The other task for thermal radiation analysis is to develop a tailored non-gray gas model in a balance between efficiency and accuracy for high steam concentration atmospheres.
- In addition to the radiation modeling, the complex interaction between thermal radiation and CFD is also investigated in containment flows. However, it is computationally unaffordable to perform the thermal radiation calculation for each CFD time step. A lot of effort has been spent on the thermal radiation solver to optimize its efficiency in large scale facilities.

In order to obtain a predictive approach, both the thermal radiation solvers as well as the spectral gas property models need to be as independent as possible from case specific user inputs. The impact of the remaining parameters is also investigated in the coupled thermal radiation and CFD simulations. After a thorough verification of the developed methods, their validity is demonstrated by comparison against application-oriented experiments. Simultaneously, their performance is compared against other existing spectral gas property models to evaluate the accuracy. The physical insight obtained in the validation experiments is used to derive a first understanding how radiative heat transfer changes the hydrogen mixing process in containment flows.

Chapter 3

Theory of Thermal Radiation Transfer

In this chapter, the fundamental theory of thermal radiation heat transfer is introduced, beginning with the black body emission law, followed by the derivation of the radiative transfer equation. Since the containment flow is filled with huge amounts of steam, a number of non-gray gas models including its advantage and disadvantage are briefly discussed in section 3.2. Furthermore, different non-gray gas models are assessed in the one-dimensional analytical test cases to compare the numerical accuracy and efficiency. The last section of this chapter discusses the radiation solver. Different radiation solvers are described in section 3.3 to shed light on thermal radiation simulations.

3.1 Fundamental Concepts and Equations

The fundamental theory of thermal radiation is totally different from conduction and convection. Conduction and convection heat transfer modes are related to the movement of molecules or atoms. However, thermal radiation is a kind of electromagnetic field. Therefore, thermal radiation can propagate over a long distance in vacuum. The speed of thermal radiation photons in vacuum is commonly denoted by c ($2.9979 \times 10^8\, m/s$). Thermal radiation can change the internal energy of molecules by radiation absorption and emission. According to the quantum theory [HEI84], the energy of an incoming photon with a wavelength λ is

$$E = h\nu = h\frac{c}{\lambda} \tag{3.1}$$

where h is the Planck constant ($6.626 \times 10^{-34}\, J \cdot s$); ν is the frequency of the incoming wave. From Eq. 3.1, the energy of the radiation photon is only related to its frequency ν. The high energy photon ($> 10\, eV$) can initiate the ionizing radiation which is widely applied in the modern diagnostic imaging machine for the healthcare system. However, in this thesis, the thermal radiation analysis in containment flows only covers a small range of wavelengths from 0.78 to 1000 μm [HOW20]. Since the energy of thermal radiation photon is relatively small ($< 1\, eV$), it is not convenient to distinguish the energy difference by its wavelength. Therefore, the wavenumber η (unit cm^{-1}) is introduced in the thermal radiation analysis [MOD13], which is the inversion of wavelength (see Eq. 3.2). As shown in Eq. 3.3, the energy of thermal radiation photon is proportional to the wavenumber.

$$\eta = \frac{1}{\lambda} \tag{3.2}$$

$$E = hc\eta \tag{3.3}$$

As shown in Table 3.1, the whole infrared radiation spectrum is divided into three regions according to its energy: near-infrared, mid-infrared, and far-infrared. For

Table 3.1: Types of infrared radiation [ISO07]

Region	Wavelength	Wavenumber	Transition
near-infrared	0.78 - 3 μm	3300 - 13000 cm^{-1}	electronic transition
mid-infrared	3 - 50 μm	200 - 3300 cm^{-1}	vibrational transition
far-infrared	50 - 1000 μm	10 - 200 cm^{-1}	rotational transition

the near-infrared radiation, the energy of the thermal radiation photon is large enough to cause the electronic transition [MOD13, HOW20], which is an important phenomenon for combustion applications. However, this thesis mainly focuses on the mid-infrared and far-infrared regions for relatively low temperature applications, e.g., atmospheric radiation [LIO02] and containment safety analysis [LIU22b].

The most accurate radiative heat transfer model is the Maxwell equation [HEI84], which is the cornerstone of modern physics. However, solving the Maxwell equation is only necessary for the nanoscale radiation heat transfer [ZHA07] and near-field thermal radiation [BAS09]. The nanoscale heat transfer mechanism and near-field thermal radiation are focused on a small region comparable to the wavelength of thermal radiation photons ($\sim nm$). It is evident that solving the Maxwell equation is tedious [TAL75]. Luckily, the computational domain in most engineering applications is much larger than the wavelength of thermal radiation photon. Therefore, it is not necessary to solve the Maxwell equation for thermal radiation heat transfer in engineering applications. In thermal radiation analysis, the number of thermal radiation photons is large enough to be considered as an energy bundle.

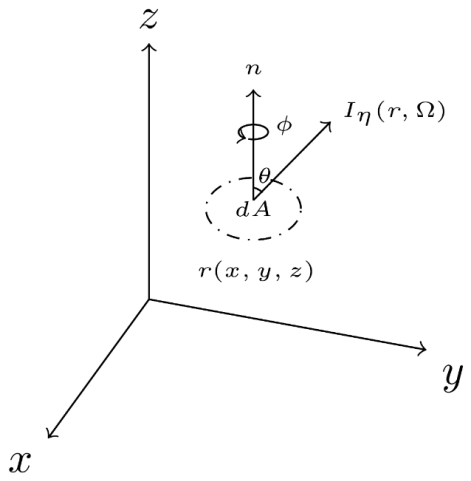

Figure 3.1: Spectral radiation intensity, modifed from [HOW20]

Consequently, the spectral radiation intensity $I_\eta(r, \Omega)$ is introduced in the thermal radiation analysis [MOD13]. The definition of spectral radiation intensity $I_\eta(r, \Omega)$ in unit $W/(m^2 \cdot sr \cdot cm^{-1})$ is the amount of radiative heat flux $dQ_\eta(r, \Omega)$ in wavenumber η at position $r(x, y, z)$ in direction $\Omega(\theta, \phi)$ projected into unit area dA [MOD13] (see Fig. 3.1)

$$I_\eta(r, \Omega) = \lim_{\Delta A, \Delta\Omega, \Delta\eta \to 0} \frac{\Delta Q_\eta(r, \Omega)}{cos\theta \Delta A \Delta\eta \Delta\Omega} \tag{3.4}$$

where $dQ_\eta(\Omega, r)$ is the spectral radiative heat flux at position r in solid angle Ω projected into the infinitesimal area dA; n is the surface normal vector; Ω is the solid angle; η is the wavenumber; θ is the angle between the incoming radiation and the surface; ϕ is the azimuthal angle.

After defining the spectral radiation intensity $I_\eta(r, \Omega)$, it is convenient to analyze the radiation heat transfer in the macroscopic scale. The radiative transfer equation is built on the energy balance of spectral radiation intensity $I_\eta(r, \Omega)$, which is related to the radiation absorption, scattering and emission. Before the deduction of radiative transfer equation, the black body emission law is introduced, which provides the relationship between the spectral emission energy $I_{b,\eta}$ and temperature T for an ideal black body. According to Planck's emission law [PLA14, MOD13, HOW20], the spectral black body intensity $I_{b,\eta}(T)$ at wavenumber η emitted from a perfect black-body surface is only related to its temperature T

$$I_{b,\eta}(T) = \frac{2hc^2\eta^3}{\exp(hc\eta/kT) - 1} \tag{3.5}$$

where T is the media temperature; k is the Boltzmann constant ($1.380649 \times$

$10^{-23} J/K$); η is the wavenumber. The integrated emission power over the whole infrared radiation spectrum can be determined from Eq. 3.6.

$$I_b(\Omega) = \int_\eta I_{b,\eta}(T) d\eta = \frac{\sigma T^4}{\pi} \tag{3.6}$$

where σ is the Stefan-Boltzmann constant ($5.67 \times 10^{-8} W/(m^2 \cdot K^4)$). According to Eq. 3.6, the thermal radiation emission is proportional to the fourth power of temperature. If the convection heat transfer is relatively weak in buoyancy flows, the thermal radiation energy can play an important role in the energy balance [SOU13].

The spectral black body intensities at different temperatures are shown in Fig. 3.2. The maximum emission intensity shifts towards a higher wavenumber region as

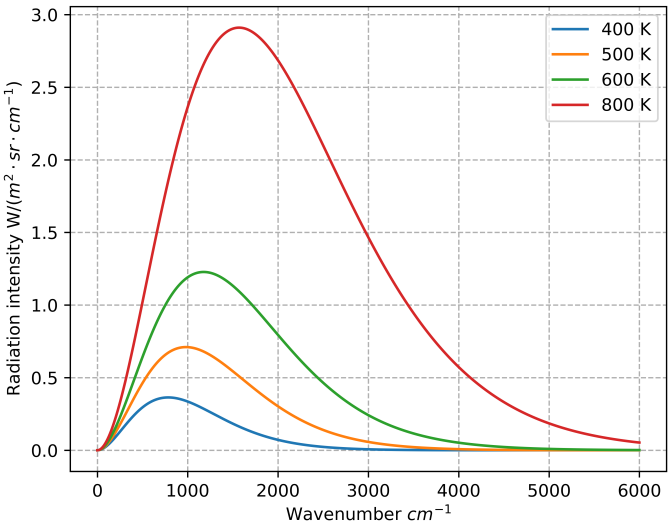

Figure 3.2: Blackbody radiation intensity $I_{b,\eta}(T)$ at different temperatures

the temperature increases. The wavenumber range of the emitted spectral radiation intensity $I_{b,\eta}(T)$ is from 0 to 6000 cm^{-1} if the temperature is less than 800 K. As shown in Fig. 3.2, the strength of radiation intensity emitted from high temperatures is much higher than that in low temperatures.

The thermal radiation emission from a perfect black-body surface is continuous over the whole infrared radiation spectrum. As discussed before, the containment flow is filled with non-gray gas media. It is necessary to quantify the total radiation emission from a volume with non-gray gas media. However, there is a significant difference between the solid surface emission and the volume emission with infrared-active non-gray gas [MOD13]. The atoms on the solid surface are packed

together within a short distance (~ $10^{-10}\ m$). According to the band theory of solids [SIN01], the allowed energy levels are so close that the surface radiation emission can be viewed as continuous over the whole infrared radiation spectrum. However, the emission of electromagnetic waves by a gas medium is also related to the concept of quantized energy levels and transitions between them. The non-gray gas emission is discrete since only the specific photon can initiate the energy transition within non-gray gas media. The detailed explanation about spectral gas properties is given in section 3.2.

In the presence of non-gray gas medium with particles/aerosols in containment flows, it is important to consider not just the surface-to-surface radiation, but also the non-gray gas radiation. The non-gray gas radiation heat transfer is also critical in many engineering applications, e.g., combustion [MAN08] and atmospheric radiation [GOO95]. Non-gray gases, such as H_2O, CO and CO_2, can absorb and emit thermal radiation energy at a variety of wavenumbers. For example, carbon dioxide can absorb the sunlight energy in the atmosphere, which plays an important role in global warming [DON14]. There are only three main absorption bands for carbon dioxide: 667 cm^{-1}, 1388 cm^{-1} and 2349 cm^{-1}. Although the concentration of carbon dioxide is just about 400 ppm in the atmosphere, it has a long term effect on the global warming. In the presence of huge amounts of steam, the thermal radiation absorption effect is also vital for the heat balance in containment flows. Theoretically, the absorption coefficient of the non-gray gas molecule is based on the molecular quantum mechanics [GOO95, TIE68] involving the energy transition between two energy states. The spectral absorption coefficient κ_η (unit m^{-1}) describes the strength of absorption effect at wavenumber η. According to the Beer's law [HUG63], the radiation intensity I_η decreases exponentially along the path length s within the absorbing medium

$$I_\eta(s) = I_\eta(0)\exp(-\kappa_\eta s) \tag{3.7}$$

where κ_η is the spectral absorption coefficient; $I_\eta(s)$ is the outcoming radiation intensity; s is the traveling distance; $I_\eta(0)$ is the incoming radiation intensity.

Similarly, the particles/aerosols suspended within the gas media in containment flows also have a contribution to thermal radiation heat transfer. When the incoming radiation intensity interacts with particles/aerosols in the gas media, it can be absorbed within the particles or scattered into other directions. The particle scattering, in most cases, only changes the direction of the incoming radiation intensity. The spectral scattering coefficient is defined as σ_η. The scattering attenuation along the path length s is given below

$$I_\eta(s) = I_\eta(0)\exp(-\sigma_\eta s) \tag{3.8}$$

where σ_η is the spectral scattering coefficient (unit m^{-1}).

The general form of the radiative transfer equation is an energy balance between absorption, emission and scattering effect along the radiation path length ds at position $r(x, y, z)$ and radiation direction $\Omega(\theta, \phi)$ (see Fig. 3.3) [MOD13]. After passing

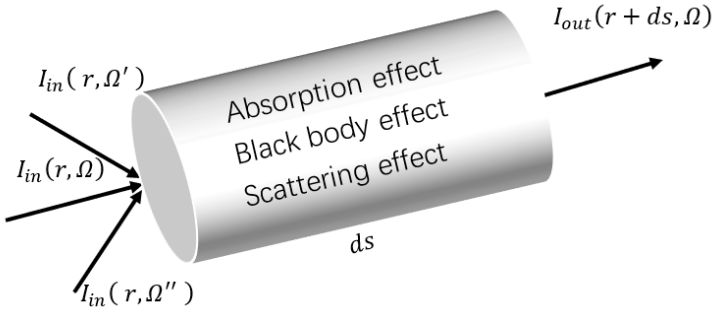

Figure 3.3: Thermal radiation energy balance within a short distance

through a short distance ds, the variation of spectral radiation intensity is

$$I_\eta(r + ds, \Omega, t + dt) - I_\eta(r, \Omega, t) = \frac{\partial I_\eta(r, \Omega, t)}{\partial s} ds + \frac{\partial I_\eta(r, \Omega, t)}{\partial t} dt \tag{3.9}$$

The first term on the right hand side of Eq. 3.9 is the spatial radiation intensity variance, while the second term is the temporal variation. Since the photon propagation velocity is the speed of light c, the time scale of radiation phenomenon is quite short in comparison with the fluid motion. In other words, the thermal radiation equilibrium is achieved within a very short time. The time dependent term $\frac{\partial I_\eta(r,\Omega,t)}{\partial t}$ is mandatory to be considered in nonlinear optics applications, e.g., fusion reactor [REB95] and high energy laser [MOR97]. However, in most engineering applications, this term can be neglected. The variation of intensity can be written as

$$\begin{aligned} \frac{\partial I_\eta(r, \Omega)}{\partial s} &= \frac{\partial x}{\partial s} \frac{\partial I_\eta(r, \Omega)}{\partial x} + \frac{\partial y}{\partial s} \frac{\partial I_\eta(r, \Omega)}{\partial y} + \frac{\partial z}{\partial s} \frac{\partial I_\eta(r, \Omega)}{\partial z} \\ &= \Omega \cdot \nabla I_\eta(r, \Omega) \end{aligned} \tag{3.10}$$

The energy attenuation by the absorption and scattering effect along the path length ds is

$$(\kappa_\eta + \sigma_\eta) I_\eta(r, \Omega) ds \tag{3.11}$$

The black body emission along the path length ds is

$$\kappa_\eta I_{b,\eta}(r, \Omega) ds \tag{3.12}$$

If the incoming radiation intensity is scattered by particles/aerosols, the outcoming angular distribution is related to the particle properties, which is called the phase function $\phi(\Omega', \Omega)$ [MOD13, HOW20]. The physical meaning of the phase function

$\phi(\Omega^{'}, \Omega)$ is the probability of the incoming direction Ω' scattering into direction Ω. The phase function can be calculated from Mie scattering theory [HER12]. When considering the scattering effect in thermal radiation, the phase function is also important for the energy balance. The energy gained from the scattering effect is

$$\frac{\sigma_\eta}{4\pi} \int_{4\pi} I_\eta(r, \Omega^{'}) \phi(\Omega^{'}, \Omega) d\Omega^{'} ds \tag{3.13}$$

The spectral radiative transfer equation (RTE) is a balance between absorption, scattering and black body emission (see Eq. 3.14).

$$\Omega \cdot \nabla I_\eta(r, \Omega) = -(\kappa_\eta + \sigma_\eta) I_\eta(r, \Omega) + \kappa_\eta I_{b,\eta}(r, \Omega) + \frac{\sigma_\eta}{4\pi} \int_{4\pi} I_\eta(r, \Omega^{'}) \phi(\Omega^{'}, \Omega) d\Omega^{'} \tag{3.14}$$

As shown in Eq. 3.14, the RTE is a six-dimensional Boltzmann transport equation: three positions $r(x, y, z)$, two solid angles $\Omega(\theta, \phi)$, and one wavenumber η. Before solving the spectral radiative transfer equation, the spectral gas property κ_η, the scattering absorption coefficient σ_η and the phase function $\phi(\Omega', \Omega)$ are necessary to be determined. The exact solution of radiative heat transfer is tedious even for two-dimensional geometries due to the numerical complexity. Therefore, a number of approximations and simplifications are mandatory to solve radiative heat transfer in a reasonable time for the reactor safety analysis. In this thesis, the scattering effect is not considered to reduce the computational effort. Otherwise, the coupled thermal radiation and CFD simulation is unaffordable for the reactor safety analysis.

In nuclear containment buildings, there are three kinds of small particles: soot, water droplets and aerosols. Soot can be generated from the cable combustion after severe accidents and is the agglomeration of carbon particles. The soot emission is an important scenario in combustion applications due to its high temperatures [SOL01, HOW20]. This effect can be neglected in the reactor safety analysis, since the media temperature is relatively low in containment flows. The other kind of small particles in containment building are water droplets formed by bulk condensation or spray systems [IAE11]. The dispersion and deposition of water droplets can provide additional momentum in containment flows. Different from combustion applications, the volume of a containment building is much larger than the fuel chamber. Therefore, the droplet size may vary remarkably in different regions due to the large volume of the containment building. Most of the computational codes can only provide the volume fraction of water droplets in the two-phase simulation, which leads to an unreasonable prediction of size distribution [DOM10]. A more detailed calculation is necessary to predict the dispersion and settlement of water droplets. Furthermore, it is difficult to measure droplet concentrations in large-scale facilities. The bulk of water droplets can change the radiative heat transfer in containment flows. The scattering properties of water droplets are well investigated in the literature [HAL73, MOD13, HOW20]. But the computational effort is too intensive to determine the scattering coefficient for a single water droplet

by using Mie theory [HER12]. The scattering effect within a bulk of water droplets is also a challenging topic, as it is related to the bulk condensation, evaporation, agglomeration and the size distribution.

The aerosols in the containment buildings are composed of different elements, such as U, Cs, Zr, I, Xe and Fe [ABE14, SEH11]. The main purpose of containment safety analysis is to prevent the release of radioactive aerosols into atmosphere. However, the fundamental theory of particles/aerosols and flow phenomena is not so clear in containment atmospheres [OEC09b]. The CFD modeling of aerosol flows is far from satisfactory due to the numerical complexity [DEH11]. Most of lumped-parameter codes obtain the empirical parameters and equations from specific experiments for the aerosol modeling [OEC09b]. From the thermal radiation point of view, the scattering coefficient of aerosols is totally different from that of soot particles, since the nuclear aerosols consist of a wide variety of materials. This is due to the complex property of aerosols, type of materials, the shape of aerosols, and the aerosol size distribution. Without an accurate prediction of aerosol deposition and dispersion in containment flows, the analysis of scattering effect in radiative heat transfer is problematic. Consequently, in this thesis, scattering effect is not considered and this thesis is mainly concentrated on the non-gray gas modeling in containment flows.

In thermal radiation analysis, there is no specific boundary treatment on walls in thermal radiation solvers. The surface emissivity is an important parameter for the thermal radiation modeling. The surface emissivity is related to the heat transfer between media and boundary walls. The radiation boundary wall is treated as a smooth surface in technically large facilities. Nonetheless, the surface smoothness assumption is not always valid with respect to wavelength. The characteristics of surface roughness depend on its material, manufacture process and surface oxidation. In the containment safety assessment, the condensation on walls can also change the emissivity [TRO22]. If the boundary surface is not ideal black, the surface reflections from the rough and condensation surfaces are illustrated in Fig. 3.4. The surface emissivity has an influence on the wall heat balance, and a more

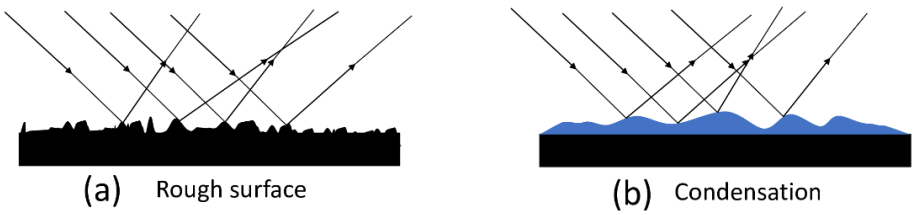

Figure 3.4: Diffusive reflection on boundary surfaces: (a) rough surface, (b) condensation surface

detailed investigation is required for the non-gray wall emissivity modeling. The emissivity of water surface is about 0.98 [TRO22, MAS88], while the steel emissivity is only around 0.3 [MOD13]. If the emissivity is close to 1.0, the radiation heat transfer between media and wall structures can be intensified.

Most of boundary walls inside the containment building are nontransparent surfaces. Since the temperature is relatively low ($< 800\,K$) in containment flows, the gray surface assumption is applied to reduce the numerical complexity. Eq. 3.15 gives the relationship between emissivity and reflectivity for a nontransparent gray surface [HOW20].

$$\epsilon + \rho = 1 \tag{3.15}$$

where ϵ is the surface emissivity; ρ is the surface reflectivity. The outcoming radiation intensity $I_\eta(r_{wall}, \Omega)$ on the boundary surface has two contributions: surface emission and reflection from incoming radiation intensities. The radiation intensity $I_\eta(r_{wall}, \Omega)$ on an opaque wall is given in Eq. 3.16 [MOD13].

$$I_\eta(r_{wall}, \Omega) = \epsilon I_{b,\eta}(r_{wall}, \Omega) + \frac{1-\epsilon}{\pi} \int_{n\cdot\Omega'<0} I_\eta(r_{wall}, \Omega')\,|n \cdot \Omega'|\, d\Omega' \tag{3.16}$$

where ϵ is the surface emissivity; n is the surface normal direction; Ω' is the incoming radiation direction; Ω is the outcoming radiation direction.

The first term on the right side of Eq. 3.16 is the black body emission from the wall, which is only related to the surface temperature and emissivity. The second term is the radiation reflection from all incoming intensities. According to Eq. 3.16, the radiation boundary condition at opaque walls is neither a Dirichlet condition nor a Neumann condition if the wall emissivity is not equal to one. Therefore, the numerical solution for the thermal radiation heat transfer is a tedious procedure. In the deterministic radiation solver, the radiation reflection on the boundary wall is not known and a numerical iteration is required to solve the radiative transfer equation beginning with the initial guess of radiation intensity $I_\eta^{initial}(r, \Omega)$. After a number of iterations, the converged radiation intensity $I_\eta^{converged}(r, \Omega)$ is obtained. The detailed description of radiation solvers can be found in section 3.3. It is apparent from the above equations that the absorption coefficient κ_η plays an important role in the radiative heat transfer, and it may introduce additional complexities to the numerical solution. Before discussing the thermal radiation solver, a detailed overview of the spectral gas property is given in section 3.2. In fact, the treatment of spectral gas property has a strong impact on the computational efficiency of radiation solvers. If the number of spectral bands is too large, the computational effort is unaffordable for engineering applications [CHU11].

3.2 Spectral Gas Properties

Theoretically, the detailed spectral gas property calculation is based on the molecular quantum mechanics [GOO95, TIE68, ROT09] involving the energy transition between two discrete energy states. The spectral gas property is extremely irregular over the infrared radiation spectrum [MOD13, HOW20]. Infrared active gas molecules, e.g., H_2O, CO and CO_2, generally have a stronger absorption effect than infrared inactive gas molecules, e.g., N_2 and O_2, over the infrared radiation spectrum [GOO95]. This is the main reason why only steam and carbon dioxide species are considered for the non-gray gas radiation modeling in combustion applications.

When a photon with the wavenumber η interacts with a gas molecule, the photon-molecule interaction is a complex physical phenomenon. The photon-molecule interaction is related to the quantum mechanical theory [ROT09, GOO89, LOU00]. The energy of thermal radiation photon is not large enough to ionize the gas molecule, but it may cause the rotation–vibration transitions changing the internal energy. Absorption, spontaneous emission, and stimulated emission are three energy transition processes in the thermal radiation heat transfer. As shown in Fig. 3.5, a gas molecule with the low energy state E_l can be in the high energy state E_h after absorbing a photon. The second one is the spontaneous emission. An excited

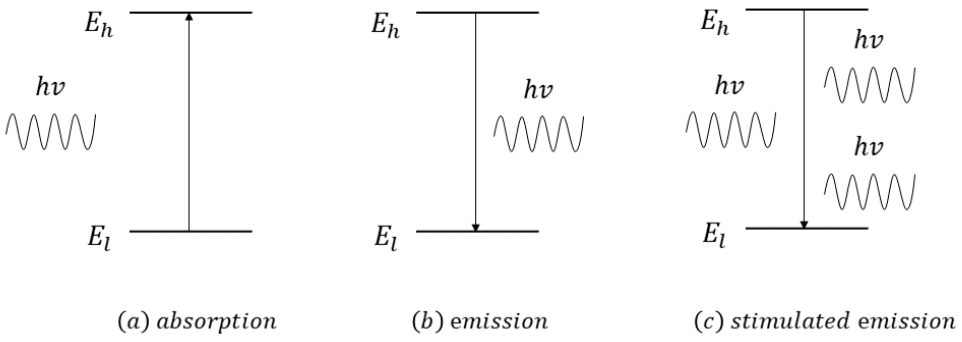

Figure 3.5: Three transitions between two energy states [LOU00]

gas molecule spontaneously decays to the low energy state E_l by emitting a photon. The energy of photon $h\nu$ is equal to the energy difference between the low and high energy states (see Eq. 3.17). If a photon with the energy $h\nu = E_h - E_l$ is ab-

sorbed by the excited gas molecule, the gas molecule undergoes the decay process by emitting two photons with the same wavenumber η. This is the fundamental theory of laser technology [CHR13] to generate monochromatic light sources.

$$\Delta E = E_h - E_l = h\nu = hc\eta \tag{3.17}$$

where ν is the frequency; η is the wavenumber. According to the above equation, only the photon with a specific wavenumber η can cause the energy transition between two states for the gas molecule. The spectral gas property is closely related to the vibration-rotation energy states of gas molecule, while the emission spectrum from the back surface is continuous. This is the main difference between non-gray gas radiation and surface-to-surface radiation.

Since the infrared active gas molecules, e.g., H_2O and CO_2, have more than one atom, the internal energy of infrared active molecules is not limited to the translational energy. Besides the translational energy, there are other ways to store potential energy for infrared active gas molecules: rotational energy, vibrational energy, and electronic energy [MOD13]. The total internal energy for the infrared active gas molecule is given in Eq. 3.18

$$E_{molecule} = E_{rotational} + E_{vibrational} + E_{electronic} \tag{3.18}$$

As shown in Fig. 3.6a, the polyatomic molecule can rotate in different axes, which is called the rotational energy. The vibrational energy is the potential energy due to the position of different atoms (see Fig. 3.6a). The rotational energy is closely linked to the vibrational energy for polyatomic molecules. If the energy state of vibration is altered during the photon-molecule interaction, the rotational energy always changes [GOO95]. Therefore, it is necessary to consider both effects in the radiation heat transfer. As shown in Fig. 3.7, the energy difference between two rotational levels is smaller than that between two vibrational levels. The interaction between vibration and rotation transitions is complex making the spectral gas property hard to resolve. The electronic energy is about the ionization transition into excited electronic molecules involving X-ray or gamma radiation, which is only important for the plasma and high energy physics [BAT85, MOR97].

Since the energy of thermal radiation photon is not large enough to cause electronic transitions, in this thesis, only the vibration-rotation energy transitions are considered for the thermal radiation analysis in containment flows. It is well known that the H_2O molecule has one oxygen and two hydrogen atoms (see Fig. 3.6a). The molecular structure of H_2O is characterized by the triangle shape where the average O-H bond length is about $0.957 \times 10^{-10}\ m$ according to the analytical chemistry [CSA05]. The steam molecule has a permanent dipole moment [CLO73]; therefore, the collision interaction between steam molecules is more significant than other abundant molecules, such as N_2 and O_2. As shown in Fig. 3.6a, there are three vibrational modes for the H_2O molecule, i.e., symmetric stretching, bend, and asymmetric stretching [MOD13]. The CO_2 molecule is relatively simple in comparison

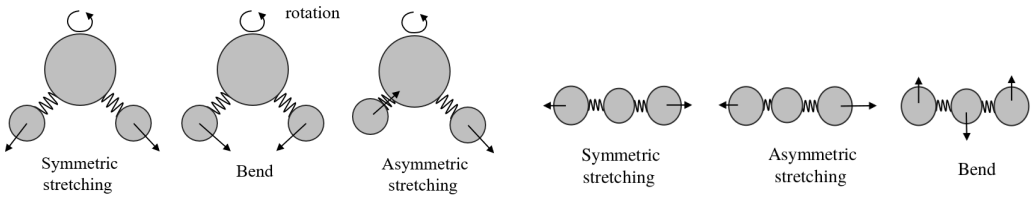

a) H_2O **b)** CO_2

Figure 3.6: Vibration modes of H_2O and CO_2 [MOD13]

with the steam molecular structure. The CO_2 molecule (see Fig. 3.6b) has one oxygen atom and two carbon atoms. Those three atoms are located in a straight line, but it has no permanent dipole moment due to the symmetric structure. There are three main vibrational modes for the CO_2 molecule, i.e., symmetric stretching, bend, and asymmetric stretching (see Fig. 3.6b).

The non-gray gas absorption is a complex phenomenon involving the complex interaction between energy states in gas molecules. As shown in Fig. 3.7, a non-gray

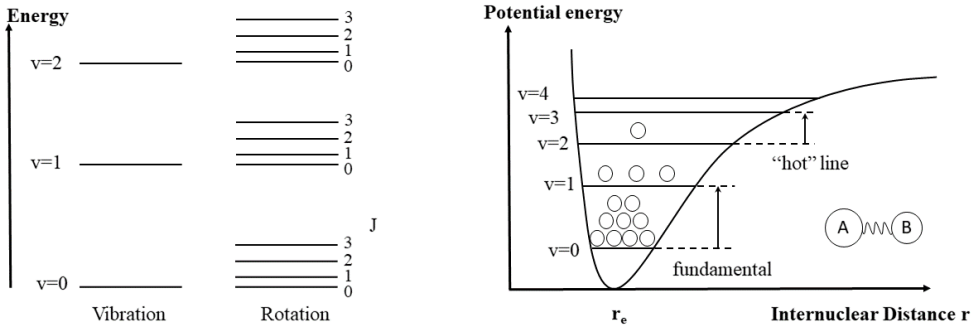

Figure 3.7: Potential well curve for a diatomic molecule, modified from [KUL18]

gas molecule may have many vibration-rotation transition lines over the infrared radiation spectrum. But only the specific wavenumber photon can cause the energy transition in non-gray gas molecules. As a result, the absorption and emission spectra for the non-gray gas molecule is discrete, not continuous. The absorption spectrum of the molecule serves as a fingerprint to analyze the type of molecule and its amount in the chemical analysis [MEN99]. As shown in Fig. 3.7, the rotational energy states are very close to each other. The vibration bands are sparser than the rotation bands (see Fig. 3.7 left). Therefore, the absorption coefficients vary remarkably within a small wavenumber interval due to the rotational transitions. The right side of Fig. 3.7 is the number of molecules at different energy states

according to the Boltzmann distribution [HUA09]. Most of the molecules are in the fundamental state $v = 0$ in relatively low temperatures, e.g., $T < 1000\ K$. Only a few number of molecules are located in high vibrational states $v > 0$. The fundamental transition lines ($v = 0 \rightarrow v = 1$) are the main contribution for absorption coefficients in low temperature applications. If the temperature is larger than one thousand Kelvin, more molecules are located in high vibration states $v > 0$. As shown in Fig. 3.7, the 'hot' transition lines become evident in combustion applications. It is noted that this thesis only considers the vibration and rotation transitions, while neglecting the ionizing radiation.

Besides, the energy state of molecules is not only related to its temperature. The spectral gas properties also depend on the total pressure, molar fraction, and wavenumber. The theoretical calculation of absorption coefficient is based on the reference temperature 296 K. However, the absorption effect is also affected by the Doppler broadening and the collision broadening effects. The Doppler broadening is the broadening of spectral lines caused by the velocity distribution of molecules; while the collision broadening is the broadening of spectral lines owing to molecular collisions. In order to accurately solve the radiative transfer equation, the spectral gas property must be carefully evaluated to reduce the numerical uncertainty. Without a reasonable approximation of the spectral gas property, the thermal radiation simulation may be unreasonable. In the following sections, a number of non-gray gas models are briefly introduced.

3.2.1 Line-by-Line Model

The most accurate model for spectral gas properties is the Line-by-Line (LBL) model, which is based on the quantum mechanics [VSI06]. The LBL model considers all transition lines over the whole infrared radiation spectrum, which may comprise thousands of transition lines in the LBL database. For each transition line in the LBL model, the Einstein A-coefficient [MOD13] is provided to represent the strength of absorption effect. A number of LBL databases [ROT09, TAS11] have been published and updated in the last few decades with the aid of the Fourier transform infrared technology [GOL64, MOD13] and the advanced quantum mechanical algorithm [GAM83, VSI06]. In this thesis, the high-resolution transmission molecular absorption database (HITRAN) is applied to calculate the absorption coefficient κ_η. The HITRAN database has been validated against by several experiments [OLS19, MEL21]. The updated HITRAN2016 [ROT09] database is a compilation of molecular absorption parameters for low temperature applications, which contains thousands of transition lines in the 10-8000 $cm^{\breve{}1}$ region. The spectral absorption coefficient κ_η at the specific wavenumber η is a complex function, which depends on the line intensity S_i, local temperature T, total pressure p, partial

pressure p_s, and associated spectral lines (see Eq. 3.19).

$$\kappa_\eta = N(p_s, T) \sum_i S_i(T) f(x_s, p, T, \eta - \eta_i) \tag{3.19}$$

where $N(p_s, T)$ is the number of non-gray gas molecules per unit volume; x_s is the species molar fraction; $S_i(T)$ is the i-th line intensity at temperature T; η_i is the i-th line location; T and p are the media temperature and pressure; $f(x_s, p, T, \eta - \eta_i)$ is the line shape function.

The physical meaning of the spectral line intensity $S_i(T)$ is the probability of a single gas molecule to interact with the incoming radiation beam which can be determined by quantum mechanics calculations [GOO95, VSI06, MOD13]. Since the spectral line intensity $S_i(T)$ is the microscopic absorption coefficient for a single molecule at wavenumber η, the total macroscopic absorption coefficient κ_η is the microscopic absorption coefficient $S_i(T)$ times the number of non-gray gas molecules $N(p_s, T)$ per unit volume. The molecular collision can influence the absorption coefficient, and the frequency of molecular collision is proportional to the media pressure and temperature. Therefore, the expression $f(x_s, p, T, \eta - \eta_i)$ is the line shape function which considers numerous factors related to the broadening of spectral absorption lines, for example, natural line broadening, collision broadening and Doppler broadening. Normally, the line intensity S_i is given at the reference temperature T_{ref} (296 K) in the HITRAN database, mainly considering the energy transition from the ground state to the first excited state for low temperature applications (see Fig. 3.7). The line intensity $S_i(T)$ is a function of media temperature T

$$S_i(T) = S_i(T_{ref}) \frac{Q(T_{ref})}{Q(T)} \frac{\exp(-c_2 E/T)}{\exp(-c_2 E/T_{ref})} \frac{1 - \exp(-c_2 \eta/T)}{1 - \exp(-c_2 \eta/T_{ref})} \tag{3.20}$$

where $S_i(T_{ref})$ is the line intensity at the reference temperature; $Q(T)$ and $Q(T_{ref})$ are the internal partition functions [GAM17] at temperature T and T_{ref} respectively; E is the lower energy state; c_2 is the second radiation constant $\frac{hc}{k}$; η is the wavenumber.

According to Eq. 3.20 the line intensity $S_i(T)$ is the microscopic absorption intensity for a single non-gray gas molecule, but there are a large number of gas molecules within the engineering system. The molecule-molecule collision has a strong impact on the absorption coefficient. The molecule-molecule collision may lead to the perturbation of energy states for gas molecules. The line shape function $f(x_s, p, T, \eta - \eta_i)$ is also important to determine the absorption coefficients [KOC16]. In this thesis, the Lorentz line profile [SPA97] is chosen to obtain the spectral absorption coefficient

$$f(\eta) = \frac{\gamma_i}{\gamma_i^2 + (\eta - \eta_i)^2} \tag{3.21}$$

where γ_i is the i-th line half-width; η_i is the center of the transition line. The effective line half-width γ depends on numerous factors, as shown in the following discussion.

- **Natural Line Broadening** The exacted non-gray gas molecules can spontaneously emit thermal radiation photon and fall into lower energy states. However, the spontaneous decay time cannot be measured with a high accuracy based on the Heisenberg's uncertainty law [BUS07]. The Heisenberg's uncertainty equation is given as follows

$$\Delta E \Delta t > \frac{\hbar}{2} \tag{3.22}$$

  Theoretically, there is a experimental uncertainty for the measured energy ΔE. It means that the experimental measurement has a theoretical limit to detect the transition energy [BOL53]. Fortunately, the natural line broadening half-width is much smaller than other line broadening effects for engineering considerations [MOD13]. The natural broadening effect is of minor importance in the thermal radiation heat transfer for containment flows. Therefore, the natural line broadening is negligible in this thesis.

- **Collision Line Broadening** The collision line broadening is also called the pressure line broadening effect [GOO95]. Under the assumption of an ideal gas, the average kinetic energy of molecules is proportional to $k_B T$ which is comparable to the energy of thermal radiation photons. The kinetic energy of molecules at room temperature is about 0.0257 eV; while the energy of thermal radiation photon is about 0.1 eV in low temperature applications. For example, the energy of photon with 10 μm wavelength is 0.124 eV. During the absorption and emission process, the energy state of non-gray gas molecule can be affected by kinetic collisions. When increasing the media temperature, the molecular oscillation due to the molecular collision becomes more significant. The molecular collision can affect the energy transition process leading to a broadening effect. Since the frequency of molecular collision is a function of the number of molecule and temperature, the collisional half-width γ_L is given by Eq. 3.23 [MUR67, MOD13].

$$\gamma_L = \sum_{species} \gamma_{species} \left(\frac{p_{species}}{p_{ref}} \right) \left(\frac{T_{ref}}{T} \right)^n \tag{3.23}$$

  where $\gamma_{species}$ is the line half-width for the gas species; n is the temperature fitting coefficient given in the HITRAN database; $p_{species}$ is the partial pressure; p_{ref} is the reference pressure (atmosphere pressure). According to Eq. 3.23, different species may have different line half-widths. Since the steam molecule has a permanent dipole moment, the line broadening effect is stronger than other non-gray gas molecules.

- **Doppler Line Broadening** The Doppler broadening effect is associated with the molecular kinetic movement, which can be determined from the Maxwell–Boltzmann velocity distribution. The receiving frequency may become lower or higher due to the kinetic movement of molecules. Thus, the observed wavenumber η_{obs} is [MOD13]

$$\eta_{obs} = \eta_0(1 \pm \frac{v}{c}) \tag{3.24}$$

where η_{obs} is the wavenumber received by the moving molecule; η_0 is the wavenumber of the incoming photon; v is the molecular velocity. When increasing the media temperature, the Doppler effect is intensified due to the movement velocity. The root mean square velocity for steam molecules is about 640 m/s at room temperature, while it is about 2038 m/s at 3000 K. Even though the kinetic movement velocity is relatively small in comparison to the speed of light, the spectral absorption coefficient has a highly irregular dependence on the wavenumber η. Therefore, the Doppler broadening effect still plays a role to determine the absorption coefficient in combustion applications. The line half-width γ_D for the Doppler effect is given in the literature [PEN60, MOD13]

$$\gamma_D = \frac{\eta_0}{c}\sqrt{\frac{2k_BT}{M}ln2} \tag{3.25}$$

where k_B is the Boltzmann constant; M is the mass of the molecule. Different from the collision and natural line broadening, the Doppler half-width is also related to the wavenumber η_0.

In engineering applications, it is hard to consider all line broadening effects during the thermal radiation simulation. The most significant line broadening effect is the collision broadening. The natural broadening effect is crucial for the high-resolution apparatus to measure spectral gas properties, while the Doppler broadening effect becomes important for high temperature applications (> 2000 K). In this thesis, the detailed implementation of LBL model is given in section 4.1.1. As stated before, the LBL absorption coefficient is calculated in fine wavenumber intervals. The spectral discretization $\Delta\eta$ is set to be 0.01 cm^{-1} to resolve the variation of absorption coefficients [ROT09]. In the following discussion, the LBL absorption coefficients for H_2O and CO_2 are illustrated at different temperatures to ease the understanding. Fig. 3.8 compares the H_2O absorption coefficient in 2.7 μm bands at different temperatures in atmospheric pressure: 1000 K, 600 K, and 400 K; while Fig. 3.9 shows the CO_2 absorption coefficient in 4.3 μm bands at same temperatures. The absorption coefficient changes considerably across the wavenumber. As shown in Fig. 3.8, each transition line corresponds to a energy transition between two energy levels for the H_2O molecule. The absorption coefficient may have a difference of orders of magnitude in different wavenumber regions. There

are a number of very sharp absorption lines within a short wavenumber region. In most regions the absorption coefficient is relatively small which can be viewed as a transparent media. Therefore, the spectral gas property is difficult to handle in the thermal radiation analysis. Thus, the gray gas assumption may lead to a large numerical error for the radiation modeling in containment flows. Furthermore, the spectral gas property is also a function of the media temperature (see Fig. 3.8 and Fig. 3.9).

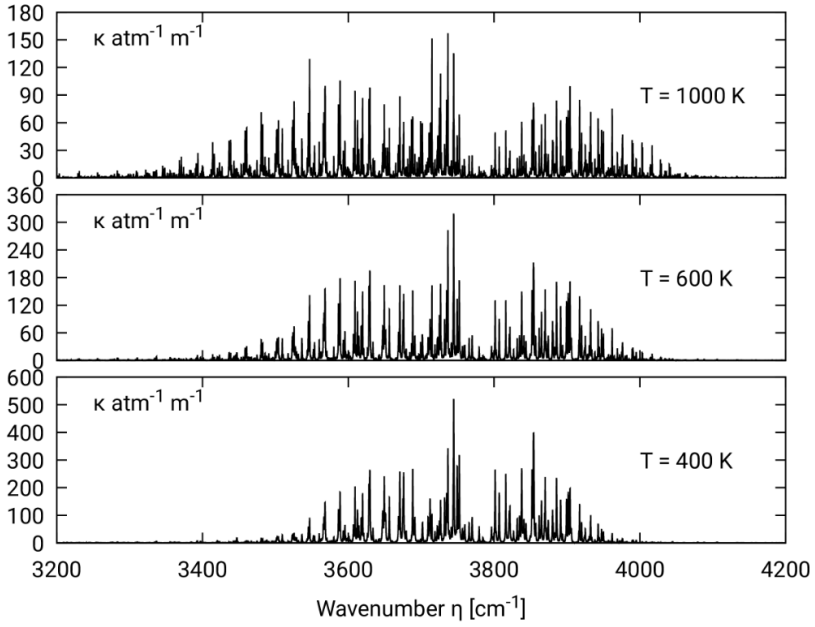

Figure 3.8: H_2O absorption coefficient in 2.7 μm bands at $p = 1\,atm$, x_{H_2O} = 1: T = 1000 K (top), 600 K (middle), and 400 K (bottom), modified from [TAI99]

The width of the absorption bands becomes wider when the media temperature increases [TAI99]. But at the same time the absorption coefficient decreases significantly, especially for the sharp absorption lines. This effect is more evident for CO_2 than that for H_2O due to the Doppler broadening effect. The CO_2 absorption coefficient is much larger than the steam absorption coefficient at 400 K. There are a number of weak lines for the CO_2 absorption coefficient (see Fig. 3.9). When increasing the media temperature, the weak absorption line may become important in combustion applications. It is clear that the CO_2 absorption coefficient is sensitive to the media temperature.

The spectral gas properties are also related to its molar fractions. The H_2O molecule is a polar molecule, meaning that the $H_2O - H_2O$ molecular collision can lead to a strong collision broadening effect, in comparison with the collision between non-

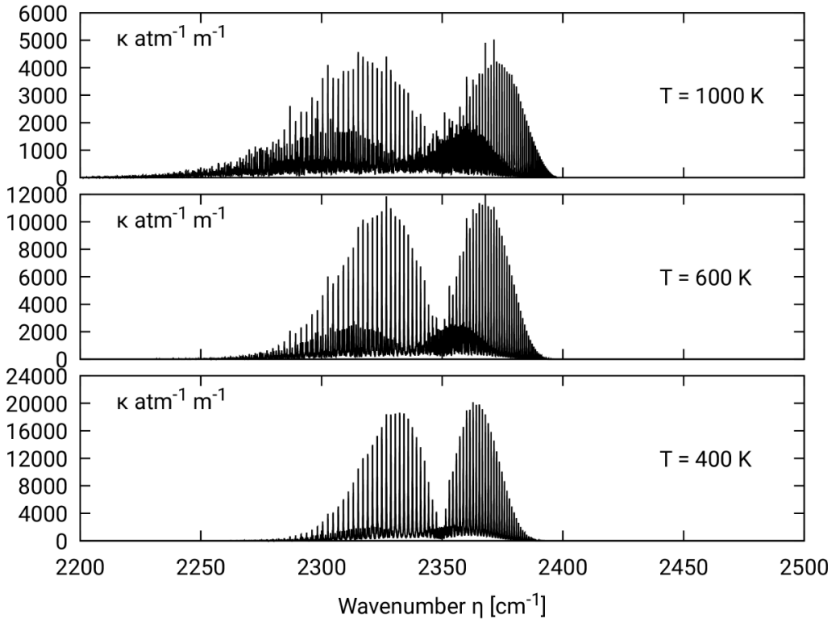

Figure 3.9: CO_2 absorption coefficient in 4.3 μm bands at $p = 1\,atm$, x_{CO_2} = 1: T = 1000 K (top), 600 K (middle), and 400 K (bottom), modified from [TAI99]

polar molecules, e.g., CO_2, N_2 and O_2. The self-broadening line width of steam γ_{H_2O} is larger than that of carbon dioxide γ_{CO_2}. Therefore, the steam absorption coefficient is sensitive to the steam molar fraction shown in Fig. 3.10. The peak of line intensity for H_2O significantly decreases when increasing the H_2O molar fraction in the media, while the line intensity for CO_2 is less sensitive to the CO_2 molar fraction (see Fig. 3.11). However, most of the non-gray gas models only provide the spectral gas property with fixed partial pressure ratios, e.g., $p_{H_2O} = 2p_{CO_2}$ for methane. The molar fraction of steam may vary widely across different regions in the containment building after nuclear severe accidents. Consequently, a tailored non-gray gas model with the description of the spectral gas properties at different steam molar fractions is mandatory for containment studies.

It is concluded that the absorption coefficient $\kappa_\eta(T, p, x)$ is a function of temperature, total pressure, molar fraction, and wavenumber. An unsuitable non-gray gas model can lead to unreasonable predictions for the radiative source term in radiative heat transfer analyses. Although the LBL model is the most accurate non-gray gas model, the LBL absorption coefficient calculation is tedious and memory-intensive in engineering applications. Therefore, it is rare to perform the LBL integration calculation in engineering applications due to the computational effort. Due to the computational cost, a variety of non-gray gas models have been devel-

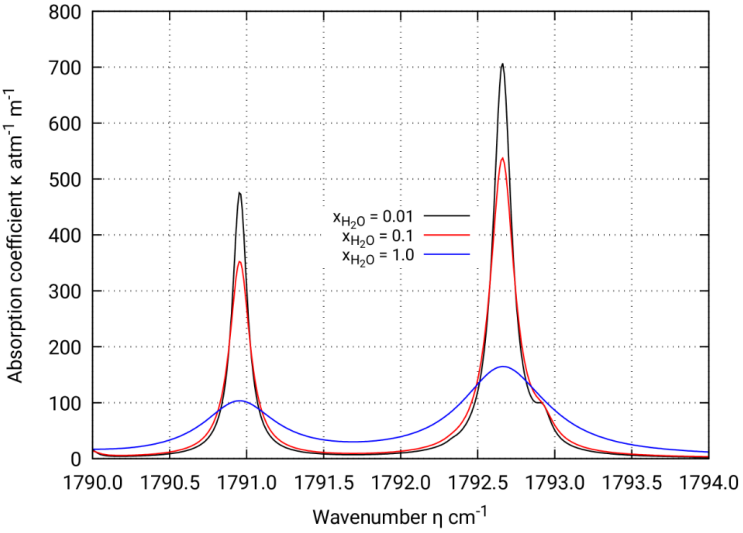

Figure 3.10: H_2O absorption coefficient in 400 K and 1 atm at different molar fractions: x_{H_2O} = 0.01, 0.1, and 1.0

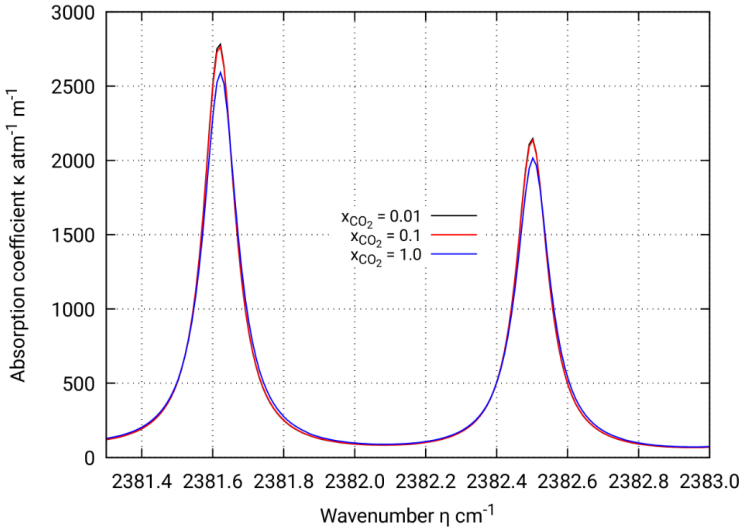

Figure 3.11: CO_2 absorption coefficient in 400 K and 1 atm at different molar fractions: x_{CO_2} = 0.01, 0.1, and 1.0

oped in combustion applications. But the LBL integration model can provide the reference for benchmark test cases to verify other non-gray models [CHU12]. The HITRAN LBL method is the most accurate approach to predict the radiative heat transfer in containment flows.

3.2.2 Narrow Band Model

It is not necessary to resolve the strong fluctuation of the absorption coefficient within a small internal wavenumber (0.01 cm^{-1}) in engineering applications. The spectral gas property can be given in a coarse wavenumber grid. In order to take account of the irregularity of spectral gas properties, the whole infrared radiation spectrum is divided into a number of small bands (10 to 50 cm^{-1}) in narrow band models. As shown in Fig. 3.8 and Fig. 3.9, there are a number of transition lines in each narrow band. Normally the average narrow band transmissivity is given within a spectral width 25 cm^{-1} in the narrow band model, which is an accuracy approximation for engineering applications [RIV95]. The average band transmissivity along the path length L for a homogeneous temperature, pressure and molar fraction non-scattering media is given by Eq. 3.26.

$$\tau_{\Delta\eta} = \frac{1}{\Delta\eta}\int_{\Delta\eta}\exp(-\kappa_\eta L)d\eta \tag{3.26}$$

As shown in Eq. 3.26, the band transmissivity is a function of absorption coefficient κ_η and path length L in homogeneous media. However, the average band transmissivity is not related to the average absorption coefficient $\frac{\int\kappa_\eta d\eta}{\Delta\eta}$ due to the Beer-Lambert law [MOD13] (see Eq. 3.27).

$$\frac{1}{\Delta\eta}\int_{\Delta\eta}\exp(-\kappa_\eta L)d\eta \neq \exp\left(-L\frac{\int\kappa_\eta d\eta}{\Delta\eta}\right) \tag{3.27}$$

According to Eq. 3.27, it is not allowed to exchange the order of integration in mathematics making the spectral gas property difficult to resolve. Therefore, the average band transmissivity is a complex integration function. This is the reason why most of the non-gray gas models give the gas property in terms of the transmissivity, not the absorption coefficient.

A number of approximations are proposed to obtain the average transmissivity [MOD13, GOO95]. The basic assumption of the narrow band model is that the average transmissivity does not rely on the position of transition lines within the narrow band [TAI99]. As shown in Fig. 3.12, there are many transition lines within the narrow band. As a result, the narrow band model is more efficient than the LBL model. The most commonly used narrow band models are the Elasser model [GOO95] and the statistical narrow band (SNB) model [SOU97]. In the Elasser model (see Fig. 3.12a), it is assumed that all transition lines have the equal line intensity S, line distance d and half width γ. In order to calculate the band transmissivity in a nonhomogeneous media, the Godson approximation [GOO95] is applied to solve the average transmissivity in engineering applications. The second kind of narrow band model is the statistical narrow band model. As shown in Fig.

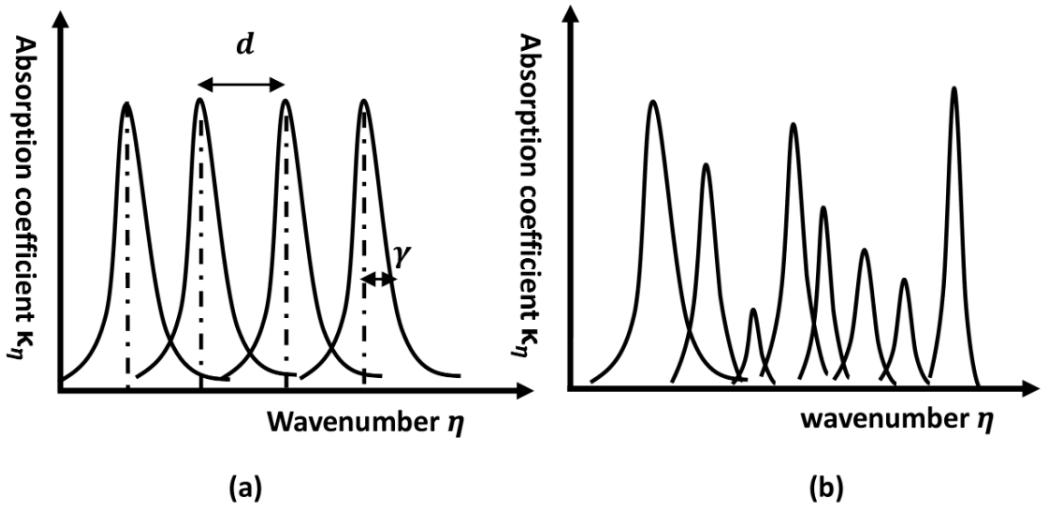

Figure 3.12: Narrow band models: (a) Elsasser narrow band model and (b) statistical narrow band model [MOD13]

3.12b, the absorption lines are randomly distributed over the narrow band with different line intensities and line spacing half-widths in the reality. Assuming the line intensities within the narrow band follow a probability distribution function $p(S)$, the average band transmissivity can be approximated by the line intensity probability distribution function $p(S)$ and the path length L. Both narrow band models are computationally efficient in engineering applications.

There are many narrow band models published in last decades [MOD13]. The first SNB model RADCAL [GRO93] is based on the Goody exponential distribution function [MOD13], which was originally developed by William Grosshandler at the National Institute of Standards and Technology. The RADCAL has been verified against several combustion experiments [BEC11]. However, the numerical resolution is relatively sparser than advanced narrow band models. The EM2C/SNB model is published in the EM2C laboratory based on the Malkmus inverse-exponential tailed distribution function in a finer grid [SOU97]. The EM2C/SNB parameters are given for combustion applications at the temperature range 300 – 2900 K and spectral range 150 – 9300 cm^{-1}, which are calculated from the HITEMP [ROT10] database [ROT10].

Since the SNB model only provides the band transmissivity, it is suitable to couple with the radiation ray tracing method, in which each ray is followed for the one-dimensional calculation. It is widely applied in the atmospheric radiative transfer calculations, and the average transmissivity for the nonuniform optical paths is

given in the literature [YOU97]. Even though it is time consuming to perform SNB calculations in the ray tracing solver, the SNB model can provide a benchmark reference if the LBL solution is not available [GOU00]. The comparison between the EM2C/SNB and the LBL transmissivity for $H_2O - CO_2 - N_2$ mixtures is illustrated in Fig. 3.13. The LBL results are averaged over the band width (25 cm^{-1})

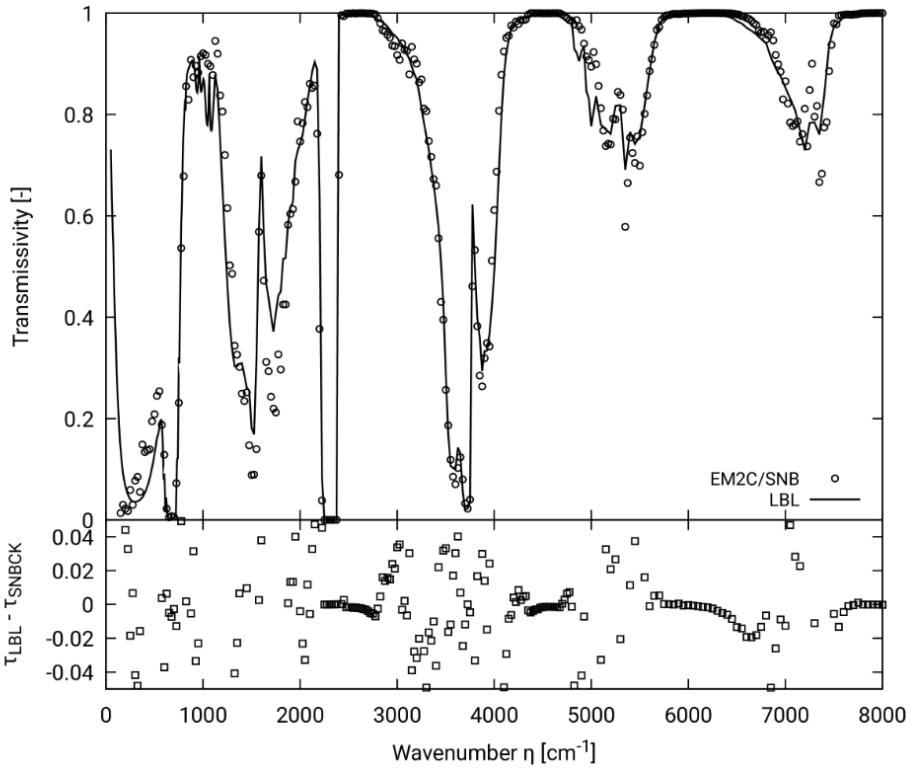

Figure 3.13: LBL and EM2C/SNB [RIV95] narrow band transmissivity comparison: T = 800 K, p = 1 atm, x_{H_2O}=0.3, x_{CO_2}=0.2, x_{N_2}=0.5, and L = 1.0 m

in order to compare with the EM2C/SNB model. The EM2C/SNB results are in excellent agreement with the LBL model in high wavenumber regions. However, the maximum deviation is about 0.06 in low wavenumber regions. This is because the EM2C/SNB model is designed for combustion applications, not low temperature applications. Therefore, it is necessary to improve the accuracy in the low wavenumber regions for the SNB model in containment flows.

The EM2C/SNB model gives the spectral gas property in terms of the average band transmissivity; however, most radiation solvers require the absorption coefficient in the radiative transfer equation. For example, it is necessary to define the mean path length [MOD13, GOU00] to obtain the absorption coefficient from the average

band emissivity, which may result in artificial errors for the thermal radiation solution. In order to solve this problem, the statistical narrow band correlated-k model (SNBCK) was proposed by Goody et al. [GOO89] to give the spectral gas property in terms of absorption coefficients and associated weights in each narrow band. The SNBCK model is based on the cumulative distribution function by reordering the absorption coefficients over the narrow band. The detailed description about the SNBCK model is given in section 4.1.2. The average band transmissivity in the SNBCK model is given as

$$\tau_{\Delta\eta} = \frac{1}{\Delta\eta}\int_{\eta}\exp(-\kappa_\eta L)d\eta \simeq \sum_{i=1}^{N}\omega_i \exp(-\kappa_i L) \tag{3.28}$$

where κ_i is the absorption coefficient; ω_i is the associating weight. As shown in Eq. 3.28, the averaged band transmissivity $\tau_{\Delta\eta}$ is approximated by N points quadrature integration. This method is not only limited to the transmissivity. Any radiation function related to the absorption coefficient can be approximated in this way

$$\phi_{\Delta\eta} = \frac{1}{\Delta\eta}\int_{\Delta\eta}\phi_\eta(\kappa_\eta)d\eta \sim \sum_{i=1}^{N}\omega_i\phi_i(\kappa_i) \tag{3.29}$$

where $\phi_i(\kappa_i)$ is obtained by solving the radiative transfer equation with the absorption coefficient κ_i. As shown in Eq. 3.29, the computational effort is significant reduced in the narrow band model in comparison with the LBL model because the number of quadrature points is small.

3.2.3 Wide Band Model

Since there are about 300 bands for the narrow band calculations, it is still computationally intensive in engineering applications. If the SNB model is coupled with the discrete ordinates solver, it is necessary to solve around 300 spectral radiative transfer equations. Only after those spectral intensities get converged, the radiative source term can be determined for the CFD energy equation. The wide band model is in a coarse resolution for spectral intensities, in which the whole infrared radiation spectrum is divided into about 10 bands mainly considering the absorption bands. For example, steam molecules have strong absorption bands in 140 cm^{-1}, 1600 cm^{-1} and 3760 m^{-1} regions, while the absorption bands of carbon dioxide are located at 667 cm^{-1}, 2410 cm^{-1} and 3660 cm^{-1} regions (see Fig. 2.7). In other regions, there is a weak absorption effect ($\kappa \sim 0\,m^{-1}$), which can be neglected in the gas radiation analysis. The most successful wide band model is the exponential wide band model (EWBM), which was developed by Edwards and Balakrishnan in 1964 [EDW64]. Assuming the absorption intensity has an exponential decay from the band center, the total band absorption for a homogeneous media is

$$A = \int_{band}\epsilon d\eta = \int_{band}(1-\exp(-\kappa_\eta L))d\eta \tag{3.30}$$

The exponential wide band model calculates the total band absorptance A in a wide band width (~ 500 cm^{-1}). In the EWBM, the band absorptance A is given in the literature [EDW64, YIN10]

$$A = \int_{band} (1 - \exp(-\kappa_\eta L))d\eta \simeq 1 - \exp\left(\frac{-(S/d)\rho_a L}{\sqrt{1 + \frac{(S/d)\rho_a L}{\beta P_e}}}\right), \quad \beta = \pi\frac{\gamma}{d} \tag{3.31}$$

where S is the mean line intensity; γ is the mean half-width; d is the mean line spacing; ρ_a is the density of the absorbing gas; P_e is the effective pressure.

The detailed description of the EWBM model can be found in the literature [YIN10]. The EWBM can give the spectral gas property for combustion mixtures including H_2O, CO_2, CO, CH_4, SO_2 and soot. The EWBM model only resolves the transmissivity in a very coarse interval, and the detailed variations over the spectral region are neglected in the EWBM model. The numerical error is relatively larger than the narrow band models. It is reported that the maximum error of the EWBM model can be as high as 50% to 80% in comparison to the experiment [MOD13]. However, those comparisons are dedicated for combustion applications. There are few investigations to examine the applicability of EWBM in relatively low temperature applications. The comparison between the EWBM and the LBL transmissivity for $H_2O - CO_2 - N_2$ mixtures is illustrated in Fig. 3.14. The gas mixture is at relatively

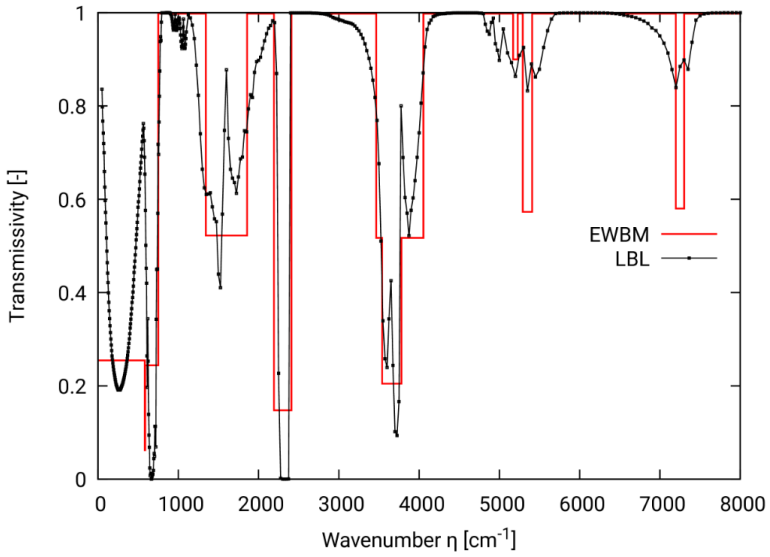

Figure 3.14: LBL and EWBM band transmissivity comparison: T = 600 K, p = 1 atm, x_{H_2O}=0.1, x_{CO_2}=0.1, x_{N_2}=0.8 and L = 1.0 m

low temperature 600 K at atmospheric pressure which are similar to temperature

and pressure conditions in containment flows after severe accidents. The gas mixture is composed of 10 vol.% H_2O and 10 vol.% CO_2 to check the band transmissivity with different non-gray gases in the media. The path length is 1.0 m in this case. The LBL band transmissivity results are averaged over 25 cm^{-1} band width. As expected, there are huge differences between the EWBM and LBL results (see Fig. 3.14). The EWBM only gives a rough estimation of the spectral gas properties. The width of the absorption band in the EWBM is underestimated in the high wavenumber region. The maximum difference is located at low wavenumber regions < 1000 cm^{-1}. This region is important to determine the radiation heat transfer between steam molecules in relatively low temperature applications.

Secondarily, the EWBM only gives the spectral gas property in terms of transmissivity not absorption coefficient. In order to couple with the discrete ordinates solver, the Gray Wide Band Model (GWBM) is recommended in Fire Dynamic Simulator (FDS) [MCG00]. In FDS, there are six bands to represent the most important absorption bands for fuel, CO_2 and H_2O, which can provide an accurate representation of the most important absorption bands for CO_2 and H_2O [HOS03]. Table 3.2 is the band structure for methane in the FDS thermal radiation solver [MCG13]. According to Table 3.2 it is clear that the main absorption bands are located below

Table 3.2: Limits of the spectral bands for methane in FDS [MCG00, MCG13]

Band	Lower bound η_L (cm^{-1})	Upper bound η_U (cm^{-1})
1	50	1000
2	1000	2174
3	2174	2400
4	2400	3400
5	3400	3800
6	3800	10000

3400 cm^{-1} regions. For each wide band, the band mean absorption coefficient κ^{band} is defined as

$$\kappa^{band} = \frac{\int_{\eta_L}^{\eta_U} \kappa_\eta I_{b,\eta} d\eta}{\int_{\eta_L}^{\eta_U} I_{b,\eta} d\eta} \tag{3.32}$$

where κ_η is the spectral absorption coefficient; $I_{b,\eta}$ is the spectral radiation intensity. According to Eq. 3.32 the gray gas assumption is also applied in the wide band model which may lead to large numerical errors. After determining the band mean absorption coefficient κ^{band} in each band, there are still six spectral radiative transfer equations to solve in FDS. The GWBM aims at a balance between computational time and accuracy; however, it cannot take account of the H_2O molar fraction effect on H_2O absorption coefficients. In containment flows, the temperature is relatively low. It is necessary to define a new band structure for the GWBM model in the thermal radiation solver for containment flows.

3.2.4 Weighted-Sum-of-Gray-Gases Model

The Weighted-Sum-of-Gray-Gases (WSGG) model is the most widely used non-gray gas model in engineering calculations due to its simplicity. This WSGG model is more efficient than other band models as there is no band resolution in the WSGG model. The first WSGG model was proposed by Smith et al. [MOD13, SMI82]. In this model, the spectral gas property is represented by the total emissivity over the path length L. The total emissivity is calculated by a few number of gray gases with different weights. The gray gas absorption coefficient remains constant over the whole infrared radiation spectrum. However, the weighting factor can change at different temperatures in the WSGG model. The total emissivity of a non-gray gas media for a path length L is given as

$$\epsilon = \sum_{i=1}^{N} a_i(T)[1 - \exp(-\kappa_i p_{species} L)] \tag{3.33}$$

$$a_i(T) = \sum_{j=0}^{N} b_{i,j} T^j \;\; (i = 1, ..., N), \;\; a_i(T) > 0 \tag{3.34}$$

where N is the number of gray gases; $p_{species}$ is the partial pressure of absorbing species; $a_i(T)$ is the fitting weight for the gray gas κ_i; and $b_{i,j}$ is the temperature fitting coefficient.

The κ_i and $b_{i,j}$ parameters are given by the WSGG model using the fitting algorithm [SMI82]. Normally the number of gray gases equals to 3 or 4. In additional to the gray gases, there is a transparent gas for $i = 0$ ($\kappa_0 = 0\ m^{-1}$). The weight of the transparent gas is calculated by $1 - \sum_{i=1}^{N} a_i(T)$. However, the WSGG model cannot resolve the spectral fluctuation over the infrared radiation spectrum. In the WSGG model, the gray absorption coefficient κ_i is fixed, but the weighting factor $a_i(T)$ is a function of media temperature T. The weighting coefficients can be generated by the fitting procedure [SMI82, LIU21]. There are many WSGG models available for combustion applications [MOD13], but not for low temperature applications. It is necessary to design a tailored WSGG model for low temperature applications in containment flows. Another limitation of the WSGG model is the fixed molar fraction of H_2O and CO_2. The molar fraction is important to determine the steam absorption coefficient in containment atmospheres. Although Cassol et al. [CAS14] proposed a new WSGG approach for arbitrary concentrations of H_2O, CO_2 and soot, the WSGG model cannot resolve the spectral intensities. The numerical error must be quantified before applying the WSGG model in containment flows.

The WSGG model gives a good approximation for the total emissivity. The total emissivities calculated from LBL and WSGG models [LIU21, CAS14] for the steam partial pressure 0.8 atm are shown in Fig. 3.15. The WSGG emissivities are in good

agreement with the LBL results for long path lengths (see Fig. 3.15). The main difference between LBL and WSGG is located at short path lengths. Even though the emissivity difference between WSGG and LBL is pretty small in Fig. 3.15, it may lead to a large numerical error in thermal radiation analyses. More investigations for the WSGG model are required. In order to obtain the absorption coefficient from

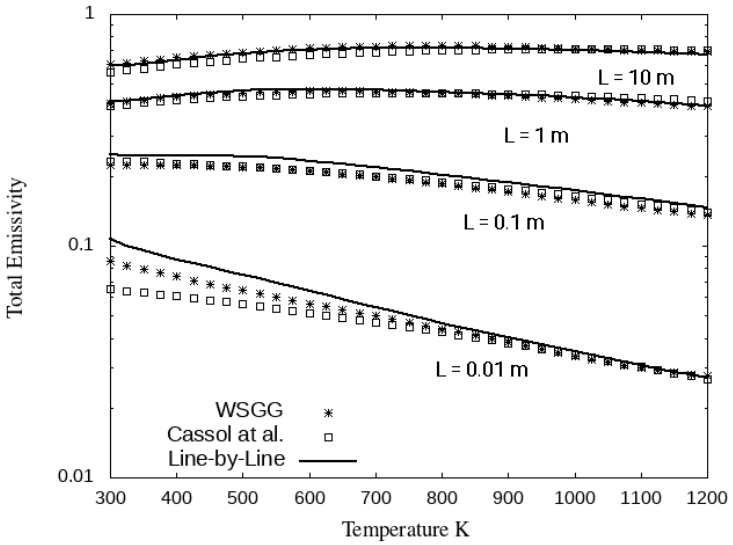

Figure 3.15: Comparison of the total emissivity between WSGG [LIU21] and LBL for p_{H_2O} = 0.8 atm

the total emissivity, the mean path length L is required as a user input to calculate the gray absorption coefficient based on the total emissivity ϵ

$$\kappa = -\frac{ln(1-\epsilon)}{L} \tag{3.35}$$

where L is the mean free path. Normally the mean free path L equals to $\frac{3.6V}{S}$ (V is the volume of computational domain and S is the surface area) [GOU00]. From Eq. 3.35, the gray absorption coefficient κ is highly sensitive to the path length. The numerical error may become large when selecting an unreasonable path length in thermal radiation simulations.

3.2.5 Gray Gas Model

The gray gas model is the simplest gas model assuming that the spectral gas property is constant over the infrared radiation spectrum. Therefore, there is no spectrum interval in the gray gas model and the radiative transfer equation is solved

over the whole infrared spectrum. As a result, the gray gas model is an efficient model to obtain a rough estimation of the absorption coefficient in radiation heat transfer. Due to its simplicity, it is much faster than other non-gray models in engineering simulations [WAN14]. The Planck mean absorption coefficient is widely used in gas radiation analyses [ZHA02] due to its efficiency. The Planck mean absorption coefficient is only a function of temperature and species partial pressure, i.e., H_2O and CO_2. The Planck mean absorption coefficient is defined as

$$\kappa_P = \frac{\int_0^\infty \kappa_\eta I_{b,\eta} d\eta}{\int_0^\infty I_{b,\eta} d\eta} \tag{3.36}$$

where κ_η is the spectral absorption; $I_{b,\eta}$ is the spectral radiation intensity. According to Eq. 3.36, the Planck mean absorption coefficient is an optically thin approximation in thermal radiation analyses.

The Planck absorption coefficients for H_2O and CO_2 at different temperatures are illustrated in Fig. 3.16. The H_2O Planck mean absorption coefficient is larger than

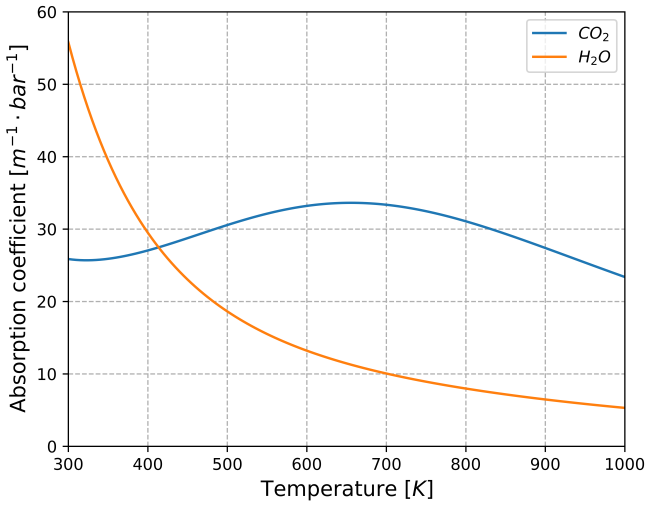

Figure 3.16: Planck mean absorption coefficient for CO_2 and H_2O

the CO_2 Planck mean absorption coefficient at low temperature regions. There is a strong decay for the H_2O Planck mean absorption coefficient with the increase of temperature [ZHA02]. Table 3.3 gives the empirical equation to calculate the Planck mean absorption coefficient for carbon dioxide and water vapor [CAS15]. Although the accuracy of gray gas model is far from satisfactory [ZHA02], the gray gas model can be applied in different thermal radiation solvers for the code-to-code verification. Under the gray gas assumption, the impact of spectral gas property can be eliminated to compare the numerical stability of different thermal radiation solvers. The gray assumption is reasonable in flame simulations considering

Table 3.3: Absorption coefficients for the gray gas model [CAS15]

Chemical species	Absorption coefficient (m^{-1})		
	$\kappa = 100 p_i (c_0 + c_1 T + c_2 T^2 + c_3 T^3 + c_4 T^4 + c_5 T^5)$		
H_2O and CO_2		$i = H_2O$	$i = CO_2$
	$c_0\,(m^{-1}atm^{-1})$	7.5702×10^{-1}	-6.4750×10^{-1}
	$c_1\,(m^{-1}atm^{-1}K^{-1})$	-1.9716×10^{-3}	4.2895×10^{-3}
	$c_2\,(m^{-1}atm^{-1}K^{-2})$	2.1998×10^{-6}	-6.6089×10^{-6}
	$c_3\,(m^{-1}atm^{-1}K^{-3})$	-1.2492×10^{-9}	4.4190×10^{-9}
	$c_4\,(m^{-1}atm^{-1}K^{-4})$	3.5385×10^{-13}	-1.3796×10^{-12}
	$c_5\,(m^{-1}atm^{-1}K^{-5})$	-3.9663×10^{-17}	1.6484×10^{-16}

the soot formation. Since the soot emission spectrum is continuous, the gray gas assumption is validated in the presence of large amounts of soot in combustion applications [DEM12]. In the past decades, the gray gas model was generally coupled with the P_1 radiation solver in combustion applications [MOD13]. But it is not suitable for the reactor safety analysis because of the numerical error. The numerical error from the thermal radiation solver can accumulate after long CFD timesteps leading to unreasonable temperature predictions [LIU22b].

3.2.6 Assessment of Different Spectral Gas Property Models

A number of non-gray gas models have been developed in last five decades for the spectral gas property in engineering applications, e.g., atmospheric radiation and combustion [MOD13, HOW20]. In the previous section, different non-gray gas models are briefly described for thermal radiation heat transfer in containment flows. Non-gray gas models, according to their complexity, can be divided into four major groups: (i) baseline model, (ii) narrow band model, (iii) wide band model, (iiii) global band model (see Table 3.4). The main difference between these non-gray gas models is the spectral resolution. The LBL calculation is the baseline reference for other non-gray gas models considering all transition lines over the whole infrared radiation spectrum. There are thousands or millions of transition lines in the LBL model to determine the spectral absorption coefficient κ_η. The whole infrared radiation spectrum is divided into a number of bands in the band models, such as the narrow band and wide band model. The narrow band resolution is about 25 cm^{-1}, while the wide band resolution is about 300 cm^{-1}. The narrow band transmissivity is in a good agreement with the experimental data. The wide band model is computationally efficient and accurate for combustion applications. The total emissivity ϵ_{tot} is calculated in the WSGG model with a small number of gray gases having different weighting factors, and the absorption coefficient can be obtained by defining the mean path length. However, the gray gas and WSGG models

Table 3.4: Overview of spectral gas properties, modified from [BEC13]

Model		Spectral resolution	Radiative property	Gas composition
Baseline model	LBL	0.01 cm^{-1}	κ_η	Variable
Narrow band model	SNB	25 cm^{-1}	τ_η	Variable
	SNBCK	25 cm^{-1}	κ_i and ω_i	Variable
Wide band model	EWBM	~ 300 cm^{-1}	τ_{band}	Variable
	GWBM	~ 300 cm^{-1}	κ_{band}	Fixed
Global model	WSGG	-	ϵ_{tot}	Fixed
	Gray	-	κ	Fixed

cannot take account of the gas composition effect on absorption coefficients. The simplest gray gas model has just one constant absorption coefficient to represent the spectral gas property. Therefore, the simplest gray gas model has a huge numerical error.

Before applying non-gray gas models for real engineering applications, it is necessary to examine the difference between different non-gray gas models. Apparently different non-gray gas models have different implementation strategies, computational times, and achievable accuracies in the radiation modeling. In the SNB and EWBM models, the spectral gas property is given in terms of band transmissivity, not the absorption coefficient which is required for the radiative transfer equation [STR02, TES11]. Therefore, both are coupled with the discrete transfer solver, which only requires the transmissivity for the light of sight tracking [COE97]. As discussed before, it is computationally expensive for the LBL and SNBCK calculations when coupling with the finite volume discrete ordinates solver. The finite volume discrete ordinates method with the WSGG model is a common strategy for fire applications [DEM12]. However, most of existing WSGG models are developed for combustion applications, not for low temperature applications.

The simplest thermal radiation solver is the P_1 solver, which only considers the gray gas model. The main drawback of the P_1 solver with gray gas model is the numerical error [SUN19]. A detailed discussion about thermal radiation solvers is given in section 3.3. Since the discrete ordinates method is widely utilized in the thermal radiation analysis for the code-to-code verification, different non-gray gas models are verified in this section with the discrete ordinate method [CHA93]. The purpose of the non-gray gas assessment is to examine the accuracy of different non-gray gas models. The simplest one-dimensional geometry is applied to obtain the radiative source term without large numerical errors. The radiative transfer equation can be solved accurately in one-dimensional parallel plates (see Eq. 3.37).

The one-dimensional radiative transfer equation is

$$\mu \frac{\partial I_\eta(x,\mu)}{\partial x} = -\kappa_\eta(x) I_\eta(x,\mu) + \kappa_\eta(x) I_{b,\eta}(x,\mu) \tag{3.37}$$

where μ is the direction cosine of solid angle. The first step is to separate the computational domain into a number of small control volumes in one-dimensional parallel plates (see Figure 3.17). The spectral radiation intensity $I_\eta(x,\mu)$ is solved on

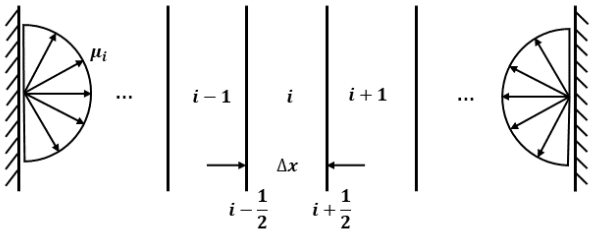

Figure 3.17: One-dimensional RTE discretization

a set of discrete solid angles μ. The finite difference method is applied to solve 1D thermal radiation problems. The 1D thermal radiation solver has been widely investigated without large numerical errors [CHU11, MOD13, KIM91, DEM12]. In the 1D geometry, the detailed LBL model can be perform to give the reference result. The finite difference approach for the 1D thermal radiation is

$$\mu \frac{I_\eta(x_{i+1/2},\mu) - I_\eta(x_{i-1/2},\mu)}{\Delta x} = -\kappa_\eta(x_i) I_\eta(x_i,\mu) + \kappa_\eta(x_i) I_{b,\eta}(x_i,\mu) \tag{3.38}$$

where $I_\eta(x_{i+1/2},\mu)$ and $I_\eta(x_{i-1/2},\mu)$ are the radiation intensities on surfaces (see Fig. 3.17); $\kappa_\eta(x_i)$ is the absorption coefficient for the cell i. In the following discussion, two different 1D test cases with different temperature and concentration conditions are simulated to evaluate the non-gray gas model.

In the test case 1, the non-gray gas media composes of 20 vol.% H_2O, 10 vol.% CO_2 and 70 vol.% N_2 at atmospheric pressure (1 atm). The media temperature is homogeneous (1000 K) within two plates. The distance between two separate plates is 1.0 m, and the two boundary walls are black and cold 0 K. Numerical calculations are performed using 100 uniform control volumes with 48 angular directions. It is found that refining the mesh does not improve the simulation results. The purpose of this test is to verify different non-gray gas models for the multi-species mixture with homogeneous temperature and concentration profiles.

The LBL absorption coefficient is generated from the HITRAN2016 database with a spectral interval $0.01\,cm^{-1}$ to resolve the rapid fluctuation. The EM2C/SNBCK

model from Taine and Soufiani [TAI99] can be downloaded from Modest's book [MOD13]. In the EM2C/SNBCK model, there are 44 bands for steam, whereas it has 17 overlapping bands for CO_2. With regard to the GWBM model, it is generated from the band Plank mean absorption coefficient [MCD08]. The WSGG parameters can be obtained from Cassol et al. [CAS14]. Numerical results using different non-gray gas models are shown in Fig. 3.18. First of all, there is a significant impact

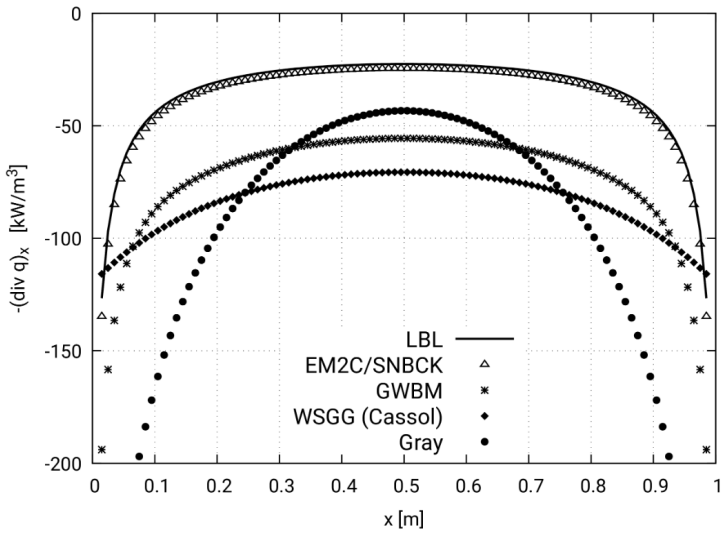

Figure 3.18: Radiative source term for different non-gray gas models in test case 1: T = 1000 K, p = 1.0 atm, x_{N_2} = 0.7, x_{H_2O} = 0.2, x_{CO_2} = 0.1 and L = 1.0 m

on the radiative source term when applying different non-gray gas models. The EM2C/SNBCK model is superior to other global gas models, and the accuracy of the EM2C/SNBCK model is similar to that of the LBL model. For other non-gray gas models, there is a virtual absorption effect at transparent bands due to the simplified approximation. For example, the gray gas model has a constant absorption coefficient over the whole infrared radiation spectrum, which is far from the reality of spectral gas property. As a result of the unreasonable simplification, other non-gray gas models over-predict the radiative source term in this test case (see Fig. 3.18). The radiative source term for the gray gas model is about two times larger than the LBL model. Although the WSGG predictions are better than the gray gas model, the numerical accuracy is still far from satisfactory. The GWBM model can provide a reasonable prediction in the radiative source term; however, the numerical deviation is relatively large for the reactor safety analysis.

From this one-dimensional homogeneous isothermal test case, it is concluded that the radiative source term varies remarkably within a short distance. There is a steep gradient near the boundary wall for the radiative source term. In the high absorption media, the radiative source term is sensitive to the temperature differ-

ences. This is the reason why thermal radiation is important for the temperature distribution with high steam concentrations in containment flows. To quantify the numerical error and the model differences, the relative error of the radiative source term is calculated according to Eq. 3.39, and the LBL model is considered as the reference [DEM12].

$$rel.error = \left| \frac{\nabla \cdot q_r^{model} - \nabla \cdot q_r^{ref}}{\nabla \cdot q_r^{ref}} \right| \tag{3.39}$$

The computational time and numerical error for the test case 1 are shown in Table 3.5. As expected, the LBL model is the most computationally expensive method

Table 3.5: Summary of relative errors and computational time for the one-dimensional test case with a homogeneous media

Model	CPU (s)	Radiative source term relative error		
		Min. error	Max. error	Ave. error
LBL	3141.11	-	-	-
EM2C/SNBCK	5.23	1.70%	4.78%	3.57%
GWBM	0.24	53.10%	146.54%	123.95%
WSGG	0.21	8.53%	213.26%	167.01%
Gray	0.22	92.22%	279.95%	180.80%

among all non-gray gas models. The simulation time for the LBL model is over 3000 s, while it only requires a few seconds for the EM2C/SNBCK model. Therefore, the LBL model is unaffordable in engineering applications owing to its efficiency. It is necessary to note that the predictions obtained with the EM2C/SNBCK model are accurate for the multi-species mixture, and the maximum error is less than 5% for the EM2C/SNBCK model. In comparison with the WSGG and gray gas models, the computational efficiency of the EM2C/SNBCK model is much slower in the multi-species mixture media. The numerical accuracy for the WSGG and Gray gas models is intolerable in the thermal radiation analysis. The simulation results from GWBM model are superior to the WSGG and gray gas models.

In the test case 2, the distance of two separate plates is also 1.0 m, but it has a non-gray gas mixture of nonhomogeneous and nonisothermal profiles at 1.0 atm. The media temperature and species concentration distributions are shown in Eq. 3.40, and the ambient gas is N_2. The two boundary walls are black and cold (0 K).

$$\begin{aligned} T &= 800 + 200\sin^2(\pi x) \\ x_{H_2O} &= 0.2 + 0.2\sin^2(2\pi x) \\ x_{CO_2} &= 0.1\cos^2(2\pi x) \end{aligned} \tag{3.40}$$

In this case, it has more than 20 vol.% steam to highlight the radiation absorption effect of steam (see Eq. 3.40). After a postulated severe accident in nuclear plants,

the temperature difference is modest in containment flows, but the distribution of steam in containment buildings is strongly variable in space and time. It is necessary to take account of this effect in the tailored non-gray gas model for containment flows. Furthermore, the ratio of H_2O and CO_2 partial pressures is not fixed in this test case.

Numerical calculations using different non-gray gas models for test case 2 are shown in Fig. 3.19. For the radiative source term, there is a steep slope near the cold wall. The maximum energy term $-\nabla \cdot q_r$ is found near $x = 0.2\ m$ and $x = 0.8\ m$ regions. In those regions, the radiative source term is not only related to the temperature difference, but also H_2O and CO_2 molar fractions. The EM2C/SNBCK result is in good agreement with the LBL model, and the EM2C/SNBCK model can deal with the gas composition effect on spectral gas properties. This model can be applied for the radiation heat transfer in containment flows. However, there is a slight deviation between LBL and SNBCK at $x = 0.5\ m$ region. It has the maximum CO_2 molar fraction at this point, and the EM2C/SNBCK result is smaller than the LBL model. The accuracy of the EM2C/SNBCK model may decrease in the presence of large amounts of CO_2 in the gas mixture. The slope of the radiative source term obtained from the GWBM model is over-predicted in near wall regions. After that, it decreases significantly in comparison with the LBL and EM2C/SNBCK models. The GWBM prediction is better than the WSGG result near the boundary walls (see Fig. 3.19). It is concluded that the GWBM model is not accurate for the non-gray

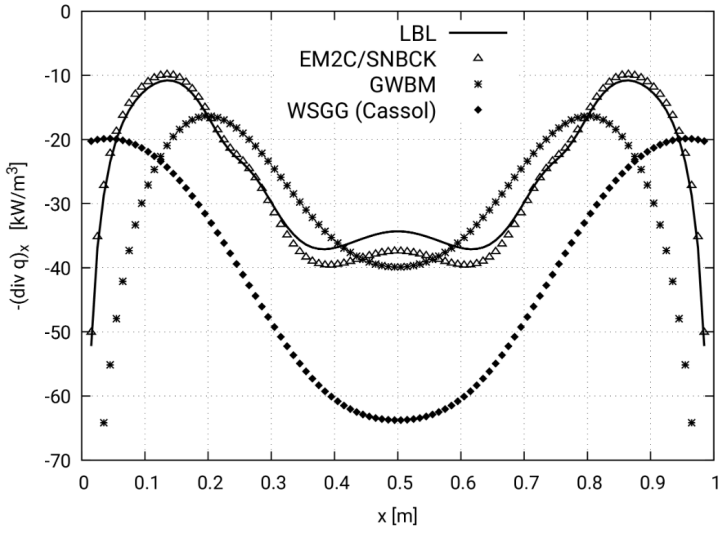

Figure 3.19: Radiative source term for different non-gray gas models in test case 2: $T = 800 + 200\sin^2(\pi x)\ K$, $p = 1\,atm$, $x_{H_2O} = 0.2 + 0.2\sin^2(2\pi x)$, $x_{CO_2} = 0.1\cos^2(2\pi x)$ and $L = 1.0\,m$

gas mixture with flexible H_2O and CO_2 molar fractions. The WSGG result is far

from satisfactory, especially near $x = 0.5\,m$ region. The band model is generally superior to the global gas model for H_2O-CO_2 mixtures. Since the numerical error of the gray gas model is too large, the gray gas model is not illustrated in Fig. 3.19. The numerical accuracy and computational efficiency for test case 2 with different non-gray gas models are given in Table 3.6.

The LBL model is considered as the most accurate result; however, the LBL model becomes more expensive in the realistic applications with random temperature and concentration distributions. The EM2C/SNBCK model is reliable and efficient for

Table 3.6: Summary of relative errors and computational time for the one-dimensional test case with a nonhomogeneous media

Model	CPU (s)	Radiative source term relative error		
		Min. error	Max. error	Ave. error
LBL	4741.11	-	-	-
SNBCK	7.38	1.23%	8.03%	5.64%
GWBM	0.23	1.18%	142.39%	45.61%
WSGG	0.22	1.05%	135.32%	72.87%
Gray	0.22	4.51%	317.60%	122.88%

the gas mixture with flexible H_2O and CO_2 molar fractions. The simulation results using the EM2C/SNBCK model are in good agreement with the LBL model. The maximum error is about 8% for the EM2C/SNBCK model. However, the numerical efficiency for the EM2C/SNBCK model decreases significantly when considering H_2O-CO_2 gas mixtures with different molar concentrations. The GWBM model can provide a reasonable estimation in multi-species media. The average error of the GWBM model is about 46% for the test case 2. When coupling the GWBM model into the CFD solver, the numerical error can be intensified over a long term (> hours). The WSGG and gray gas models widely overestimate the radiative source term in this test case. According to the above two simplified one-dimensional test cases, it is found that the non-gray gas model has a strong impact on the accuracy of thermal radiation analysis. Although applying the same numerical solver in the thermal radiation calculation, the radiative source terms are completely different in a number of non-gray gas models. The LBL model is super expensive in comparison with other non-gray gas models. The EM2C/SNBCK model is a compromise between accuracy and efficiency. However, the EM2C/SNBCK model is dedicated for combustion applications. An accurate non-gray gas model is mandatory to calculate the radiation heat transfer in containment flows. After the spectral gas property is calculated, an efficient thermal radiation solver is also important for the thermal radiation analysis. It is difficult to resolve the radiation intensity in the containment building due to its large volume (70,000 m^3). In the following section, different thermal radiation solvers are briefly introduced to evaluate the numerical error from thermal radiation solvers.

3.3 Numerical Methods for Radiative Transfer Equation

There are two kinds of methods to solve the radiative transfer equation: the deterministic method, e.g., P_1 and finite volume discrete ordinates method (fvDOM), and the stochastic method, e.g., Monte Carlo method. The radiative transfer equation without scattering effect is shown in Eq. 3.41, which can be formulated in two coordinate systems: Cartesian coordinate and Lagrange coordinate. In the Cartesian coordinate system, the radiative transfer equation is similar to the CFD momentum equation in a fixed direction Ω (see Eq. 3.41). This equation can be easily solved in the fvDOM solver. However, the numerical error of the fvDOM solver originates from the 'diffusion' term $\Omega \cdot \nabla I_\eta(r,\Omega)$, which is related to the surface interpolation scheme and the computational mesh.

$$\underbrace{\Omega \cdot \nabla I_\eta(r,\Omega)}_{\text{'diffusion' term}} = -\kappa_\eta I_\eta(r,\Omega) + \kappa_\eta I_{b,\eta}(r,\Omega) \tag{3.41}$$

Furthermore, it is necessary to solve a set of radiative transfer equations at different solid angles in the fvDOM solver. Therefore, the computational effort becomes expensive in complex 3D geometries. The detailed discussion about the fvDOM method can be found in section 3.3.2.

In the Lagrange coordinate system, the characteristic form of radiative transfer equation is given in Eq. 3.42 for the discrete tracing method [COE97].

$$\frac{dI_\eta(r,\Omega)}{ds} = -\kappa_\eta I_\eta(r,\Omega) + \kappa_\eta I_{b,\eta}(r,\Omega) \tag{3.42}$$

The discrete tracing method follows the radiation intensity $I_\eta(r,\Omega)$ from the boundary wall to its position r along the light of sight. Consequently, the numerical diffusion error is eliminated in the discrete ray tracing method. However, the Lagrangian ray tracing solver is time-consuming in comparison with other Euler solvers.

After the spectral radiation intensity $I_\eta(r,\Omega)$ is solved in the computational domain, the radiation energy balance within a control volume is shown in Fig. 3.20. The divergence of radiative heat fluxes q_r within a control volume is called the radiative source term $\nabla \cdot q_r$. The radiative source term is equal to the energy difference between absorbed and emitted radiative energy (see Eq. 3.43)

$$\nabla \cdot q_r = \int_\eta \int_{4\pi} \kappa_\eta I_{b,\eta}(r,\Omega) d\eta d\Omega - \int_\eta \int_{4\pi} \kappa_\eta I_\eta(r,\Omega) d\eta d\Omega \tag{3.43}$$

The first term on the right hand side of Eq. 3.43 is the black body emission, and the second term is the radiative absorption within the control volume. The black

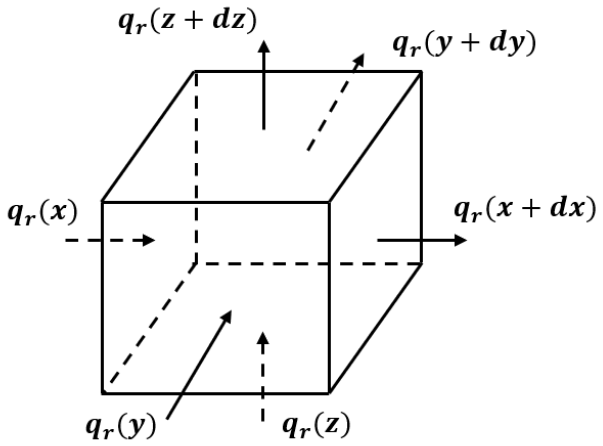

Figure 3.20: Radiative energy balance within a small control volume

body radiation intensity $I_{b,\eta}(r,\Omega)$ is only related to the media temperature. But the radiation intensity $I_\eta(r,\Omega)$ is difficult to resolve in complex geometries, which is a function of temperature, molar fraction, pressure and surface emissivity. Similarly, the radiative wall heat flux q_r is the energy difference between absorbed radiative heat flux and emitted heat flux on the boundary wall

$$q_r = \epsilon \int_0^\infty \int_{\Omega' \cdot n<0} I_\eta(r_w,\Omega')|\Omega' \cdot n| d\Omega' d\eta - \epsilon \int_0^\infty \pi I_{b,\eta}(r_w,\Omega) d\eta \tag{3.44}$$

where n is the boundary surface normal vector; r_w is the boundary wall position; ϵ is the surface emissivity; $I_{b,\eta}(r_w,\Omega)$ is the black body emission intensity on the surface. After obtaining the radiative source term $\nabla \cdot q_r$ and radiative wall heat flux q_r, these terms are considered as additional heat source terms in the energy equation (see Eq. 2.13).

Besides the spectral gas property, another issue about thermal radiation analysis is the thermal radiation solver. A number of different radiation solvers have been published in the last few decades [FIV87, MOD13, FAR98], but the high resolution of the thermal radiation heat transfer is still a challenging task [MOD13]. As shown in Eq. 3.43 and Eq. 3.44, the thermal radiation solver is related to the treatment of spectral gas properties. Therefore, in the following section the numerical solution methods are discussed under the gray gas assumption to simplify the explanation. The detailed discussion about the advanced thermal radiation solver with non-gray media is shown in Chapter 4. The radiative transfer equation with the gray gas assumption is

$$\Omega \cdot \nabla I(r,\Omega) = -\kappa I(r,\Omega) + \kappa I_b(r,\Omega) \tag{3.45}$$

where κ is the gray absorption coefficient.

3.3.1 P_1 method

Since the radiation intensity $I(r,\Omega)$ is a complex function of the spatial $r(x,y,z)$ and directional $\Omega(\theta,\phi)$ variables, the method of variable separation is a common technique in mathematics to simplify the complex partial differential equation [STR07]. The spherical harmonics method provides an approximation solution to decompose the complex coupling between the spatial and directional variables for the radiation intensity [MOD13]. The radiation intensity $I(r,\Omega)$ can be expanded as a linear combination of spherical harmonics $Y_n^m(\Omega)$ and position variation $I_n^m(r)$.

$$I(r,\Omega) = \sum_{n=0}^{\infty} \sum_{m=-n}^{m=n} I_n^m(r) Y_n^m(\Omega) \tag{3.46}$$

where $I_n^m(r)$ is the position function representing the spatial variation (see Eq. 3.47)

$$I_n^m(r) = \int_0^{4\pi} I(r,\Omega) Y_n^m(\Omega) d\Omega \tag{3.47}$$

$Y_n^m(\Omega)$ is the spherical harmonics function representing the directional variation

$$Y_n^m(\Omega) = Y(\phi,\theta) = \begin{cases} cos(m\phi) P_n^m(cos\theta) \\ sin(|m|\phi) P_n^m(cos\theta) \end{cases} \tag{3.48}$$

P_n^m is the associated Legendre function [MOD13]. According to Eq. 3.46, the numerical accuracy is related to the order of expansions N for the P_N method. If the order of expansions N is large enough, the P_N approximation can converge to the original value $I(r,\Omega)$. It is cumbersome to solve the P_N approximation, if the order of expansions N is larger than 5. Normally, the $N > 1$ terms are truncated in Eq. 3.46 to simplify the complexity, which is called the P_1 method. After the decoupling of spatial and directional variables, the computation effort is significantly reduced in the P_1 method.

This approximation is only accurate in the optically thick media. In such conditions, the radiation intensity $I(r,\Omega)$ is assumed to be homogeneous in all solid angles Ω. The P_1 solver is usually coupled with the gray gas model. It is difficult to consider non-gray gas models in the P_1 solver, since the numerical error may become large in optically thin bands. The P_1 solver with the gray gas model can be written as

$$\nabla \cdot \left(\frac{1}{3\kappa} \nabla G(r) \right) - G(r) = -4\sigma T^4 \tag{3.49}$$

where κ is the absorption coefficient; T is the media temperature; σ is the Stefan-Boltzmann constant; G is the incident intensity

$$G(r) = I_0^0(r) = \int_0^{4\pi} I(r,\Omega) d\Omega \tag{3.50}$$

From Eq. 3.49, the original radiative transfer equation is converted to a diffusion equation assuming the radiation intensity $I(r, \Omega)$ is near-isotropic. Therefore, the false scattering and ray effect are eliminated in the P_1 model. Although the P_1 method is not an accurate model, it is the fastest model to consider the gas absorption effect. The numerical accuracy is highly related to the number of expansions. This method provides a poor prediction for the radiative wall heat flux, as the radiation intensity $I(r, \Omega)$ is not isotropic on boundary walls. To improve the numerical accuracy, the higher order P_N approximation is required. However, the high-order P_N method is complex in mathematics. The simplified P_N method [FRA07] was introduced to reduce the numerical complexity. Before applying the P_N method in thermal radiation analyses, it is necessary to have the code-to-code comparison to quantify the numerical error.

3.3.2 Finite Volume Discrete Ordinate Method

Among the thermal radiation solvers, the most widely applied method is the finite volume discrete ordinates method (fvDOM), which solves the radiation intensity $I(r, \Omega)$ in a set of quadrature directions. The discrete ordinates algorithm was firstly proposed by Lee et al. [LEE62] for the neutron transport equation using the finite difference scheme in the 1960s. After several decades of development, the fvDOM can be applied to complex geometries in fire simulations. Furthermore, the scattering effect of soot can be included in the fvDOM model for fire simulations.

Unfortunately, the fvDOM model suffers from the false scattering [CHA93], which is the numerical error due to surface interpolation schemes. This effect can be reduced by increasing the number of control volumes in the mesh grid, whereas it requires more computational time to solve the radiative transfer equation. When applying the fvDOM solver in fire applications, the common approximation of spectral gas property is the gray gas model, which neglects the spectral dependency of the absorption coefficient. However, this assumption is not sufficient in high humidity environments. The reliable thermal radiation solver and the accurate non-gray gas model are critical to understand the strength of thermal radiation heat transfer in containment flows. If the narrow and wide band non-gray gas models are applied in the fvDOM solver, it is necessary to solve the spectral radiation intensity $I_\eta(r, \Omega)$ in each energy band. Consequently, the non-gray gas consideration in the fvDOM solver may become unaffordable owing to its computational efficiency.

Besides the non-gray gas model, the greatest difficulty in solving thermal radiation heat transfer is the complexity of radiation intensity $I(r, \Omega)$. The radiation intensity $I(r, \Omega)$ is a function of the solid angle and position [MOD13]. In the fvDOM model

the solid angle Ω ($0 < \Omega < 4\pi$) is discretized into a set of quadrature directions Ω_i. For each solid angle Ω_i, the radiation intensity $I(r, \Omega_i)$ is assumed to be constant at this direction. Therefore, the integration of solid angles for the radiation intensity $I(r, \Omega)$ can be approximated as

$$G = \int_{4\pi} I(r, \Omega) d\Omega \simeq \sum_{i=1}^{N} w_i I(r, \Omega_i) \tag{3.51}$$

$$\int_{4\pi} d\Omega = \sum_{i=1}^{N} w_i = 4\pi \tag{3.52}$$

where radiation intensity $I(r, \Omega_i)$ can be obtained by solving the radiative transfer equation at the solid angle Ω_i; ω_i is the quadrature weight. An example of solid angle discretization on the $\frac{1}{8}$ spherical shell is shown in Fig. 3.21. Since the radiation intensity $I(r, \Omega)$ is resolved at each solid angle, the computational effort is expensive when considering a large number of solid angles. If the number of solid directions is not large enough in the fvDOM method, it may suffer from the ray effect in the optically thin media [LAT68].

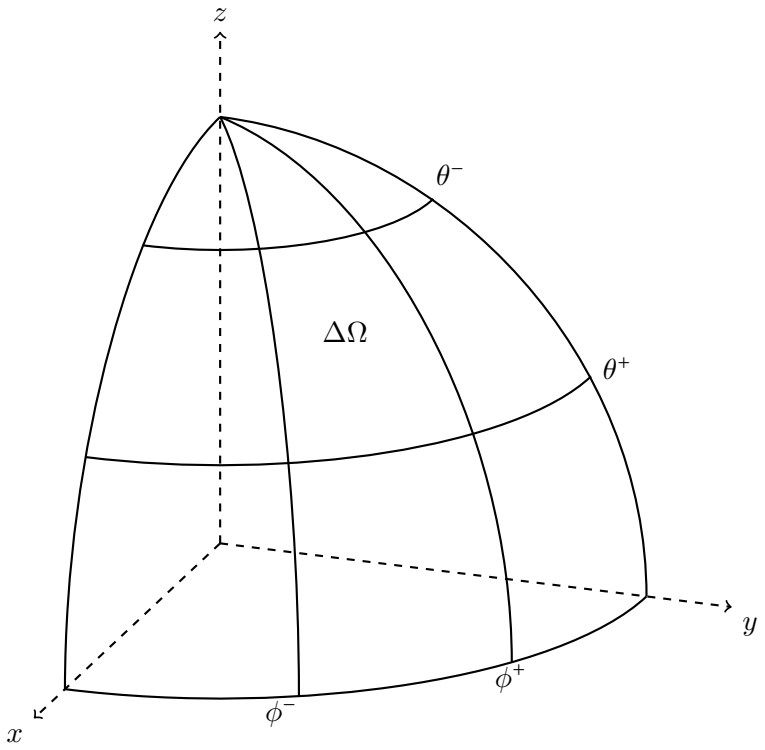

Figure 3.21: Discretization of solid angle Ω, modified from [CHA93]

The radiation intensity at a specific direction Ω_i is solved using the finite volume approach [CHA94, MOD13, MAN08]. The unstructured mesh is widely applied in

CFD simulations to represent the complex geometries. In order to couple with the CFD solver, it is convenient to resolve the radiation intensity with the same mesh. After integrating over the control volume ΔV and the solid angle $\Delta\Omega$, Eq. 3.41 can be written as

$$\int_{\Delta V}\int_{\Delta\Omega}\Omega\cdot\nabla I(r,\Omega_i)dVd\Omega = \int_{\Delta V}\int_{\Delta\Omega}-\kappa I(r,\Omega_i)dVd\Omega+\int_{\Delta V}\int_{\Delta\Omega}\kappa I_b(r,\Omega_i)dVd\Omega \tag{3.53}$$

After applying the Gauss theorem [MOU16], the left hand side term in Eq. 3.53 can be converted into the surface integration.

$$\begin{aligned}\int_{\Delta V}\int_{\Delta\Omega}\Omega\cdot\nabla I(r,\Omega_i)dVd\Omega &= \int_{\partial V}\int_{\Delta\Omega}\Omega\, I_f(r,\Omega_i)d\Omega dV\\ &= \sum I_f(r,\Omega_i)\int_{\Delta\Omega}\Omega\cdot S_f d\Omega\end{aligned} \tag{3.54}$$

where S_f is the surface direction vector; I_f is the radiation intensity on the surface center. The physical meaning of this term is the out-coming radiation energy on boundary surfaces. The $\int_{\Delta V}\int_{\Delta\Omega}-\kappa I(r,\Omega_i)dVd\Omega$ term is the radiative absorption within the control volume, whereas the $\int_{\Delta V}\int_{\Delta\Omega}\kappa I_b(r,\Omega_i)dVd\Omega$ term is the radiative emission.

After defining the interpolation scheme, a numerical matrix about radiation intensity $I^n(r,\Omega_i)$ can be built based on the previous value $I^o(r,\Omega_i)$ (see Eq. 3.55).

$$\sum I_f^n(r,\Omega_i)\int_{\Delta\Omega}\Omega\cdot S_f d\Omega = -\kappa I^o(r,\Omega_i)\Delta V\Delta\Omega+\kappa I_b^o(r,\Omega_i)\Delta V\Delta\Omega \tag{3.55}$$

This is the most widely applied fvDOM solver in fire simulations [MAN08]. There is no specific boundary layer for the thermal radiation solver. If the surface emissivity is ϵ, the radiation intensity on the wall surface $I^n(r_{wall},\Omega)$ is calculated according to Eq. 3.56.

$$I^n(r_{wall},\Omega) = \epsilon I_b(r_{wall},\Omega)+\frac{1-\epsilon}{\pi}\int_{n\cdot\Omega'<0}I^o(r_{wall},\Omega')|n\cdot\Omega'|d\Omega' \tag{3.56}$$

As shown in Eq. 3.56 this is not a Dirichlet boundary condition or a Neumann boundary condition. Actually it is a mixed boundary condition, if the surface is not black ($\epsilon \neq 1$) [MOU16]. If the emissivity of the boundary wall is not equal to one, an initial guess about the wall radiation intensity $I(r_{wall},\Omega)$ is required. The numerical iteration procedure is required until all radiation intensities converge in the computational domain.

In order to ease understanding, the fvDOM is illustrated in a two dimensional cavity (see Fig. 3.22). For three dimensional geometries the computational procedure is analogous. The fvDOM solver stores the radiation intensity $I(r,\Omega)$ at each cell center. As shown in Fig. 3.22, the solid circles are the radiation intensities, e.g., I_N

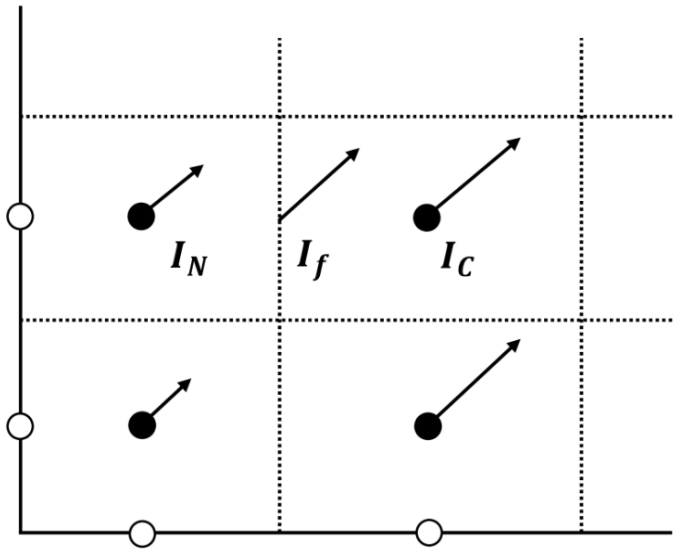

Figure 3.22: Finite volume discrete ordinates method

and I_C at cell centers. The hollow circle represents the radiation intensity on walls. In order to solve the radiative transfer equation, the surface intensity I_f is approximated by the linear interpolation between two control volumes (I_N and I_C). The numerical interpolation is illustrated in Eq. 3.57 (see Fig. 3.22).

$$I_f = \omega I_N + (1 - \omega) I_C \tag{3.57}$$

There are many spatial differencing schemes available in the literature [CHA93, COE14]. The most widely used schemes are the step, central, and exponential schemes [JOS05]. However, the surface radiation intensity is only related to the downstream intensity in physically, not neighbouring radiation intensities (see Fig. 3.22). The inaccurate numerical interpolation is called the false scattering effect in the fvDOM solver. The false scattering effect can lead to large numerical error for the fvDOM model [MOD13] if the computational mesh is coarse. The false scattering effect is originated from the discretization of convection term $\Omega \cdot \nabla I$ in the radiative transfer equation. The step scheme, as the first order scheme, can enhance the false scattering effect in numerical simulations. The nonphysical simulation results can be obtained by using the diamond and exponential schemes [JOS05]. Even though applying linear upwind scheme or higher order scheme, this phenomenon is difficult to eliminate in the fvDOM model. For the upwind scheme, the x-direction term $\partial I(x)/\partial x$ in Eq. 3.53 is approximated by [JAS96]

$$\xi \frac{\partial I(x)}{\partial x} \approx \xi \frac{I(x + \Delta x) - I(x)}{\Delta x} \tag{3.58}$$

According to the Taylor expansion, the $I(x+\Delta x)$ term can be expanded as [HOF00]

$$I(x+\Delta x) = I(x) + \frac{\partial I(x)}{\partial x}\Delta x + \frac{1}{2}\frac{\partial^2 I(x)}{\partial x^2}\Delta x^2 + O(\Delta x^2) \tag{3.59}$$

Therefore, the modified equation for the $\partial I(x)/\partial x$ term is [HOF00]

$$\xi\frac{I(x+\Delta x) - I(x)}{\Delta x} = \xi\frac{\partial I(x)}{\partial x} + \underbrace{\frac{1}{2}\xi\frac{\partial^2 I(x)\Delta x}{\partial x^2} + O(\Delta x^2)}_{\text{truncation error}} \tag{3.60}$$

An additional diffusion term $\frac{1}{2}\xi\frac{\partial^2 I(x)\Delta x}{\partial x^2}$ for the upwind scheme appears in Eq. 3.60. This numerical diffusion, but not physical diffusion, makes the radiation intensity homogeneous in the fvDOM solver. In order to minimize the false scattering effect, it is necessary to increase the number of cells in the computational mesh for the fvDOM solver.

Besides the false scattering effect, the number of solid angles in the fvDOM solver is also important for the numerical accuracy. If the number of solid angles is not large enough, it may have the over-lapping effect [KIM01]. As shown in Fig. 3.23, the representative out-coming radiation intensity I_f does not completely leave the control volume because of the overlapping effect. Although Eq. 3.54 is the conser-

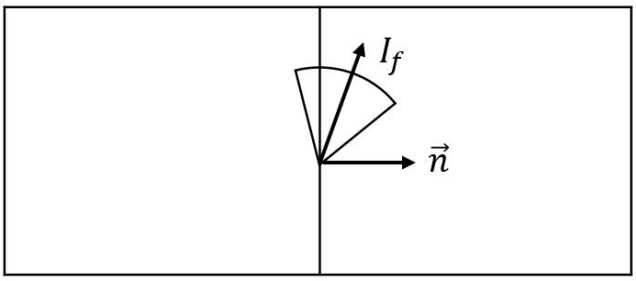

Figure 3.23: Solid angle overlapping effect in the fvDOM model

vation form of radiation intensity in mathematically, it may have some numerical errors due to finite number of rays. It becomes more computationally expensive when considering the non-gray gas model with a large number of solid angles. If the number of spectral bands in the non-gray gas model is N_{band}, there are N_{angle} radiative transfer equations need to be solved for each spectral band. It is necessary to solve $N_{angle} \times N_{band}$ radiative transfer equations in the fvDOM solver. Moreover, the iterative algorithm is used to solve the radiation intensity field owing to the mixed boundary condition. Therefore, this method also requires a lot of computational resource for the non-gray gas consideration.

Finally the fvDOM model also suffers from the ray effect [LAT68, CHA93], if the number of directions is not large enough (see Fig. 3.24). The ray effect may become worse in large 3D geometries with complex components. The illustration of ray effect is shown in Fig. 3.24. This is a 2D box with a hot temperature at the bottom; while other regions are relatively low. According to the black body emission law, the cold region has a negligible contribution on the radiative source term in Fig. 3.24. The radiative heat source is located at the bottom of the box. The left side of Fig. 3.24 is the incident intensity with 8 solid angles, whereas it has 64 solid angles on the right side of Fig. 3.24. As shown in Fig. 3.24, there is a shadowy corner at

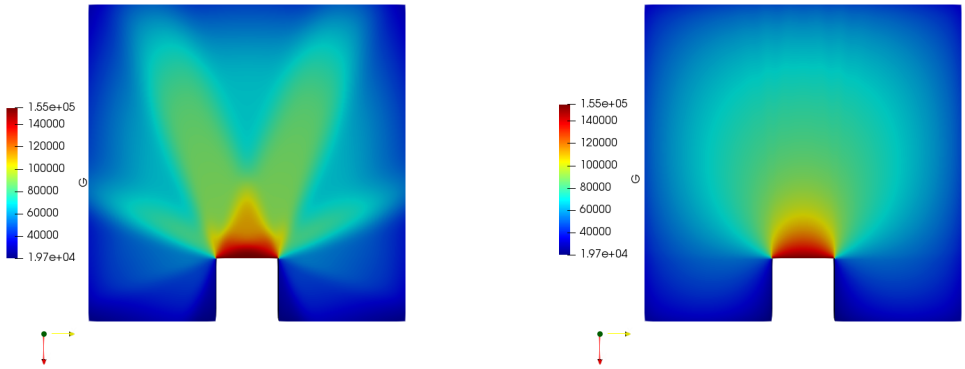

a) Incident intensity G with 8 rays **b)** Incident intensity G with 64 rays

Figure 3.24: Ray effect in the fvDOM solver

the top since the number of rays is not large enough. The ray effect is intensified in the 3D large facilities. The ray effect can be significantly reduced by increasing the number of rays in the fvDOM solver. However, there is a trade-off between the numerical efficiency and accuracy.

3.3.3 Discrete Transfer Method

The discrete transfer method (DTM) solves the charactersitic form of the radiative transfer equation, which was firstly introduced by Lockwood and Shah in 1981 [LOC81]. The DTM method is considered as a straightforward method for complex geometries, which is a method of characteristics [BOY14]. The DTM solver tracks the radiation intensity from the downstream boundary wall to the control volume. As shown in Eq. 3.61, the radiation intensity $I(r, \Omega)$ within the computational domain has two contributions. One is the wall emission with the media

attenuation; the other one is the black body emission from the media.

$$I(r,\Omega) = I(r_{wall},\Omega)\tau(r_{wall}\rightarrow r) + \int_0^s I_b(r')\frac{\partial\tau(r'\rightarrow r)}{\partial s'}ds' \tag{3.61}$$

$$s' = |r' - r| \tag{3.62}$$

where s is the distance from the boundary wall r_{wall} to the the position r; $I_b(r^{'},\Omega)$ is the black body emission in the position $r^{'}$; $\tau(r^{'}\rightarrow r)$ is the media transmissivity from the position $r^{'}$ to the position r.

Similar to most of thermal radiation solvers, the computational domain is divided into a number of boundary surfaces and control volumes in the DTM solver. After determining the temperature T and absorption coefficient κ in each control volume, the radiation intensity $I(r,\Omega)$ is calculated on a set of solid angles. Finally Eq. 3.61 can be rewritten in a discretized form [LIU97, SOU91].

$$I(r,\Omega) = I(r_{wall},\Omega)\tau(r_{wall}\rightarrow r) + \sum_{i=1} I_b(T_i,\Omega)[\tau(r_{i+1}\rightarrow r) - \tau(r_i\rightarrow r)] \tag{3.63}$$

According to Eq. 3.63, the DTM solver is suitable for applications with high boundary emissivities ($\epsilon \sim 1$). If all surface emissivities within the coputational domain are equal to 1.0, the wall surface intensity can be easily determined by the surface temperature T_{wall}. In such cases, the radiation intensity is only calculated once in the DTM solver. Otherwise, numerical iteration is required to evaluate the radiation intensity $I(r_{wall},\Omega)$ on walls. The situation becomes worse when having reflective boundary conditions in the computational domain.

The recommended DTM [CUM95] tracking algorithm is shown in Fig. 3.25. The computational domain is divided into nine control volumes and twelve boundary surfaces. In this example, there are ten solid angles need to be tracked for each control volume in the DTM solver (see Fig. 3.25). Four solid angles are tracked on the boundary wall. Obviously, the numerical accuracy of the DTM solver is also sensitive to the number of tracking rays. Although the false scattering effect can be eliminated in the DTM solver by calculating the radiation intensity from the downstream radiation intensity, it may have the ray effect if the number of tracking rays is not large enough (see Fig. 3.24). In order to calculate the radiation intensity $I(r,\Omega)$ at point O in Fig. 3.25, the downstream starting point P on the boundary surface is determined by the Lagrangian tracking procedure. From boundary radiation intensity $I(r_{wall},\Omega)$ to radiation intensity $I(r,\Omega)$ in Fig. 3.25 there are five step points. Then, following its direction, the radiation intensity $I(r,\Omega)$ is updated based on Eq. 3.63. Different from the DOM model, the radiation intensity is not calculated by the surface interpolation. Hence, the numerical error of DTM model is limited in thermal radiation analyses. According to Fig. 3.25, it is necessary to track a large number of rays for each control volume and surface boundary in

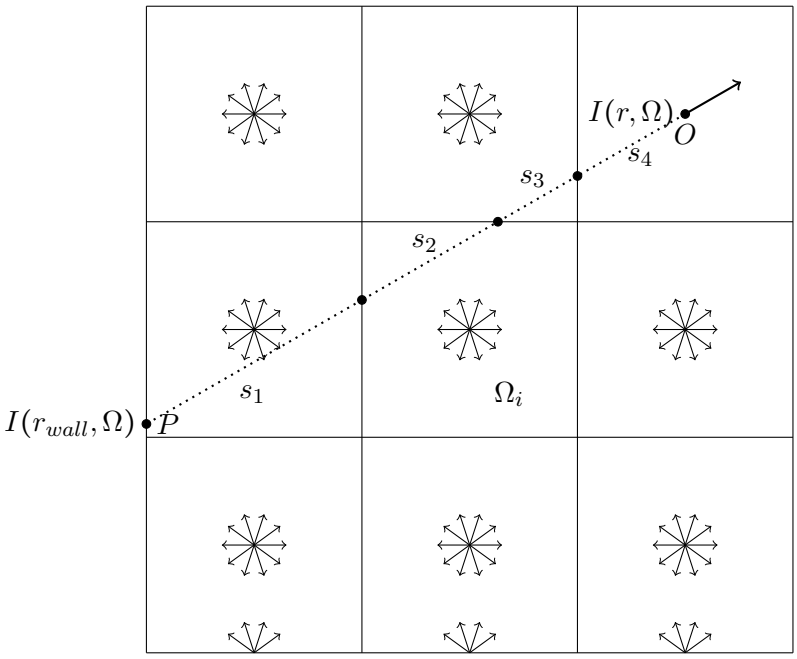

Figure 3.25: Ray tracking procedure in the discrete transfer method

the computational grid. Consequently, the ray tracing method is also computationally expensive. Although the ray tracing calculation can be performed once at the beginning of the thermal radiation simulation, it may require a huge amount of memory space to store the ray tracing information for each control at different solid angles. Therefore, it is computationally infeasible in engineering applications. This method can provide a benchmark reference for the analytical test cases in simple geometries [GOU00]. When considering the spectral gas property, the spectral radiation intensities $I_\eta(r,\Omega)$ are resolved in each band. Therefore, a large amount of computational memory are needed in the DTM solver with non-gray gas models. The Curtis-Godson approximation is applied to calculate the transmissivity for the nonisothermal and nonhomogeneous media [KRA66] in the atmospheric radiation.

The DTM solver is similar with the Monte Carlo method; however, the sampling solid angles are fixed in the DTM. These rays are tracked from the control volume to the boundary surface. The tracking algorithm is similar to the Monte Carlo method. The statistical variation can be calculated in the Monte Carlo method to evaluate numerical uncertainty. The computational error cannot be evaluated in the DTM solver. Therefore, before performing productive simulations by using DTM solvers, the numerical uncertainty is mandatory to quantify to avoid large numerical errors. More investigation about the numerical efficiency of DTM solver is required [CUM95]. For technical scale applications, the implementation of DTM solver must be carefully designed and optimized to save computational resources.

3.3.4 Monte Carlo Method

Monte Carlo method, as the most accurate method, is allowed to consider complex aspects of thermal radiation, e.g., complex 3D geometries, spectral gas properties and soot scattering effect. Although it is considered as a time-consuming and inefficient method, there have been huge developments in parallel computational techniques (MPI, OpenMP and GPU) [BIS04, SIL19] over last decades making Monte Carlo method affordable in engineering applications. The Monte Carlo method is a stochastic algorithm to represent the realistic physics, which can provide the reference solution in many computational fields, e.g., neutron physics [STA18], molecular dynamics [SAT10] and thermal radiation transportation [MOD13]. The first procedure of the Monte Carlo method in thermal radiation analyses is to sample a large amount of energy bundles/photons in the computational domain. After the sampling procedure is finished, those sampling bundles/photons are transported within the participating media by the Lagrangian tracking library in OpenFOAM [HEI20]. During its tracking produce, the energy of emitted bundles is decreased exponentially according to the Lambert-Beer law [HUG63]. Obviously, only a small amount of bundles can be tracked in the Monte Carlo method in order to save computational time. The disadvantage of Monte Carlo method is the statistical error, which is difficult to reduce in containment applications. In this thesis, a number of variation reduction techniques are investigated to reduce the statistical error, which is discussed in Chapter 4. In this section, only the basic principle of the Monte Carlo method is illustrated.

Theoretically, the Monte Carlo method solves the integral form of radiative transfer equation. Consequently, the spectral radiation intensity $I_\eta(r, \Omega)$ is not resolved in the Monte Carlo method. In the derivation of the radiative transfer equation, it is found that the radiative source term $\nabla \cdot q_r$ for a small control volume is related to the energy difference between the emitted energy and the absorbed energy (see Eq. 3.64).

$$\nabla \cdot q_r = \frac{cell\ black\ emission\ energy - cell\ absorption\ energy}{\Delta V} \tag{3.64}$$

According to Eq. 3.64, the radiative source term can be determined, if the emission and absorption energy can be calculated for each control volume and boundary surface in the Monte Carlo method.

In order to couple with the CFD solver, the same mesh is applied in the Monte Carlo radiation solver in *containmentFoam*. The whole computational domain is discretized into a number of isothermal control volumes V_i and boundary surfaces A_j. Before the Monte Carlo simulation starts, the total radiative emission from the control volume i needs to be determined. Under the gray gas approximation, the

total emission from the cell i is defined as Qe_i

$$Qe_i = 4\kappa_i \sigma T_i^4 V_i \tag{3.65}$$

where σ is the Stefan–Boltzmann constant; V_i is the volume of cell i; T_i is the media temperature within cell i; κ_i is the absorption coefficient in cell i. The radiative emission from the boundary surface j is defined as Qe_j.

$$Qe_j = \epsilon \sigma T_j^4 A_j \tag{3.66}$$

where A_j is the surface area; ϵ is the surface emissivity; T_j is the surface temperature. The initial emission points $r(x, y, z)$ are evenly distributed over the control volume and the boundary surface. The emission direction $\Omega(\theta, \phi)$ from the control volume is uniformly distributed over the solid angle, whereas the boundary surface emission radiates uniformly over a hemisphere. The detailed discussion about the photon sampling procedure can be found in section 4.2.1.

The total black body emission from control volume or boundary surface is not difficult to determine according to Eq. 3.65 and Eq. 3.66. After obtaining the total emission energy from control volume or surface, the governing equation for the radiative source term $\nabla \cdot q_r$ [MOD13] is

$$\int_{V_i} \nabla \cdot q_r dV = 4\sigma\kappa_i T_i^4 V_i - \sum_{m=1}^{M} \sigma \epsilon_m T_m^4 A_m \mathcal{F}_{m \to i} - \sum_{k=1}^{K} 4\sigma\kappa_k T_k^4 V_k \mathcal{F}_{k \to i} \tag{3.67}$$

where $\mathcal{F}_{k \to i}$ is the view factor, which describes the proportion of emitted energy from the control volume k projected into the cell i; κ_i is the absorption coefficient in the cell i. Similarly, the governing equation for the wall heat flux q_r [MOD13] on the boundary surface is

$$\int_{A_j} q_r dA = \sum_{m=1}^{M} \sigma \epsilon_m T_m^4 A_m \mathcal{F}_{m \to j} + \sum_{k=1}^{K} 4\sigma\kappa_k T_k^4 V_k \mathcal{F}_{k \to j} - \epsilon_j \sigma T_j^4 A_j \tag{3.68}$$

where $\mathcal{F}_{m \to j}$ is the view factor, which describes the proportion of emitted energy from the surface m projected into surface j; ϵ_j is the surface emissivity of the surface j. According to Eq. 3.68, the radiative wall heat flux is related to the temperature, absorption coefficient and boundary emissivity. Since thermal radiation can transfer energy over a long distance, the solution of radiation heat transfer is a complex task.

The most computationally expensive part of Monte Carlo method is the calculation of view factor matrix $\mathcal{F}$ by the Lagrangian photon tracking algorithm. When updating the thermal radiation, the Monte Carlo solver obtains pressure, temperature and molar fraction from the previous CFD time step. After calculating the spectral gas property, a large number of photons/bundles are sampled according to the

black body emission law. In this thesis, the radiative energy absorption distribution approach is applied to track photons within the computational domain [MOD13]. The advantage of Monte Carlo method is that it can provide a reference solution for other radiation solvers, if the statistical error is small enough. Furthermore, the spectral gas property can be considered in the Monte Carlo method without a significant increase of computational effort. When considering the spectral gas property in the Monte Carlo method, the spectral radiation intensity $I_\eta(r, \Omega)$ is not calculated. Therefore, it is not necessary to solve the spectral radiation intensity $I_\eta(r, \Omega)$ for each spectral band in the Monte Carlo method. The spectral gas property is treated by the sampling wavenumber η in the Monte Carlo method. Since the wavenumber sampling algorithm with the non-gray gas model is complex, the details about the non-gray gas modeling in the Monte Carlo method are given in section 4.2.1.

3.3.5 Assessment of Different Numerical Solution Methods

In this section, the accuracy of different thermal radiation solvers is evaluated in the simplified 2D geometry. Under the gray gas assumption, the numerical error introduced by the spectral gas property can be eliminated to verify different radiation solvers. The results from different radiation solvers are compared to the analytical solution in the 2D geometry (see Fig. 3.26). The verification case is a

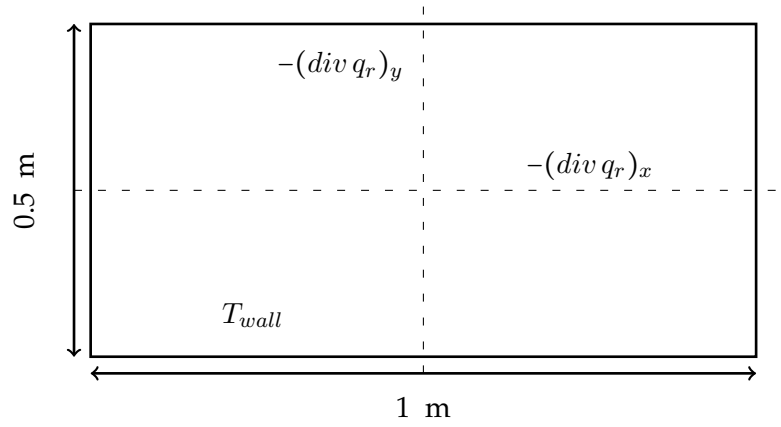

Figure 3.26: 2D rectangular test case [GOU00]

two-dimensional rectangular box (1 m width and 0.5 m height) filled with gray gas media [GOU00]. The walls in the 2D box are assumed pure black and maintain at the absolute zero temperature (0 K). Therefore, the boundary walls have no contribution to the radiative source term in this test case. The medium temperature is homogeneous over the 2D box with 1000 K, and the spectral property of media is

gray gas with 0.5 m^{-1}. The computational mesh is the 201 * 101 orthogonal grid. This computational mesh is fine enough to capture the gradient of radiative source term. This is a steady state test case with a zero velocity. The complex interaction between CFD and thermal radiation is not included in this test case. In order to quantify the accuracy of radiation solvers, the radiation solver is verified against the literature reference [GOU00]. The accuracy of thermal radiation solver is also important in thermal radiation analyses. It is reported that the unsuitable thermal radiation solver can give a misleading quantification of radiative source term resulting in inaccurate temperature predictions in CFD-thermnal radiation coupled simulations [PAL19].

Fig. 3.27 gives the comparison of radiative source terms by using different radiation solvers. The number of rays in the fvDOM solver is 256 to minimize the ray effect, whereas there are 128 solid angles in the DTM solver. The number of sampling bundles per cell in the Monte Carlo method is 400, and the total sampling bundles is 8120400. Therefore, this is the most time-consuming method. First of

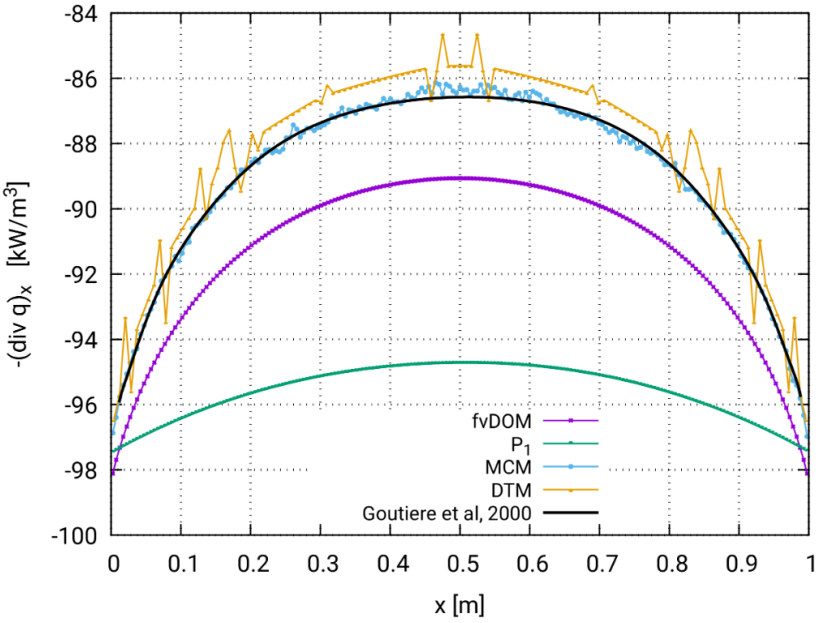

Figure 3.27: Radiative source term $-\nabla \cdot q_r$ at the $x-th$ central line

all, the radiative source term of P_1 method is smoother than that of other solvers. This can be explained by the diffusion approximation in the P_1 method. Therefore, the P_1 method is not suitable to solve the radiative heat transfer in optically thin applications. The numerical error is larger than other thermal radiation solvers. After calculating a large number solid angles in the fvDOM solver, there is no ray effect on the radiative source term. However, there is a small difference between

the fvDOM and the literature reference owing to the false scattering effect. The simulation result obtained from the DTM solver is characterized by the jagged line (see Fig. 3.27). The DTM is in consistent with the reference solution. It is necessary to increase the number of tracked rays in the DTM to reduce the numerical fluctuation. The MCM is in good agreement with the literature reference. Although the total number of sampling bundles is about 8 million, it still has a numerical fluctuation in the Monte Carlo simulation. It is found that both MCM and DTM solvers are superior to the fvDOM solver. This is because both MCM and DTM solvers apply the Lagrangian tracking procedure to calculate the radiative source term. There is no numerical diffusion in the MCM and DTM solvers.

Fig. 3.28 illustrates the comparison of radiative wall heat fluxes on the bottom wall by using different thermal radiation solvers. The P_1 diffusion approximation

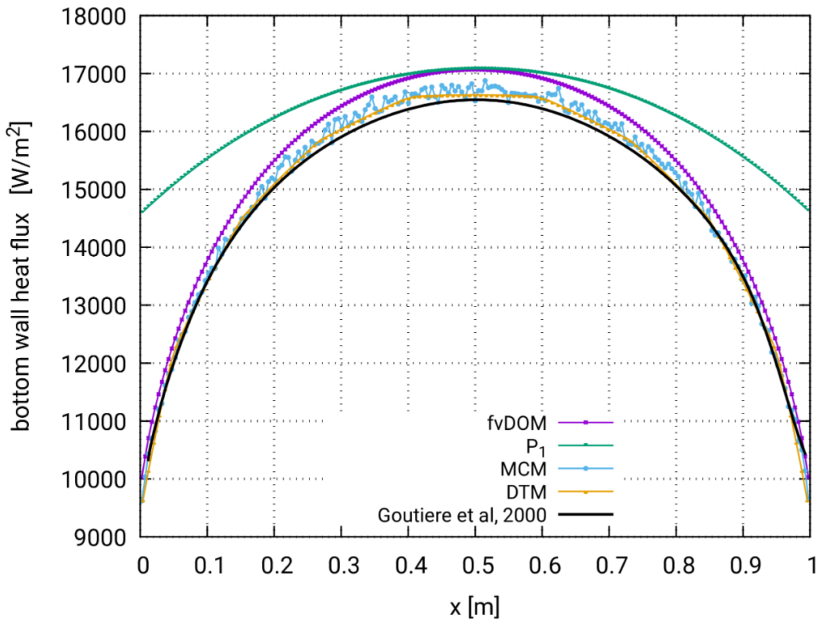

Figure 3.28: Radiative wall heat flux q_r at the bottom wall

leads to a strong heat transfer between gas media and structures in P_1 method. The radiation intensity near the boundary wall is not isotropic. Therefore, it has a strong deviation for radiative wall heat flux on the boundary wall. This is also related to the optical thickness and the scale of facility. More investigation is needed to quantify this effect. The other thermal radiation solvers give a similar evaluation on the wall heat flux. The wall heat flux for the fvDOM method is larger than the literature reference owing to the false scattering effect. The MCM and DTM solvers can give accurate predictions on the radiative wall heat flux.

In order to compare the numerical efficiency and accuracy, the computational time and relative error for this test case are shown in Table 3.7. The average relative error of the radiative source term is about 8% for the P_1 method. Although P_1

Table 3.7: Summary of numerical errors and computational time for the Goutiere's 2D case

Model	CPU (s)	Relative error estimation			
		Radiative source term		Wall heat flux	
		Max	Mean	Max	Mean
P_1	0.39	9.72%	7.76%	35.44%	7.48%
fvDOM	13.27	3.45%	2.89%	4.27%	1.87%
DTM	240.86	2.21%	0.68%	2.56%	0.55%
MCM	1819.59	1.26%	0.27%	2.58%	0.59%

method is not an accurate method, it is the most efficient method among those thermal radiation solvers. Different from other radiation solvers, only one diffusion equation is solved in the P_1 method. The average relative error for the fvDOM method is about 3% due to the false scattering effect. It is found that both DTM and Monte Carlo solvers are much slower than other radiation solvers, but both of them can provide accurate predictions for the radiative source term. The Monte Carlo method is the most time-consuming method, and it takes about 1800 s to finish the Lagrangian tracking procedure. The numerical difference between MCM and literature reference is negligible in this 2D test case. It is concluded that the numerical implementation of Monte Carlo solver with gray gas model in *containmentFoam* is correct. However, it is necessary to optimize the MCM and DTM solvers in *containmentFoam*.

3.4 Summary of Thermal Radiation Modeling in Containment Flows

This chapter has presented the thermal radiation modeling including non-gray gas models in containment flows. The thermal radiation heat transfer is one mode of heat transfer mechanism, which is an important energy source term in the CFD energy equation. The fundamental theory of thermal radiation, the deduction of the radiative transfer equation, spectral gas properties and the implementation of different radiation solvers are provided as distinctly and precisely as possible. The spectral gas property is the most difficult part in the thermal radiation analysis. Generally, spectral gas properties are given in terms of transmissivity in SNB and EWBM models. However, the absorption coefficient is required in most of thermal radiation solvers. A free path length is defined by users to obtain the absorption

coefficient. This may introduce some numerical errors in thermal radiation simulations. The most widely applied non-gray gas model is the WSGG model. Unfortunately, the WSGG simulation results are far from satisfactory in the comparison with the LBL reference. In containment flows, the radiative source term must be predicted in a high accuracy for the coupled simulation of thermal radiation and CFD. Therefore, the narrow band model is recommended for engineering applications. It is necessary to develop the LBL model to provide the reference solution. If the spectral gas property is considered in the thermal radiation solver, the numerical implementation becomes complex in order to resolve the spectral radiative intensity I_η. There are few investigations on the narrow band models in engineering applications owing to the computational effort. According to the one-dimensional test cases, the correlated-k model provides a good compromise between efficiency and accuracy. However, it is necessary to develop a tailored non-gray gas model in containment flows for the severe accident assessment.

Even though applying the gray gas model for the spectral gas property, the numerical solution for the radiative transfer equation is still a difficult task. It has been found that different radiation solvers have their own drawbacks, which hinders the coupling of thermal radiation solver into CFD solver. The P_1 method is an efficient solution for the radiative heat transfer; however, it is necessary to increase the numerical accuracy. It is difficult for the fvDOM solver to consider the spectral gas property. The spectral radiation intensity is calculated for each spectral band in the fvDOM solver when considering the spectral gas property. It may take a lot computational time in the fvDOM solver to resolve the spectral radiation intensity. The DTM and Monte Carlo solvers are better than the fvDOM solver, because there is no numerical interpolation in the DTM and Monte Carlo methods. The main drawback of DTM and Monte Carlo methods are numerical efficiency for the Lagrangian particle tracking procedure. It is necessary to increase the computational efficiency for the Lagrangian particle tracking algorithm.

Chapter 4

Modeling Gas Radiation Transport for Application to Containment Flows

This chapter focuses on the development of an advanced thermal radiation modeling approach for containment flows and is separated into two parts, namely the development of a model of the spectral properties of the gas mixture and an efficient Monte Carlo approach to represent the thermal radiation transport. Most non-gray gas models are formulated for combustion applications, i.e., conditions in terms of gas temperature, pressure and mixture composition, which are considerably different from those in containment flows. Two dedicated spectral gas models (SNBCK and LBL) are derived for the specific temperature range ($< 1000\,K$), pressure ($< 10\,atm$) and high humidity in the containment flows in sections 4.1.1 and 4.1.2. The SNBCK model is a reliable non-gray gas model and represents a good compromise between efficiency and accuracy. It enables to consider more spectral bands for the H_2O absorption coefficient in low wavenumber regions, which is needed to account for the strong variations of the amounts of steam in containment flows. In order to provide a reference solution for model verification, a LBL model is also derived and implemented for the specific conditions.

Based on the converged fluid parameters from CFD, i.e., p, T, and Y_i, both spectral models can provide the spectral absorption coefficient $\kappa_\eta(p, T, Y_i)$ for the thermal radiation transport solver. Its formulation is also important for the accuracy and efficiency of the coupled thermal radiation and CFD simulation since it affects the gas temperature via the radiative source term in the energy equation as well as the overall calculation time. In order to reduce the numerical error associated with

solving the radiative transfer equation along with spectral properties in complex 3D geometries, a Monte Carlo approach is developed (see section 4.2). To improve its computational efficiency, a number of advanced variation reduction algorithms are implemented in section 4.3, such as the shifted and emission reciprocity Monte Carlo methods [TES02, SOU13, PAL19]. Applying those advanced Monte Carlo algorithms, it is found that the statistical error is significantly reduced. This enables the tracking of a lower photon count at an acceptable statistical error level and thus makes the coupled application to technical scales feasible. The coupling algorithm between CFD algorithm and the Monte Carlo solver is discussed in section 4.4. In particular, it is shown that updating the radiative source term with a lower frequency than the fluid flow is sufficient and can further reduce the computational cost significantly.

4.1 Development of Tailored Non-gray Gas Model for Containment Flows

The participating non-gray gases in the containment atmosphere are H_2O, CO_2 and CO. In particular the spectral gas properties of H_2O vary strongly across the infrared radiation spectrum [MOD13]. Since the absorption coefficient has a strong impact on the radiative source term in the energy equation, it is the starting point for thermal radiation modeling. The most accurate model for spectral gas properties is the LBL model, which is based on the quantum mechanics [ROT09]. The LBL model can provide a reference solution for code-to-code verification. However, the LBL model is prohibitively demanding for engineering applications due to large number of transition lines [PAL19]. The non-gray gas model implemented in *containmentFoam* for productive applications is the SNBCK model. It can provide reliable spectral gas properties for a non-gray gas medium without significant increase of computational effort [GOO89, SOU97].

4.1.1 Line-by-Line Model

A LBL model based on the HITRAN database is implemented in *containmentFoam* to provide the reference solution in thermal radiation analyses. Since all non-gray gas models are based on the LBL model, it is mandatory to implement it in *containmentFoam*. Before performing a LBL calculation, an existing LBL database has to be selected, suitable for the intended application conditions. It has been found that different LBL databases have a strong impact on the absorption coefficient [CHU12]. There are many LBL databases published in recent decades with

the help of the Fourier transform infrared technology [GOL64] and the advanced quantum mechanical algorithms [GAM83]. The HITRAN database was released by the Air Force Geophysics Laboratory in the late 1960s for low temperature applications [ROT87]. The HITRAN database is updated every four years according to the latest experimental data and advanced theoretical calculations [ROT09]. The HITRAN database has been validated by many experiments [MEL21, OLS19] for a temperature range from 296 to 1000 K. Since the HITRAN database is dedicated to atmosphere remote sensing, the high temperature transition lines (> 1000 K) are not included. In order to provide the LBL data for combustion applications, an analogous database, HITEMP [ROT10], is released to consider transition lines under high temperatures. Therefore, the HITEMP database is much larger than the HITRAN database which only considers the fundamental transition lines. Another high temperature database is the Carbon Dioxide Spectroscopic Databank (CDSD) developed by the V.E. Zuev Institute of Atmospheric Optics [TAS11], which provides carbon dioxide transition lines at high temperatures ($2500 - 5000\ K$). Furthermore, the GEISA database [JAC15] has been published by the Laboratoire de Météorologie Dynamique in France since 1974.

In this thesis, the updated HITRAN2016 database [ROT09] is employed. There are about 50 types of molecules considered in the HITRAN database, e.g., H_2O, CO_2 or NO_2, which contains thousands of transition lines in the wavenumber range of 10-8000 cm^{-1} for low temperature applications. The LBL absorption coefficient κ_η is related to the media temperature T, total pressure p, partial pressure $p_{species}$, wavenumber η, number of molecules N and associated transition lines S_i. The absorption coefficient κ_η considering all associated transition lines ($i = 1, ..., N$) can be calculated using Eq. 4.1

$$\kappa_{\eta,species} = N(p_{species}, T) \sum_{i=1}^{N} S_i(T) f(x, p, T, \eta - \eta_i) \tag{4.1}$$

where $N(p_{species}, T)$ is the number of absorption gas molecules in media; x is the species molar fraction; $S_i(T)$ is the i-th line intensity; η_i is the i-th line location; $f(x, p, T, \eta - \eta_i)$ is the line shape function. The detailed discussion of those parameters can be found in section 3.2.1.

The line shape function is important to determine the H_2O absorption coefficients in containment flows under high humidity conditions. The molecular collision can cause a perturbation of energy states for the gas molecule. A small perturbation of energy state leads to the line broadening effect, changing LBL absorption coefficients. In this thesis, the Lorentz profile [SPA97] is chosen to obtain the spectral absorption coefficient

$$f(\eta) = \frac{\gamma_i}{\gamma_i^2 + (\eta - \eta_i)^2} \tag{4.2}$$

where γ_i is the i-th line half-width; η_i is the center of the line. The half-width γ_i can

be computed from HITRAN2016 database [ROT09]

$$\gamma_i = \left(\frac{T_{ref}}{T}\right)^{n_{air}} [p_{species}\gamma_{species,i} + (p - p_{species})\gamma_{air,i}] \tag{4.3}$$

where n_{air} is the temperature fitting coefficient for the broadening half-width; $\gamma_{species}$ is the line half-width for the non-gray gas species; $p_{species}$ is the species partial pressure; and γ_{air} is the air broadening half-width. These parameters are provided in the HITRAN database (see Table 4.1).

Normally, the line intensity in the HITRAN database is given at the reference temperature 296 K, mainly considering the energy transition between the ground state and the first excited state. As shown in Table 4.1, the HITRAN database provides the total line intensity S_i, center of the spectral line η_i, and half-width γ for each transition line. Before performing the LBL calculation, these parameters must be read in with the specified accuracy from the HITRAN database to avoid numerical errors.

Table 4.1: HITRAN LBL database parameters [ROT09, ROT05]

Column	Fortran format	Description
Mol	I2	Molecule number
Iso	I1	Isotopologue number
η_i	F12.6	Wavenumber (center of the spectral line)
S_i	E10.3	Line intensity
A_i	E10.3	Einstein-A coefficient of a line transition
γ_{air}	F5.4	Air-broadened half-width
γ_{self}	F5.4	Self-broadened half-width
E''	F10.4	Lower state energy
n_{air}	F4.2	Coefficient of temperature dependence air-broadened half-width
δ_{air}	F8.6	Air-broadened pressure shift of line transition

After the line profile function f is defined, the absorption coefficient for each species can be determined from Eq. 4.1-4.2. The containment atmosphere consists of different participating and transparent gas species, e.g., H_2O, N_2 and CO_2. In order to obtain the total absorption coefficient of media, all infrared active species must be considered in the thermal radiation analysis. Therefore, the total spectral absorption coefficient κ_η for multi-species mixtures is the sum of the species absorption coefficients (see Eq. 4.4).

$$\kappa_\eta = \sum_{species} \kappa_{\eta,species} \tag{4.4}$$

where $\kappa_{\eta,species}$ is the species absorption coefficient. There are only some overlapping bands for H_2O-CO_2-CO mixtures. The same fine bands need to be considered for all species to employ in Eq. 4.4 even if there is no significant line

in this band. This is another reason why the LBL model is time-consuming and memory-intensive in technical applications. A tailored LBL spectral model is implemented in *containmentFoam* using the HAPI program to derive the library coefficients [KOC16]. The calculation procedure consists of three steps.

- **Initialization of the HITRAN database** The first is the definition of line center positions, line intensities, line widths and temperature coefficients. The HITRAN database contains thousands of transition lines. In order to reduce computational effort, the line intensity below $3 \cdot 10^{-27} mol^{-1} cm^{-1} cm^2$ is neglected in the LBL model [HAR84]. The total partition function $Q(T)$ for H_2O and CO_2 is used according to the literature [GAM21]. After obtaining the line parameters, the line intensity $S(T)$ at the media temperature T can be determined by using Eq. 3.20.
- **Calculation of the absorption coefficient** Next, the absorption coefficients based on the fluid parameters temperature, molar fractions, and total pressure are determined. The program calculates the spectral absorption coefficient in a fine wavenumber grid ($\Delta\eta$ = 0.01 cm^{-1}) for the absorbing species, e.g., H_2O and CO_2. It is found that the CO_2 absorption coefficient is sensitive to the wavenumber interval, since it has a strong absorption band around $\eta \sim 2200\, cm^{-1}$. If the spectral interval is not fine enough, it may broaden the absorption coefficient leading to numerical errors in thermal radiation calculations. The molar fraction has a strong impact on the effective half-width γ for the H_2O absorption coefficient. After the line parameters and line half-width are calculated, the species absorption coefficient can be determined according to Eq. 4.1.
- **Determination of the total absorption coefficient** After calculating the LBL absorption coefficient for each absorbing species, the total absorption coefficient of the gas mixture is evaluated according to Eq. 4.4. Here, for a multi-components mixture, the spectral grid must be the identical for all species. The final step is to write the total absorption coefficients into output files. Since the total absorption coefficient is given in a fine wavenumber interval, the memory size of each output file is about 30 MB. Therefore, increasing the number of LBL files (species) can pose a burden to the system memory.

The illustration of species absorption coefficient calculation is shown in Fig. 4.1 to ease the understanding of the numerical implementation. There are four transition lines which line parameters are calculated according to the aforementioned equations. Afterwards, the line parameters and half-widths are fixed, a uniform interval grid is set up to store the species absorption coefficient $\kappa_{species}$. The wavenumber grid must be fine enough to resolve the strong variation of absorption coefficients. The absorption coefficient is evaluated at each point on the wavenumber grid. As

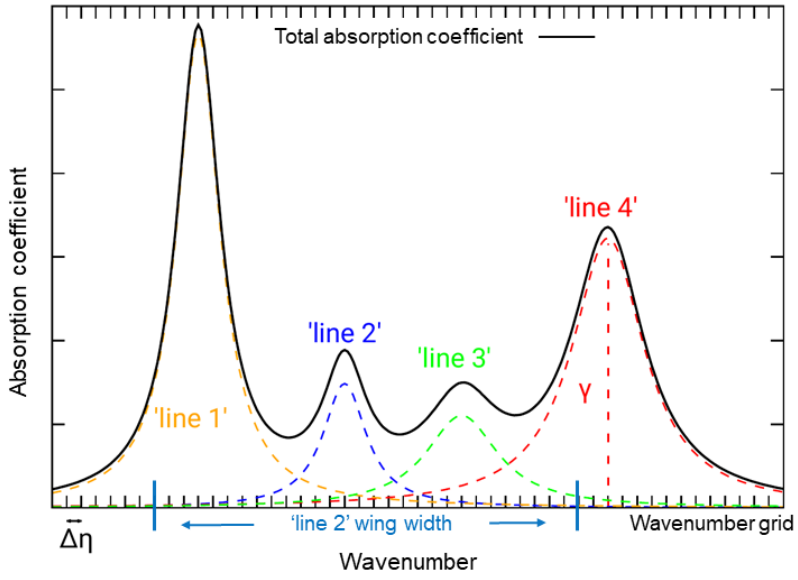

Figure 4.1: LBL absorption coefficient illustration

shown in Fig. 4.1, different transition lines may have different effective half-widths. In this thesis, the spectral discretization is set as 0.01 cm^{-1} to calculate the spectral absorption coefficient. For each grid point, it is necessary to calculate the contribution from all transition lines (see Fig. 4.1). In this case only four transition lines are considered, and it is possible to calculate the contribution from all transition lines. If there are thousands of transition lines over the whole spectrum, a wing width ($\sim 10\ cm^{-1}$) is defined in order to save the computational power. The wing width is the wavenumber distance from the center of line to the point where the absorption coefficient is practically zero (see Fig. 4.1).

The computational procedure for the LBL absorption coefficient given above is computed for each cell conditions; however, the fluid temperature in containment flows may vary from 300 to 1000 K with different steam molar fractions. As a result, it is prohibitively demanding to perform an on-the-fly LBL calculation within the thermal radiation solver. In order to reduce the computational effort, a LBL data library is generated at specific temperatures and molar fractions. While performing the radiation calculation the local absorption coefficient is determined by the bilinear interpolation. In this thesis, the temperature interval is defined at 50 K to avoid large deviations, while the molar fraction points for the steam absorption coefficient are 0.01, 0.1, 0.2, 0.4, 0.6, 0.8 and 1.0. For other species the effect of molar fraction on the absorption coefficient is not important. In this way, the LBL model can be applied to practical applications.

4.1.2 Statistical Narrow Band Correlated-k Model

In the literature, the narrow band model is often considered as the reference model, if a LBL calculation is not available. As stated before, different non-gray gas models have different implementation strategies in the radiation solver. The SNBCK model represents the spectral gas properties by a set of absorption coefficients κ_i and correlated quadrature weights ω_i, which can be coupled with fvDOM and Monte Carlo solvers without numerical approximation. However, there is no specific SNBCK model for relatively low temperatures ranging from 300 to 1000 K, suitable for the thermal radiation analysis in containment flows. In order to solve the gas radiation heat transfer accurately, a tailored and efficient narrow band model is developed for containment flows.

The strategy of the narrow band model is to divide the whole infrared radiation spectrum into a number of small bands, which are still large enough to contain relevant transition lines ($\Delta\eta \sim 50\,cm^{-1}$). It is assumed that in such a narrow band the blackbody intensity $I_{b,\Delta\eta}$ remains constant [LIU00]. The comparison of absorption coefficients calculated by the SNBCK and LBL models is illustrated in Fig. 4.2. There is no strong fluctuation on the band average absorption coefficient in the SNBCK model. Even though it contains a number of transition lines within the narrow bands, the SNBCK model can represent the spectral gas property without large errors. The LBL absorption coefficient reveals strong variations within small wavenumber ranges, which may have several orders of magnitude difference. The absorption coefficient can change from 0 $m^{-1}bar^{-1}$ to 25000 $m^{-1}bar^{-1}$ in the LBL model.

In the Fig. 4.2 there is only one absorption coefficient in the SNBCK model to represent the spectral gas property. However, it is not sufficient to represent a number of transition lines within the narrow band. Actually this approximation may lead to large errors in thermal radiation analyses. In order to increase the accuracy, there are a set of absorption coefficients κ_i and associated weights w_i ($i = 1, 2, ..., N$) to statistically represent the narrow band transmissivity. Generally the 7 points Gauss integration scheme is sufficient to approximate the spectral gas property in the narrow band. For a homogeneous media with constant pressure and temperature, the averaged transmissivity along the path length L is given in Eq. 4.5.

$$\tau_{\Delta\eta} = \frac{1}{\Delta\eta}\int_{\Delta\eta}\exp(-\kappa_\eta L)d\eta \tag{4.5}$$

The basic idea of correlated-k method is that the average band transmissivity is only related to the absorption coefficient κ_η, not the wavenumber η. The average band transmissivity can then be expressed as

$$\tau_{\Delta\eta} = \frac{1}{\Delta\eta}\int_{\Delta\eta}\exp(-\kappa_\eta L)d\eta = \int\exp(-\kappa L)f(\kappa)d\kappa \tag{4.6}$$

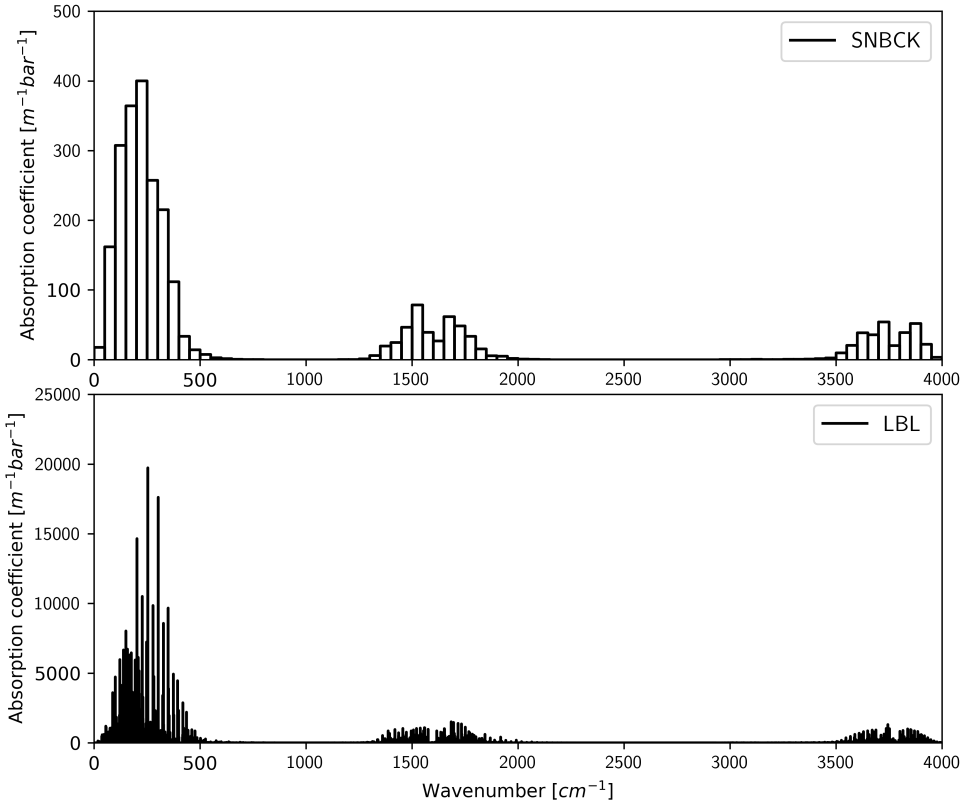

Figure 4.2: Comparison of absorption coefficients calculated by the SNBCK and LBL models for H_2O

$$f(\kappa) = \frac{1}{\Delta\eta}\frac{d\eta}{d\kappa} \tag{4.7}$$

As shown in Eq. 4.6 and Eq. 4.7 the narrow band k-distribution is an integral transformation technique. The k-distribution function $f(\kappa)$ can be calculated in two ways. The first one is the Laplace transformation of the gas transmissivity [LIU00, MOD13]. The second one is to calculate the k-distribution function from the LBL absorption coefficient [MOD13, PAL19]. In this thesis, the k-distribution function is calculated from the LBL absorption coefficient with a high accuracy. The meaning of k-distribution function is the fraction of wavenumber $\delta\eta$ for which the absorption coefficient varies from κ to $\kappa+\delta\kappa$ [LIU00, PAL19]. This is the integration over the entire range $\Delta\eta$ where the absorption coefficient is within the range from κ to $\kappa + \delta\kappa$ [MOD13].

$$f(\kappa) = \frac{1}{\Delta\eta}\sum_i \frac{\delta\eta}{\delta\kappa} \tag{4.8}$$

The computational procedure of k-distribution function is illustrated in Fig. 4.3. The LBL absorption coefficient may have a strong variation in small wavenumber

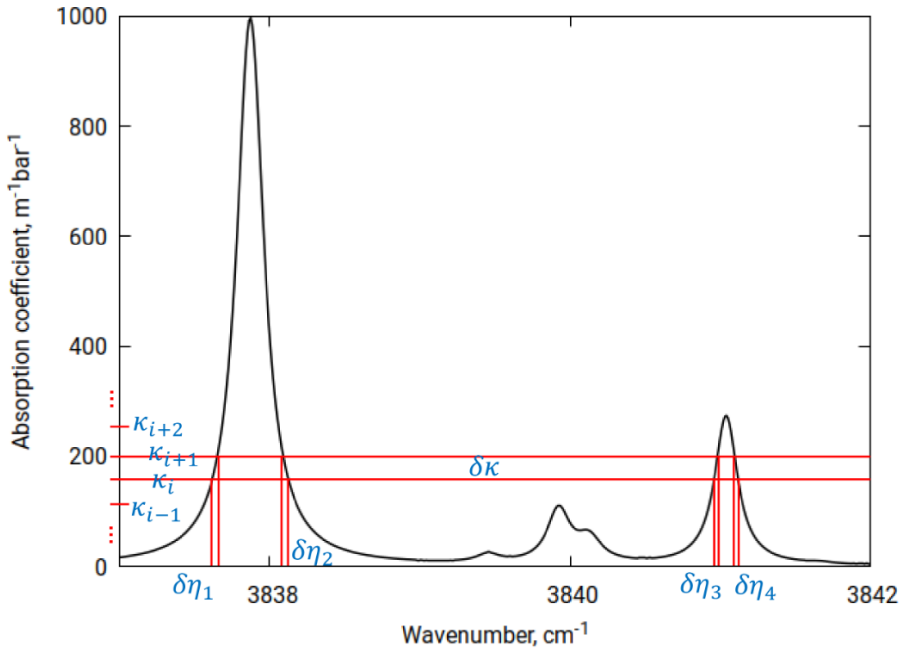

Figure 4.3: Evaluation of k-distribution function from the LBL absorption coefficient for H_2O ($p = 1.0\,atm$, $x_{H_2O} = 0.1$ and $T = 400\,K$), modified from [MOD13]

regions. As depicted, the absorption coefficient κ is divided into small ranges $\kappa_i, i = 1, ..., N$. The minimum absorption coefficient is κ_1 and the maximum absorption coefficient is κ_N over the narrow band. The k-distribution function is evaluated at each absorption coefficient point κ_i. For example, the k-distribution $f(\kappa_i)$ in the range from κ_i to κ_{i+1} is related to all small wavenumber regions $\delta\eta$ in Fig. 4.3. According to the absorption coefficient variation $\delta\kappa$ ($\delta\kappa = \kappa_{i+1} - \kappa_i$), there are four inverse wavenumber regions: $\delta\eta_1$, $\delta\eta_2$, $\delta\eta_3$ and $\delta\eta_4$ (see Fig. 4.3). Therefore, the k-distribution function $f(\kappa_i)$ in Fig. 4.3 is

$$f(\kappa_i) = \frac{1}{\Delta\eta}\frac{\delta\eta_1 + \delta\eta_2 + \delta\eta_3 + \delta\eta_4}{\delta\kappa} \tag{4.9}$$

The k-distribution function can be evaluated using this way, and the more detailed discussion about the numerical calculation can be found in the textbook [MOD13].

It is not necessary to evaluate the k-distribution function during the run-time. In order to simplify the procedure, the cumulative distribution function $g(\kappa)$ is introduced (see Eq. 4.10) [MOD13].

$$g(\kappa) = \int f(\kappa)d\kappa \tag{4.10}$$

Since the absorption coefficient may repeat many times in the narrow band, it is advantageous to reorder the absorption coefficient into a smooth and monotonically increasing function $g(\kappa)$ [MOD13]. The cumulative distribution function $g(\kappa)$ represents the probability that the absorption coefficient is less than κ in this narrow band. Actually the cumulative distribution function $g(\kappa)$ can be evaluated from the k-distribution function.

$$dg(\kappa) = f(\kappa)\delta\kappa \simeq \frac{1}{\Delta\eta}\sum_i \frac{\delta\eta}{\delta\kappa}\delta\kappa = \frac{1}{\Delta\eta}\sum_i \delta\eta_i \tag{4.11}$$

The cumulative distribution function is evaluated in this way at different small ranges κ_i (see Fig. 4.3) by counting the inverse wavenumber regions. After calculating the cumulative distribution function $g(\kappa)$, the average transmissivity $\tau_{\Delta\eta}$ can be written as a function of $g(\kappa)$. The average band transmissivity can be approximated by the Gaussian quadrature method to reduce the computational effort (see Eq. 4.12).

$$\tau_{\Delta\eta} = \int \exp(-\kappa L) f(\kappa) d\kappa = \int_0^1 \exp[-\kappa(g)L] dg \simeq \sum_{i=1}^{N} \omega_i \exp(-\kappa_i L) \tag{4.12}$$

where N is the number of quadrature points; ω_i is the $i-$th quadrature weight; κ_i is the $i-$th absorption coefficient in the narrow band. As shown in Eq. 4.12, the averaged transmissivity over the narrow band is converted to a standard mathematical task. Gauss quadrature is an efficient method to approximate the functional integration (see Eq. 4.12). It is noted that the spectral variation of the absorption coefficient within the narrow band is not considered in the SNBCK model. In this way, the spectral gas property within the narrow band is provided with N absorption coefficients κ_i and associated weights w_i. Generally 7-points Gauss quadrature integration for the SNBCK model is sufficient, and it can significantly improve the computational accuracy and efficiency in comparison with the LBL model.

Obviously, this correlated-k method is not only limited to the band transmissivity $\tau_{\Delta\eta}$. Any radiative quantity $\phi_{\Delta\eta}(\kappa)$, which is related to the fluctuation of absorption coefficients, can be approximated in this way

$$\phi_{\Delta\eta}(\kappa) = \frac{1}{\Delta\eta}\int_{\Delta\eta} \phi_\eta(\kappa_\eta) d\eta \simeq \sum_{i=1}^{N} w_i \phi_i(\kappa_i) \tag{4.13}$$

For example, the averaged band radiative intensity $I_{\Delta\eta}$ is approximated by Eq. 4.14.

$$I_{\Delta\eta} = \frac{1}{\Delta\eta}\int_{\Delta\eta} I_\eta(\kappa_\eta) d\eta \sim \sum_{i=1}^{N} w_i I(\kappa_i) \tag{4.14}$$

where $I(\kappa_i)$ is the radiative intensity calculated by the absorption coefficient κ_i in the radiative transfer equation. According to Eq. 4.14, only N number of thermal

radiation equations are solved in the SNBCK model for each narrow band. After all radiative intensity $I(\kappa_i)$ is obtained by the fvDOM solver, the average radiative intensity within this narrow band is approximated by $\sum_{i=1}^{N} w_i I(\kappa_i)$. Therefore, the SNBCK model is more efficient than the LBL model.

The Gauss quadrature scheme published by Rivière and Soufiani [RIV92] is a reliable quadrature scheme for the SNBCK model. The 7-points Gauss quadrature scheme yields accurate simulation results in the comparison with the SNB model, and the Gauss-Labatto 7-points cumulative values g_i and weights ω_i are summarized in Table 4.2. According to Table 4.2, the quadrature weights are mainly located at $g < 0.8$ regions. The most successful SNBCK model was published by

Table 4.2: Gauss quadrature points and weights for the SNBCK model [RIV92]

i	g_i	w_i
1	0.00000005	0.04500000
2	0.15540584	0.24500000
3	0.45000000	0.32000000
4	0.74459415	0.24500000
5	0.90000000	0.05611111
6	0.93559510	0.05124858
7	0.98449489	0.03764030

Soufiani and Taine [SOU97] at EM2C laboratory, which has 7 Gauss quadrature points for each narrow band (see Table 4.2). However, the EM2C/SNBCK database is dedicated to combustion applications in which the temperature field varies from 300 to 3000 K. The number of narrow bands for H_2O is 44 in the EM2C/SNBCK model, whereas there are 17 narrow bands for CO_2. The number of EM2C/SNBCK bands is relatively small to save computational time for engineering applications. Furthermore, the EM2C/SNBCK non-gray gas model mainly focuses on the near-infrared range (from 3300 to 13000 cm^{-1}) for fire applications.

Since the spectral gas properties play an important role in thermal radiation analyses, it is necessary to develop a tailored SNBCK model from 300 to 1000 K for the hydrogen mixing analysis in containment flows [SEH11]. According to the black body emission law, the mid-infrared (from 200 to 3300 cm^{-1}) thermal radiation becomes important in containment flows. In this thesis, the number of spectral bands is 159 for H_2O from 50 cm^{-1} to 8000 cm^{-1} with a uniform spectral interval ($\Delta\eta$ = 50 cm^{-1}). There are two main considerations for this spectral discretization. Within such small bands the spectral blackbody intensity can be constant, but it is still wide enough to contain a number of transition lines. The fine spectral interval is required for the steam absorption coefficient, since steam has a strong pure-rotational band in low wavenumber regions (< 1000 cm^{-1}). The CO_2 molecule has fewer absorption bands (667 and 2410 cm^{-1}) than the H_2O molecule.

After determining the number of quadrature points and the narrow band structure, a new tailored SNBCK database for steam and CO_2 can be generated by calculating the cumulative distribution function $\kappa(g)$ (see Fig. 4.4). The first procedure of

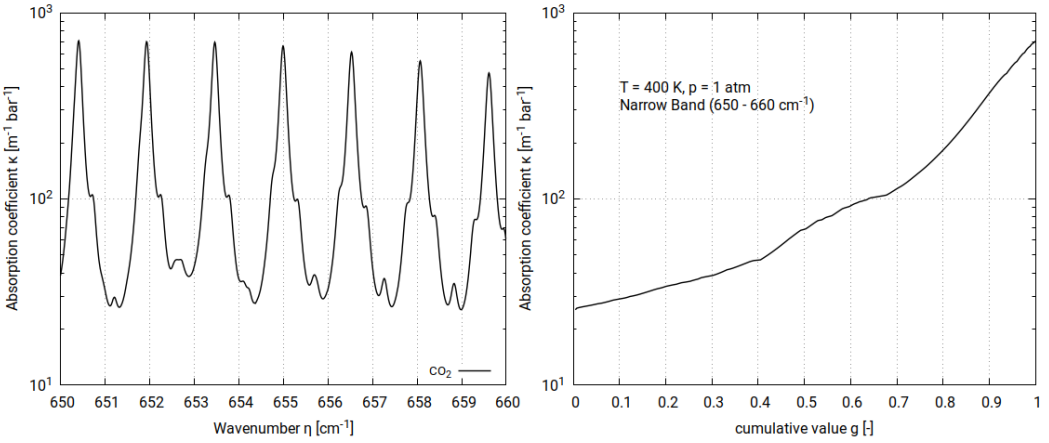

Figure 4.4: Evaluation of cumulative function from the LBL absorption coefficient for the SNBCK model [MOD13]

generating the SNBCK database is to calculate LBL absorption coefficients at different temperatures and molar fractions using the HITRAN database. The cumulative k-distribution function $g(\kappa)$ is calculated at different bands with the specific temperature and molar fraction. As shown in Fig. 4.4 the minimum and maximum absorption coefficients (κ_{min} and κ_{max}) can be determined by the searching algorithm. After determining the minimum and maximum absorption coefficients, the absorption coefficient range $(\kappa_{min}, \kappa_{max})$ is divided into a number of small intervals $\kappa_i < \kappa < \kappa_i + \delta\kappa$, $i = 1, ..., N$. In the small interval $\kappa_i < \kappa < \kappa_i + \delta\kappa$ the cumulative increment $dg(\kappa)$ is evaluated by the sum of inverse wavenumber regions $\sum_j \delta\eta_j$ (see Eq. 4.11 and Fig. 4.3). The cumulative distribution function $g(\kappa)$ must be exactly evaluated in order to avoid numerical errors in thermal radiation calculations. Fig. 4.4 right is the inverse cumulative function $\kappa(g)$ for the CO_2 species in the narrow band region from 650 to 660 cm^{-1}. After the inverse cumulative distribution function $\kappa(g)$ is fixed, the Gauss quadrature absorption coefficients $\kappa(g_i)$ and associated weights ω_i listed in Table 4.2 can be determined. The detailed description of the numerical algorithm is given in the literature [MOD13].

As stated before, the H_2O collisional line half-width also depends on its molar fraction. The inverse cumulative distribution function $\kappa(g)$ for H_2O at 400 K and 1 atm in the wavenumber range from 400 cm^{-1} to 450 cm^{-1} with different steam molar fractions is shown in Fig. 4.5. For relatively low steam molar fractions, the inverse cumulative distribution function $\kappa(g)$ is steeper than that for high steam molar fractions due to a smaller collision broadening effect. The gradient of the in-

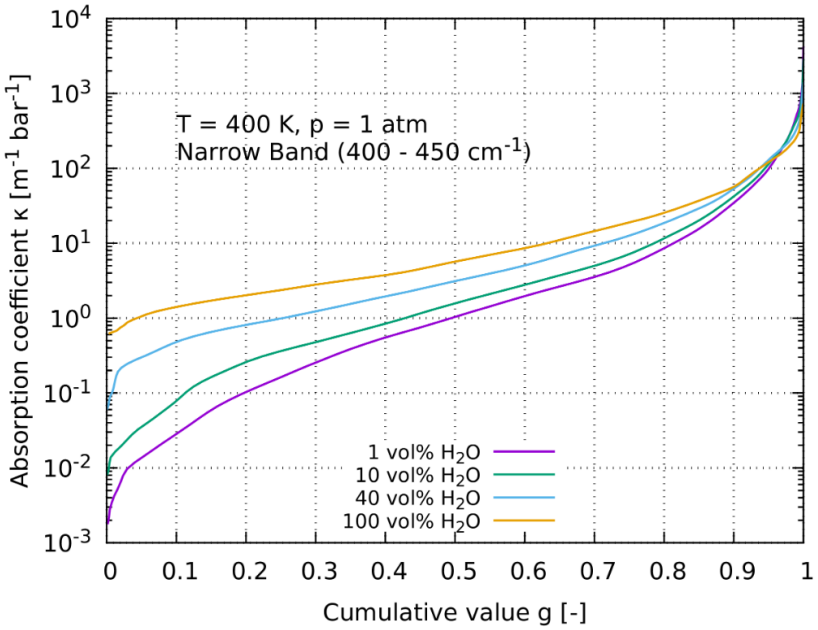

Figure 4.5: H_2O cumulative distribution function with different molar fractions x_{H_2O} = 0.01, 0.1, 0.4, and 1.0 under p_{tot} = 1.0 atm

verse cumulative distribution function becomes smooth when increasing the steam molar fractions. For the cumulative probability $g < 0.95$, the profile is mainly affected by the steam molar fraction; while the remaining part is less sensitive to the steam molar fraction. This phenomenon is non-linear process and numerical interpolation is recommended to take into account the nonhomogenity of the participating media. There are 10 molar fraction data points (0.02, 0.04, 0.06, 0.08, 0.1, 0.2, 0.4, 0.6, 0.8 and 1.0) to consider the steam molar fraction effect from low to high steam concentrations. The CO_2 SNBCK parameters are less sensitive to its molar fractions (see section 3.2.1). Therefore, the CO_2 SNBCK parameters are only tabulated in terms of temperature. The parameter generation procedure is similar to the H_2O. The CO_2 absorption spectrum is sparser than the H_2O absorption spectrum. There are only two main absorption bands in the infrared spectrum for CO_2: 667 cm^{-1} and 2000 cm^{-1}. In order to consider the H_2O – CO_2 mixture in the thermal radiation solver, the CO_2 spectral band structure is the same as the H_2O spectral band structure.

Before applying the SNBCK model in engineering applications, it is necessary to compare the averaged band transmissivity with the LBL model. Fig. 4.6 compares the narrow band transmissivities obtained from LBL and SNBCK-FZJ calculations. The LBL transmissivity is averaged over the narrow band to compare with the SNBCK-FZJ transmissivity (see Eq. 4.5). In this test case the non-gray gas

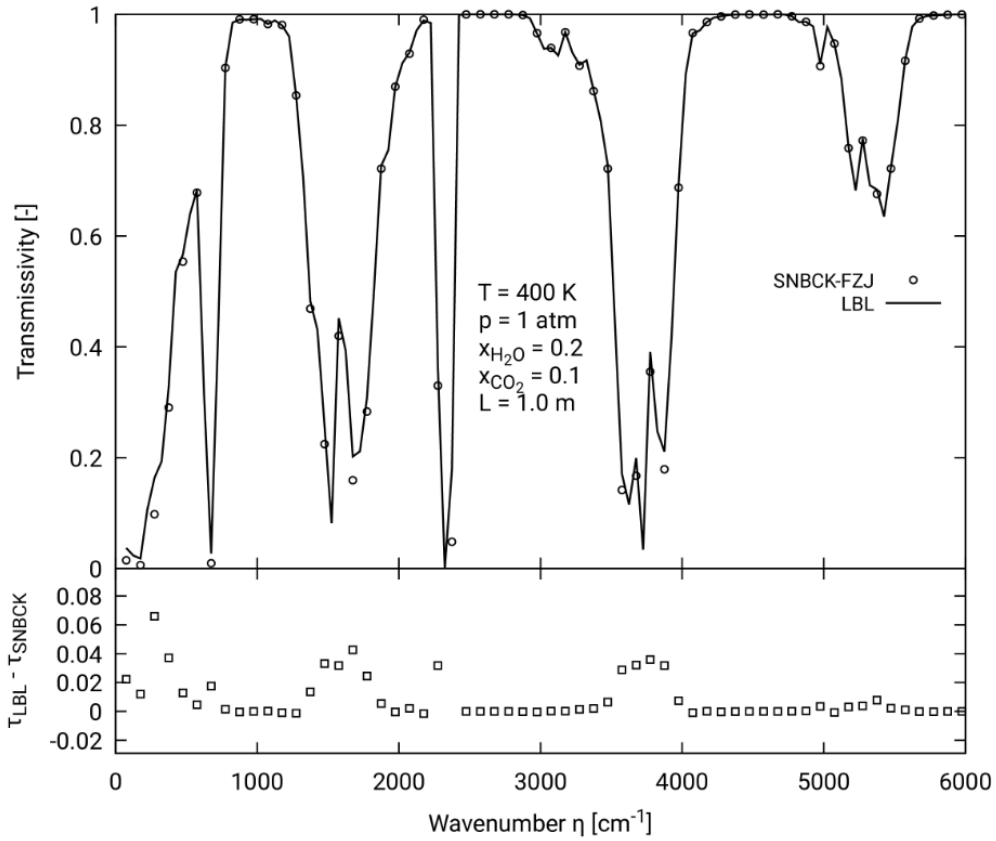

Figure 4.6: LBL and SNBCK-FZJ band transmissivity comparison: T = 400 K, p = 1 atm, x_{H_2O} = 0.2, x_{CO_2} = 0.1, x_{N_2} = 0.7 and L = 1.0 m

media composes of 20 vol.% H_2O, 10 vol.% CO_2 and 70 vol.% N_2 at atmospheric pressure (1 atm) with the media temperature 400 K. The SNBCK-FZJ results are in excellent agreement with the LBL results; however, the SNBCK-FZJ transmissivities are still acceptable at < 1000 cm^{-1} regions due to the strong variation of the H_2O absorption coefficient. In the spectral range from 1200 to 2000 cm^{-1}, there is a small difference between the SNBCK-FZJ model and the LBL model. It is noted that the SNBCK result is generally smaller than the LBL result. This systematic deviation is caused by the number of quadrature points in the SNBCK model. Nevertheless, this deviation can be neglected in engineering applications. The SNBCK model is a good compromise between accuracy and efficiency. The average transmissivity difference is less than 0.01, and the maximum difference is about 0.07. According to this verification case, the SNBCK-FZJ database is reliable to provide the spectral gas property for H_2O and CO_2 in containment flows. Both H_2O and CO_2 non-gray gases can be considered in the SNBCK-FZJ model with high accuracy.

4.2 Monte Carlo Algorithm within Participating Media

Among the available RTE numerical solvers, the most widely applied method is the fvDOM solver in fire and combustion simulations. Unfortunately, the computational effort becomes infeasible for the fvDOM solver in containment applications with a fine mesh (~ millions of cells) when considering transient analysis involving non-gray gas models. Furthermore, the fvDOM solver is not efficient for point source problems [CHE05]. During a severe accident the released hot steam and hydrogen from the primary loop can be viewed as a dominant heat source for the thermal radiation analysis, while the cold region has a minor effect on the radiative source term in containment flows (see Fig. 2.2). The fvDOM solver suffers from false scattering and ray effect in the calculation of large scale nuclear facilities. Therefore, it is mandatory to develop a new thermal radiation solver for containment studies.

As depicted in Fig. 4.7 the Monte Carlo method has a linear increase in the computational time when increasing the numerical complexity, e.g., considering the spectral gas property and fog scattering effect. In contrary, there is an exponential increase in the computational time for other RTE solvers, e.g., fvDOM, especially in technical scale 3D geometries. The conventional technique is based on the algebraic equation $Ax = b$, and the numerical complexity of solving $Ax = b$ increases rapidly for large scale applications [MOD13]. Different to conventional methods, the Monte

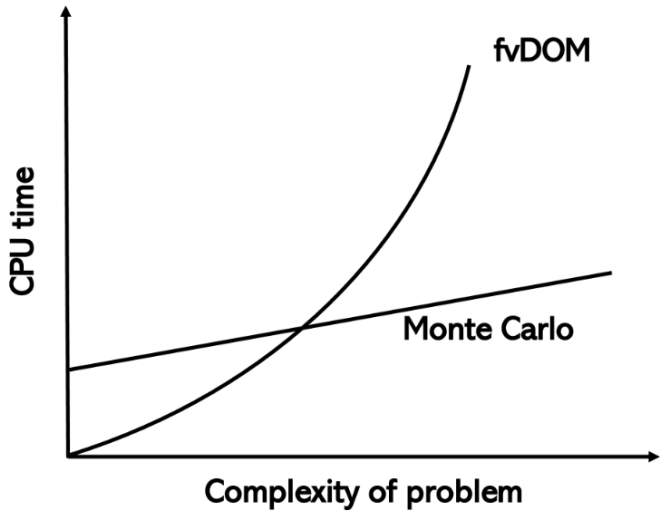

Figure 4.7: Comparison of Monte Carlo and conventional techniques for thermal radiation analyses [MOD13]

Carlo method solves the integral form of radiative transfer equation. It is not neces-

sary to resolve the spectral radiative intensity $I_\eta(r, \Omega)$ for each non-gray gas band in the Monte Carlo method. The Monte Carlo method can consider the spectral gas property by sampling photon with a specific wavenumber. Consequently, the computational complexity of the Monte Carlo solver does not significantly increase when coupling with the non-gray gas model. The Monte Carlo method is a statistical technique, which was firstly applied in neutron physics to solve the neutron transport equation [MET49]. With the development of computational techniques, the Monte Carlo method has been successfully applied in many computational fields because of its efficiency and stability, e.g., molecular dynamics [SAT10], machine learning [AND03] and thermal radiation [MOD13, TES02, ZHA11, FLE71]. The computational efficiency of the Monte Carlo method is no longer a critical issue by considering the rapid development of computer technology. The Monte Carlo method can deal with the high angular and spatial variations, spectral dependency of absorption coefficients, fog and particle scattering effects, and transparent boundary surfaces without significantly increasing the computational effort. In comparison with the fvDOM solver, undoubtedly this method eliminates the false scattering and ray effect by applying the Lagrangian tracking algorithm.

Therefore, in this thesis, the Monte Carlo method along with non-gray gas models (LBL and SNBCK) is applied for thermal radiation analyses within CFD analyses of containment flows. It is noted that the Monte Carlo with LBL model is considered as the reference for the code-to-code verification. The main drawback of the Monte Carlo method is the statistical error which results from a small number of sampling photons owing to computational limits. It is mandatory to reduce the statistical error in the Monte Carlo solver. Three optimization techniques have been implemented in the radiation module in *containmentFoam*: the global mesh, the shifted Monte Carlo method, and the emission-based reciprocity Monte Carlo method. The global mesh technique is an optimized MPI communication algorithm, reducing the MPI communication time for the parallel computation. The shifted and emission-based reciprocity Monte Carlo methods are two advanced Monte Carlo algorithms, aiming for the reduction of variance in applications with modest temperature differences, e.g., containment flows. Both advanced Monte Carlo methods can reduce the statistical error in a faster way than the original Monte Carlo method.

In the Monte Carlo solver, the radiative source term $\nabla \cdot q_r$ is evaluated for each control volume, and the radiative heat flux q_r is calculated on every boundary surface in the computational domain. As stated before, the radiative source term $\nabla \cdot q_r$ and radiative heat flux q_r can be calculated based on the energy difference between emission and absorption. The total emission Qe_j on the boundary surface is only related to the temperature and emissivity under the assumption of gray surface emissivity ϵ. The total emission from the control volume with non-gray gas media is a complex function depending on the media temperature and spectral gas prop-

erties. The total emission energy from the cell i with non-gray gases is denoted as Qe_i. The absorbed radiation energy for each control volume and boundary surface can be calculated in the Lagrangian tracking procedure. After determining the absorbed energy, the radiative heat flux on surface j is given in Eq. 4.15 [TES02]

$$q_r^j = \frac{1}{A_j}\left[\sum_{k=1}^{N_{cell}+N_{face}} Qe_k \mathcal{F}_{k\to j} - Qe_j\right] \tag{4.15}$$

and the radiative source term in the control volume i is

$$\nabla \cdot q_r^i = \frac{1}{V_i}\left[Qe_i - \sum_{k=1}^{N_{cell}+N_{face}} Qe_k \mathcal{F}_{k\to i}\right] \tag{4.16}$$

where $\mathcal{F}_{k\to j}$ can be viewed as the view factor, which is the proportion of emitted energy from the element k absorbed by the surface j; $\mathcal{F}_{k\to i}$ is the view factor, which is the proportion of emitted energy from the element k absorbed by the cell i.

According to Eq. 4.15 and Eq. 4.16, radiative heat transfer is not a local phenomenon. The radiative source term at the control volume i is related to all control volumes and boundary surfaces within the computational domain. In order to calculate the radiative source term, the radiation contribution from all control volumes and boundary surfaces must be evaluated. The Monte Carlo method must track a significant number of photons along the computational domain to obtain convergent results without large statistical errors. Normally, the Monte Carlo calculation is related to four steps in the coupled CFD and radiation simulation (see Fig. 4.8). The first step is the Monte Carlo initialization. The complex geometry, fluid parameters from the previous CFD time step and radiation wall boundary conditions are updated during the initialization process. The non-gray gas absorption coefficients κ_η are calculated using LBL or SNBCK based on the fluid parameters. The non-gray gas absorption coefficient is the fundamental parameter for the thermal radiation solver. A detailed discussion about LBL and SNBCK models can be found in section 4.1. It is not difficult to determine the total emission in the radiation solver (see section 4.2.1); however, the total absorbed radiation energy is related to the temperature and absorption coefficient distributions and boundary conditions within the computational domain.

After the Monte Carlo initialization, a number of representative photon bundles are sampled per cell according to the probability distribution functions in thermal radiation physics. The wavenumber of the energy bundle is sampled according to the non-gray gas emission spectrum, while the position of emission is uniformly distributed within the control volume. The emission direction from the control volume follows a uniform distribution among the solid angle; whereas the boundary surface radiates energy over a hemisphere. The interaction between non-gray gas media and radiative intensity, i.e., the energy attenuation along the photon path,

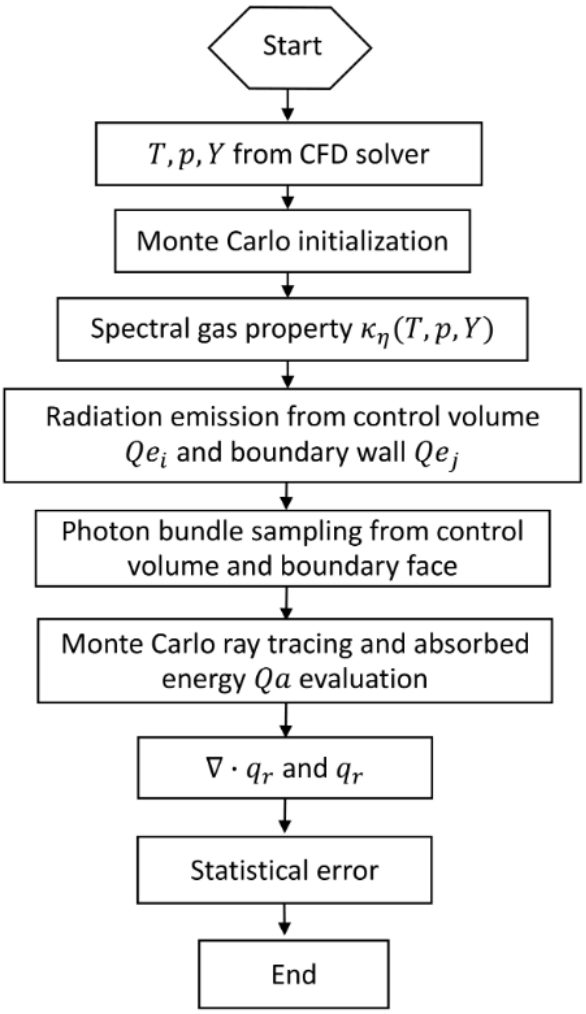

Figure 4.8: Monte Carlo computational flow chart

is calculated by the Beer–Lambert law [MOD13, TES02]. The Lagrangian tracking procedure continues until the bundle energy is small enough to stop the tracking procedure. The absorption energy in each control volume and boundary surface can be calculated in this way. After all energy bundles are tracked within the computational domain, the radiative source term $\nabla \cdot q_r$ and radiative heat flux q_r are evaluated according to the energy balance between emission and absorption. The energy bundle tracking procedure is time-consuming. The bottleneck of the Monte Carlo method is the statistical error, which can be estimated based on the statistical theory. If the statistical error is too large, it is necessary to increase the number of sampled photon bundles for the Monte Carlo solver in the next time step. If the statistical error is too large, it may lead to an unreasonable temperature field in CFD simulations.

4.2.1 Monte Carlo Sampling

The starting point of the sampling procedure is the random number generator or the uniformly distributed random number. Monte Carlo calculations always require a large amount of high-quality random numbers. Otherwise, the simulation result obtained from Monte Carlo method is biased due to the random number generation itself. The choice of a deficient random number generator can cause systematic errors in Monte Carlo simulations [COD94]. In fact, the pseudo-random number is a deterministic number sequence without repetition. Since a large amount of random numbers are needed in the Monte Carlo method, a simple, efficient and reliable random number generator with an excellent statistical quality is important for Monte Carlo simulations. The most common random number generator is the linear congruential generator, proposed by D. H. Lehmer in 1951 [LEH51]. The random number generator can provide a sequence of random numbers uniformly distributed in the unit interval (0, 1). The linear congruential generator can produce an integer sequence

$$X_{i+1} = (aX_i + c) \ mod \ M, \ \ i = 0, 1, 2... \tag{4.17}$$

$$\xi_{i+1} = \frac{X_{i+1}}{M}, \tag{4.18}$$

where a is the multiplier; c is the increment; M is the modulus; ξ_{i+1} is the random number. The linear congruential generator in POSIX [RIP90] is applied in this thesis, named the rand48 ($a = 25214903917$, $c = 11$, and $M = 2^{48}$). The rand48 generator can provide random numbers with high-quality. The maximum period of the number generator rand48 is 2^{48}, which is large enough to prevent a repetition of random numbers in the Monte Carlo solver, and the impact of numerical uncertainty from the random number generator can be minimized.

The probability distribution sampling relies on the random number ξ. First of all, the thermal radiation process is described by a probability distribution function $P(x)$. The distribution of a random variable X is denoted by the cumulative distribution function $F(x) = P(X \leq x)$. If $F(x)$ is a cumulative distribution function with the inverse function $F^{-1}(y)$ and ξ is a random number with the uniform distribution over $(0, 1)$, then $x = F^{-1}(\xi)$ is a sampling value for the random variable X. This is the standard procedure to generate a random sampling x from a known cumulative distribution function $F(x)$. The sampling process is as follows:

- Evaluate the cumulative distribution $F(x)$ of random variable X from the physical distribution
- Generate a random number ξ from the unit interval distribution $\xi \sim U(0, 1)$

- Determine the sampling value x by the inverse cumulative distribution function $x = F^{-1}(\xi)$

Before discussing the Monte Carlo photon sampling algorithm, the physical behavior of photon bundles must be represented accurately. Otherwise, the Monte Carlo simulation is biased. It is noted that the thermal radiation solver uses the same mesh as the CFD code to enable an easy coupling. The whole computational domain is divided into a number of finite volume cells V_i and boundary surfaces A_j. The first step of Monte Carlo photon/bundle sampling is to determine the total emission energy from cells and wall boundary surfaces. The radiation emission energy from the boundary surface j (temperature T_j and area S_j) with a gray surface emissivity ϵ is

$$Qe_j = \epsilon \pi S_j \int_0^\infty I_{b,\eta}(T_j) d\eta \tag{4.19}$$

The total emission energy from the control volume is difficult to quantify, since the spectral gas property has a highly irregular dependence on the wavenumber. Consequently, the modeling of radiative heat exchange within participating gases becomes more complex. The spectral absorption coefficient is a function of temperature T, pressure p, and mass fraction Y. The total radiation emission energy from the control volume i (temperature T_i, pressure p, mass fraction Y and volume V_i) is

$$Qe_i = 4\pi V_i \int_\eta \kappa_\eta(T_i, p, Y) I_{b,\eta}(T_i) d\eta \tag{4.20}$$

After determining the total radiation emission energy, a number of energy bundles/photons $Nbundles$ are sampled from the emission source. The radiative exchange within the computational domain can be tracked by the energy bundle. It is advantageous to have the energy bundle containing a number of photons, as the energy of single photon is too small. In each energy bundle it also has a wavenumber η to take into account of spectral gas properties [HOW20]. Since the radiative source term is evaluated for each control volume, it is necessary to generate a number of energy bundles on each control volume. As a result, the total number of sampling bundles (~ 100 times of the mesh size) is quite large in order to reduce the statistical error. This is the reason why the Monte Carlo method is more time-consuming than other methods. The energy of emitted bundle depends on its wavenumber, but it is convenient to have the same energy for each energy bundle. The energy E for the emitted bundle from the control volume i is

$$E = \frac{Qe_i}{Nbundles} \tag{4.21}$$

The number of sampled photon bundles $Nbundles$ is not the same for different control volumes. More energy bundles are sampled in the important regions, which is called the biased sampling. The biased sampling method is one of the variance

reduction technique to accelerate Monte Carlo simulations [HEN85], and the basic idea of the biased sampling is to determine the important scenario in large simulations. In this thesis, the importance sampling technique is based on the global maximum temperature T_{max} and minimum temperature T_{min} obtained from the previous CFD time step. Due to the fact that the emission energy is proportional to the fourth power of fluid temperature, it is meaningful to have more sampling photons in hot regions than that in cold regions. In this way, the total number of photons is significantly reduced typically by a factor of two without losing computational accuracy, making the Monte Carlo method feasible in practical/engineering applications. Moreover, the biased sampling method is not only limited to the temperature. Other physical quantities, e.g., emission wavelength, emission direction and emission position can be introduced by this technique to further save computational effort without losing statistical significance.

During the sampling procedure, the properties of each sampling bundle are characterized by seven variables: position $r(x, y, z)$, emission direction $\Omega(\theta, \phi)$, emission energy E, and wavenumber η, which are based on the physical interaction between photon and matter. The emission position and direction can be easily determined assuming a homogeneous distribution. The wavenumber η of the energy bundle is sampled based on the non-gray gas emission spectrum, which is the most important parameter for the spectral gas property treatment. In the Monte Carlo method, it is not necessary to resolve the spectral radiation intensity $I_\eta(r, \Omega)$ in each spectral band. The spectral gas property treatment is characterized by the emission wavenumber η. Therefore, the Monte Carlo method is more efficient than the fvDOM when considering non-gray gas media in the thermal radiation analysis. According to the total emission energy within the control volume i, the inverse cumulative distribution function $F^{-1}(\eta)$ for the emission wavenumber η can be calculated with Eq. 4.22.

$$F^{-1}(\eta) = \frac{\int_0^\eta \kappa_\eta(T_i, p, Y) I_{b,\eta}(T_i) d\eta}{\int_0^\infty \kappa_\eta(T_i, p, Y) I_{b,\eta}(T_i) d\eta} \tag{4.22}$$

where η is the wavenumber; $I_{b,\eta}(T_i)$ is the black body emission intensity from the control volume i; $\kappa_\eta(T_i, p, Y)$ is the LBL absorption coefficient at the control volume i. For the gray surface emission, the inverse cumulative distribution function for wavenumber η which is emitted from the boundary surface j is

$$F^{-1}(\eta) = \frac{\int_0^\eta I_{b,\eta}(T_j) d\eta}{\int_0^\infty I_{b,\eta}(T_j) d\eta} \tag{4.23}$$

where $I_{b,\eta}(T_j)$ is the black body emission intensity from the boundary surface j.

As shown in Eq. 4.22 and Eq. 4.23, the wavenumber sampling procedure is complex for the control volume [SOU13]. In order to illustrate the wavenumber sampling procedure, the wavenumber sampling for the non-gray gas emission within

the control volume is illustrated in Fig. 4.9, assuming that the gas mixture is composed of 10 vol.% H_2O and 90 vol.% N_2 at 1 atm with 400 K temperature. The

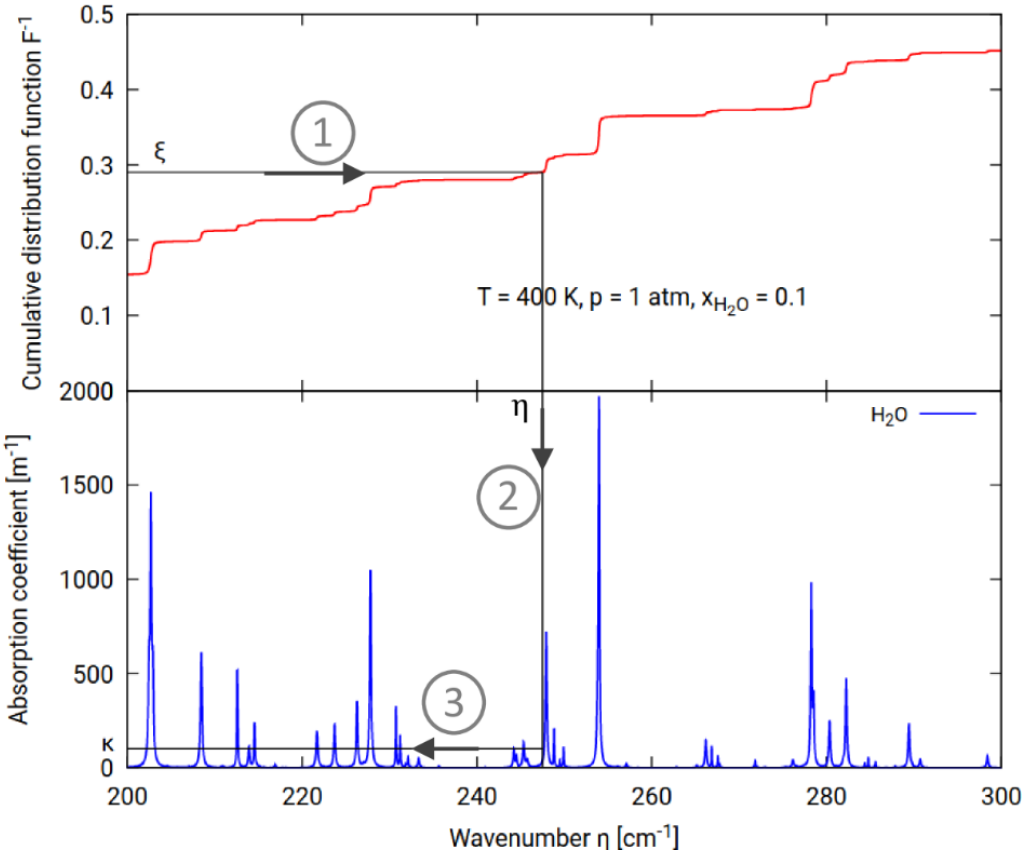

Figure 4.9: Monte Carlo wavenumber sampling algorithm (T= 400 K, x_{H_2O} = 0.1 and P_{tot} = 1 atm), modified from [SOU13]

bottom part of Fig. 4.9 is the LBL absorption coefficient for steam at 400 K from 200 cm^{-1} to 300 cm^{-1}. The upper part of Fig. 4.9 is the associated inverse cumulative distribution function $F^{-1}(\eta)$ which can be calculated by Eq. 4.22. It is noted that only a small spectral interval (from 200 to 300 cm^{-1}) is shown in the Fig. 4.9. After the associated inverse cumulative distribution function $F^{-1}(\eta)$ is computed, a random number ξ = 0.29 is generated. According to this random number ξ, the sampling wavenumber η can be evaluated by the binary search algorithm in the inverse cumulative distribution function $F^{-1}(\eta)$ (see the upper part of Fig. 4.9). Because of the irregularity of absorption coefficients in such a small spectral interval, the sampling wavenumber η must be accurately evaluated in the Monte Carlo method. A small shift in the sampling wavenumber η can lead to a significant change in the absorption coefficient κ_η, which is an important parameter for the photon tracking procedure. Therefore, the LBL absorption coefficient must be eval-

uated at a fine interval [WAN07]. Otherwise, the simulation result is biased. Once the sampling wavenumber η is determined, the absorption coefficient κ_η also can be calculated by the interpolation scheme (see the bottom part of Fig. 4.9). During the tracking procedure, the exponential attenuation law is related to this sampling wavenumber η. The detailed discussion about the photon tracking procedure is given in section 4.2.2. For the code implementation, the particle class in the radiation module has a private member variable, called $eta_$, to store the wavenumber η information. Moreover, a LBL database is generated before the Monte Carlo simulation on a set of temperature and molar fraction points. During the Monte Carlo simulation, the absorption coefficient κ_η is calculated by bilinear interpolation. As shown in Fig. 4.9, the LBL absorption coefficient κ_η is highly variable across the whole infrared radiation spectrum. Therefore, a numerical fluctuation is expected for the Monte Carlo solver with the LBL model. It is necessary to apply advanced Monte Carlo method to reduce the statistical error. The variation reduction technique is discussed in section 4.3.

The Monte Carlo method with the LBL model is computationally intensive in the energy bundle sampling procedure. The Monte Carlo method with the LBL model also requires a huge amount of computational memory. To reduce the computational cost the SNBCK model is selected in terms of accuracy and efficiency. As discussed in section 4.1.2, the tailored SNBCK model has 7 Gauss quadrature points to describe the variance of absorption coefficient in each narrow band. The total number of narrow bands is 159 over the whole spectrum (N_b = 159). The total black body emission from the control volume i can be approximated by

$$Qe_i = 4\pi V_i \sum_{b=1}^{N_b} \sum_{q=1}^{N_q} \omega_q \kappa_{b,q} I_{b,\eta}(T, \eta_b) \Delta\eta_b \tag{4.24}$$

where ω_q is the Gauss quadrature weight; $\kappa_{b,q}$ is the absorption coefficient in narrow band b for the quadrature point q; $I_{b,\eta}(T, \eta_b)$ is the black body emission intensity in the narrow band b; $\Delta\eta_b$ is the narrow band width.

Different from the LBL model, the spectral gas property treatment in the Monte Carlo method with SNBCK model is related to two parameters (b, q). The first parameter b is the emission band, and the second one is the quadrature index q within this narrow band b. The first step is to determine the emission band b of the sampling bundle. The emission band b variable follows the discrete probability distribution $P(b)$ (see Eq. 4.25).

$$P(b) = \frac{\sum_{q=1}^{N_q} \omega_q \kappa_{b,q} I_{b,\eta}(T, \eta_b) \Delta\eta_b}{\sum_{b=1}^{N_b} \sum_{q=1}^{N_q} \omega_q \kappa_{b,q} I_{b,\eta}(T, \eta_b) \Delta\eta_b} \tag{4.25}$$

The probability distribution $P(q|b)$ for the quadrature point q at the narrow band b

is obtained by Eq. 4.26.

$$P(q|b) = \frac{\omega_q \kappa_{b,q}}{\sum_{q=1}^{N_q} \omega_q \kappa_{b,q}} \tag{4.26}$$

During the photon bundle tracking procedure, those two sampling parameters (b, q) are mandatory to calculate the absorption coefficient $\kappa_{b,q}$ in the SNBCK model. According to Eq. 4.25 and Eq. 4.26, the non-gray gas treatment for the SNBCK model is simpler than the LBL model. The numerical fluctuation is less significant for the SNBCK model. There are the only differences between the LBL and SNBCK models in the Monte Carlo method.

After determining the emission wavenumber η, the emission position $r(x, y, z)$ and direction $\Omega(\theta, \phi)$ are also sampled based on the physical probability functions on the control volume and the wall boundary surface as shown in Eq. 4.27 and Eq. 4.28.

$$f(x, y, z)_{volume} = \frac{1}{\int\int\int_{\Delta V} dxdydz} \tag{4.27}$$

$$f(x, y, z)_{surface} = \frac{1}{\oint\oint\oint_{S} dxdydz} \tag{4.28}$$

Using the above two equations, the emission position is evenly distributed within the control volume or wall boundary surface. For the emission direction $\Omega(\theta, \phi)$, the direction of the energy bundle emitted from cell i follows a uniform distribution among the solid angle. The polar angle θ and the azimuth angle ϕ within the control volume can be determined using Eq. 4.29 and Eq. 4.30

$$f(\theta, \phi) = \frac{sin\theta}{4\pi};\ 0 \le \theta \le \pi,\ 0 \le \phi \le 2\pi \tag{4.29}$$

$$\begin{aligned} \theta &= arccos(1 - 2\xi) \\ \phi &= 2\pi\xi \end{aligned} \tag{4.30}$$

where ξ is the random number. For a diffusive boundary wall, it is a hemispherical distribution (see Fig. 4.10). The polar angle θ ranges from 0 to $\frac{\pi}{2}$, while the azimuth angle ϕ is uniformly distributed over the circle (from 0 to 2π). As shown in Fig. 4.10, the emission angle $\Omega(\theta, \phi)$ on the boundary surface is uniformly distributed on the hemispherical surface. Therefore, the polar angle θ and the azimuth angle ϕ emitted from the boundary surface can be determined using Eq. 4.31 and Eq. 4.32

$$f(\theta, \phi) = \frac{cos\theta sin\theta}{2\pi};\ 0 \le \theta \le \frac{\pi}{2},\ 0 \le \phi \le 2\pi \tag{4.31}$$

$$\begin{aligned} \theta &= arccos(\sqrt{\xi}) \\ \phi &= 2\pi\xi \end{aligned} \tag{4.32}$$

where ξ is the random number.

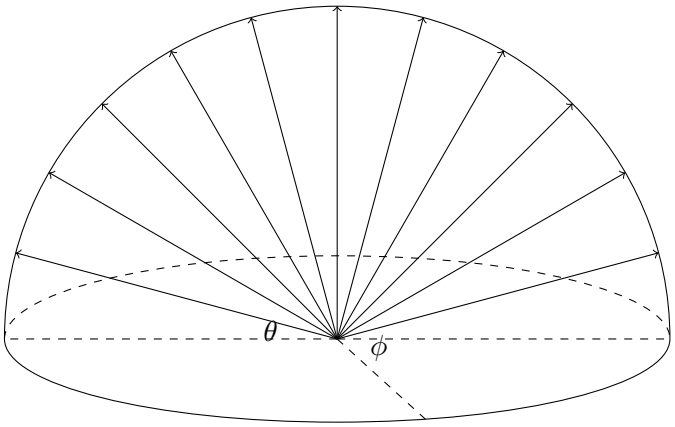

Figure 4.10: Diffusive emission from the gray surface

According to the above equations, the emitted photon bundles from all control volumes and wall boundary surfaces ($r(x, y, z), \Omega(\theta, \phi), E, \eta$) are calculated in the Monte Carlo method. The energy bundle in the Monte Carlo method has an important impact on the radiative source term for thermal radiation analyses. Therefore, all probabilistic functions must represent the physical scenario and thermal radiation phenomena with high accuracy in the Monte Carlo method. It is necessary to verify that all sampling energy bundles are unbiased in the Monte Carlo method before performing the tracking procedure. This has been tested step by step during solver implementation.

In the developed Monte Carlo solver there are three input parameters (*minPhoton*, *maxPhoton* and *facePhoton*) to control the number of energy bundles. The parameter *minPhoton* defines the minimum number of sampling bundles for the control volume, and the parameter *maxPhoton* sets the maximum number of sampling bundles in the hottest control volume. The parameter *facePhoton* specifies the number of sampling energy bundles on the boundary face. The numerical tests reveal a good practice of settings without significant numerical error: $minPhoton$ 40, $maxPhoton$ 80 and $facePhoton$ 40. With this setting, the total number of sampling photons is about two orders of magnitude larger than the number of cells in computational mesh. After the sampling photon is identified, the following procedure is to calculate the energy deposition along its path length, which is based on the physical interaction between photon and matter. This is the most time-consuming part for the Monte Carlo method.

4.2.2 Monte Carlo Ray Tracing

Based on a sampled set of the representative bundles/photons from each control volume and wall boundary face, the Monte Carlo tracking algorithm is discussed in the following. In order to ease the understanding, the photon tracking procedure is explained in a two dimensional mesh, but the same principles and algorithms are applied to three dimensional meshes as well. In the CFD mesh the computational domain is divided into a number of nonoverlapping cells with constant fluid parameters. Each control volume is accurately specified by several characteristics: point positions, internal surfaces, boundary surfaces, volumes, and neighboring cells. As shown in Fig. 4.11, the 2D computational domain has five control volumes and eight boundary surfaces. The control volume is marked as circle ◯; while the

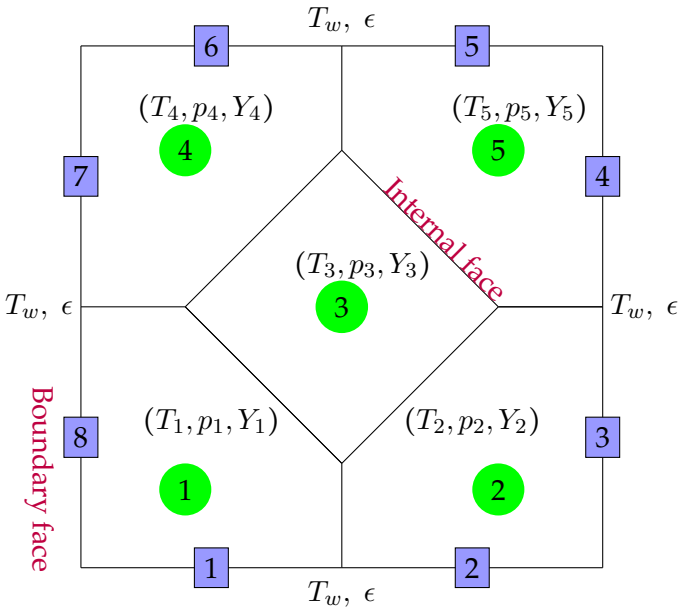

Figure 4.11: Initial fluid conditions for the Monte Carlo simulation

wall boundary face is pointed as square □ in Fig. 4.11. The other surfaces inside the computational domain are called internal surfaces in the following discussion. Two control volumes are connected by an internal face, while a boundary face is only associated with one boundary cell. For example, the internal surface in Fig. 4.11 has two control volumes ⑤ and ③. The boundary face 8 is only related to the control volume ①. The Monte Carlo solver can obtain the temperature T (including wall temperature T_w), pressure p and mass fraction Y fields for each control volume from the previous CFD time step. Besides, the Monte Carlo solver also requires the surface emissivity ϵ on boundary walls. The total radiation emission can be calculated according to this initial condition.

After that, a number of energy bundles are sampled from each control volume and boundary face. As shown in Fig. 4.12, there are two sampling photons for each control volume. Only one sampling photon is on the boundary surface in Fig. 4.12. In the engineering applications, it is necessary to increase the number of sampling photons to reduce the statistical error. The limit of the Monte Carlo method is the computational efficiency, but the main advantage of Monte Carlo method is the random energy bundle sampling and high-fidelity modeling [LIU22b]. The Monte Carlo tracking procedure is based on the Lagrangian tracking algorithm on the unstructured mesh in OpenFOAM (see Appendix A). After identifying the location of energy bundle in the computational domain, the distance to the nearest face with the emission direction can be determined.

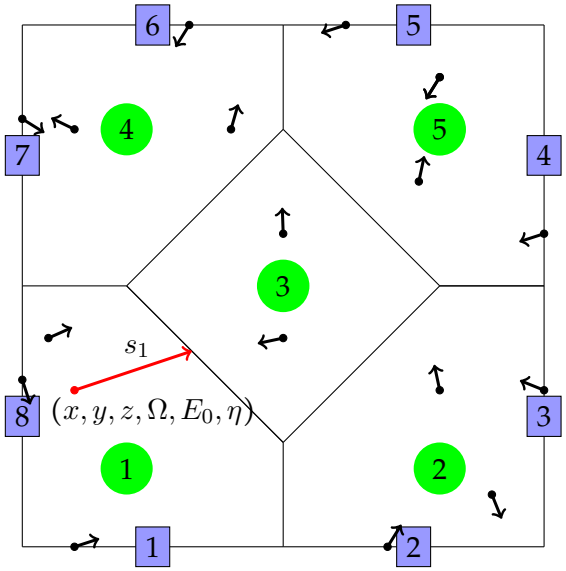

Figure 4.12: Monte Carlo energy bundle sampling procedure

The emission bundle from the control volume ① with the red color in Fig. 4.12 is selected to illustrate the bundle tracking procedure. The cell ① is bounded by five faces in Fig. 4.12. Two surfaces are wall boundary surfaces (8 and 1) on the wall, and other three faces are internal faces within the computational domain. When a photon bundle is generated from the cell ① in the sampling procedure, the initial positions (x, y, z), direction $\Omega(\theta, \phi)$, emission energy E and wavenumber η, $(x, y, z, \Omega, E_0, \eta)$, are determined from the photon/bundle sampling algorithm described in the previous section. The next step is to calculate the path distance to the nearest face at the starting position (x, y, z) with the emission direction $\Omega(\theta, \phi)$. From its initial position, according to the direction Ω, the nearest face distance s_1 is calculated by the Lagrangian particle tracking library in OpenFOAM [HAS07] (see Fig. 4.12).

After wards, the next step is to evaluate the energy deposition along path length s_1 within the control volume ①. The energy deposition within the control volume is related to the absorption coefficient κ_η within the current cell (cell ①) and the path length s_1. It is worthwhile to note that the absorption coefficient κ_η is a function of (T_1, p_1, Y_1) within cell ① and the wavenumber η. For the SNBCK model, the absorption coefficient $\kappa_{b,q}$ is related to the narrow band b and the quadrature index q. This is the only difference between LBL and SNBCK models. The bundle emission energy is attenuated along the path length according to the Beer-Lambert law. The fraction of energy that is absorbed by the medium through the distance s_1 can be defined as the absorbance

$$\alpha = 1 - \exp(-\kappa_\eta[cell\,①]\,s_1) \tag{4.33}$$

The energy deposition within cell ① along the path length s_1 is given in Eq. 4.34. In order to store the absorbed energy within the control volumes, an array variable Qa (absorbed energy) is allocated in the Monte Carlo solver. Before the Monte Carlo tracking procedure, this array Qa is initialized as zero. This array is the accumulation of the absorbed energy within the control volumes.

$$Qa[cell\,①]^{new} = Qa[cell\,①]^{old} + E_0(1 - \exp(-\kappa_\eta[cell\,①]\,s_1)) \tag{4.34}$$

As the media attenuation is relatively small within the distance s_1, it is necessary to consider the residual energy for the following bundle tracking procedure. The residual energy for the emitted energy ray is

$$E_1 = E_0 \exp(-\kappa_\eta[cell\,①]\,s_1) \tag{4.35}$$

The position of energy bundle is updated according to Eq. 4.36.

$$(x, y, z)^{new} = (x, y, z)^{old} + s_1\,\Omega \tag{4.36}$$

where $(x, y, z)^{old}$ is the starting position; $(x, y, z)^{new}$ is the new position; s_1 is the path length; Ω is the emission direction.

At that moment, the photon bundle reaches the face between cell ① and cell ③ (see Fig. 4.13). The Monte Carlo program checks whether this is an internal face or not. If it is an internal face between two connecting cells, the energy bundle/photon enters into the neighbour cell ③. It is noted that the direction of energy bundle is not changed in the tracking procedure as there is no scattering effect considered in this work. After entering the cell ③, the absorption coefficient is updated $\kappa_\eta(T_3, p_3, Y_3)$ according to the local temperature, pressure, and mass fractions in the cell ③ (see Fig. 4.11). The energy deposition within cell ③ along the path length s_2 (see Fig. 4.13) is given as

$$Qa[cell\,③]^{new} = Qa[cell\,③]^{old} + E_1(1.0 - \exp(-\kappa_\eta[cell\,③]s_2)) \tag{4.37}$$

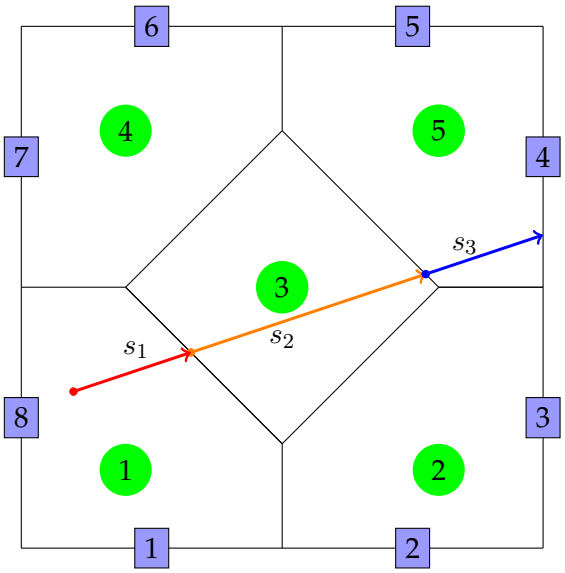

Figure 4.13: Monte Carlo tracking process over the computational domain

$$E_2 = E_1 \exp(-\kappa_\eta [cell\ ③] s_2) \tag{4.38}$$

$$(x, y, z)^{new} = (x, y, z)^{old} + s_2\, \Omega \tag{4.39}$$

At that moment, the energy bundle is located on the internal face between cell ③ and ⑤. Therefore, the photon enters into the neighbour cell ⑤. After entering the cell ⑤, the absorption coefficient $\kappa_\eta(T_5, p_5, Y_5)$ is updated according to the local temperature, pressure, and mass fractions in the cell ⑤. The distance to the nearest face s_3 is calculated. The energy deposition within the cell ⑤ is

$$Qa[cell\ ⑤]^{new} = Qa[cell\ ⑤]^{old} + E_2(1.0 - \exp(-\kappa_\eta [cell\ ⑤] s_3)) \tag{4.40}$$

$$E_3 = E_2 \exp(-\kappa_\eta [cell\ ⑤] s_3) \tag{4.41}$$

$$(x, y, z)^{new} = (x, y, z)^{old} + s_3\, \Omega \tag{4.42}$$

This time the energy bundle hits on the boundary face $\boxed{4}$ (see Fig. 4.14). If it is a black boundary surface ($\epsilon = 1$), the photon is absorbed on the boundary wall, and the tracking procedure is finished. If the wall emissivity ϵ is less than 1.0, the absorbed energy on the wall $\boxed{4}$ is calculated by Eq. 4.43. In order to store the absorbed energy on the boundary wall surfaces, an array variable qra (absorbed energy) is allocated in the Monte Carlo solver. Before the Monte Carlo tracking procedure, this array qra is initialized as zero. The array variable qra is the accumulation of the absorbed energy on the boundary wall.

$$qra[wall\ \boxed{4}]^{new} = qra[wall\ \boxed{4}]^{old} + \epsilon[wall\ \boxed{4}] E_3 \tag{4.43}$$

If the boundary wall $\boxed{4}$ is not a black wall, the incoming energy bundle can be reflected on the boundary wall. The reflected energy from the opaque wall is

$$E_4 = (1.0 - \epsilon[wall\,\boxed{4}])E_3 \tag{4.44}$$

The emission direction of residual energy bundle has to be resampled on the wall boundary surface. As shown in Fig. 4.14, the diffusive wall can reflect the incoming bundle into any direction with a uniform distribution over the hemisphere. The emission direction sampling algorithm on the boundary wall can be found in section 4.2.1.

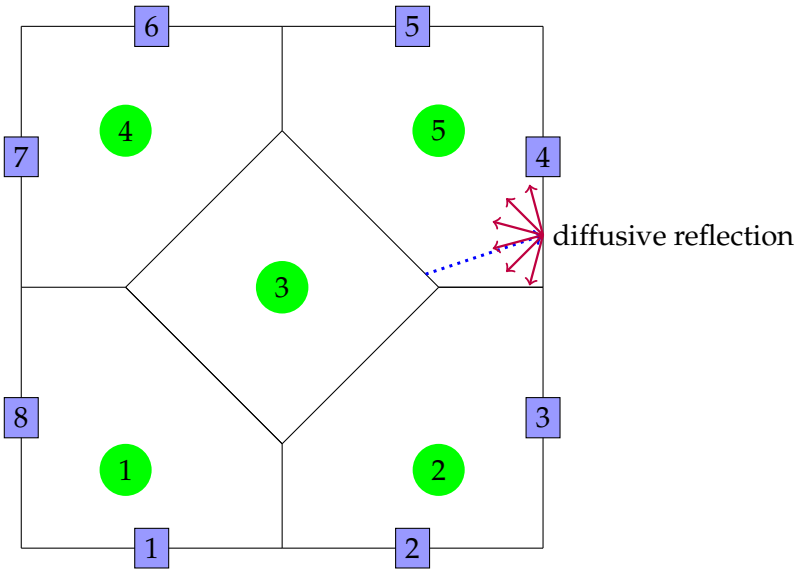

Figure 4.14: Monte Carlo diffusive wall reflection

Besides the diffusive wall boundary condition, the symmetry boundary condition is also a common boundary condition in the CFD simulation of symmetric geometries. Defining a symmetric boundary condition in CFD simulations can remarkably reduce the computational effort. It is noted that there is no sampling photon on the symmetry boundary in the Monte Carlo solver. For the symmetry boundary condition, a specular reflection condition is defined on the symmetry wall in the Monte Carlo solver. The reflective direction Ω_{out} and the outcoming energy E_{out} are given in the Eq. 4.45 and Eq. 4.46.

$$\Omega_{out} = \Omega_{in} - 2(\Omega_{in} \cdot n) \cdot n \tag{4.45}$$

$$E_{out} = E_{in} \tag{4.46}$$

where Ω_{in} is the incoming direction; n is the surface normal vector; E_{in} is the incoming energy.

The tracking procedure continues until the bundle energy E drops below the cutoff energy E_{cut}. After all sampled energy bundles are tracked over the computational domain, the absorbed energy Qa is evaluated in the Monte Carlo method. Therefore, the radiative source term and wall heat flux are calculated according to Eq. 4.15 and Eq. 4.16. It is noted that there is a huge uncertainty for the absorbed energy Qa if the number of sampled energy bundles is not large enough due to limits in computational power. This is the only limitation of the Monte Carlo method.

The implemented Monte Carlo method with LBL model is illustrated in the following algorithm (see Algorithm 1). It can be easily transferred to the SNBCK model. When solving the CFD energy equation, the CFD solver *containmentFoam* asks for the radiative source term. After that, it launches the Monte Carlo radiation solver. At the beginning, the absorption coefficient is updated based on the CFD fluid conditions (p, T, Y) and a photon tracking cloud is initialized in the Monte Carlo solver. The cloud class comprises the management of the energy bundle initialization, photon tracking and radiative source term calculation. The energy bundles emitted from cells and surfaces are sampled. The information of sampling bundles is stored in the cloud class, which is memory consuming, since there are millions of energy bundles within the system. The reason for storing all tracking photons in a cloud class is to achieve a better performance in parallel computations.

After finishing the photon sampling, the following step is to track the photon bundle one by one. The most time consuming function is the $Distance_Next_Face()$ in the Monte Carlo algorithm. This function calculates the nearest face distance on the unstructured 3D mesh using the Lagrangian particle tracking module in OpenFOAM. After passing through the small control volume, the photon energy is attenuated due to the media absorption effect. The path of energy bundle is traced until it leaves the computational domain or its energy is small enough to be killed ($< 10^{-3} E_{initial}$). The absorption energy is evaluated during photon bundle tracking procedure for each control volume and boundary surface. After all sampled energy bundles are tracked over the computational domain, the final radiative source term is determined by the balance between emitted and absorbed energy. It is obvious that the Monte Carlo code implementation must be optimized since it requires a huge amount of system memory and CPU time. If the code is not optimally implemented, the system memory can be easily exhausted and it takes a longer time to finish the numerical computation. The Monte Carlo method suffers from slow convergence for the radiative source term. In the Monte Carlo method, for each control volume or boundary surface, it is required to calculate the radiative source term or wall heat flux. In other words, each finite volume cell or surface requires a large number of photons in order to reduce the statistical error. The statistical error estimation is given in the following section to evaluate the numerical uncertainty.

Algorithm 1: Monte Carlo LBL implementation

```
/* cells: number of cells on the CFD mesh                    */
/* boundaryFaces: number of boundary faces                   */
/* Nbundles: number of sampled energy bundles                */
/* NTotalBundles: total sampled energy bundles               */
/* Ecutoff: cutoff energy limit                              */
/* Qe: total emission energy in control volume               */
/* Qa: total absorbed energy in control volume               */
/* qre: total emission energy on boundary wall               */
/* qra: total absorbed energy on boundary wall               */
for i = 1 →cells do
    Qe[i] = Cell_Emission(κ, p, Y, T) ;    // Cell emission Eq. 4.20
    Qa[i] = 0 ;                        // Initialize abs. energy Qa
    for ray = 1 →Nbundles do
        E = Qe[i]/Nbundles ;                  // Initial bundle energy
        Sample_Bundle_inCell(x, y, z, Ω, η) ;
        add_Bundle_toBank(x, y, z, Ω, E, η) ;
    end
 end
 for i = 1 →boundaryFaces do
    qre[i] = Surface_Emission(ϵ, T) ; // Surface emission Eq. 4.19
    qra[i] = 0 ;                       // Initialize abs. energy qra
    for ray = 1 →Nbundles do
        E = qre[i]/Nbundles ;                 // Initial bundle energy
        Sample_Bundle_onSurface(x, y, z, Ω, E, η) ;
        add_Bundle_toBank(x, y, z, Ω, E, η);
    end
  end
  for bundle = 1 →NTotalBundles do
     while E > Ecutoff do
        cell = Cell_Location() ;                    // Bundle location
        s = Distance_Next_Face() ;          // Distance to next cell
        κ = Absorption_Coefficient(T, p, Y, η) ;
        Qa[cell] = Qa[cell] + E(1 − exp(−κs)) ;     // Energy deposition
        E = E exp(−κs) ;                           // Energy attenuation
        if onBoundary_Wall() then
            wall = Wall_Location() ;                // Bundle location
            qra[wall] = qra[wall] + ϵE ;           // Energy deposition
            E = E(1 − ϵ) ;                         // Energy attenuation
            Boundary_Treatment() ;
        end
     end
  end
  for i = 1 →cells do
     divQr[i] = (Qe[i] − Qa[i])/ΔV[i] ;              // ∇·q_r evaluation
  end
  for j = 1 →boundarys do
     qr[j] = (qra[j] − qre[j])/ΔS[j] ;                 // q_r evaluation
  end
```

4.2.3 Estimation of Statistical Error

The statistical error is the main disadvantage of the Monte Carlo method, and it is necessary to quantify the statistical error for all Monte Carlo simulations. The principle of the Monte Carlo method is to estimate the mean value $E(\psi(X))$ in the physical system, where ψ is the physical quantity and X is the independent variable related to the quantity ψ.

$$E(\psi(X)) = \int \psi(X) f(X) dX, \quad X \sim f(X) \tag{4.47}$$

For example, ψ can be the radiative source term in the Monte Carlo radiation solver, and X is the independent variable that can affect the radiative source term, e.g., temperature, pressure, mass fraction, and the number of sampled energy bundles. The energy bundle is sampled according to the physical probability function related to the positions, wavenumber, and emission directions. Hence, it is extremely difficult to estimate the statistical error theoretically.

A stochastic approximation is applied to calculate the statistical error for the integral value $E(\psi(X))$ by producing a number of samples. According to the law of large numbers, the expected value can converge to the true value when increasing the number of trials [MEN12]. Assuming the $\psi_1, \psi_2, ..., \psi_N$ are the sampling sequences of value $\psi(X)$, the expected value of $\overline{\psi}$ is

$$\overline{\psi} = \frac{1}{N} \sum_{i=1}^{N} \psi_i \tag{4.48}$$

According to statistical theory [PAL19] the variance σ^2 of the mean value $\overline{\psi}$ is

$$\sigma^2 = \frac{1}{N-1} \left[\sum_{i=1}^{N} \psi_i^2 - \frac{1}{N} \left(\sum_{i=1}^{N} \psi_i \right)^2 \right] \tag{4.49}$$

As shown in Eq. 4.49, the Monte Carlo standard deviation σ is proportional to the square root of the inverse of the number of trials N. A number of studies have been performed to improve the efficiency of Monte Carlo methods [TES02, MOD13, LIU22b]. In order to quantify the statistical error, the Monte Carlo simulation is divided into N batches [TES11]. If the total number of photon bundles is 10^8 and the batch number N is 10, the radiative source term is calculated 10 times (per 10^7 photons each batch) in the Monte Carlo solver. In this way, the statistical error is calculated according to the Eq. 4.49. The statistical fluctuation deteriorates the prediction of the temperature field, leading to nonphysical simulation results. This is the main consequence of the statistical error. This measure has been used to determine the ideal number of energy bundles for practical applications.

4.2.4 First Verification of the Monte Carlo Solver

Before applying the Monte Carlo method for thermal radiation analyses in containment flows, it is thoroughly verified. A often used test case is a two-dimensional rectangular box filled with the non-gray gas media [GOU00]. The box (1.0 m width and 0.5 m height) is discretized by an orthogonal mesh (see Fig. 3.26) with the mesh size $100 * 50$. The 2D box is filled with an isothermal H_2O-N_2 mixture (p = 1 atm, T = 1000 K, x_{H_2O} = 0.2 and x_{N_2} = 0.8). The temperature of bounding walls is 0 K and the wall emissivities are 1. Therefore, there is no radiation emission from the boundary walls in this 2D test case. The non-gray gas emission is investigated in this 2D test case to quantify the numerical difference between the SNBCK model and the LBL model. This is a pure thermal radiation test case, where the fluid motion is neglected, to compare the radiative source term and wall heat flux against the literature reference [GOU00] for the Monte Carlo method.

In order to obtain the converged results from the Monte Carlo solver, the number of sampling bundles is defined to be up to 1000 for each control volume to reduce the statistical error. In the following discussion, the finite volume Monte Carlo method with LBL model is denoted as fvMCM-LBL, while the SNBCK model is specified as fvMCM-SNBCK. Fig. 4.15a is the radiative source term $-\nabla \cdot q_r$ at the x-central line, and Fig. 4.15b is the radiative wall heat flux on the bottom wall. There are

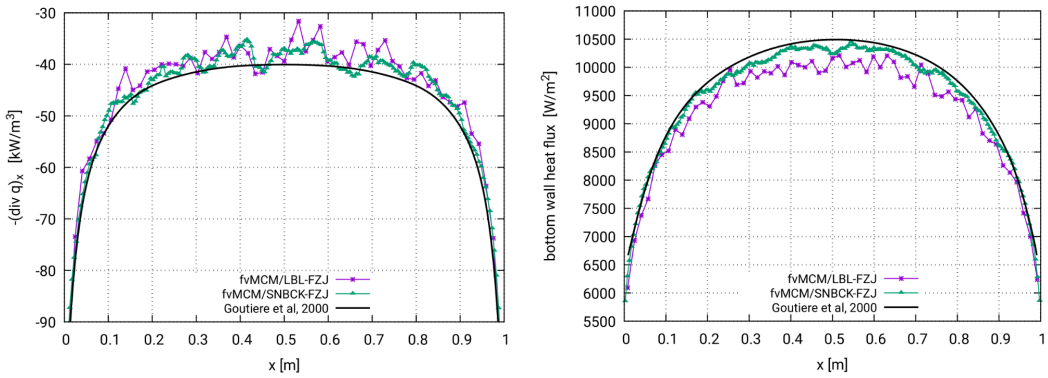

a) Radiative source term $-\nabla \cdot q_r$ **b)** Radiative wall heat flux q_r

Figure 4.15: Evolution of the radiative source term $-\nabla \cdot q_r$ and radiative heat flux q_r for the Goutiere's 2D case [GOU00]

numerical fluctuations for the Monte Carlo results. But the fvMCM-SNBCK and fvMCM-LBL results are in good agreement with the literature reference [GOU00]. The average relative error is less than 4% for the radiative source term $-\nabla \cdot q_r$ at the x-th central line in the fvMCM-SNBCK model. The maximum relative error is about 5% for the radiative wall heat flux on the bottom wall in the fvMCM-LBL

model. As shown in Fig. 4.15a, the radiative source term $-\nabla \cdot q_r$ from SNBCK and LBL models are smaller than the literature reference. As expected, the reference radiative wall heat flux is slightly larger than the LBL and SNBCK models. This is due to the difference between the HITRAN and HITEMP databases. The HITEMP database is applied in the literature reference [GOU00]; whereas the HITRAN database is employed in the developed Monte Carlo solver. It is interesting to note that the SNBCK model is closer to the literature reference. This is because the LBL absorption coefficient varies rapidly within a small spectral interval. Therefore, it is difficult to reduce the numerical fluctuation in the fvMCM-LBL model.

Besides, the average relative errors are also calculated using different energy bundles in the Monte Carlo method. The increase of cost is not directly proportional due to the parallel acceleration in Monte Carlo methods due to parallel acceleration. As shown in Table 4.3, the standard deviation decreases when increasing the number of bundles per cell in the Monte Carlo simulation. As expected, the

Table 4.3: Statistical error evaluation using the Monte Carlo method with LBL and SNBCK non-gray models for the Goutiere's 2D case [GOU00]: T = 1000 K, T_{wall} = 0 K, p = 1.0 atm, x_{H_2O} = 0.2 and x_{N_2} = 0.8

Bundles per cell	CPU (s)		Ave. $\nabla \cdot q_r$ relative error (%)	
	fvMCM-LBL	fvMCM-SNBCK	fvMCM-LBL	fvMCM-SNBCK
10	259.55	39.98	79.62%	65.31%
100	375.82	176.69	17.49%	14.01%
1000	2163.06	1211.21	5.23%	4.03%

fvMCM-LBL model is more time-consuming than the fvMCM-SNBCK model, since the energy bundle sampling procedure is a tedious task. After increasing the number of tracking bundles, the statistical error decreases slowly in both Monte Carlo methods. The statistical error must be reduced in a faster way as the convergence rate of Monte Carlo solvers is quite slow. Based on the above results, it is concluded that the newly developed Monte Carlo solvers with LBL and SNBCK non-gray gas models reveal good agreement with the literature reference.

4.3 Monte Carlo Variance Reduction Technique

As discussed in the previous section, a statistical error is introduced in the Monte Carlo radiation solver if the number of sampling bundles is not large enough. This statistical error results in a nonphysical temperature fluctuation. In order to obtain reasonable results, it is necessary to track a large number of bundles since the sta-

tistical error decreases with the square root of the number of photons/energy bundles. There is a variety of advanced variance reduction techniques for the Monte Carlo method in the literature [MOD13, TES02] to reduce the numerical fluctuations without increasing the number of photon bundles. Three variation reduction techniques are implemented for the Monte Carlo solver in *containmentFoam*: the global mesh method, the emission-based reciprocity Monte Carlo method, and the shifted Monte Carlo method. After these optimizations, the fluctuation of Monte Carlo method is not fully eliminated, but notably reduced. Consequently, the Monte Carlo solver in *containmentFoam* is rated as robust and efficient, and it can be integrated into CFD to perform complex 3D engineering calculations.

4.3.1 Shifted Monte Carlo Method

The difference between the emission cell temperature and the absorption cell temperature is relatively small (< 50 K) for natural convection flows. Therefore, it is hard to reduce the statistical error in engineering applications. The shifted Monte Carlo method proposed by Soucasse et al. [SOU13] can significantly reduce the number of photons to accelerate the computation time. The basic idea of shifted Monte Carlo method is to solve the shifted radiative transfer equation based on the local minimum temperature. The original radiative transfer equation without scattering effect is

$$\Omega \cdot \nabla I_\eta(r,\Omega) = -\kappa_\eta I_\eta(r,\Omega) + \kappa_\eta I_{b,\eta}(r,\Omega) \tag{4.50}$$

It is a linear partial differential equation. According to the linearity definition, if $I_\eta(r)$ is a solution for the radiative transfer equation, then $I_\eta(r)+C$ is also a solution (C is a constant value). In natural convection applications with small temperature differences, the radiative source term is difficult to quantify in the Monte Carlo method, since the exchange energy between two control volumes is pretty small. In order to increase the sampling efficiency, the shifted radiative transfer equation is built based on the local minimum temperature T_{min}. There is no thermal radiation contribution for the computational domain if this region has the local minimum temperature. This region can only absorb thermal radiation from other regions. If a constant black body emission $I_{b,\eta}(T_{min})$ is subtracted on both sides in Eq. 4.50, it becomes

$$\begin{aligned}\Omega \cdot \nabla[I_\eta(r,T,\Omega) - I_{b,\eta}(T_{min},\Omega)] = \\ -\kappa_\eta[I_\eta(r,T,\Omega) - I_{b,\eta}(T_{min})] + \kappa_\eta[I_{b,\eta}(r,T,\Omega) - I_{b,\eta}(T_{min},\Omega)]\end{aligned} \tag{4.51}$$

where T_{min} is the minimum temperature within the system. The shifted equilibrium intensity $i(r,\Omega)$ is defined as

$$i_\eta(r,\Omega) = I_\eta(r,T,\Omega) - I_{b,\eta}(T_{min},\Omega) \tag{4.52}$$

If the local temperature is equal to the minimum temperature T_{min}, the shifted total emission is also equal to zero (see Eq. 4.52). The original radiative transfer equation can be written into the shifted radiative transfer equation. In the shifted Monte Carlo method, the shifted radiative transfer equation is solved to increase the computational efficiency (see Eq. 4.53).

$$\Omega \cdot \nabla i_\eta(r,\Omega) = -\kappa_\eta i_\eta(r,\Omega) + \kappa_\eta i_{b,\eta}(r,\Omega) \tag{4.53}$$

As stated before, the radiative source term is related to the energy difference between emission and absorption. The shifted total emission for the control volume cell i is

$$Qe_i^{shifted} = 4\pi V_i \int_\eta \kappa_\eta(T_i,\, p,\, Y) i_{b,\eta}(T_i) d\eta \tag{4.54}$$

As shown in Eq. 4.54, the shifted total emission highlights the small temperature difference within the computational domain. The shifted Monte Carlo calculation procedure is similar to the normal Monte Carlo method. The radiative source term in the shifted Monte Carlo method can be evaluated using Eq. 4.55.

$$\nabla \cdot q_r^i = \frac{1}{V_i}\left[Qe_i^{shifted} - \sum_{k=1}^{N_{cell}+N_{face}} Qe_k^{shifted} \mathcal{F}_{k\to i} \right] \tag{4.55}$$

The shifted Monte Carlo increases the sampling efficiency, because only the energy difference $\int_\eta \int_{4\pi} \kappa_\eta [I_{b,\eta}(T,\, \Omega) - I_{b,\eta}(T_{min}, \Omega)] d\eta d\Omega$ is related to the radiative source term within the computational domain. In other words, the minimum temperature region cannot emit radiative energy to other regions. It is not necessary to sample the same amount of photons in the minimum temperature regions. Hence, the number of photons is fewer than the normal Monte Carlo method. Furthermore, the fluctuation of the shifted Monte Carlo rapidly diminishes when increasing the number of photons. The shifted Monte Carlo is suitable for natural convection flows making it applicable for technical scale analyses.

4.3.2 Emission Reciprocity Monte Carlo Method

During a postulated severe accident, there are huge amounts of steam in the containment building. The normal Monte Carlo is not so efficient in the optically thick media, since the mean free path of photon in the optically thick media is shorter than that in the optically thin media. Due to its efficiency, the emission-based reciprocity Monte Carlo (ERMC) method [TES02] has been implemented in *containmentFoam* radiation library. The ERMC method significantly improves the efficiency without increasing photon histories in the optically thick media. The key consideration of the ERMC method is the direct exchanged energy between two

control volumes within the computational domain. The radiative energy emitted from the control volume i and absorbed by the control volume j is defined as $P_{i\to j}$

$$P_{i\to j} = Qe_i \mathcal{F}_{i\to j} \tag{4.56}$$

where Qe_i is the total emission from the control volume i; $\mathcal{F}_{i\to j}$ is the view factor. Reversely, the energy emitted from the control volume j and absorbed by the control volume i is defined as $P_{j\to i}$

$$P_{j\to i} = Qe_j \mathcal{F}_{j\to i} \tag{4.57}$$

Then, the exchanged radiative energy between two cells is defined as $P^{ex}_{i,j}$

$$P^{ex}_{i\rightleftarrows j} = P_{i\to j} - P_{j\to i} \tag{4.58}$$

As discussed in section 4.2.2, a small number of sampling energy bundles may lead to a large difference between $\mathcal{F}_{i\to j}$ and $\mathcal{F}_{j\to i}$, especially for optically thick media. The normal Monte Carlo method becomes inefficient owing to the random distribution of solid angles in control volumes. If there is a energy bundle from the control volume i to the control volume j, it does not ensure that it has a similar energy bundle from the control volume j to the control volume i. This situation becomes worse by applying a fine computational grid in the Monte Carlo solver. In order to obtain reliable results from the Monte Carlo method, a significant amount of energy bundles are needed to be tracked to reduce the statistical error.

In the normal Monte Carlo method, the path from cell i to cell j maybe totally different from that one from cell j to cell i. This is the reason why the normal Monte Carlo method suffers from low efficiency in containment flows, since a huge number of sampling bundles are need to be tracked in the normal Monte Carlo method to reduce the statistical error. The basic concept of the ERMC method is the principle of reversibility of light. If there is a path from cell i to cell j, it must have a same reverse path from cell j to cell i (see Fig.4.16). In other words, it can virtually double the number of energy bundles in this algorithm. The strategy of ERMC method is to formulate a direct exchange energy between any two cells within the computational domain [TES02, MOD13]. The statistical error from the Monte Carlo method can be significantly reduced by introducing the deterministic formulation. It is found that the quasi-Monte Carlo can significantly improve the numerical efficiency [PAL19]. The exchanged energy $P^{ex}_{i\rightleftarrows j}$ between two cells can be approximated as [TES02]

$$\begin{aligned} P^{ex}_{i\rightleftarrows j} = & \int_0^\infty \kappa_\eta(T_i,p,Y)[I_{b,\eta}(T_j) - I_{b,\eta}(T_i)]\cdot \\ & \int_{V_i}\int_{4\pi}\sum_{path}\tau_\eta(path)[1-\exp(-\kappa_\eta(T_j,p,Y)s)]d\Omega\, dV_i\, d\eta \end{aligned} \tag{4.59}$$

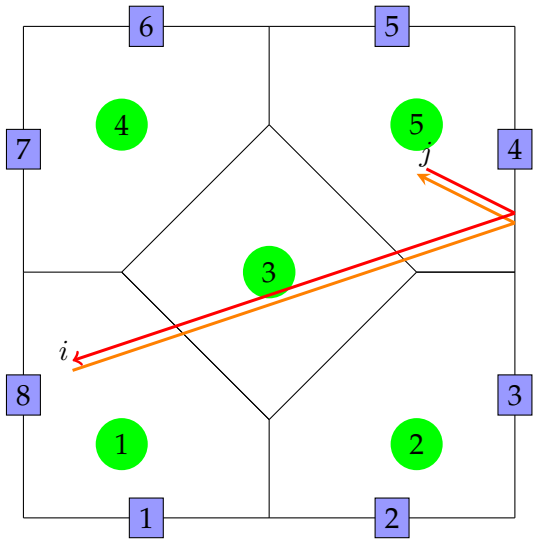

Figure 4.16: ERM reverse path, modified from [TES02]

where $\kappa_\eta(T_i, p, Y)$ is the spectral absorption coefficient in the control volume i; $I_{b,\eta}(T_j)$ is the black body emission intensity in the control volume j; $I_{b,\eta}(T_i)$ is the black body emission intensity in the control volume i; $\tau_\eta(path)$ is the spectral transmissivity along the path from the control volume i to the control volume j; $\kappa_\eta(T_j, p, Y)$ is the spectral absorption coefficient in the control volume j; $[1 - \exp(-\kappa_\eta(T_j, p, Y)s)]$ is the absorption energy within the control volume j.

In the ERMC method, the energy bundle sampling procedure is similar to the normal Monte Carlo. However, the absorbed energy is not accumulated in the ERMC method. The radiative source term in the ERMC method is based on the exchanged energy between two elements (see Eq. 4.60).

$$\nabla \cdot q_i = -\frac{1}{V_i}\left[\sum_{j=1, j\neq i}^{N_{cell}+N_{face}} P^{ex}_{i\rightleftarrows j}\right] \tag{4.60}$$

The implementation of the ERMC method applies a global mesh technique (see section 4.3.4) during the simulation, since the information about the emission source point is required to calculate the exchange energy $P^{ex}_{i\rightleftarrows j}$ [ZHA11]. According to Eq. 4.59, there is no energy exchange between two cells with the same temperature. Consequently, the temperature fluctuation due to the unconverged radiative source term can be eliminated in quasi-isothermal regions. The implementation of ERMC algorithm is also similar to the normal Monte Carlo method. However, the radiative source term is evaluated by the energy exchange between two control volumes. This method is superior to the shifted Monte Carlo algorithm.

4.3.3 Comparison of Different Monte Carlo Algorithms

In order to investigate the computational efficiency of different Monte Carlo methods, the behavior of three different Monte Carlo algorithms (Normal MC, Shifted MC and ERMC) with the same number of sampling photons is studied for a one-dimensional test case. Besides, the verification has been performed in 3D geometries to check the numerical stability. In this one-dimensional test case, the distance of two separate plates is 0.1 m with a mixture of gases composed of 20 vol.% H_2O and 80 vol.% of N_2 at 1 atm. The media temperature is 500 K and the two boundary walls are relatively cold (400 K). The number of cells in this one-dimensional test case is 100 with a uniform distribution. In the previous test cases, the surface emissivity is set as 1.0 to neglect the radiation contribution from boundary walls. However, most of boundary surfaces are not black in the containment building, e.g., steel surface and transparent window. The effect of non-black surfaces is considered in this test case, and the wall emissivity is set as 0.3 to model the highly reflective surface. It is noted that this is a pure thermal radiation test case without fluid motion. The purpose of this one-dimensional test is to verify and assess different Monte Carlo algorithms with real gas properties and reflective walls.

All Monte Carlo methods are applied the same non-gray gas database to minimize the numerical uncertainty, and the non-gray gas properties are treated in the SNBCK model. As discussed in the previous section, the Monte Carlo numerical accuracy depends on the number of photon bundles within the computational domain. In order to evaluate the statistical error for different Monte Carlo methods, 20 batches with 500 bundles in each cell per batch are considered in the Monte Carlo settings. Simulation results using different Monte Carlo algorithms are shown in Fig. 4.17 by comparing the radiative source term for this 1D test case. There is a visible numerical fluctuation for all Monte Carlo results in Fig. 4.17, even though the total number of sampling bundles is quite large to reduce the statistical error. There is no significant difference between those Monte Carlo methods. However, the numerical fluctuation of the normal Monte Carlo method is larger than other two advanced Monte Carlo methods. The shifted MC and ERMC mean results are comparable to the normal Monte Carlo method with the same number of sampling photons. This confirms that the two advanced Monte Carlo solvers are correctly implemented and the mathematical formulation is correct.

Furthermore, the relative error with the same sampling photons is illustrated in Fig. 4.18. When using the same photon bundles N in the Monte Carlo method, the relative error of the normal Monte Carlo method is about 3 times larger than that of the advanced Monte Carlo algorithms. It has a strong numerical deviation near the wall in the normal Monte Carlo method owing to the temperature gradient. As shown in Fig. 4.18, the range of standard deviation for the normal Monte Carlo

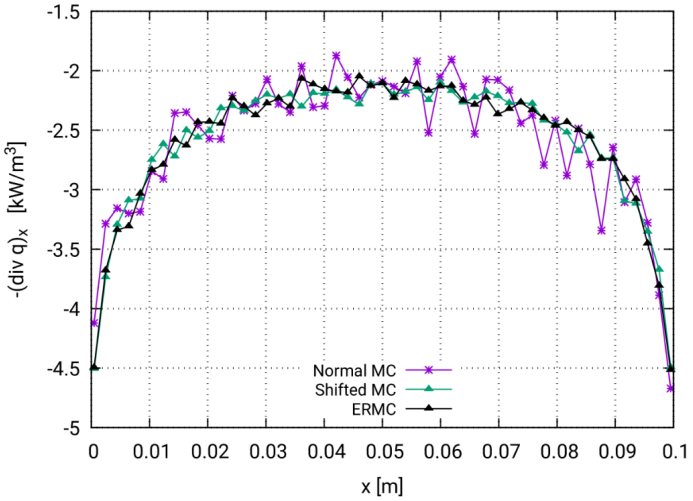

Figure 4.17: Radiative source term evaluation using different Monte Carlo methods: T = 500 K, p = 1.0 atm, x_{H_2O} = 0.2 , x_{N_2} = 0.8 and L = 0.1 m

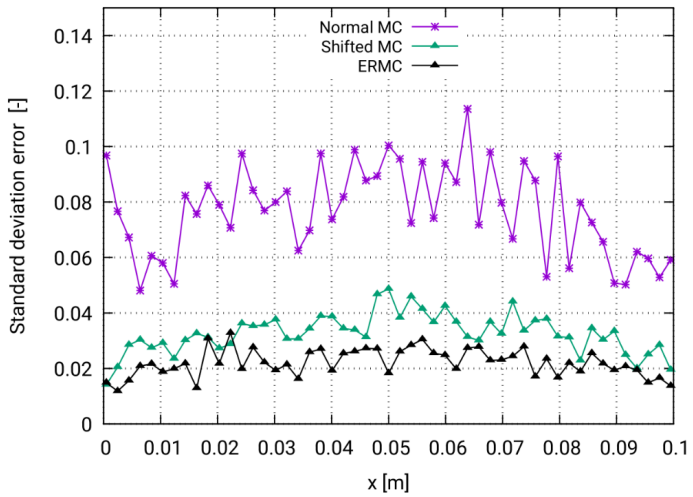

Figure 4.18: Relative error evaluation using different Monte Carlo methods: T = 500 K, p = 1.0 atm, x_{H_2O} = 0.2, x_{N_2} = 0.8 and L = 0.1 m

method is from 0.05 to 0.1. As a result, the radiative source term has a significant variation for the normal Monte Carlo method, leading to unreasonable predictions. However, the variation of standard deviation error for the shifted and ERMC methods are pretty small. The ERMC method is slightly better than the shifted Monte Carlo method. This is only a one-dimensional test case, and the numerical acceleration is more evident in 3D complex geometries.

4.3.4 Efficient Parallelization Implementation Using Global Mesh

The Monte Carlo method is computationally intensive in most applications even with the help of high performance computers. It tracks a large number of energy bundles through the computational domain in complex 3D geometries. As stated in the previous section, the Lagrangian particle tracking is the most time-consuming part. The most common particle tracking algorithm is typically carried out on constructive solid geometries [ROM15]. But the constructive solid geometry is only suitable for simple geometries. In order to resolve the complex geometries in CFD, OpenFOAM applies the barycentric coordinate tracking algorithm (see Appendix A). Each finite volume within the CFD mesh is subdivided into a number of tetrahedrons; in this way, the particle position is tracked within a tetrahedron. The advantage of the barycentric coordinate tracking is the use of unstructured meshes and flexibility of applications for the Lagrangian tracking in CFD simulations.

The Monte Carlo algorithm is parallelizable due to the independence of emission bundles. Thus, one of the characteristics of the Monte Carlo method is the parallel scalability to a large number of MPI processors. Generally the supercomputer is built on a number of computational nodes with a high-speed network. There are two ways to accelerate the Monte Carlo method: GPU [SIL19] and CPU [AND16]. However, the numerical implementation in GPU clusters is difficult due to the limitation of GPU memory. The Message-Passing-Interface (MPI) library is commonly applied in the distributed memory supercomputer system [GRO99]. In the parallel computing, a large engineering application is calculated in multiple processors, and all processors are connected through a high-speed network (see Fig. 4.19). In the master-slave parallel architecture, there is a master processor to manage a number of slave processors. The master processor equally distributes the computational task into the slave processors. After all slave processors finish the computational task, the master processor collects all simulation results together.

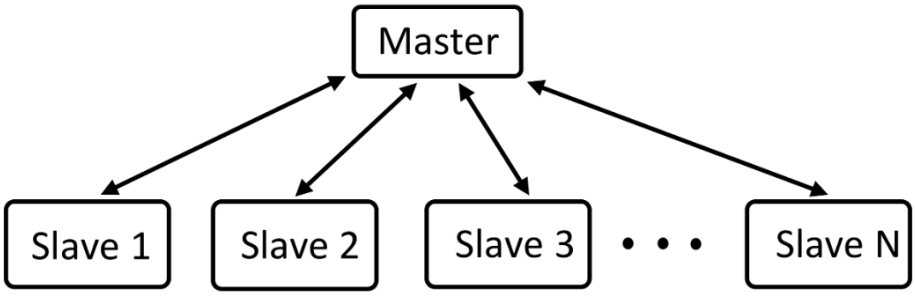

Figure 4.19: Master-slave parallel computing architecture

One of the main challenges for efficient parallel codes is the CPU load balancing in distributed memory message-passing supercomputers. It is necessary to minimize the MPI communication [BIS04] time and ensure equal load on all processors. The photon tracking module is based on the the Lagrangian library in OpenFOAM using the same CFD mesh. However, it becomes inefficient for the Monte Carlo photon tracking procedure due to the MPI communication. Basically a photon can travel through many mesh partitions per time step. If a huge number of photons are tracked along the decomposed meshes, the MPI communication time becomes intolerable [WHI18]. The photon information has to be transferred to the associated processor every time when it passes a processor boundary patch. The processor boundary patch is the boundary patch in the decomposed mesh for the CFD parallel computation. In order to reduce the MPI communication, Monte Carlo radiation transport is computed on the global mesh, while the number of photon histories is distributed among the slave processors.

As shown in Fig. 4.20, the example of PANDA facility test (used in Chapter 5 for validation) is partitioned into 4 different regions (4 MPI processors). Each proces-

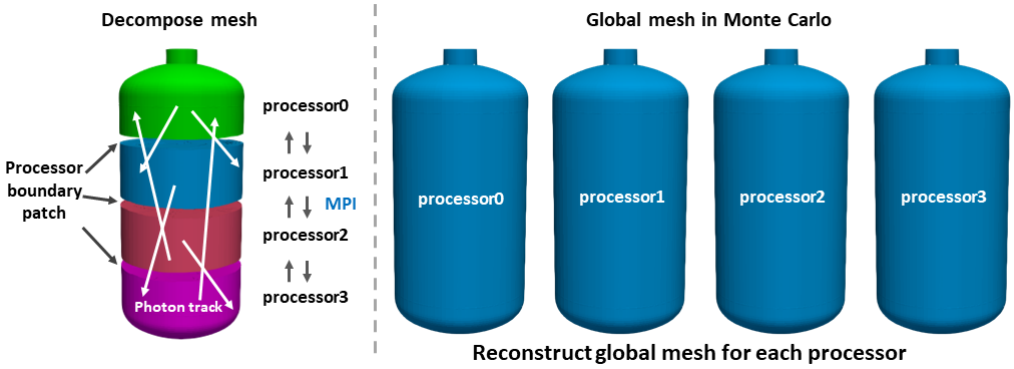

Figure 4.20: Monte Carlo global mesh algorithm

sor only stores a part of the fluid fields (left side of Fig. 4.20) in the decomposed mesh. Different processors exchange computational information on the processor boundary patch by MPI communication. For example, each processor samples a huge number of photons in Monte Carlo simulations. However, if a photon passes the processor boundary patch, it is necessary to perform the MPI communication between two processors to continue the photon tracking procedure. In such case, the photon tracking process is forced to stop for the MPI communication, and the program asks for the system resource to communicate with the associated processors (see Fig. 4.20). This MPI communication slows down the Monte Carlo simulations during the photon bundle tracking procedure. The original Lagrangian particle tracking algorithm in OpenFOAM is designed for the aerosol particle track-

ing. The motion velocity is relatively small for aerosol/soot particles. Most of the aerosols tend to move within a small distance during a CFD timestep. In contrast, the thermal radiation photon can propagate at the speed of light over a long distance within an integration time step. Therefore, a large number of photons need to be transmitted through the MPI communication. It is time consuming and inefficient to transfer the photon information among processors when tracking a large amount of photons.

In order to minimize the MPI communication time, the global mesh algorithm [EIB17] is implemented for the Monte Carlo thermal radiation solver in *containmentFoam* (see Algorithm 2). Before the Monte Carlo simulation, the global

Algorithm 2: Monte Carlo global mesh algorithm

reconstruct the global mesh in all processors;
send local T, p, Y to master processor;
construct global T, p, Y in master processor;
send global T, p, Y to slaves;
for *all processors* **do**
    sample thermal radiation photons;
    track thermal radiation photons on the global mesh;
end
wait for all processors finish the tracking procedure;
if *master processor* **then**
    gather all local $divQr$, q_r from slave processors;
    calculate global $divQr$, q_r;
    broadcast global $divQr$, q_r to slave processors;
else
    send local $divQr$, q_r to master processor;
end
update local $divQr$, q_r in slave processors;
update energy equation;

mesh is reconstructed in each processor (Fig. 4.20), while the number of photon histories is distributed among the slave processors. Since the temperature field is stored in the decomposed mesh, the global temperature T_{global}, pressure p_{global} and mass fraction Y_{global} fields are also reconstructed in the Monte Carlo solver for all processors. During the Lagrangian tracking procedure, there is no photon message transmission among the slave processors when applying the global mesh algorithm. In this way, there is no CPU imbalance within the slave processors. The radiative source term and wall heat flux are collected and calculated on the master processor. Finally, the radiative source terms are mapped into the decomposed mesh. However, this technique also has some drawbacks. Firstly, reconstructing

the global mesh for each processor increases the memory requirement. To track the energy bundle in the global mesh, a number of global fields, e.g. T, p and Y, are maintained by the Monte Carlo solver. If the global mesh size is too large, it is unfeasible to perform Monte Carlo simulation in this way. Furthermore, it is complex to handle two separate meshes in *containmentFoam*. The code implement becomes cumbersome when taking into account of the global mesh.

The OECD/NEA SETH-2 PANDA ST1 test [OEC12] is selected to demonstrate the efficiency of the global mesh algorithm. The PANDA is a large-scale and multi-compartment facility, which is designed for the containment safety assessment. There are two main vessels in the ST1 test case, each 4 m in diameter and 8 m in height with a total volume of 90 m^3. The detailed discussion about the ST1 experiment is given in section 5.3.1. This section mainly focuses on the computational efficiency comparison between the normal mesh and the global mesh in the Monte Carlo solver with the SNBCK model. The number of control volumes in the ST1 mesh is 782634 for this simulation. There are around 40 energy bundles for each cell in the PANDA ST1 test, and more than 30 millions of photons are tracked in the Monte Carlo solver. The computational times for updating the Monte Carlo solver with different MPI processors are given in Table 4.4. Without the help of

Table 4.4: Efficiency comparison between the normal mesh and the global mesh for the PANDA ST1 experiment

Num. processors	Normal mesh CPU (s)	Global mesh CPU (s)	Ratio (Normal/Global)
1	1547.93	1547.93	1
2	844.71	784.02	1.07
4	496.02	401.67	1.23
8	320.17	208.36	1.54
16	165.34	106.83	1.55
32	94.32	58.87	1.60
64	61.32	38.07	1.61

parallel computations, it requires around 1500 s to finish the particle tracking procedure in the Monte Carlo thermal radiation solver for the ST1 test case. It is clear that the computational time can be significantly reduced when increasing the number of MPI processors in the Monte Carlo radiation solver. However, the normal mesh method requires more MPI communication time in slave processors leading to a longer computational time. There is about a 50% efficiency increase for the global mesh compared to the normal mesh when increasing the number of processors. It only needs 38 seconds to update the radiative source term by using the global mesh, whereas the computational time for the normal mesh is 62 seconds. It is highly recommended to apply the global mesh method for engineering applications to efficiently utilize the computational resources.

4.4 Monte Carlo Solver Coupled into CFD

After the development of the Monte Carlo thermal radiation solver, the coupling between thermal radiation and fluid solver is investigated in this section. In CFD analysis temperature is the measure of the energy, which is a combination of three heat transfer phenomena: conduction, convection and thermal radiation. In *containmentFoam*, the total enthalpy h_{tot} equation is solved

$$\begin{aligned}\frac{\partial(\rho h_{tot})}{\partial t} \quad + \quad \nabla\cdot(\rho U h_{tot}) = \rho U\cdot g + \frac{\partial p}{\partial t} + \nabla\cdot\left[\left(\lambda + \frac{\rho c_p \nu_t}{Pr_t}\right)\nabla T\right] \\ + \sum_{i=1}^{n}\nabla\cdot\left[\rho h_i\left(D + \frac{\nu_t}{Sc_t}\right)\nabla Y_i\right] - \nabla\cdot q_r \end{aligned} \tag{4.61}$$

where U is the fluid velocity; p is the fluid pressure; g is the gravitational acceleration; Y_i is the i-th specie mass fraction; D is the molecular diffusion coefficient; ν_t is the kinematic viscosity; λ is the thermal conductivity; h_i is the i-th specie enthalpy.

As shown in Eq. 4.61, the radiative source term is just one of energy source terms in the energy equation. The fluid temperature is also related to conduction and convection heat transfer phenomena in containment flows. The nonlinearity of the combined thermal radiation and CFD may lead to a chaotic behavior. Consequently, a numerical iteration algorithm is necessary to simulate the coupled CFD-thermal radiation application until all fluid parameters have converged, e.g., U, T, and Y_i. In other words, it is expected to update the thermal radiation heat transfer at each CFD time step to resolve a strong interaction between turbulence and thermal radiation, e.g., in combustion applications [COE03]. However, this coupling algorithm is extremely time-consuming, which requires a huge amount of CPU time to update the thermal radiation solver. For containment flows, the thermal radiation solver is executed every $N-th$ fluid time steps owing to the fact that thermal radiation is not the dominant heat transfer mode in containment or natural convection flows. The turbulence fluctuation within a CFD time step in containment flows is not intensive compared to fire applications [LIU22b]. The local temperature deviation in containment flows is not as large as in combustion applications, and the radiative heat source can remain constant within $N-th$ CFD time steps. This algorithm is valid for slowly changing temperature and concentration fields in URANS analyses, especially for containment flows, and enables considerable saving of computational time.

The CFD and thermal radiation coupling algorithm is shown in Fig. 4.21. When solving the radiative transfer equation, the transient temperature T, total pressure p, and mass fractions Y are given to the Monte Carlo thermal radiation solver. The absorption coefficient is updated based on the fluid state, and the Monte Carlo photon tracking is performed. After finishing the thermal radiation calculation,

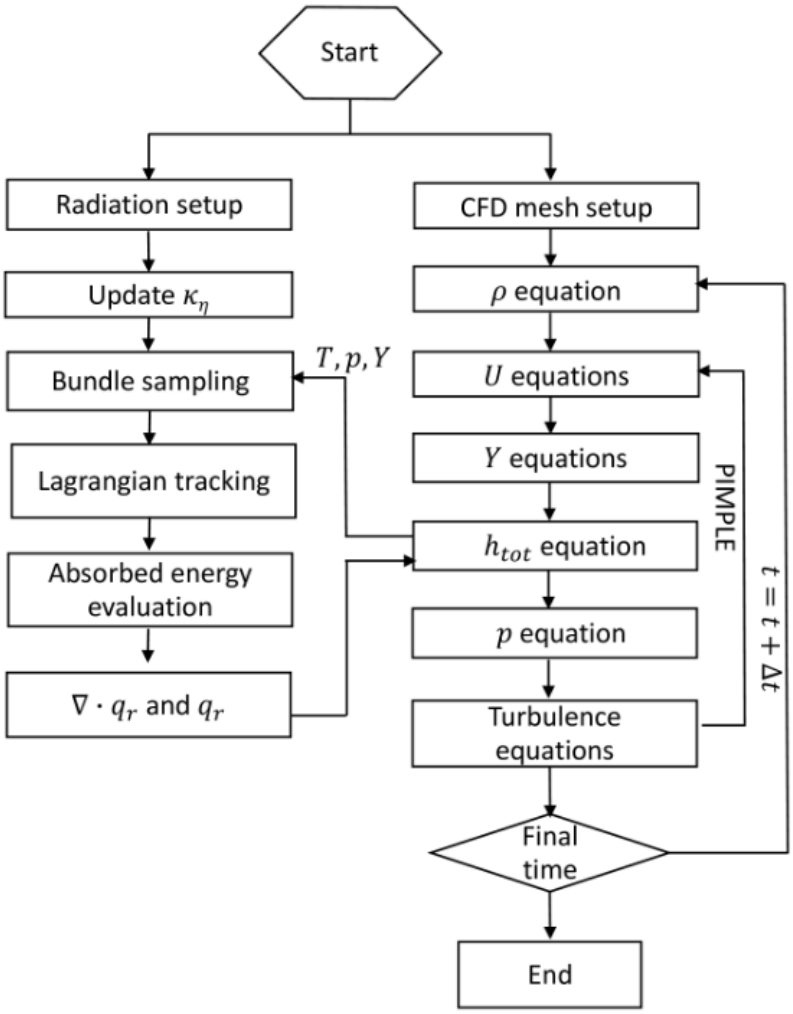

Figure 4.21: Monte Carlo and CFD coupling algorithm

the radiative source term is mapped into the CFD energy equation. In spite of all simplifications adopted for thermal radiation analyses, the coupling of thermal radiation with CFD is still expensive for engineering applications with a large computational mesh. In CFD modeling, the time step is relatively small following the best practice guideline (CFL < 1). If the thermal radiation is updated in each time step, it is computationally inefficient and requires a lot of CPU hours. Therefore, an updated frequency is defined by the user to solve the thermal radiation at every $N-th$ CFD time step if the flow dynamics allows it. In this thesis, thermal radiation is updated every 100 CFD timesteps (see Appendix B).

Since the radiative source term is an additional heat source term per control volume, the implicit source term technique is applied to coupled into the energy equation in CFD simulations [PAT18]. After numerical discretization for the energy equation, an algebraic equation at a typical point p for the total enthalpy h_p is constructed as shown in Eq. 4.62. The detailed discussion about the numerical discretisation for CFD method is given in section 2.2.2.

$$a_p h_p + \sum_{l}^{neighbour} a_l h_l = b + S'''_{rad} \tag{4.62}$$

where a_p is the linear coefficient for the control volume p; a_l are the linear coefficients for the neighboring control volumes l; b is the linear source term; S'''_{rad} is the additional radiation source term. If the radiation source term S'''_{rad} is considered as a linear source term in an explicit way, the total enthalpy at the control volume p is

$$h_p = \frac{b + S'''_{rad} - \sum_{l}^{neighbour} a_l h_l}{a_p} \tag{4.63}$$

A small fluctuation in the coefficient a_p can lead to a numerical divergence in Eq. 4.63. The numerical divergence becomes worse when the radiative source term S'''_{rad} is large. Therefore, the implicit scheme is recommended in the coupling of thermal radiation and fluid flow (see Eq. 4.64).

$$h_p = \frac{b - \sum_{l}^{neighbour} a_l h_l}{a_p + S_p}, \; S_p = -\frac{S'''_{rad}}{h_p} \tag{4.64}$$

The radiative source term is always negative in high temperature regions. In such a case, a positive coefficient S_p is obtained in Eq. 4.64. After applying this implicit scheme in the energy equation, it can significantly increase the numerical stability for the coupled thermal radiation and CFD simulations.

4.5 Summary of Model Development

In this thesis, two non-gray gas models (LBL and SNBCK) have been implemented in *containmentFoam* for containment flows. The HITRAN16 database is selected to calculate the absorption coefficient in the LBL model, whereas the SNBCK model is generated using the correlated-k distribution method. Both models can handle the molar fraction effect on the absorption coefficient for H_2O, and the band transmissivities calculated from the SNBCK model are well comparable with the reference. In order to solve the thermal radiation in high accuracy, the Monte Carlo thermal radiation solver with the spectral gas property is investigated. The advanced Monte

Carlo algorithm with LBL and SNBCK models is developed to solve the gas radiation heat transfer in containment flows. The Monte Carlo method is verified against the Goutiere's test [GOU00] in a 2D box geometry. The advanced Monte Carlo method is in good agreement with the reference, and the average relative error is less than 4%.

The limitation of the Monte Carlo method is the statistical error. In order to solve this problem, comprehensive efforts have been made to improve the computational efficiency. The first strategy is to apply advanced Monte Carlo algorithms: the shifted Monte Carlo method, and the ERMC method. It is concluded that the Monte Carlo numerical acceleration is significant when introducing a mathematical formulation in the Monte Carlo method. Furthermore, the global mesh algorithm can significantly reduce the MPI communication time. The last part of the chapter is about the coupling algorithm for the CFD/thermal radiation multi-physical simulation. Even though the advanced radiation solver is well implemented, the computational effort to update the radiative source term is still expensive. More investigation is required to clarify the complex interaction between CFD and thermal radiation in containment flows. Thus, owing to the nature of containment flows, an update frequency of the thermal radiation is only performed every $N - th$ CFD time steps. The implicit source term can improve the numerical stability. After the model development, validation against experiments is mandatory to quantify the complex interaction between thermal radiation and CFD. Theoretically, there is no simple conclusion for how the thermal radiation can affect the hydrogen mixing process in containment flows over a long term. The CFD and thermal radiation coupling is a nonlinear problem. If the thermal radiation is important, the simulation result becomes totally different when applying different radiation solvers/spectral gas properties. Therefore, it is necessary to apply an accurate thermal radiation solver in the containment safety analyses.

Chapter 5

First Validation and Discussion

This chapter is dedicated to the validation of thermal radiation solvers in *containmentFoam*. The difficulty for the radiation solver validation arises from the CFD uncertainty and numerical error, since the radiation is not the dominant heat transfer phenomenon in containment flows. The turbulent fluctuations are treated in a simplified manner in *containmentFoam*, e.g., $k-\epsilon$ and $k-\omega$ SST models. The turbulence model has a strong impact on the temperature prediction and mixing process. Therefore, the modeling strategy, mesh sensitivity and numerical setting are clearly outlined before discussing different thermal radiation models. In order to illustrate the thermal radiation effect, all CFD settings are similar except for the different thermal radiation models. The newly developed models are validated against two sets of experimental data: PANDA H2P2 and ST1 experiments.

Both experiments were conducted in the large scale thermal-hydraulic PANDA facility in Switzerland at the Paul Scherrer Institute (PSI). The PANDA facility is designed to investigate the containment safety behavior and related phenomena during postulated severe accidents, such as, spray system, hydrogen recombiner, hydrogen mixing and transport, and wall condensation. Moreover, the PANDA facility is equipped with CFD-grade instrumentation to provide a high resolution database for CFD and lumped-parameter codes validation and verification. The first set of validation experiments is the PANDA H2P2 test series, which is composed of gas compression experiments to investigate the thermal radiation effect in containment atmospheres and to enhance the understanding of steam absorption at different molar fractions, temperatures, and pressures. The helium is injected into an enclosed vessel to increase the atmosphere pressure and temperature. The gas radiation with different steam concentrations can affect the temperature distribution within the vessel. In the H2P2 test experiments, the convection heat transfer is weakened to highlight the thermal radiation heat transfer. Even though it is cou-

pled with convection flows, the H2P2 test series is designed to evaluate the effect of thermal radiation. In these experiments, thermal radiation does not affect the mixing process, but only changes the temperature field. Therefore, the experiments are suitable to validate the radiation solver including different non-gray gas models in *containmentFoam*.

The second set of experiments is the PANDA ST1 test series, which is composed of helium mixing with different momentum jets from low to high injection rates (30/60 g/s). The PANDA ST1 experiment series is conducted to investigate the influence of a low momentum vertical buoyant jet on the erosion of an initially helium-rich layer. Thermal radiation may affect the temperature field, changing the density field. The interaction between thermal radiation and fluid motion is difficult to quantify. Previous computational analyses in containment validation benchmarks have illustrated the possible role of thermal radiation in hydrogen mixing predictions [OEC07b]. Besides the comparison of temperature profiles from the experimental data, the transient helium concentration is another consideration in the validation procedure.

5.1 Validation Strategy

Based on the open-source CFD package OpenFOAM, *containmentFoam* is developed at Forschungszentrum Jülich for containment safety analysis related to the atmosphere mixing, pressurization, and condensation. Despite the substantial increase of computing capabilities, DNS and LES simulations are still computationally expensive for containment flows. Thus, an unsteady Reynolds Averaged Navier-Stokes (U-RANS) approach is applied in *containmentFoam* to save the computational power. The detailed discussion of the *containmentFoam* algorithms can be found in Chapter 2; the numerical models and boundary conditions are summarized in Table 5.1.

The fluid domain is solved by the Navier-Stokes equation with the buoyancy $k-\omega$ SST model, and the species equation is also considered in the fluid domain for the gas mixing process. Furthermore, the energy transfer due to the species diffusion effect is taken into account in the energy equation to avoid unphysical temperature results [KEL21]. The mixture density is computed according to the ideal gas equation in *containmentFoam*, and the specific heat capacity of the mixture is weighted by the corresponding species mass fractions Y_i. Since the development of flow is originated from the injection pipe, the CFD simulation results are highly sensitive to the inlet profiles, i.e., mass flow rate and temperature. Therefore, the inlet boundary conditions are given by the measured transient evolution of the mass flow rate, kinetic energy, and temperature. The turbulent kinetic energy and eddy frequency

are calculated assuming a turbulent intensity of $I = 5\%$ and eddy viscosity ratio of 10. The no-slip boundary is defined at all boundary walls. The fluid temperature and helium concentration are initialized according to the vertical temperature sensors and the vertical gas concentration sensors. The second order schemes are applied for the space and time discretization. For the CFD time step, the mean CFL number is less than 1.0, while a local maximum CFL number 5.0 is tolerated in simulations [AND08].

Table 5.1: Summary of the governing equations in *containmentFoam* simulations

Governing equations	$\partial\rho/\partial t + \nabla(\rho U) = 0$	Continuity equation
	$\partial(\rho U)/\partial t + \nabla(\rho UU) = -\nabla p + \nabla\tau + \rho g$	Momentum equation
	$\partial(\rho Y_i)/\partial t + \nabla\cdot(\rho UY_i) = \nabla(\rho D_{eff}\nabla Y_i)$	Species equation
	$\partial(\rho h)/\partial t + \nabla(\rho Uh) = \rho Ug + \partial p/\partial t + \nabla\cdot\lambda_{eff}\nabla T - \sum_{i=1}^{n} h_i\nabla J_i - \nabla\cdot q_r$	Energy equation
Explicit equations	$P_{k,b} = -\nu_t/\sigma_\rho(g\nabla\rho)$	Buoyancy production for k
	$\tau = \rho(\nu+\nu_t)\left[\nabla U + \nabla U^T - \frac{2}{3}\delta\nabla U\right]$	Reynolds stress
	$\rho = \frac{pM}{RT}$	Ideal gas equation
	$c_p = \sum_{i=1}^{n} c_{p,i}Y_i$	Mixture c_p
Boundary conditions	$\nabla U = 0$ $\nabla T = 0$ p_{outlet} : experiment data	Outlet
	$\dot{m}$: experiment data U and k : experiment data T : experiment data	Inlet
	$\nabla k = 0$ ω : omegaWallFunction T : Fixed value	No slip wall

Thermal radiation is included in the energy equation as an additional source term. The detection of radiative heat fluxes in a large-scale volume is technically impossible. Therefore, the temperature field is a characterization of the radiation heat transfer. Since thermal radiation is not the dominant heat transfer mode, a reliable and accurate CFD solver is vital for the radiation model validation. Several studies have shown that the relation between radiation and fluid motions in natural convection flows is complex, and the simulation results are related to different radiative property models and CFD numerical settings. In order to minimize the numerical error from different kinds of thermal radiation solvers, the Monte Carlo radiation solver is applied but with different non-gray gas models, e.g., LBL, SNBCK, WSGG and Gray gas. The main objective of this chapter is to assess different non-gray gas models in the containment flows. The LBL model is the baseline

model for spectral gas properties, while the SNBCK model is a compromise between accuracy and complexity. The WSGG and Gray models are two common gas models and widely applied in thermal radiation considerations. Furthermore, the impact of different non-gray gas models is highlighted by using the same Monte Carlo radiation solver. In this section, fvDOM and P1 solvers are not considered to avoid the numerical uncertainty from different kinds of radiation solvers.

5.2 PANDA H2P2 Test Series

5.2.1 H2P2 experimental setup

The setup of the PANDA H2P2 experiment is illustrated in Fig. 5.1, which is a gas compression experiment using one of the dry vessels in the original PANDA facility. On the left of Fig. 5.1 the x-axis is the horizontal line, while the y-axis is the height above the ground in millimeters. The injection pipe and the circular disk to disperse the jet momentum are shown on the right of Fig. 5.1. Before the H2P2 experiment, a helium stratification layer with a nominal helium content of $X_{He} \approx 50$ $vol.\%$ is built up above at the top of PANDA vessel (> 6.0 m). The helium profile along the height at the initial phase is shown by the sky-blue solid line on the left of Fig. 5.1. The vessel pressure is kept constant by the venting pipe at the bottom of vessel during the build-up of the helium layer. After the helium stratification layer is created, the initial conditions about fluid and wall temperatures, steam concentrations and initial pressure are measured by the sensing system to provide accurate conditions for numerical simulations.

The main procedure of the PANDA H2P2 experiment is the injection of helium from the man-hole of the vessel with a constant flow rate $\dot{m}$ = 10 g/s for about 1200 s [LIU22a]. At the same time, the venting pipe is closed to have the gas compression effect. The temperature and pressure are detected during the gas compression procedure. Consequently thermal radiation heat transfer can affect the temperature distribution during the gas compression phase. The injection from the top of vessel (see Fig. 5.1) is intentionally designed to weaken the convection heat transfer. A circular disk with a diameter of 800 mm was placed at the helium injection pipe to disperse the jet momentum without important convective flows resulting in a homogeneous gas compression [OEC21]. The initial 50 vol.% helium stratification is also important to reduce the buoyancy effect, and the complex interaction between injected helium and air in the bottom of PANDA vessel is avoided. Therefore, the 2D treatment of the respective numerical calculations can save computational time. In this thesis, two (out of five) H2P2 experiments with different initial temperatures and different steam contents are considered (see Table 5.2). The initial fluid

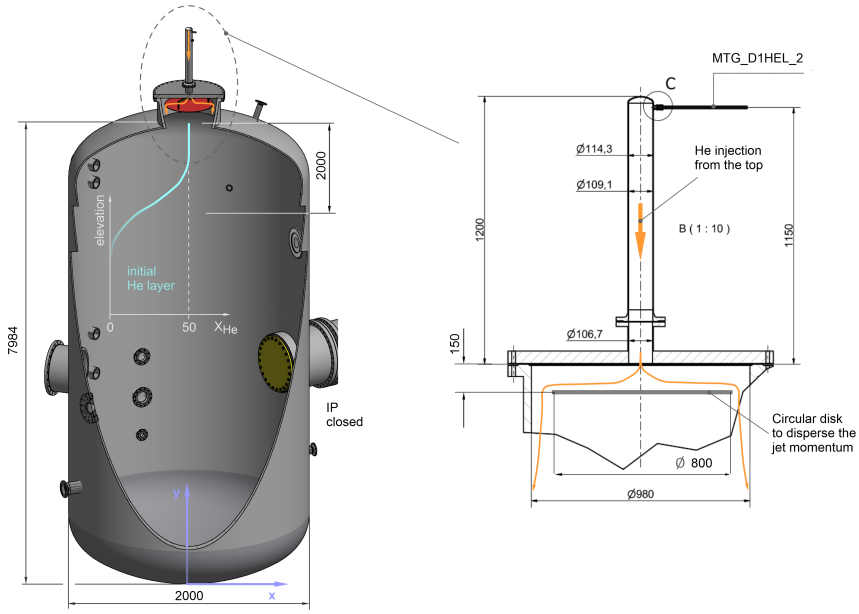

Figure 5.1: PANDA facility for H2P2 test series (dimensions in mm) [OEC21, KAP23]

temperature in the experiment H2P2_2_2 is about room temperature (T_r) with a low humidity ($2\,\%$). The other experiment H2P2_5 is more similar to accident con-

Table 5.2: Test matrix for the selected two H2P2 experiments

Experiment		H2P2_2_2	H2P2_5
Parameters	Units		
Initial temperature	K	T_r	T_{el}
Initial atmosphere		air	air
Steam/humidity	x_{steam}	**2**%	**60**%
Stratification	x_{He}	50	50
He mass flow	g/s	10	10
Compression time	s	1200	1200
Initial pressure	atm	1.0	1.0

ditions starting at an elevated temperature level T_{el} and has a high initial steam content of 60 vol.%. For the H2P2_5 experiment it is expected that the gas radiation plays an important role during the gas compression phase. Thus, the selected experiments comprise the low and high steam concentrations. To avoid steam condensation during the experiment, the PANDA facility is equipped with electrical heaters with a maximum power of 1.5 MW to prepare hot steam for the experiment preconditioning and to maintain the vessel temperature. Various sensing systems are installed in the PANDA facility to record the experiment data, such

as fluid and wall temperatures, pressure, injection temperature and rate, velocities and gas concentrations. For the temperature measurements, there are about 100 K-type thermocouples installed in the vessel to monitor the fluid temperature (see Fig. 5.2). A 2D contour plot can be generated based on these temperature sensors to validate different non-gray gas models. Additionally a number of thermocouples

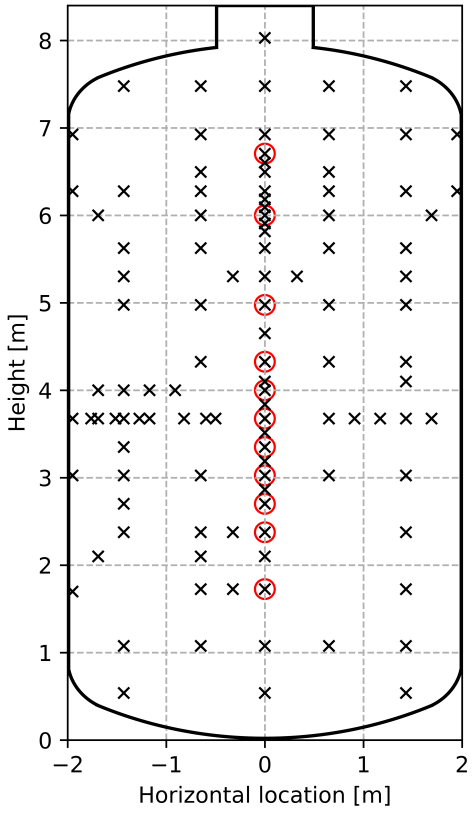

Figure 5.2: Sensor locations for H2P2 experiment, thermocouples are indicated by $\times$ and Helium mass spectrometer measurements by $\bigcirc$

are located on the wall to check the constant boundary temperature. The temperature data in the H2P2 facility are recorded at each second, providing a sufficient measurement dataset for the validation and development of radiation solvers. Furthermore, there are a number of concentration sampling capillaries at the central line for the gas concentration measurements (see Fig. 5.2). The uncertainties for the temperature, pressure and gas concentration sensors are about 0.8 K, 0.02 atm and 0.1 $\%$, respectively.

5.2.2 H2P2 CFD Setup

As stated before, the axis-symmetry of the 2D setup is applicable to the H2P2 analysis and the 2D wedge mesh with 15 degree angle is illustrated in Fig. 5.3 [LIU22a]. The mesh resolution is evenly distributed in the bulk and refined towards the vessel walls to resolve the wall shear stress [LIU22a]. The helium is injected through a central pipe line at the top and impinges into a baffle plate to disperse the initial momentum (see Fig. 5.3). Mesh quality has been optimized in terms of face

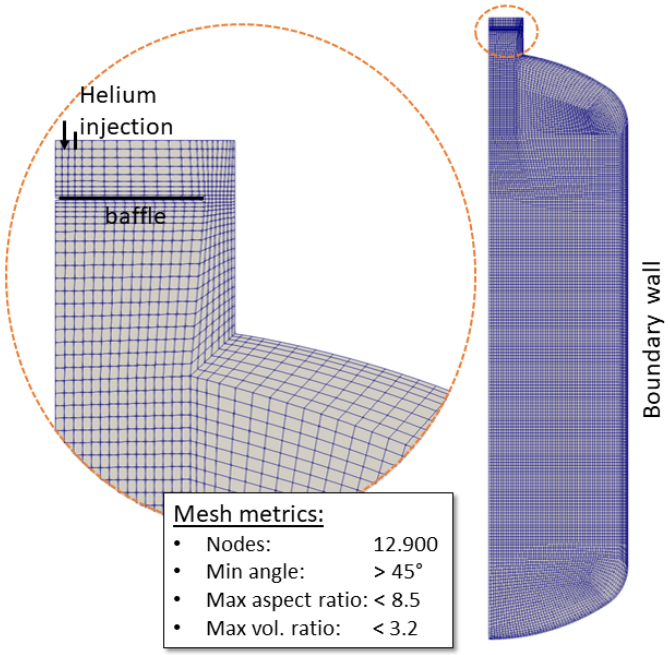

Figure 5.3: PANDA H2P2 2D wedge mesh with 15 degree angle

angle, aspect ratio and volume ratio. Those mesh parameters are well above the minimum quality recommended in the best practice guideline [AND08]. The baffle structure is considered in the CFD mesh which can significantly change the helium mixing process at the top of vessel (see Fig. 5.3). Preliminary, a simplified simulation without considering the baffle structure neglects the heat transfer between the hot structure walls and the injected cold helium resulting in wrong temperature predictions for the H2P2_5 experiment [LIU22a]. The injection region including the circular disk is resolved by the mesh grid in order to predict the helium mixing process. The other regions have a marginal impact on the mixing process. It is noted that some of the axis scales are not presented in the following figures to prevent the release of the experimental data.

For these two experiments H2P2_2_2 and H2P2_5, the helium is injected at room temperature (T_r) with a constant mass flow rate (10 g/s) via the vertical centered tube at the top of the vessel. For the H2P2_2_2 experiment, the initial fluid and wall temperatures are about the room temperature T_r; while the initial temperatures for the H2P2_5 experiment are about the elevated temperature T_{el}. The initial helium and H_2O concentrations inside the vessel are prescribed according to the measured vertical profile (see Fig. 5.2). The inlet boundary condition is given by the measured transient evolution of the helium mass flow rate and temperature. The gas radiation heat transfer is modeled by the Monte Carlo thermal radiation solver. The wall emissivity ϵ inside the vessel is defined as 0.3, which is measured by PSI for a dry steel sample in the relevant temperature range. The numerical models and boundary conditions are given in Table 5.1. The numerical schemes in *containmentFoam* are of second order order accuracy [KEL21]. The validation cases are run at time step of Δt = 0.005 s, which corresponds to a average CFL number less than one.

Before discussing the numerical setting about radiation solvers, the mesh uncertainty is evaluated by using three different grids. The coarsen mesh has 12446 hexahedra cells, and there is a 4 times increment (only x and y directions in the 2D mesh) for the medium and fine mesh grids. The total number of cells for the finest mesh is 191606. Table 5.3 describes the statistics of three different mesh grids for the H2P2_2_2 test case. The total amount of heat on the boundary wall (see Fig. 5.3)

Table 5.3: Mesh sensitivity study for the H2P2_2_2 experiment

Mesh	Number of grid cells	yPlus (ave.)	Boundary wall total heat flow rate (W)
Coarse	12446	4.75	246.02
Medium	47677	3.71	235.78
Fine	191606	0.29	234.24

is also given in Table 5.3 illustrating that the simulation results are reliable for the medium mesh grid. The total heat flux on the boundary wall is evaluated using the following equation, since there is no condensation in the validation experiment.

$$q''_{total} = q''_{sensible} + q''_{rad} = -\lambda_{eff} \frac{\partial T}{\partial x}\bigg|_{x=0} + q''_{rad} \tag{5.1}$$

where λ_{eff} is the effective heat conductivity; q''_{rad} is the radiative heat flux. The total heat flow rate $\sum q''_{total} A$ is the integration of heat flux on the boundary wall. In comparison with the medium and fine mesh grids, there is a larger total heat flow rate for the coarse mesh owing to numerical diffusion. But the medium and fine mesh grids are almost the same for the total heat flow rate. It is concluded that the medium mesh grid is suitable for engineering calculations. Gas radiation is

modeled by the Monte Carlo solver with different non-gray gas models. Between 40 and 80 photon histories are tracked per cell (~ 180000 in total) to calculate the radiative source term for every second in the coupled CFD and thermal radiation simulation. A number of CFD simulations with different Monte Carlo settings have been conducted to ensure the independence of parameter settings, e.g., radiation update frequency and number of photon histories. In the following section, only five of them are discussed to highlight the impact of certain modeling decisions. The impact of gas radiation is highlighted by neglecting thermal radiation (No rad); while the finite volume Monte Carlo results with LBL, SNBCK, WSGG and gray gas models are labeled as LBL, SNBCK, WSGG and Gray, respectively.

The general transient progression is illustrated with the example of the H2P2_2_2 case in Fig. 5.4. It is noted that thermal radiation heat transfer is combined with

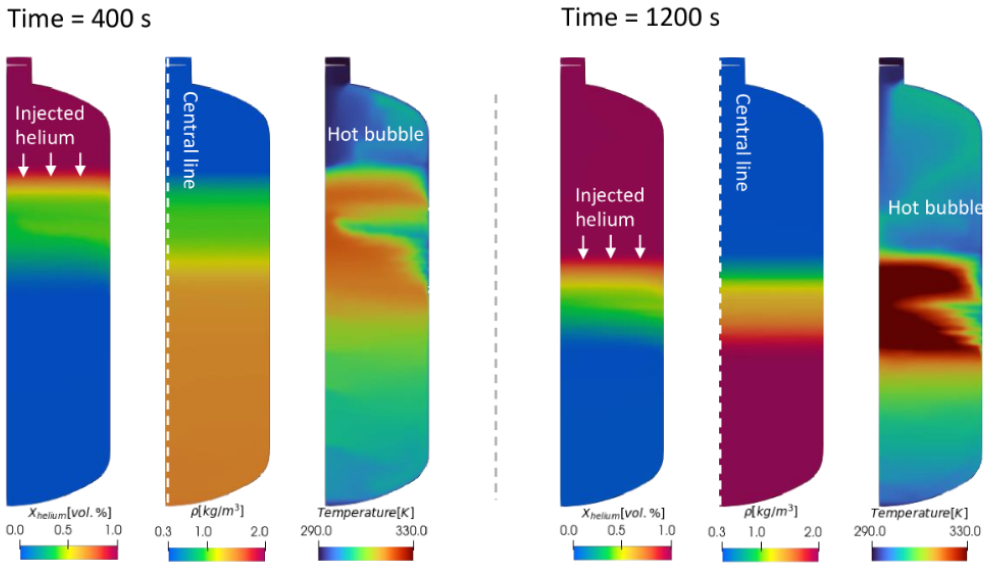

Figure 5.4: H2P2_2_2 test scenario: Time=400s (left), Time=1200s (right)

conduction and convection heat transfer, even though the conduction and convection are minimized in the H2P2 experiment. During the helium injection procedure, a nearly pure helium layer is created at the top of vessel, and the air/steam mixture media is compressed in the bottom of vessel (see Fig. 5.4). The gas compression leads to the formation of a hot gas bubble below the helium cloud and in the region of the helium concentration gradient. While the media temperature at the upper part is primarily governed by the injection temperature and the vessel walls, the temperature increase in the hot bubble is related to the mixture density ρ and the mixture heat capacity c_p.

5.2.3 H2P2 Results and Discussion

5.2.3.1 H2P2_2_2 Experiment

The pressure evolution serves as a first check of the heat and mass balance. As shown in Fig. 5.5, the pressurization is over-predicted by $< 5\%$ compared to the experiment for all simulation results at the end of the injection phase (1200 s). The small fluctuation of pressure in the experiment data is caused by the measurement uncertainties. It has around 0.02 atm uncertainty in the pressure measurement. In the early transient phase (< 150 s), there is a linear pressure increase for both simulation and experiment. After that, the experiment shows a slightly reduced pressurization rate, while all simulations cannot predict this scenario.

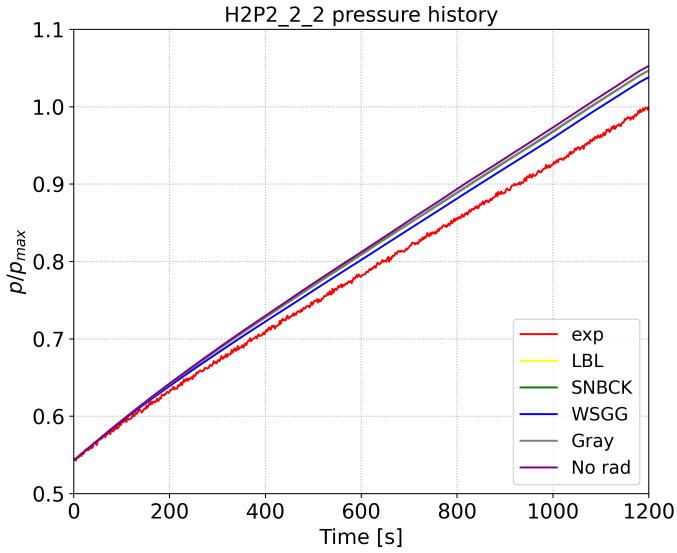

Figure 5.5: H2P2_2_2 evolution of the pressure history

The simulation case with the WSGG model gives the lowest pressure at the end of the injection phase, while the no radiation case gives the maximum pressure. The pressure prediction for the LBL and SNBCK models is in the middle (see Fig. 5.5). Other non-gray gas models give similar results in the pressure prediction. Obviously, the gas radiation heat transfer has a minor impact on the pressure in the H2P2_2_2 test case. The reasons for this discrepancy in the pressure level may originate from both the helium injection rate and the gas heat transport within the vessel. This over-prediction in the vessel pressure can also affect the prediction of the gas temperatures. These discrepancies in the pressure level require further analysis to minimize the numerical error from CFD codes.

To quantify the numerical error from different non-gray gas models, the relative error of the pressure $Error_p$ is calculated at the end of injection phase 1200 s (see Eq. 5.2) to evaluate the model differences.

$$Error_p = \left| \frac{p_{sim.} - p_{exp.}}{p_{exp.}} \right| \tag{5.2}$$

where $p_{sim.}$ is the simulation pressure; $p_{exp.}$ is the measured pressure in the experiment. The comparisons of relative error, maximum temperature and total heat flow rate at the end of the injection phase for different radiation models are given in Table 5.4. According to Table 5.4, there is a minor difference for the pressure error among different non-gray gas models, but the non-gray gas model has a strong impact on the maximum temperature evaluation. Without considering thermal radiation, the maximum simulation temperature at the end of injection phase is larger than that in the cases with thermal radiation. The simulation results using the SNBCK model are in good agreement with the LBL model. However, the WSGG model may overpredict the strength of gas radiation in the H2P2_2_2 test case. Therefore, the SNBCK model is reliable and efficient for the gas radiation heat transfer. It is concluded that thermal radiation heat transfer plays an important role on the temperature distribution in the H2P2_2_2 experiment.

Table 5.4: Summary of simulation results for the H2P2_2_2 at 1200 s

Model	$Error_p$	max $T_{sim.}(K)$	Boundary wall radiative heat flow rate (W)	Boundary wall total heat flow rate (W)	CPU (h)
LBL	4.02%	329.61	21.75	233.86	62.79
SNBCK	4.03%	329.94	22.25	229.84	53.24
WSGG	3.18%	314.72	65.57	239.16	54.45
Gray	4.07%	332.69	28.59	237.62	59.28
No rad	4.63%	340.88	-	234.59	40.83

Additionally, in all of these simulations, the radiative heat flow rates occupy only a small part on the total heat flow rate (around 10%). This is because the temperature difference between gas media and wall structure is modest. In comparison with the computational efficiency, as expected, the LBL model is the most expensive among those radiation settings. But the computational effort of LBL simulation is affordable if it is coupled with the Monte Carlo method. The behavior of computation efficiency is similar for other non-gray gas models. It is interesting to note that the simulation time of the SNBCK model is less than that of the Gray model. The Monte Carlo simulation time is related to the mean free path of photons. Under the gray gas assumption, a smaller absorption coefficient is expected in the Gray model. Therefore, it takes a longer time to track the energy bundles in the Gray model. Based on the simulation results, it is affordable to update the radiative source term for each second in the radiation/CFD multi-physics simulation.

As the radiative heat flux can not be measured directly, its effect is indirectly evaluated based on the measured gas temperature field. In order to evaluate the effect for different radiation models on the temperature field, the 2D temperature profile at 1200 s is shown in Fig. 5.6. It is noted that the temperature is normalized by a reference temperature T_{ref2} in H2P2_2_2. The experimental temperature contour is reconstructed using a number of thermocouple sensors (see Fig. 5.2). The

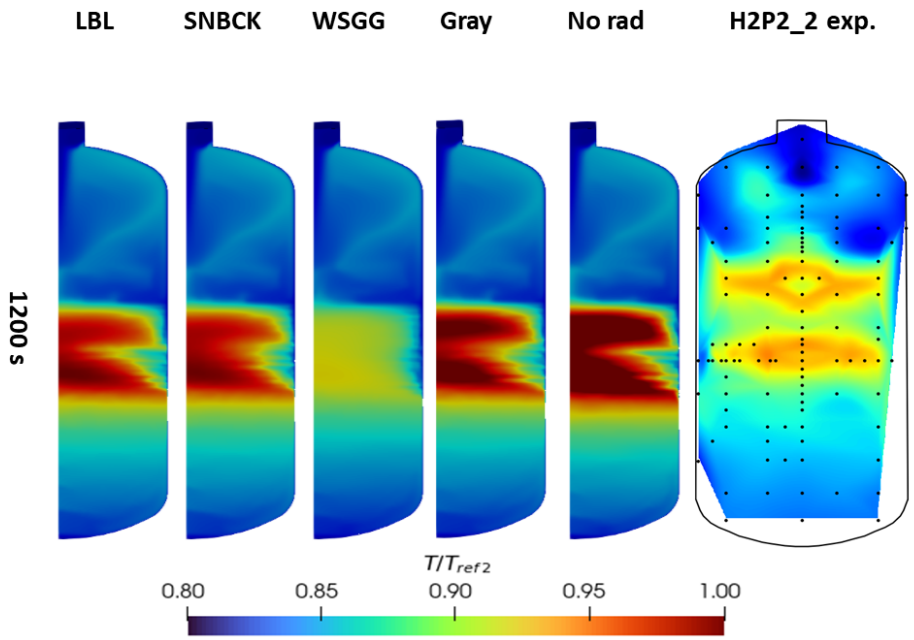

Figure 5.6: H2P2_2_2 2D temperature profile at the end of injection phase

experimental temperature contour is obtained by the interpolation of temperature sensors. Consequently, it has a numerical interpolation error in the temperature contour (see Fig. 5.6). Even though the H2P2_2_2 experiment has a small amount of steam within the vessel, thermal radiation effect is visible in the low-velocity flows. However, the smooth temperature decay above the hot bubble is related to thermal radiation heat transfer in low-velocity flows. Only thermal radiation heat transfer can redistribute the energy over a long distance. All simulation results give a lower hot bubble position than the experiment. The numerical uncertainty from CFD codes is difficult to eliminate for the thermal radiation validation and further investigation is needed to minimize the numerical uncertainty. There is a remarkable variance for the temperature at the center of PANDA vessel by using different non-gray gas models. The SNBCK and LBL models are consistent with the experiment. At the end of injection phase, the WSGG model significantly overpredicts the radiative heat transfer, leading to a homogeneous temperature profile in the hot

bubble region. As shown in Fig. 5.2, there are two separate hot bubbles in the experiment. However, there is only one hot bubble at the center in the WSGG model. The temperature field is completely different from the experiment data in the Gray and No rad models. The temperatures at the center for both models are larger than that in the other non-gray gas models.

According to Fig. 5.6, the temperature profile at the horizontal axis is nearly homogeneous. Therefore, the central temperature profile can represent the radiation heat transfer within the non-gray gas media and vessel structures. The temperature profile at the central line is given in the Fig. 5.7 at three different times: 400 s, 800 s and 1200 s. From Fig. 5.7, it is clear that the models considering the thermal radiation

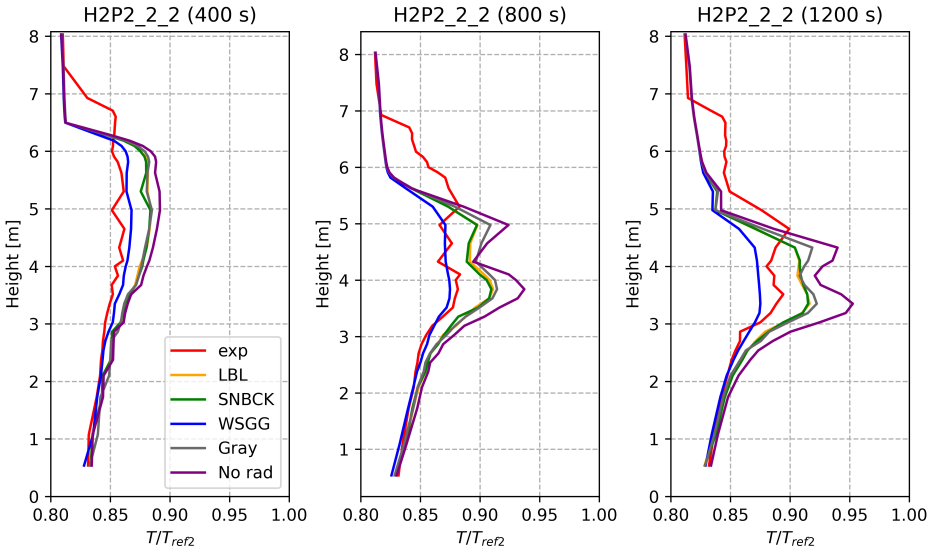

Figure 5.7: H2P2_2_2 evolution of temperature at the central line

model are consistent with the experiment data. If thermal radiation heat transfer is not included in the numerical modeling for the H2P2_2_2 experiment, it may lead to a hotter temperature profile at the central line which is far from the experiment (see Fig. 5.7). The SNBCK results are almost identical to the LBL results for the temperature prediction in the H2P2_2_2 experiment. It is concluded that the accuracy of SNBCK model is similar to the LBL reference model. However, there is a considerable difference between the LBL and WSGG cases, which is totally unexpected with a small steam concentration in the H2P2_2_2 experiment. Even though thermal radiation is not dominant heat transfer mode in the H2P2_2_2 experiment, it may have a strong impact on the temperature field after a long term operation. The temperature profile obtained from the WSGG model is smaller than the experiment data, whereas other non-gray gas models provide a hotter temperature field. If the

strength of gas radiation heat transfer is overestimated, there is a visible difference on the temperature distribution. It is noticed that the temperature difference can result in different density fields and thus has an impact on the hydrogen mixing in containment flows. The temperature difference between the no radiation simulation and the experiment is still far from satisfactory for H2P2_2_2. It is concluded that the LBL and SNBCK models are superior to other non-gray gas models. Besides these observations, the temperature field from 6.0 to 7.0 m in the H2P2_2_2 experiment is larger than the simulation. It has a number of flanges and supporting structures at the top of vessel (see Fig. 5.1), which may change the mixing process in the H2P2_2_2 experiment. These findings again may indicate uncertainties in the helium mixing at the top of the vessel and require further analysis.

The helium concentration histories along the central line for the simulations against the H2P2_2_2 helium measurements are shown in Fig. 5.8. The helium distribution is measured by 11 sampling lines along the central vessel axis in the PANDA facility, and the positions of helium sensors are depicted in Fig. 5.2. The injection of helium results in the formation of a nearly pure helium cloud in the upper volume of the facility, which continuously expands during the injection phase and compresses the initial gas mixture in the bottom of vessel [LIU22a]. Since the density of helium is lighter than the density of air, there is a steep helium gradient along the central line in the H2P2 experiments. Therefore, the numerical error from the discretization scheme can influence the accuracy of simulation results. Thermal radiation can affect the temperature, but the gas radiation is not strong enough to change the gas compression process, which is governed by the helium injection rate.

According to Fig. 5.8, all simulation results depict a large helium concentration in the helium/air interaction regions. For the H2P2_2_2 case, the five simulation cases are in reasonable agreement with the measured helium concentrations, but all of them depart from the measured gradient in the helium-air interaction region (see Fig. 5.8). In the late transient phase (800 s), the pure helium layer is formed at about 6 m height in all simulations, but the helium concentration measured by the experiment is about 75 vol.%. However, the helium difference between the simulation and the experiment is not significant at the end of injection phase (1200 s). In order to illustrate the deviation from the experiment data, the helium concentration difference between experiment and simulation $He_{exp.} - He_{sim.}$ is shown at the bottom of Fig. 5.8. There is no significant difference between LBL and SNBCK models for the helium prediction. The WSGG result shows the poorest helium prediction at the central line from 3.0 to 5.0 m among the non-gray gas models. It is concluded that the WSGG model is not suitable for gas radiation analysis with low steam concentrations. At the end of injection phase, the no radiation case gives a better prediction for the helium concentration. However, the temperature field in the no radiation case is worse than other non-gray gas models (see Fig. 5.7). The

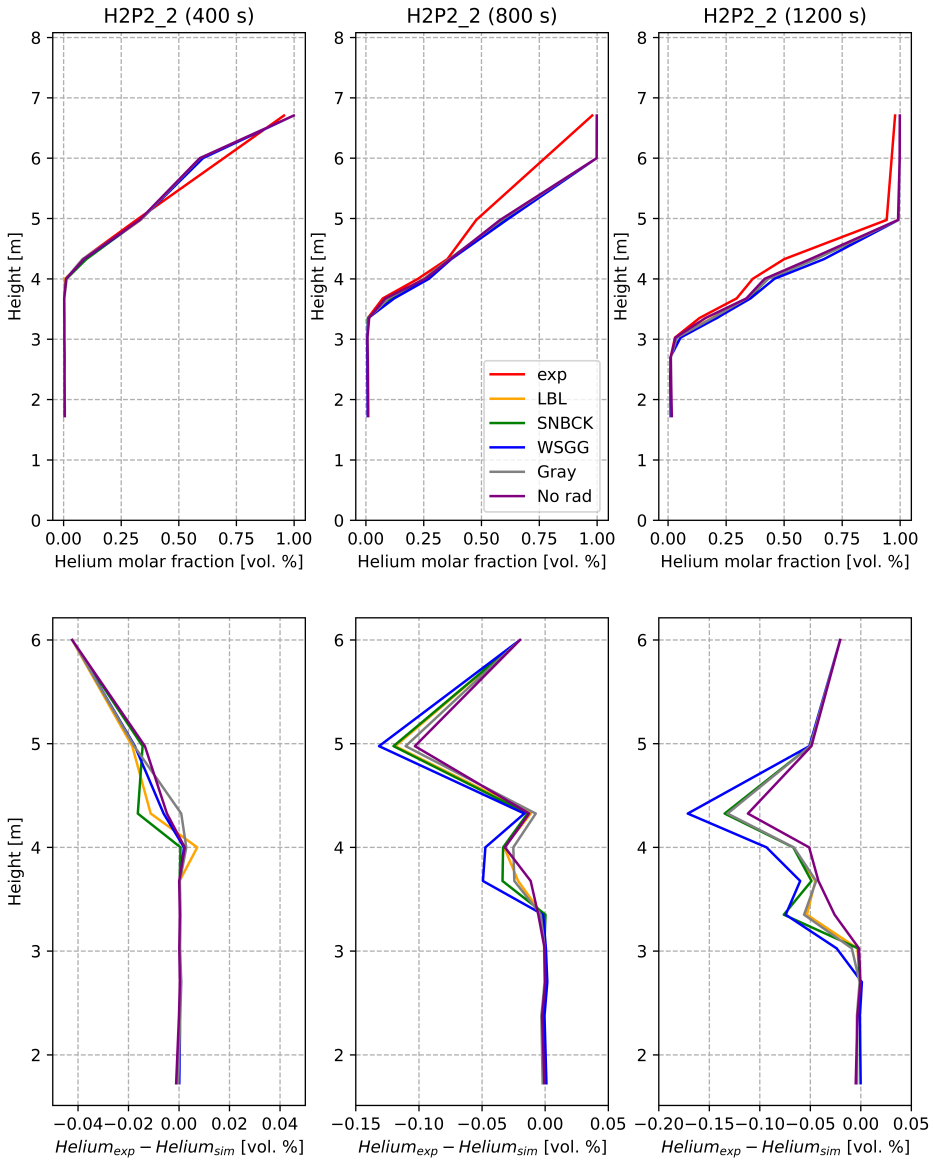

Figure 5.8: H2P2_2_2 evolution of helium concentration at the central line

gas radiation validation is related to the helium and temperature profiles, and the temperature field is more important than the helium concentration. The unacceptable helium deviation between simulation and experiment may originate from CFD code and experimental uncertainty. The experimental uncertainty from the helium measurement sensors requires more investigations.

5.2.3.2 H2P2_5 Experiment

For the H2P2_5 case, the initial steam concentration is around 60 vol.% at the evaluated temperature T_{el}. Therefore, the gas radiation plays an important role in the heat transport and temperature profile. As shown in Fig. 5.9, the pressurization for different radiation models is over-predicted by 7% compared to the experiment. Different from Fig. 5.5, the pressure deviation starts at the early beginning. In comparison with the experiment data, a steep pressure rise is unexpected for all simulations after 100 s in Fig. 5.5. This deviation can be explained by the numeri-

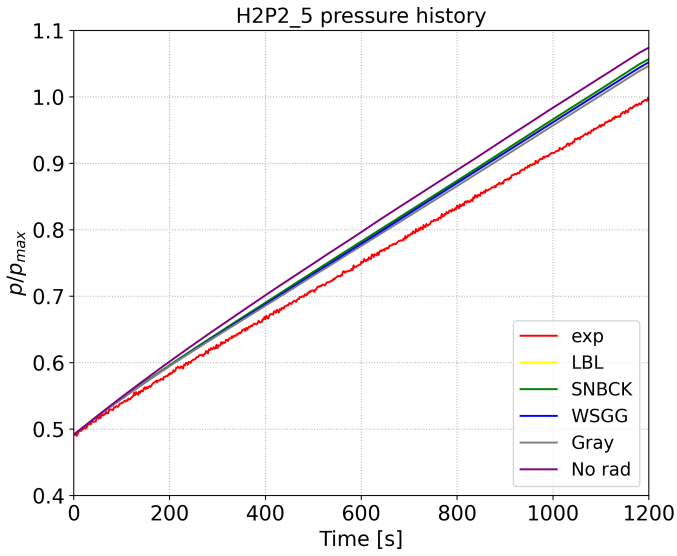

Figure 5.9: H2P2_5 evolution of the pressure history

cal uncertainty from the CFD solver, since the media temperature is still relatively small at that moment. When considering thermal radiation in the H2P2_5 experiment, the pressure increase in radiation cases is smaller owing to the smooth temperature distribution. However, the pressure difference between simulation and experiment is still unacceptable for the H2P2_5 test case.

The comparisons of relative error, maximum temperature and total heat flow rate on the vessel wall at the end of injection phase for the H2P2_5 experiment are given in Table 5.5. According to Table 5.5, the non-gray gas model has a strong impact on the pressure error and the maximum temperature. The maximum temperature is 452.28 K for the no radiation setting, while the maximum temperature in the LBL model (406.71 K) is much smaller than the no radiation setting. There is a minor difference in the maximum temperature for simulations when considering gas radiation. After considering thermal radiation heat transfer, the pressure predictions

are close to the measured pressure in the H2P2_5 experiment. It is evident that radiation heat transfer has an impact on the pressure prediction in high humidity environments. For the radiative heat flow rate on the boundary wall the SNBCK result is similar to the LBL model. In the WSGG and Gray models, the optically thin assumption over the whole spectrum can lead to a stronger radiation heat transfer between media and wall structures than other non-gray gas models. The total heat flow rates on the boundary wall in the WSGG and Gray models are smaller than the radiative heat flow rates. On the contrary, the total and radiative heat flow rates on the boundary wall in the LBL model are 124.39 W and 80.20 W, respectively. It is clear that the radiative heat flow rate has a big share of the total heat flow rate in simulations with thermal radiation modelings. The radiation heat transfer between media and wall structures can be intensified in the presence of large amounts of steam in containment flows. However, the total heat transfer between media and vessel structures is not as strong as the H2P2_2_2 experiment (see Table 5.4), since cold helium (room temperature) is injected into the vessel. The wall temperature in the H2P2_5 experiment is about the elevated temperature T_{el} to avoid bulk condensation in the H2P2_5 experiment. In comparison with the computational efficiency,

Table 5.5: Summary of simulation results for the H2P2_5 at 1200 s

Model	$Error_p$	max $T_{sim.}(K)$	Boundary wall radiative heat flow rate (W)	Boundary wall total heat flow rate (W)	CPU (h)
LBL	4.92%	406.71	80.20	124.39	121.24
SNBCK	4.95%	406.62	81.39	121.42	95.48
WSGG	4.43%	404.36	127.97	91.01	98.87
Gray	3.92%	405.95	148.61	54.75	93.15
No rad	6.67%	452.28	-	127.74	58.16

the simulation time for the LBL model is about two times larger than that of the no radiation setting. The LBL model takes more time to update the spectral gas properties in the presence of large amounts of steam in the H2P2_5 experiment. If the gas radiation is considered in the Monte Carlo solver, the computational increase in the simulation time is about 50% in the H2P2_5 experiment. According to these simulation results, it is still affordable to update the Monte Carlo solver at each second with large mounts of steam in containment flows.

As shown in Table 5.5, there is a minor difference for the maximum temperature in different non-gray gas models. In order to quantify the effect of gas radiation heat transfer on the temperature distribution for the H2P2_5 experiment, the 2D temperature profile for different radiation models at the end of injection phase (1200 s) is shown in Fig. 5.10. It is noted that the temperature is normalized by a reference temperature T_{ref5} in H2P2_5. Different from the H2P2_2_2 experiment, only one separate hot bubble is presented in the H2P2_5 experiment at the center of vessel due to large amounts of steam. Also the temperature increment in the H2P2_5 experiment is much smaller than in the H2P2_2_2 experiment. As shown in Fig. 5.10,

the gas radiation model has a striking impact on the temperature prediction in all simulations. All simulations illustrate a lower hot bubble position in comparison with the experiment data. Even though the SNBCK result is in agreement with the LBL model, it has a small numerical fluctuation in Fig. 5.10 due to the statistical error. Simulations with the SNBCK and LBL models are comparable with the experiment. Both models can predict the smooth temperature variation at the center of vessel, which is consistent with the experiment data. This scenario can not be given by the other non-gray gas model in the H2P2_5 experiment (see Fig. 5.10). Glob-

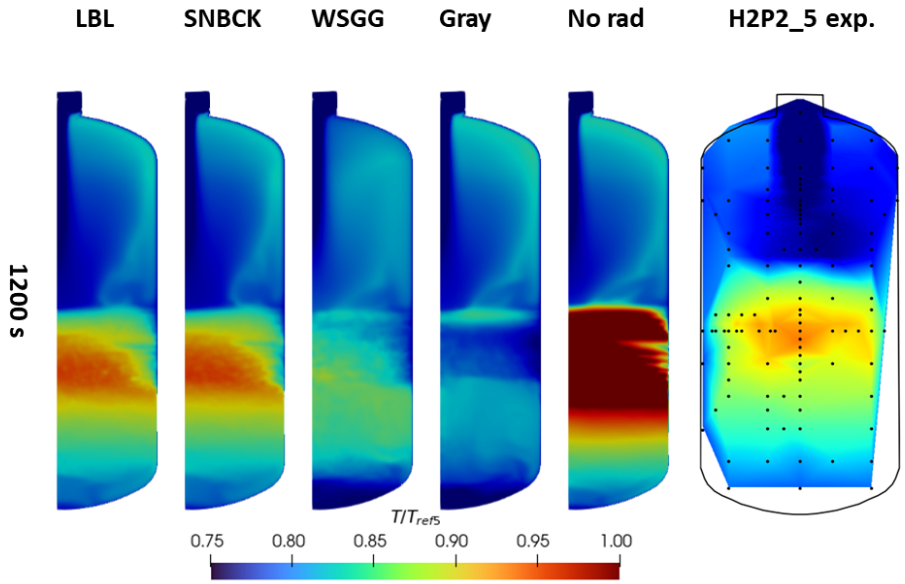

Figure 5.10: H2P2_5 2D temperature profile at the end of injection phase

ally the Gray and WSGG models are completely different from the SNBCK model in the temperature distribution. The hot bubble cannot be evaluated in the Gray and WSGG models owing to the optically thin approximation over the infrared radiation spectrum. The heat transfer between media and structure is weakened in the Gray and WSGG models owing to the homogeneous temperature profile. This is the reason why the total heat flow rate is smaller than the radiative heat flow rate (see Table 5.5). The strength of thermal radiation heat transfer is intensified in the Gray and WSGG models leading to a homogeneous temperature profile in the H2P2_5 test case with high humidity. Therefore, the Gray and WSGG models are not suitable for thermal radiation analyses with high steam concentrations in containment flows. Last but not least, the no radiation setting leads to a large hot bubble at the center giving a poor prediction. It is concluded that different non-gray gas models have a strong effect on the temperature field within the whole system in the H2P2_5 experiment.

In order to quantity different non-gray gas models in radiation heat transfer in the experiment H2P2_5, the temperature profiles at the central line are shown in Fig. 5.11. It is interesting to note that the measured temperatures are larger than all simulation results from 6.0 to 8.0 m at all time steps. The turbulence mixing at the top of vessel plays a vital role in temperature evolution. As shown in Fig. 5.3, the distance between baffle and helium injection pipe is short enough to have turbulence vortexes. It is required to improve the accuracy of standard $k-\omega$ turbulence models in the complex geometries, especially the wall boundary condition for a vertical plate. For the temperature profile at the central line, the SNBCK result is in good agreement with the LBL model and experiment data under the high steam concentration. But the highest temperature point is not well predicted in both models. Globally, the LBL and SNBCK results are reliable to demonstrate the heat transfer mode in the H2P2 experiments.

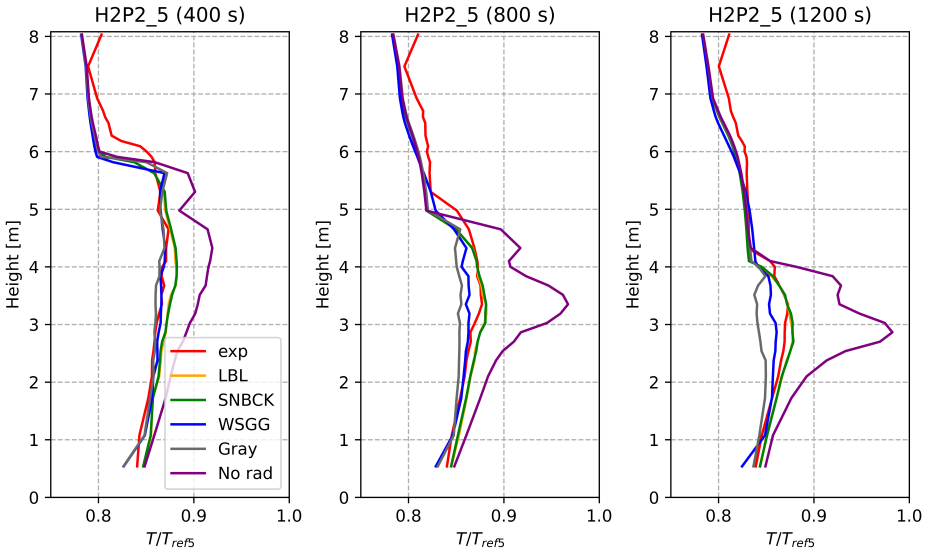

Figure 5.11: H2P2_5 evolution of temperature at the central line

Therefore, the SNBCK and LBL models are reliable in high steam concentration environments. The smallest temperature prediction is shown in the Gray model, and the gray gas assumption can lead to a homogeneous temperature profile in high steam concentrations. The WSGG results are superior to the Gray model; however, the temperature is still underestimated in comparison with the experiment. In summary, a consistent temperature profile is obtained when applying gas radiation model in the simulations. The no radiation case has two separate hot bubbles in the bottom of vessel which is far from the experiment data. The temperature difference becomes very large by neglecting thermal radiation.

The helium concentration is also measured by 11 sampling lines along the central vessel axis in the H2P2_5 experiment, and the transient helium evolution along the height is depicted in Fig. 5.12. The results of the helium distribution in all simula-

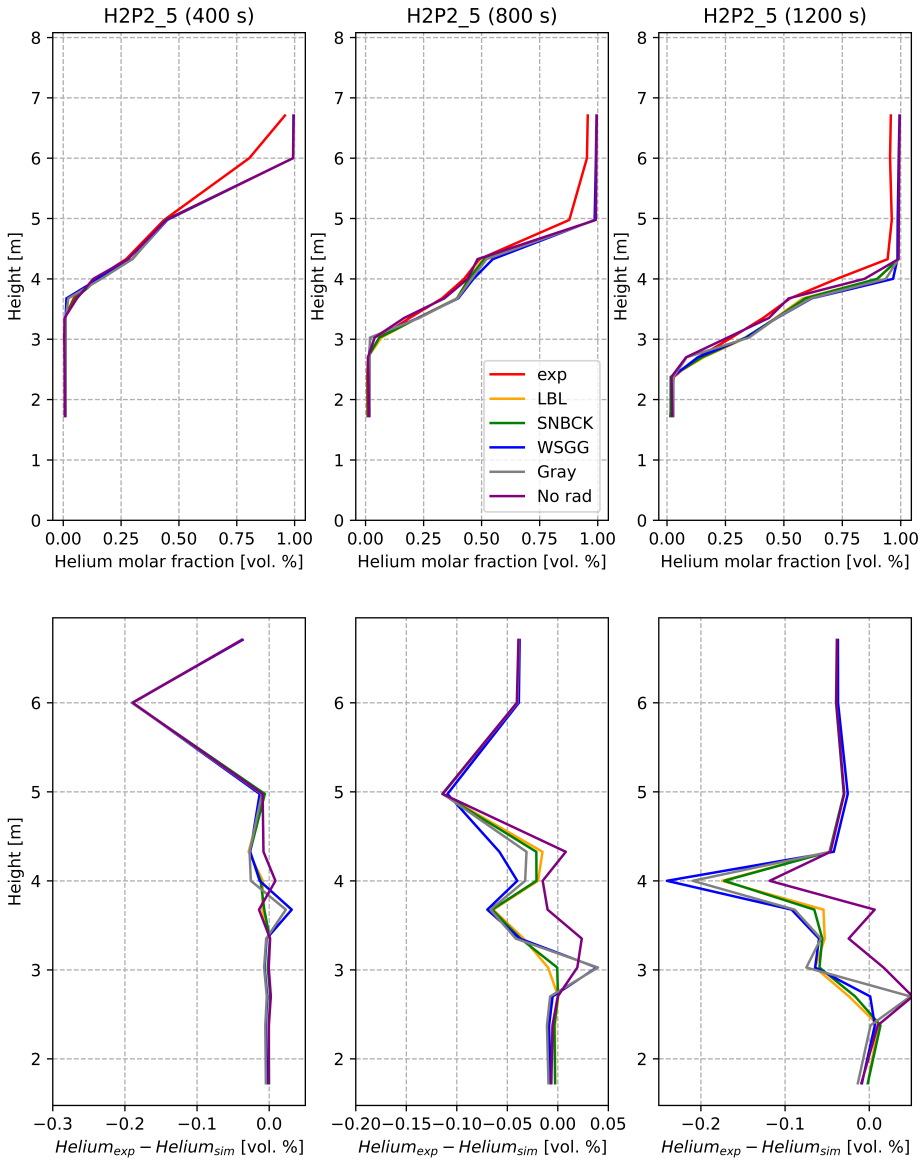

Figure 5.12: H2P2_5 evolution of helium concentration at the central line

tion cases are generally comparable to the H2P2_5 experiment. All simulations give a pure helium concentration at the top of vessel; however, the measured helium concentration is about 97% at the end of the compression phase. There is an overestimation for the helium profile at an earlier time in 5.12, which is also observed

in the H2P2_2_2 experiment. Because of huge amounts of steam in the H2P2_5, the atmosphere density is lighter than that of H2P2_2_2 and a smaller buoyancy force is expected after the helium injection. From the measured helium profiles, the gradient of helium concentration is relatively smooth in the interface region between helium cloud and air atmosphere in the bottom. However, a steeper helium concentration gradient is obtained in all simulations. This may be related to the buoyancy force and additional turbulence mixing in the H2P2_5 experiment. Furthermore, all simulations results give reasonable prediction in the interface region between helium cloud and air atmosphere at the bottom of vessel. The biggest deviation between the calculation and experiment is given for the WSGG model. Even though the no radiation case has a superior prediction in the helium profile, the temperature is remarkably overestimated in the no radiation case. According to the ideal gas equation, the mixture density ρ is calculated with the ideal gas equation $\rho = \frac{pM}{RT}$. Since the temperature prediction in the no radiation is larger than other non-gray gas models, a smaller density field ρ is expected in the no radiation case. Therefore, there is a reduced helium concentration in the no radiation case due to the buoyancy effect. It is concluded that the numerical error from CFD codes must be minimized in the H2P2 experiments.

5.2.4 Summary of H2P2 Test Series

In the frame of the OECD/NEA HYMERES-2 project, the H2P2 test series are conducted in the large-scale thermal-hydraulics PANDA facility. These experiments can be considered as separate effect tests for thermal radiation modeling. They comprise the compression of a gas mixture in the closed vessel, while its initial composition, temperature and pressure levels are varied. In this section work, two of these experiments (H2P2_2_2 and H2P2_5) are analyzed to assess and validate the integration and coupled performance of the CFD and Monte Carlo thermal radiation solvers in *containmentFoam*. Globally, the simulations with thermal radiation yield a comparable temperature field prediction in the H2P2 experiment validation. Even though there is a small amount of steam in the H2P2_2_2 experiment, gas radiation still plays a role in heat transfer processes over a long term. Without considering thermal radiation, the temperature is visibly overestimated, and the maximum temperature difference is about 60 K between the SNBCK model and the no radiation setting in the H2P2_5 experiment. This modeling error can affect the water/steam balance in containment applications and thus needs to be considered carefully. Furthermore, the no radiation case exhibits two temperature peaks at the center of PANDA vessel, which do not occur in the H2P2_5 experiment. The gray and WSGG models, which apply the optically thin approximation, can amplify the strength of gas radiation heat transfer in the presence of large amounts of steam in the H2P2_5 experiment. The simulation results using the Monte Carlo

method with SNBCK and LBL are in good agreement with the H2P2 experimental data. These results prove the validity of the Monte Carlo solver and non-gray gas models at least qualitatively [LIU22a]. The H2P2_2_2 and H2P2_5 results demonstrate that the newly developed Monte Carlo method with SNBCK and LBL models can provide an accurate thermal radiation prediction for low and high steam mixtures in low temperature applications, especially for containment flows.

However, there are visible deviations between CFD simulation and experimental data, which are not related to radiation modeling. It is noted that only the test and experimental data available at the time of writing the thesis could be used for validation. Recently a repetition of the tests was performed in the Japanese CIGMA facility [HAM23]. The remaining deviations observed for the temperature and pressure and in particular the unexpected influence of the treatment of helium molecular mass diffusion requires further investigations. This work motivated ongoing investigations to clarify the effect of pressure, temperature and helium concentration in the gas mixture during the injection procedure [KAP23] within the OECD/NEA PANDA project. In case new insights are obtained within the project discussions and new experiments, the validation should be repeated.

Furthermore, the computation efficiency of the Monte Carlo solver with different non-gray gas models are also evaluated in this section. The statistical error originated from the Monte Carlo method is significantly reduced after implementing advanced Monte Carlo algorithms in *containmentFoam*, which makes it affordable to couple with CFD codes. When considering the non-gray gas radiation in the Monte Carlo method, it may double the simulation time in comparison to the unphysical no radiation setting. According to the computation times in Tables 5.4 and 5.5, it is concluded that the Monte Carlo computational efficiency is not particularly related to non-gray gas models. This is a big advantage of Monte Carlo method as the most time consuming part in the Monte Carlo solver is the photon tracking procedure, not the complex spectral gas properties treatment. The thermal radiation separate effect is qualitatively validated in the H2P2 experiment and once again confirms the consistent implementation and physical validity of the model and solver. In the containment flows, the temperature field can significantly change with unsuitable non-gray gas models. The inaccurate temperature prediction may lead to an unreasonable density field in natural convection flows which has a strong impact on the hydrogen mixing in containment flows. The interaction between hydrogen mixing and thermal radiation in containment flows needs to be further investigated. The interaction between thermal radiation and hydrogen mixing process is a complex issue. Since thermal radiation is not the dominant heat transfer mode in containment flows, whether thermal radiation affects the mixing depends on the relative strength of conduction and convection. In the next section, the PANDA ST1 experiment test series are analyzed to quantify this complex interaction.

5.3 PANDA ST1 Test Series

5.3.1 ST1 Experimental Setup

The OECD/NEA SETH-2 PANDA ST1 experiments [OEC13] are conducted to investigate the interaction of a low momentum jet with an initially helium-rich layer. In this thesis, two ST1 experiments with different steam injection flow rates (30/60 g/s) are considered to validate the Monte Carlo thermal radiation solver. These experiments are performed at PSI in the PANDA vessel, which is a large-scale and multi-compartment facility. There are two main vessels in the PANDA facility, as shown in Fig. 5.13. Each cylindrical vessel is about 4 m in diameter and 8 m in height with a total volume of 90 m^3. Vessel 1 and 2 are connected by a large bent interconnecting pipe (1 m diameter) in Fig. 5.13.

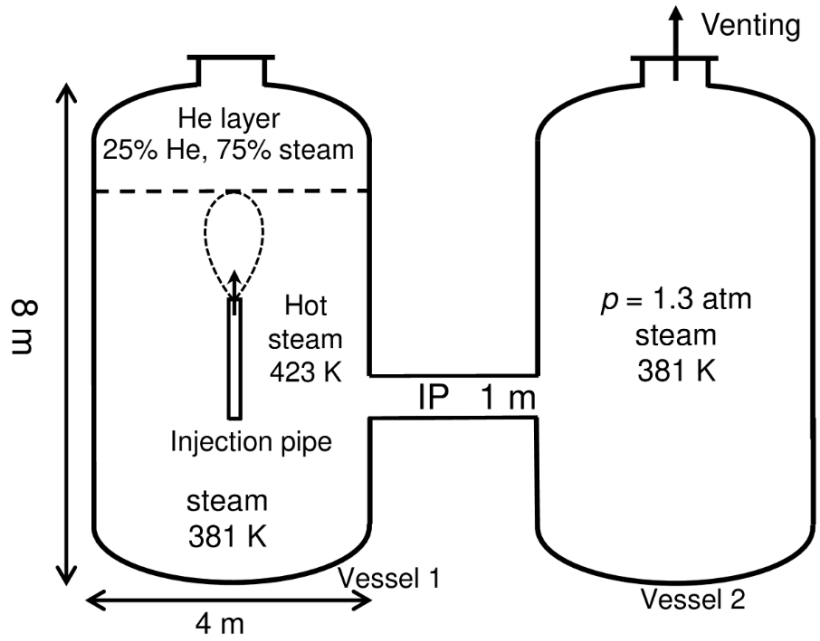

Figure 5.13: PANDA ST1 experiment, modified from [OEC13]

The precondition of ST1 test series is depicted in Figure 5.14. At the experiment preparation procedure for the ST1 experiment series, both vessels are filled with 100 vol.% saturated steam at 381 K under 1.3 atm conditions to avoid steam condensation. The following step of the ST1 experiment is to create a helium-rich layer (~ 20%) of approximate 2.0 m height by a horizontal helium jet. During this procedure, the pressure in both two vessels is kept constant at 1.3 atm and the venting system is located at the top of the Vessel 2 in Fig. 5.13. After the helium rich layer

is created at the top of vessel, the helium layer is eroded by a vertical hot steam jet (423 K) in the central line with different steam flow rates (30/60 g/s) from the bottom section in the Vessel 1. The injection outlet is at 4 m height from the bottom of Vessel 1 (see Fig. 5.13).

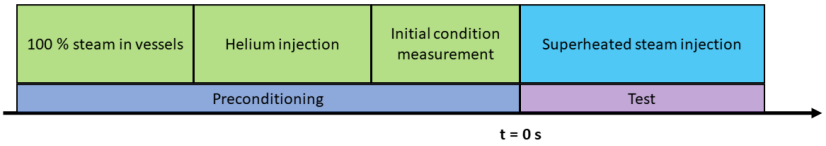

Figure 5.14: PANDA ST1 experiment precondition, modified from [OEC13]

The height difference between the injection outlet and the bottom part of the helium rich layer is about 2.0 m. After the hot steam is injected into the Vessel 1, the jet becomes a plume due to the density difference and the initial momentum. Therefore, the buoyancy turbulence source term must be considered in CFD simulations. After interacting with the stratification layer, the density, velocity, and temperature of the plume are different from the initial jet. The heat transfer (including thermal radiation) between hot steam injection and ambient atmosphere can influence the temperature, density and thereby velocity distribution before impinging into the bottom of helium layer. Obviously, the helium mixing process is mainly controlled by the initial momentum and buoyancy force. If the heat transfer between hot jet and ambient atmosphere is not accurately predicted, there may be significant differences in the evaluation of the helium mixing process.

The test parameters for ST1 series are shown in Tab. 5.6. The ST1_1_2 test is a low

Table 5.6: Test matrix for the selected two ST1 experiments

Experiment		ST1_1_2	ST1_2_2
Parameters	Units		
Initial temperature	K	381	381
Initial atmosphere		steam	steam
Steam mass flow	g/s	30	60
Injection temperature	K	423	423
Initial pressure	atm	1.3	1.3
Fr_{inter}		1.3	2.6

helium injection experiment. Therefore, the thermal radiation heat transfer in the ST1_1_2 experiment is more important than the ST1_2_2 experiment with a high injection rate 60 g/s. According to Table 5.6, there are huge amounts of steam (> 70 $vol.\%$) in the ST1 experiments. Therefore, the radiation transfer between the hot jet and ambient environment is the key consideration for the Monte Carlo solver validation. Furthermore, the interaction Froude number (Fr_{inter}) is also given in

Table 5.6 to characterize the ratio of flow momentum and buoyancy force. The definition of Fr_{inter} is related to the jet velocity impinging onto the helium layer u_{in}, the characteristic length L and the reduced gravity g' [KAM21]

$$Fr_{inter} = \frac{u_{in}}{\sqrt{g'L}} \tag{5.3}$$

The reduced gravity g' is given as follows

$$g' = g\frac{\rho_{ambient} - \rho_{in}}{\rho_{ambient}} \tag{5.4}$$

where $\rho_{ambient}$ is the density of ambient atmosphere; g is the gravity accelerator; ρ_{in} is the density of the jet impinging into the helium layer. According to Eq. 5.3, the interaction between momentum jet and buoyancy force becomes complex when the Fr_{inter} number is small, especially for the ST1_1_2 experiment.

The PANDA experiment provides the measurements of three main parameters: temperature, helium concentration, and velocity profile. For the temperature measurement, there are 374 K-type thermocouples installed in two vessels to monitor the fluid temperature, the wall temperature, and the interconnection pipe temperature. To measure the mixing process, there are 118 concentration sampling capillaries inside Vessel 1 and 2. The most important helium and temperature sensors are illustrated in Fig. 5.16. The particle image velocimetry system is applied to measure the velocity field. The temperature sensor data are reconstructed to visualize the temperature field in a 2D contour plot, and the mixing process is validated against the helium concentration data along the injection line.

5.3.2 ST1 CFD Setup

Before introducing the CFD model, a block-structure hexahedral mesh grid is employed in both vessels (see Fig. 5.15). The the second vessel is discretized in a coarse way as the turbulence mixing in Vessel 2 has a minor impact on the experimental validation. The main fluid momentum is along the injection pipe in Vessel 1; therefore, the grid is refined in those regions to resolve the free shear stress and wall shear stress. In order to resolve the turbulence near walls, the vessel wall region is also refined according to the best practice guideline [OEC07a], in particular the minimal face angle and the maximum volume and aspect ratios (see Fig. 5.15). The steel structure of the both vessels are also taken into account for the conjugate heat transfer.

The fluid domain is solved by the Reynolds-Averaged Navier-Stokes equation using the pressure-based PIMPLE algorithm with the buoyancy $k-\omega$ SST model. Two

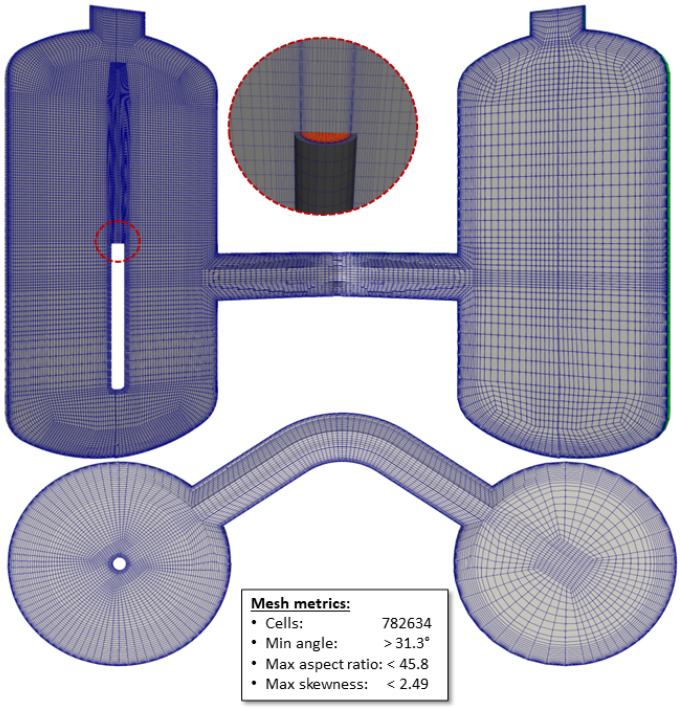

Figure 5.15: PANDA ST1 mesh

species (He and H_2O) equations are solved to resolve the gas mixing process in the ST1 experiments. The density field of the gas media is calculated by the ideal gas law in *containmentFoam*, not Boussinesq approximation. The heat capacity of the mixture c_p^{mix} is weighed by the species mass fractions for the ST1 experiments. The conjugate heat transfer is also modeled by solving an additional enthalpy equation to consider heat transfer between wall and environment. All numerical equations of the CFD modeling are shown in Table 5.1. The fluid temperature and He and H_2O concentrations are initialized according to the vertical temperature sensors and the vertical concentration sensors respectively. The inlet boundary conditions are modeled by the measured steam mass flow rate and temperature at the injection pipe (see Table 5.6). The main focus of the ST1 experiment validation is on the complex interaction between thermal radiation and CFD codes, using the Monte Carlo solver with different non-gray gas models to quantify the numerical difference in *containmentFoam*. The adjustable time step is applied during the numerical simulation to maintain a mean CFL number less than 1, while the maximum CFL number less than 5 is tolerated according to the best practice guideline [AND08].

Before discussing the numerical setting about thermal radiation solvers, the mesh uncertainty is evaluated to minimize the CFD numerical error from the mesh grid. Three different mesh grids are used to perform the mesh sensitivity study for the

ST1_2_2 experiment which is characterized by the high Reynolds number (60 g/s). It has a steeper velocity gradient in the ST1_2_2 experiment than that in the ST1_1_2 experiment. The thermal radiation heat transfer is not considered in the mesh sensitivity study for the ST1_2_2 experiment to reduce the computational effort. The coarse mesh grid has 164868 hexahedral cells, whereas there are 4930096 hexahedral cells for the fine mesh grid. The medium mesh is illustrated in Fig. 5.15. The mesh sensitivity for three different mesh grids is summarized in Table 5.7 at the final equilibrium state (~ 500 s) for the ST1_2_2 experiment. In the comparison of the boundary wall total heat flow rate and $yPlus$ values for three different mesh grids, there is a numerical error for the coarse mesh. In the coarse mesh grid, the

Table 5.7: Mesh sensitivity study for the ST1_2_2 experiment

Mesh	Number of cells	yPlus (avg.)	Boundary wall total heat flow rate (W)	GCI_U
Coarse	164868	9.82	4613.39	6.21%
Medium	782634	4.41	4751.75	1.84%
Fine	4930096	2.13	4787.84	0.38%

numerical diffusion can lead to a less steep temperature gradient on the boundary wall than other two meshes for the ST1_2_2 test case; as a result, the total heat flow rate on the boundary wall is much smaller than for the other two mesh grids. Furthermore, the mesh uncertainty for the fluid velocity is evaluated by the Grid Convergence Index (GCI) method [MAN18]. The velocity point is located at the 7 m height in the Vessel 1. It is concluded the velocity prediction in the coarse mesh grid is far from satisfactory in comparison with the other mesh grids. According to Table 5.7, the media mesh is a comprise between computational efficiency and accuracy. Therefore, the medium mesh grid is applied for the validation of the Monte Carlo solver with different non-gray gas models.

In order to save the computational effort, the radiation source term is updated every 1 s in the ST1 experiments. This approximation is valid for the low velocity flows especially containment flows in RANS analyses. The advanced ERMC algorithm with the global mesh is applied to the large scale calculations, and the Monte Carlo efficiency study about the global mesh grid is given in section 4.3.4. As discussed in section 5.2, different non-gray gas models have a strong impact on the temperature field. However, the complex interaction between thermal radiation and CFD is still unclear. In the ST1 test cases the Monte Carlo with the LBL, SNBCK, WSGG and Gray non-gray gas models are labelled as LBL, SNBCK, WSGG and Gray in the following discussion to quantify the strength of thermal radiation in containment flows. The WSGG coefficients for steam in low temperatures can be found in the literature [CAS14], whereas the gray gas absorption coefficient for steam is defined as 1.0 $m^{-1} \cdot bar^{-1}$ in this thesis.

The general transient flow for the ST1 experiments is shown in Fig. 5.16. After releasing from the injection pipe, the hot jet becomes a plume at the center of vessel. Before the hot jet reaching the helium layer at the top of vessel, the flow velocity is governed by the competition between initial momentum and buoyancy force. As shown in Fig. 5.16, the accuracy of density field is important for the helium mixing process, especially for the ST1_1_2 experiment. If thermal radiation heat transfer is not modeled in the ST1_1_2 experiment, it may lead to a numerical error. Different non-gray gas models can be assessed in the ST1_1_2 experiment. Hence, the helium erosion process is measured by means of the point-wise concentration histories for the numerical validation. As show in Fig. 5.16, only the vertical part of injection

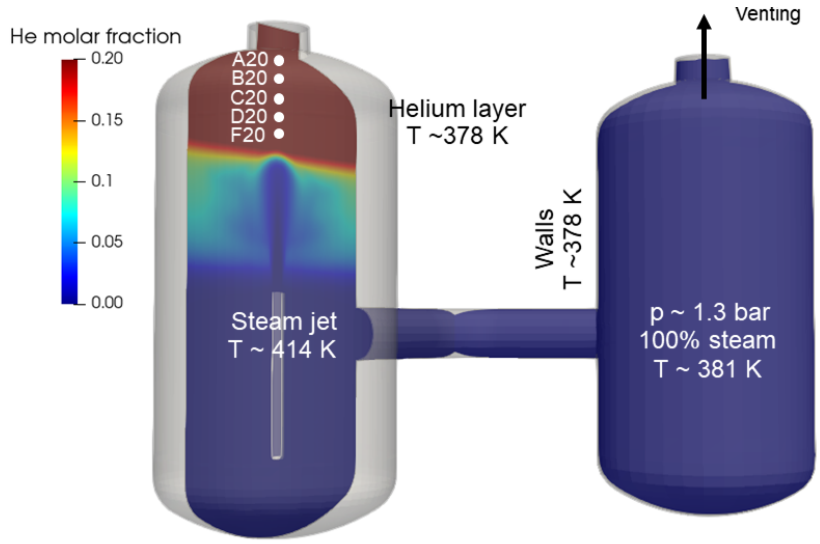

Figure 5.16: PANDA ST1 numerical model in OpenFOAM [LIU22b]

pipe is modeled in the CFD simulations. The outter surface of injection pipe is thermally insulated; therefore, there is no conjugate heat transfer near the vertical injection pipe in Fig. 5.16. The initial hot steam injection conditions are important for the mixing process prediction. The development of plume flow above the injection line originates from the injection outlet. In other words, the ST1 simulation results are highly sensitive to the outlet profile. Therefore, the outlet velocity and turbulence kinetic energy (TKE) along the radius are measured in the ST1_1_2 experiment with 30 g/s flow rate. The velocity and TKE on the inlet boundary patch are interpolated according to the experimental data. When applying this boundary condition, the CFD simulation results are well comparable to the experimental data [LIU22b]. The inlet boundary conditions for the ST1_2_2 experiment with 60 g/s mass flow rate are similar to the ST1_1_2 experiment.

5.3.3 ST1 Results and Discussion

5.3.3.1 ST1_1_2 Experiment

After the hot steam released from the outlet in the ST1_1_2 experiment (see Fig. 5.16), there is a strong temperature decay along the central line owing to heat transfer between hot steam and cold environment. As shown in Fig. 5.17 the vertical temperature profiles above 4 meters in the quasi-steady state obtained by different non-gray gas models are compared with the experiment data. The red dotted

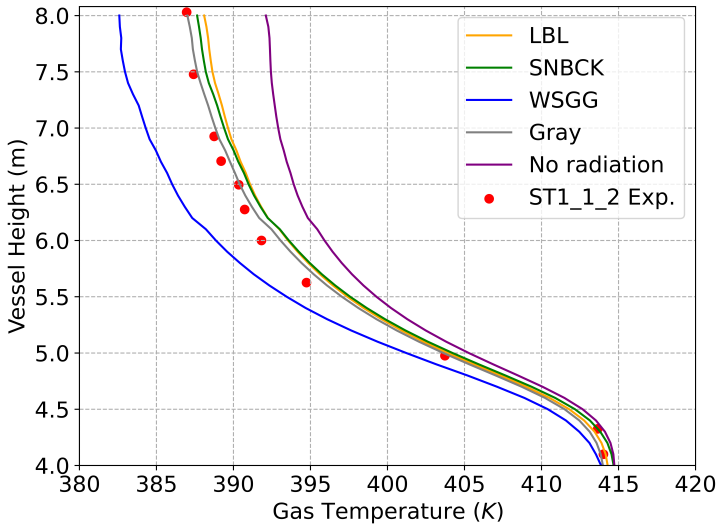

Figure 5.17: Vertical temperature profile above 4 m for the ST1_1_2 experiment

points are the measured temperatures from thermocouple sensors along the injection line. There is a significant temperature decay above the injection line due to thermal radiation heat transfer between hot jet and ambient atmosphere. But the no radiation case cannot represent this physical scenario. The LBL and SNBCK models give similar predictions for the temperature field along the injection line, which are in excellent agreement with the experimental data. The temperature profile without considering thermal radiation heat transfer is relatively high in comparison with the experimental data. Another interesting finding is that different non-gray gas models lead to different temperature fields. The lowest temperature field is obtained by the WSGG model, which is far from the experiment data. The other three non-gray gas models are more reasonable than the WSGG model. Therefore, it may over-estimate the strength of thermal radiation heat transfer using the WSGG model in containment flows.

A qualitative comparison of the temperature field surrounding the jet is performed on the basis of the 2D temperature contour plots (see Fig. 5.18) at three different time steps: 400 s, 800 s and 1200 s. The experiment contour plot is obtained by

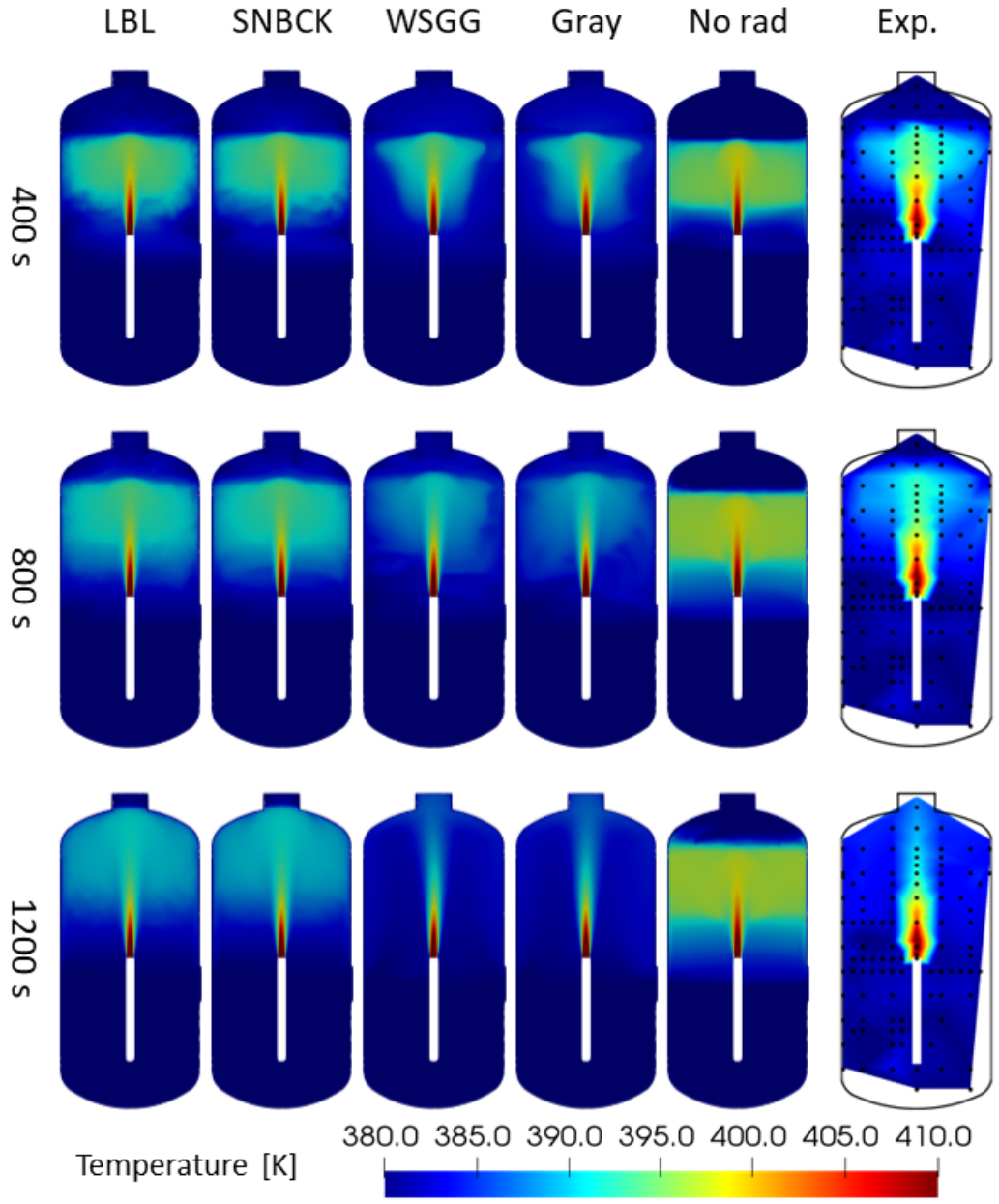

Figure 5.18: Comparison of the temperature field for the ST1_1_2 experiment

the linear interpolation based on the thermocouple temperature sensors within the Vessel 1. Therefore, the experiment contour plot has an artificially broader illustra-

tion of the hot jet than simulation results owing to the finite number of temperature sensors. According to Fig. 5.18 the gas radiation has a strong impact on the temperature distribution in the ST1_1_2 experiment. First of all, there is a mushroom-shaped temperature profile above the injection line in the experiment. The thermal radiation promotes heat transfer between the hot steam jet and ambient atmosphere resulting in a decline of temperature along the injection line. The simulations with radiation can represent this physical phenomena in Fig. 5.18. Since the hot jet emits thermal radiation in all directions, a smooth temperature field is obtained in all simulations with radiation heat transfer. However, it has a steep temperature gradient in the case without thermal radiation which can only transfer heat horizontally by conduction or convection. Hence, the gas radiation can affect the temperature field over a long distance in large facilities, e.g., containment buildings, which is completely different from the turbulent convection near the plume regions. The turbulent convection heat transfer tends to have a short distance effect in comparison with the gas radiation, which can be demonstrated in comparison with the no radiation setting in Fig. 5.18.

At the beginning (< 400 s), the difference between the cases with radiation and without radiation is modest. In other words, thermal radiation heat transfer does not affect the fluid field in the initial stage. It is evident that radiative heat transfer is not important with modest temperatures within a short term. After that, thermal radiation heat transfer can heat up the stagnation region at the top of vessel, even though the position of hot jet is relatively low (see Fig. 5.18 800 s). Even though thermal radiation heat transfer is not the dominant heat transfer mode, it still plays a role on the heat balance with modest temperature differences over a long term. The effects of radiation heat transfer for the WSGG and Gray cases are more pronounced than that for the LBL and SNBCK cases, leading to a highly homogeneous temperature field at the top of vessel. At 800 s, the no radiation simulation is totally different from the radiation simulations, since the radiation heat transfer can significantly change the temperature field and thereby the density distribution. If the initial momentum is not large, the density field has a strong impact on the mixing process. However, it also requires a long time to reach the homogeneous density field by thermal radiation heat transfer. In comparison with other non-gray gas models, the LBL and SNBCK results are in agreement with the measured temperature along the central line. Although the vertical temperature profile of the Gray model is similar to the SNBCK model in Fig. 5.17, the 2D temperature field is totally different from the SNBCK model in Fig. 5.18. The optically thin approximation for the Gray model over-estimates the strength of radiation heat transfer leading to homogeneous temperature distributions. The temperature difference may cause a density difference, which again affects the mixing process in the ST1_1_2 experiment. It is interesting to note that the mixing process for the no radiation case is much slower than that in other radiation cases at 1200 s. A detailed discussion about this effect is given in the following part about the helium erosion history.

To evaluate the temperature history, Fig. 5.19 and Fig. 5.20 show the evolution of temperature at $C20$ and $C14$ sensors in the ST1_1_2 experiment. The $C20$ temperature sensor is located at the center injection line, and its height is about 7 m from the bottom of vessel. The $C14$ temperature sensor has a different horizontal position near the wall. According to these two sensors, thermal radiation heat between hot jet, ambient atmosphere and wall boundary layer can be clearly quantified. There is a temperature increment in the experiment data before 500 s in Fig. 5.19. At that moment, the hot steam jet is still in the middle part of vessel, not reaching the 7 m height. The temperature increment is only related to thermal radiation heat transfer. There is a faster temperature increment for the WSGG and Gray models than that for other numerical settings. If thermal radiation heat transfer is neglected, the temperature at the $C20$ position stays almost constant before the arrival of the hot jet (see Fig. 5.19). It takes around 500 s for the initial hot jet to reach the $C20$

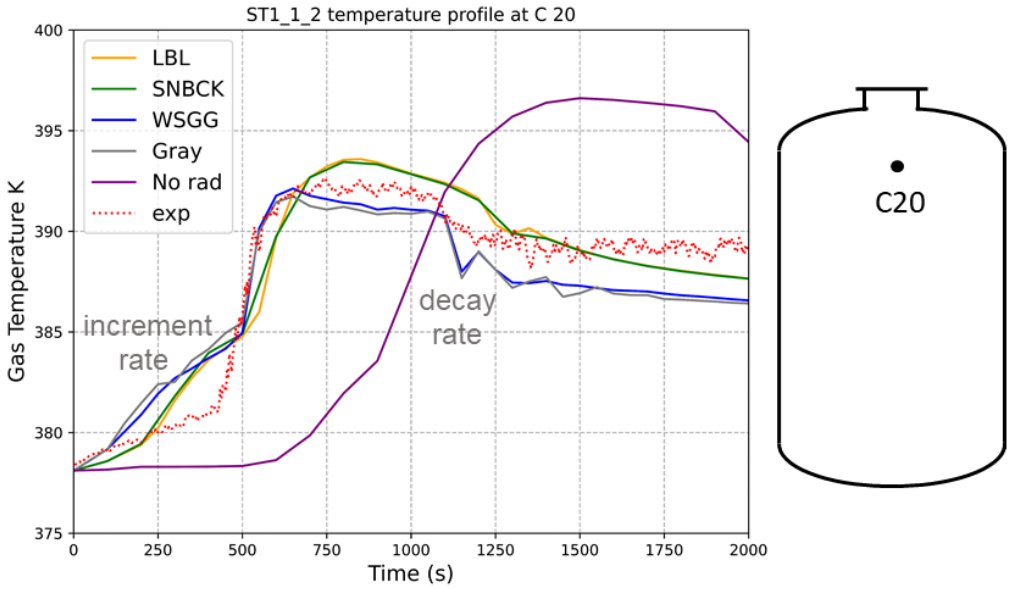

Figure 5.19: ST1_1_2 temperature sensor C20

position in the experiment, since it has a steep temperature increment at 500 s in Fig. 5.19. All simulation with thermal radiation modelings can represent this scenario. However, it has a time delay for the hot jet to reach the $C20$ position in the no radiation setting.

The second temperature sensor $C14$ has the same height 7 m but with a different horizontal position (see Fig. 5.20). The temperature difference between simulation and experiment at the starting point is due to the CFD initial conditions. The temperature field in CFD simulations is initialized according to the tempera-

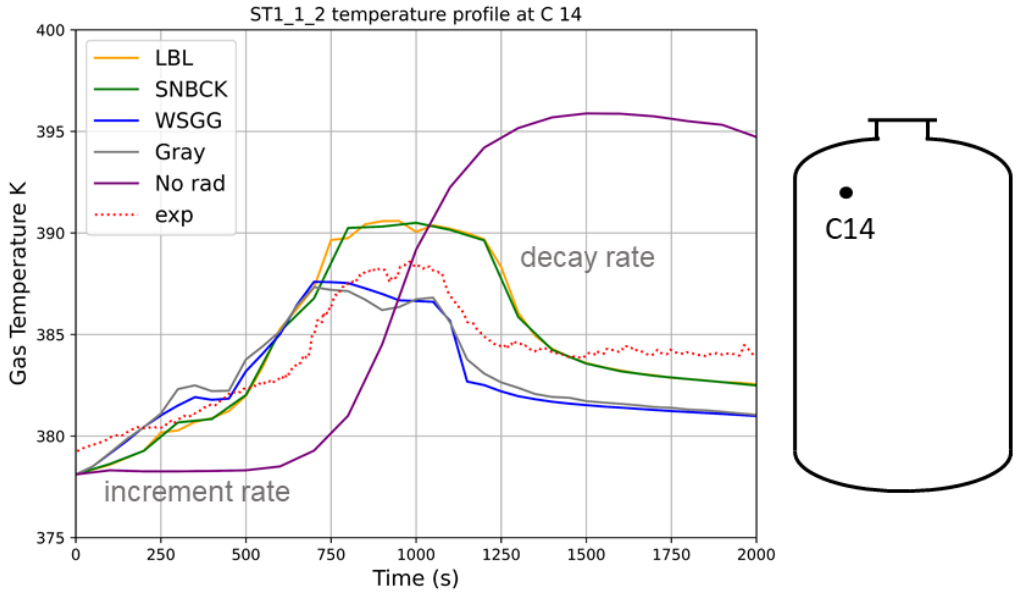

Figure 5.20: ST1_1_2 temperature sensor C14

ture sensors at the central line, e.g., the $C20$ sensor. It is noted that the LBL and SNBCK models can exactly provide the same increment rate for the sensor $C14$ in Fig. 5.20. After the hot jet arrives at the $C14$ position, it has a steep temperature increase at around 750 s. The temperature decrease rate in the simulation is also related to the non-gray gas model. A strong temperature decrease effect is seen in the WSGG and Gray models (see Fig. 5.20). According to these findings, it is concluded that the simulations considering thermal radiation are consistent with the experiment in the temperature field. In contrast, the no radiation results illustrate visibly different phenomena at the top of the vessel. Furthermore, the numerical fluctuations become relatively small after applying advanced Monte Carlo algorithms. The Monte Carlo thermal radiation solver in *containmentFoam* is numerically stable for the large facility simulations, e.g., containment flows.

As stated before, gas radiation may affect the helium mixing process in the ST1_1_2 experiment. Fig. 5.21 compares the helium concentration histories using different non-gray gas models against the ST1_1_2 helium concentration measurements in the uppermost sampling positions. The helium sensor positions are shown in Fig. 5.16. For the helium concentration measurement gases are sampled in the PANDA vessel through 0.8 mm inner diameter capillaries, and the gas concentration is measured by a mass spectrometer [OEC08]. This is a time-consuming procedure, and it has a specific response time for the mass spectrometer system. Therefore, the experimental helium concentration is given in a large time step (around 180 s) in

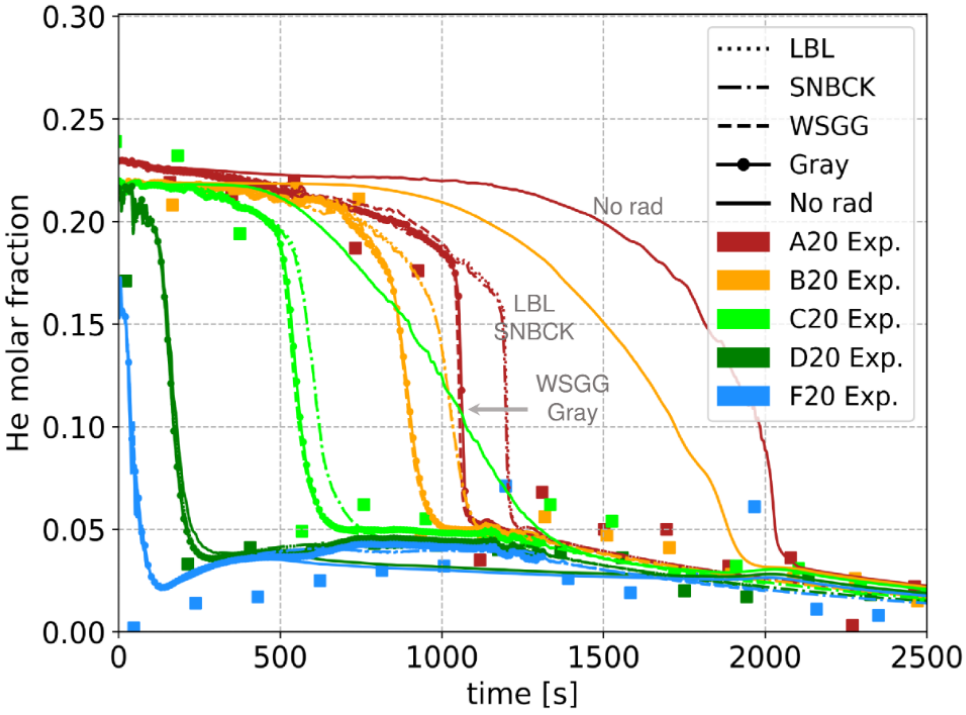

Figure 5.21: ST1_1_2 transient helium dilution process

Fig. 5.21. At the beginning < 200 s the helium erosion process is similar for all simulations, since thermal radiation is not the dominant heat transfer mode in the ST1_1_2 with modest temperature differences. After the initial hot jet arrives at the top of PANDA vessel, neglecting thermal radiation in the simulation leads to a visible slowness of the mixing process compared to the experiment, especially for the highest helium sensor $A20$. The numerical differences obtained from different non-gray gas models become significant at the $A20$ helium sensor. The slope of the concentration decay in the stagnant layer increases for all thermal radiation simulations; while there is only a weak slope in the simulation without considering radiative heat transfer owing to molecular diffusion. The SNBCK and LBL models can predict this helium erosion in coincidence with the experimental data. This is because the non-gray gas radiation can transfer heat into the stagnant region at the top of PANDA vessel, where the convective transport is hindered by the helium layer (see Fig. 5.16). Nevertheless, the increased slope in the concentration history is explained by means of a secondary buoyancy circulation in the stagnant layer which is driven by small density differences. It is noticed that the heat transfer between hot injection and ambient environment is vital for the helium mixing process.

A detailed look at the transient density and velocity fields (see Fig. 5.22 and Fig. 5.23) allows to identify the reason. The pressure in the ST1 experiments is kept constant during the injection phase with a venting pipe at the top of secondary vessel. The mixture density ρ is calculated by Eq. 5.5 according to the ideal gas equation.

$$\rho = \frac{pM}{RT} \tag{5.5}$$

where M is the molecular weight of a mixture of gases; p is the pressure; R is the ideal gas constant; T is the media temperature. According to Eq. 5.5 thermal radiation heat transfer in the ST1_1_2 can lead to a larger density field near the injection region if the temperature of injection line becomes smaller (see Fig. 5.17) owing to the radiative heat transfer.

Fig. 5.22 shows the density profile at different time steps (400/800/1200 s) for the ST1_1_2 experiment. Only the simulation results obtained from different non-gray gas models are available in Fig. 5.22, because it is difficult to measure the fluid density in the experiment. Similarly to the temperature field in Fig. 5.18, the gas radiation does not affect the density at the beginning. The gas radiation heat transfer has a strong impact on the density field at 800 s in Fig. 5.22, which coincides with the temperature field. It is concluded that the radiation heat transfer can not be neglected in containment flows over a long term. There is a density increase near the hot steam region with a temperature decline due to thermal radiation. The fluid with considering thermal radiation tends to move horizontally in comparison with the no radiation model. The LBL and SNBCK cases have a smooth density field; while the density field in the WSGG and Gray cases are more homogeneous than that in other non-gray gas models by reason of the optically thin approximation. Without considering thermal radiation, the density field has a very steep gradient along the injection line, and the hot injection steam tends to fall down after losing the initial momentum. This effect can be amplified after a long injection time, since the density field can change the buoyancy forces in the ST1_1_2 (see Fig. 5.22).

Fig. 5.23 is the velocity profile at different time steps (400/800/1200 s) for the ST1_1_2 experiment. In the early transient (400 s) gas radiation may change the density of the media near the hot jet, but the velocity difference between the no radiation and other radiation cases is negligible. The helium mixing process is mainly controlled by the injection momentum. With an increase in the mixing process (800 s) the plume is mainly controlled by the negative buoyancy before and while impinging into the layer interface. From Fig. 5.23 it is evident that the plume can spread radially at the stagnation point in the SNBCK and LBL cases, while it tends to fall down in the no radiation case after losing its initial momentum. There is an enhancement for the helium mixing process in a horizontal direction for the cases with thermal radiation settings which is mainly related to the buoyancy balance near the stagnant point of the jet.

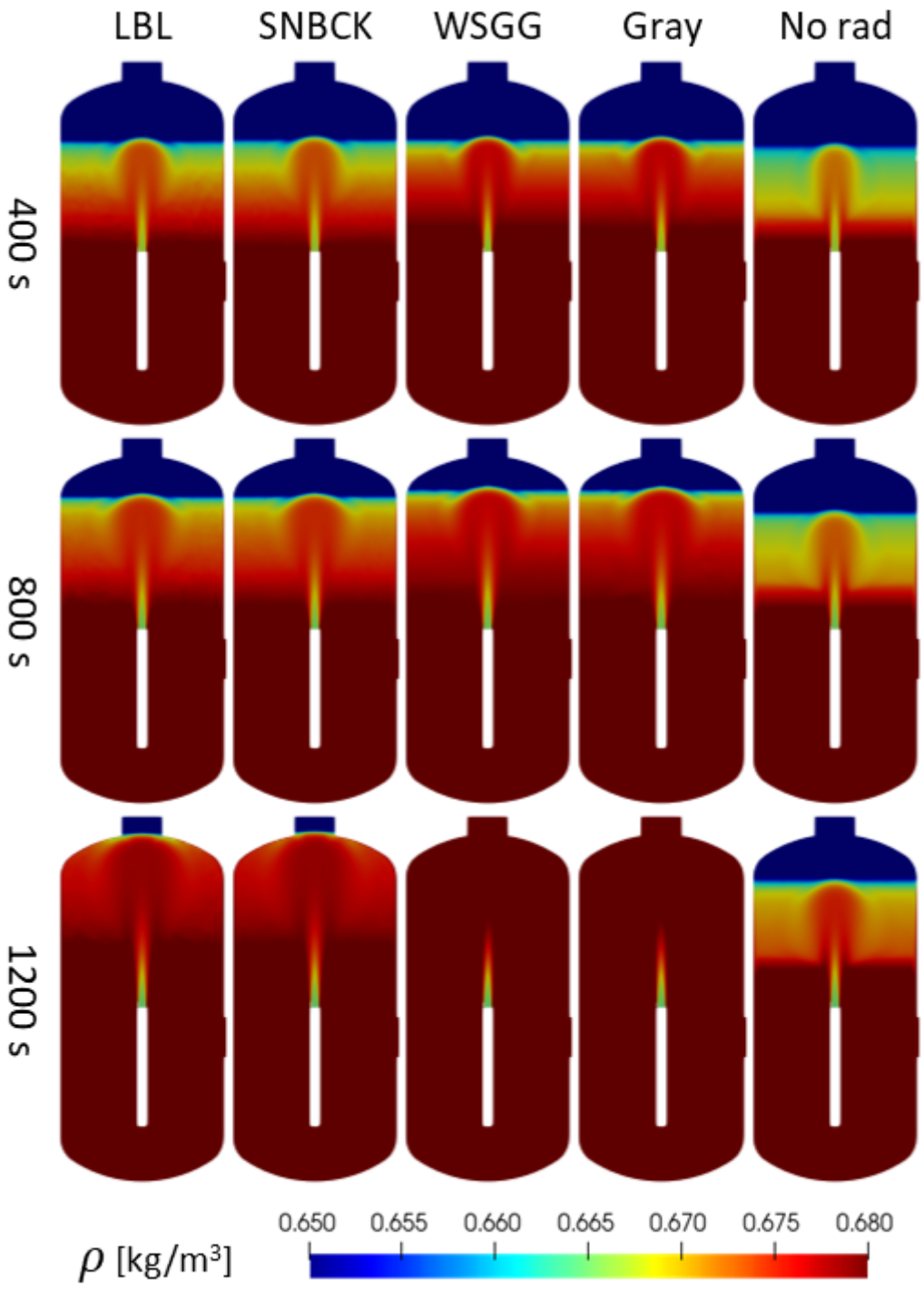

Figure 5.22: Comparison of the density distribution for the ST1_1_2 experiment

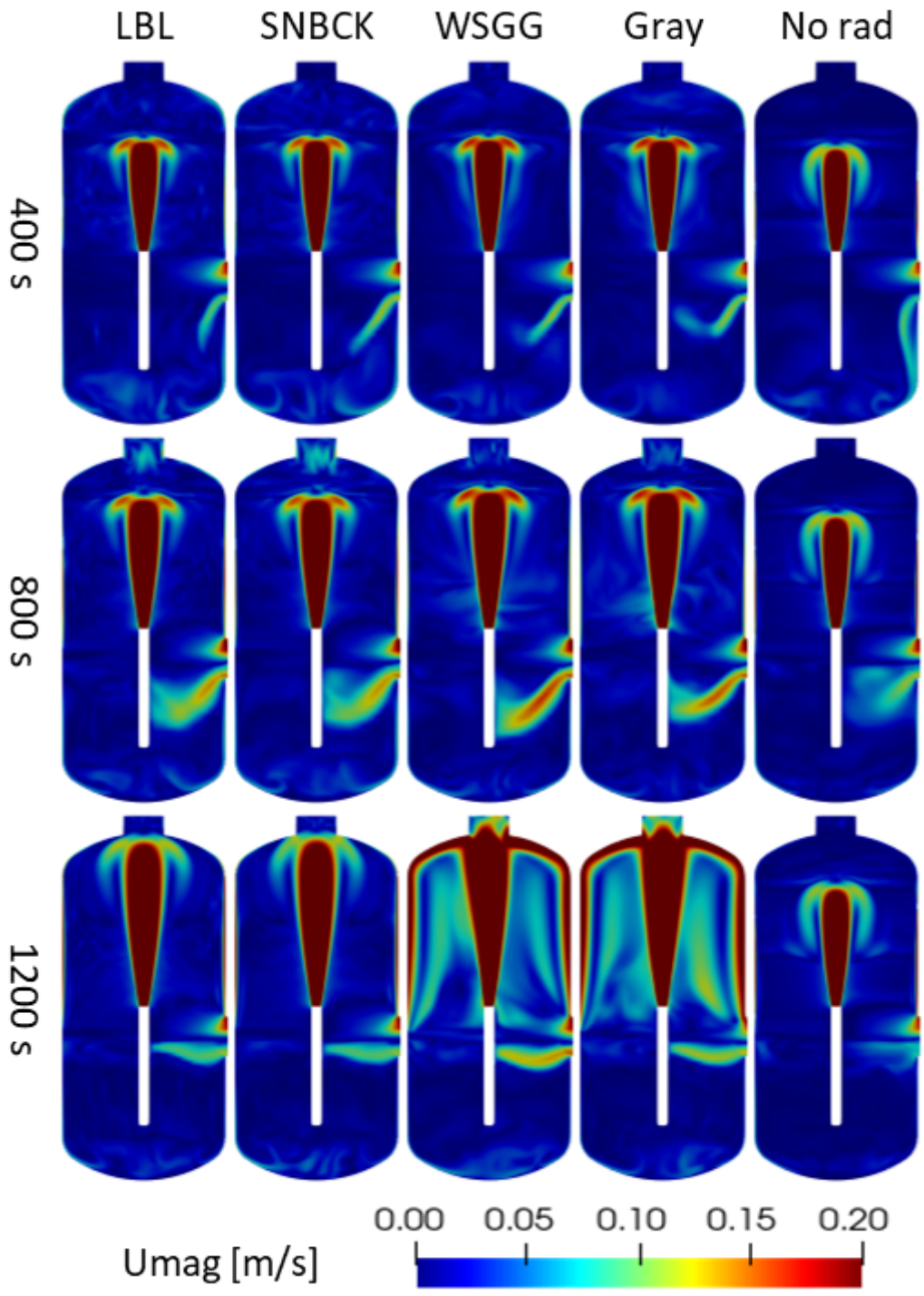

Figure 5.23: Comparison of the velocity distribution for the ST1_1_2 experiment

Another important finding is the appearance of a weak secondary circulation in the stagnant gas region in all radiation cases, especially for the LBL and SNBCK models at 800 s in Fig. 5.23. By comparing the velocity field without thermal radiation, it is obvious that the thermal radiation mechanism can affect the fluid motion over a certain distance. This internal circulation in the stagnant layer promotes the mixing process in the ST1_1_2 which results in an enhanced concentration decay at the helium sensor A20 (see Fig. 5.21), and thus a globally faster erosion of the helium layer in the cases considering thermal radiation than the no radiation case.

From the above figures, the gas radiation heat transfer can lead to a homogenization of the temperature field (i.e. less steep temperature gradients between jet, bulk and wall). This effect is evident in low-velocity flows with high steam concentrations even though having small temperature differences (jet-ambient $\Delta\, T < 30\ K$). However, different thermal radiation solvers can lead to totally different temperature profiles in the coupled thermal radiation and CFD simulations. Although the thermal radiation is not the dominant heat transfer mode, the accuracy of the thermal radiation solver is mandatory to avoid unreasonable temperature predictions. The steam spectral gas property may be more important than the thermal radiation solver. It is found that the WSGG and gray gas models can over-estimate the strength of thermal radiation due to the optically thin approximation [MOD13]. As stated before, the heat transfer phenomena, including thermal radiation, are closely linked to the velocity in low-velocity flows, especially for containment flows. It is concluded that the observed helium mixing process is a result of the complex interaction between radiative heat transfer and convective heat and mass transfer in the turbulent buoyancy-affected flow.

5.3.3.2 ST1_2_2 Experiment

The importance of thermal radiation has been demonstrated in the ST1_1_2 experiment with a low injection rate (30 g/s). However, the importance of thermal radiation also depends on the relative strength of convective and conductive heat transport in low-velocity flows. It has a competition between thermal radiation and convection to determine whether thermal radiation is of significant importance in the heat balance or not. When increasing the mass flow rate (60 g/s), the effect of thermal radiation on the mixing process is evaluated in the ST1_2_2 experiment. The vertical temperature profiles above 4 meters in the quasi-steady obtained from different non-gray gas models are compared with the ST1_2_2 experiment data (see Fig. 5.17). The red dotted points are the measured temperatures from the thermo-

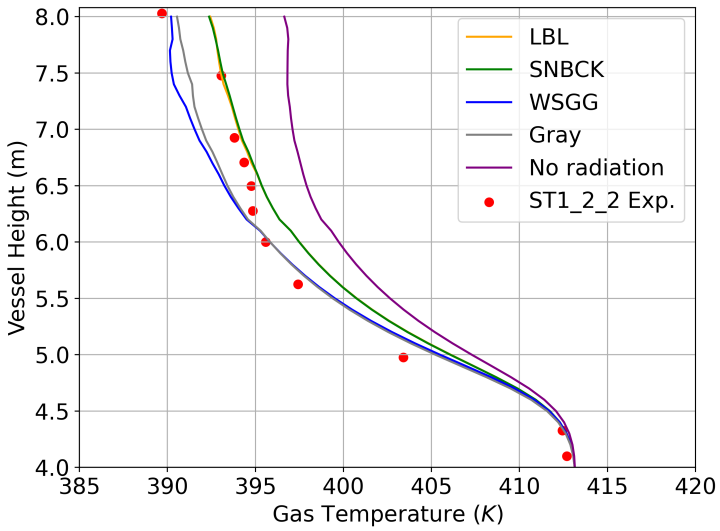

Figure 5.24: Vertical temperature profile above 4 m for the ST1_2_2 experiment

couples at the central line. The last temperature point at the 8 m height in Fig. 5.24 is significantly off track due to the heat loss from the upper part of vessel, which is not considered in CFD simulations. As expected, the LBL and SNBCK models give similar predictions for the temperature field along the jet. Even though increasing the injection mass flow rate (60 g/s), the different non-gray gas models can result in different temperature predictions along the injection line. The lowest temperature field is also obtained by the WSGG model, and the Gray model has an identical result. Without considering thermal radiation, the temperature is larger than that in the other non-gray gas models. Therefore, thermal radiation also has an effect on the temperature field when increasing the injection velocity.

Fig. 5.25 illustrates the evolution of the temperature field (100/200/300 s) for the ST1_2_2 experiment. In comparison with the experiment, there is a systematic dif-

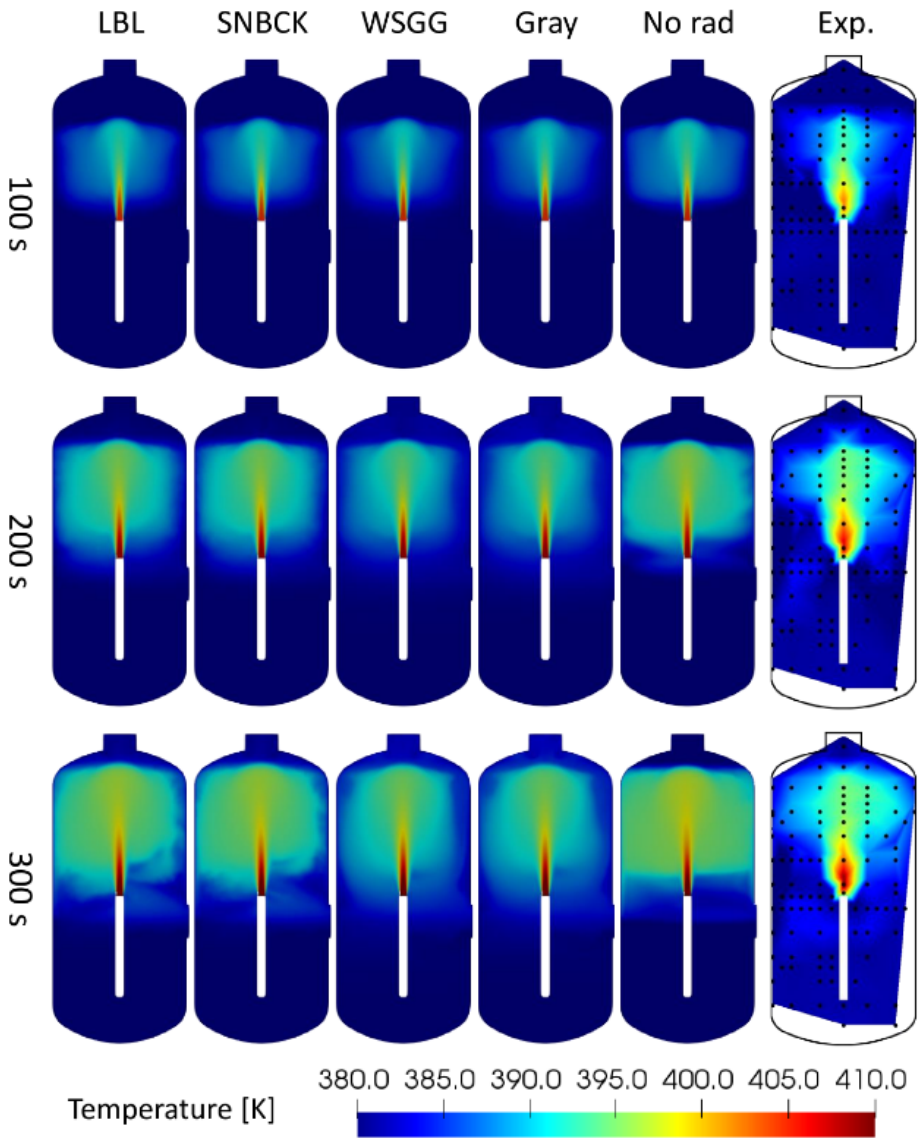

Figure 5.25: Comparison of the temperature field for the ST1_2_2 experiment

ference for the temperature profile between numerical simulation and experiment. The heat transfer between hot jet and ambient environment is over-estimated in numerical simulations (see Fig. 5.25). This is mainly due to the numerical error from the CFD modeling, not radiative heat transfer modeling. It is difficult to model the turbulence mixing after increasing the injection rate (60 g/s) in the ST1_2_2 experiment. More investigations on the initial velocity and turbulence kinetic energy at

the injection outlet are required to minimize the numerical uncertainty from CFD codes. Globally there is no significant difference between with or without thermal radiation models. Only at the 300 s, the temperature difference among these models becomes significant. After increasing the strength of convection, thermal radiation heat transfer may play a less important role in temperature predictions. Under the gray gas assumption, the fluid temperature has a decay effect in the horizontal direction within a short distance for the WSGG and Gray models. According to Fig. 5.25, the LBL and SNBCK cases give smooth temperature field from hot steam jet to the wall structure in the horizontal direction. It is concluded that the non-gray gas model can affect the heat transfer on the boundary wall. In the ST1 experiment, the wall temperature is kept constant at about 381 K to avoid condensation. However, radiation heat transfer may affect wall condensation and thus change the wall boundary condition in the CFD simulations. When applying the gray gas model to containment flows, there may be a strong condensation effect on the boundary wall.

As shown in Fig. 5.25, the temperature difference between different non-gray gas cases in the ST1_2_2 experiment cannot be distinguished. In order to compare different non-gray gas models, Fig. 5.26 and Fig. 5.27 are the evolution of temperature $C20$ and $C14$ sensors in the ST1_2_2 experiment. First of all, there is a huge difference between experiment and simulations at around 150 s in Fig. 5.26 and Fig. 5.27 because the momentum jet is not well captured by CFD. Different from the low

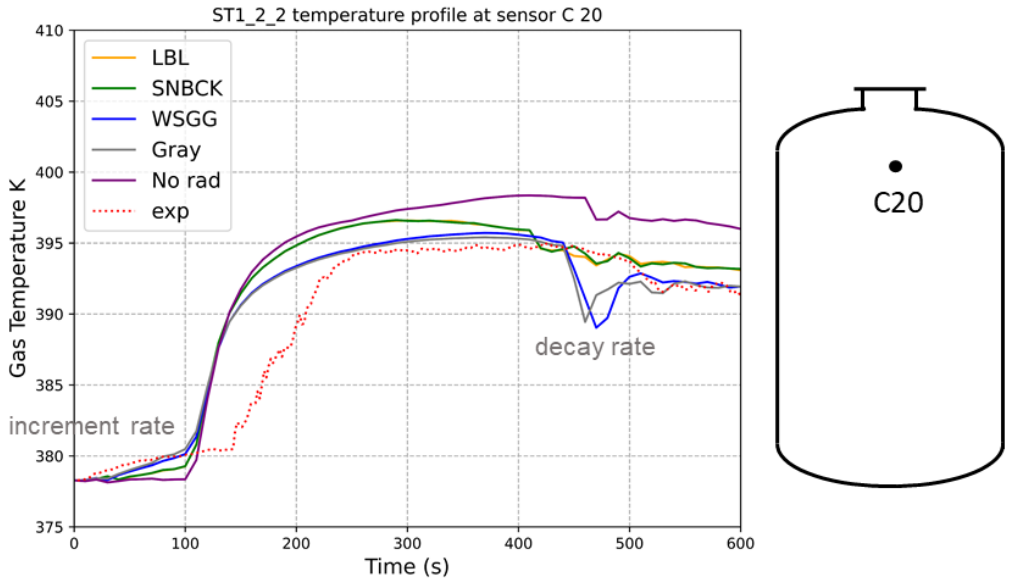

Figure 5.26: ST1_2_2 temperature sensor C20

injection experiment, e.g., ST1_1_2, the temperature profiles at the $C20$ and $C14$ sensors in the ST1_2_2 experiment are mainly controlled by the initial momentum. Before the hot jet arrives at the $C20$ sensor, there is a modest temperature increase in the experimental data (< 100 s). The temperature increase at the $C20$ sensor is related to thermal radiation heat transfer during the modest heat up phase. Overall, the no radiation case cannot predict this modest heat-up phase. The increase rates for the LBL and SNBCK cases are in good agreement with the experiment data in Fig. 5.26. After the hot jet arrives at the $C20$ sensor, the temperature difference in all simulations becomes negligible, since the strength of radiation heat transfer is much smaller than that of convection. At the end of injection phase, it has a strong temperature decay for the WSGG and Gray cases, which is not seen in the experiment. A smooth temperature decay is provided in the LBL and SNBCK results.

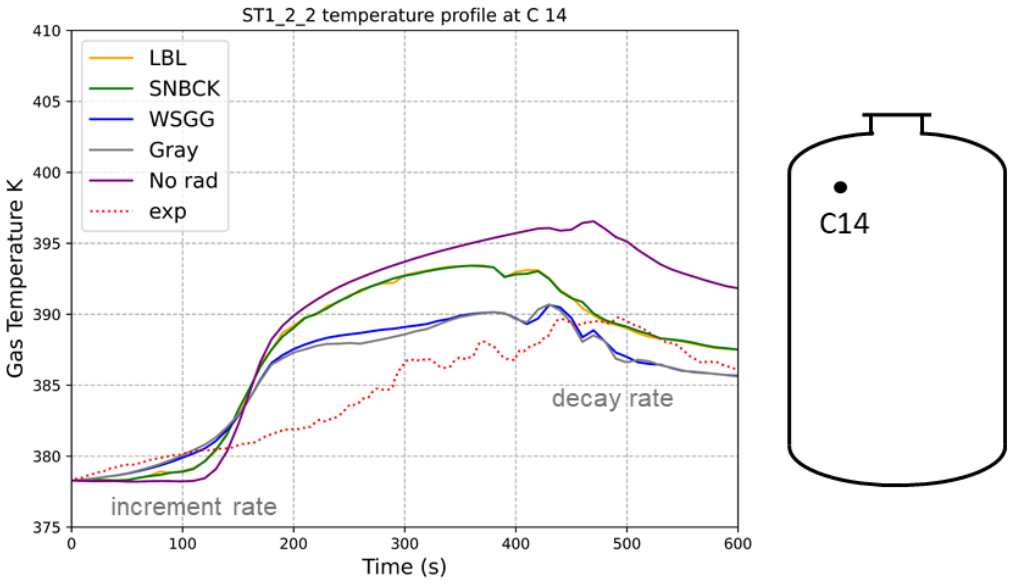

Figure 5.27: ST1_2_2 temperature sensor C14

Fig. 5.27 is the temperature history for the sensor $C14$. As expected, the modest temperature increase is also seen in the sensor $C14$ even though it has a long distance between the hot jet and sensor $C14$. There is a steeper temperature increase rate for the WSGG and Gray models than the other non-gray gas cases. After the hot jet arrives at the 7 m level, the difference between simulations and the experiment is significant. This may be explained by the CFD numerical diffusion in the ST1_2_2 experiment with a high injection rate. However, the simulation results from the SNBCK and LBL models are superior to the other non-gray gas cases.

Fig. 5.28 depicts the temporal change of helium concentration for the ST1_2_2 experiment. For the experiment data, only a small number of helium sensors are available, since the erosion process is much faster than in the ST1_1_2 experiment (30 g/s). The 60 g/s injection flow rate leads to a strong turbulence mixing when impinging into the helium layer at the top of vessel. Furthermore, the initial momentum is still large at the equilibrium point, where the gravity force equals the buoyancy force. In other words, the density field may become less important in the ST1_2_2 experiment for the helium mixing process.

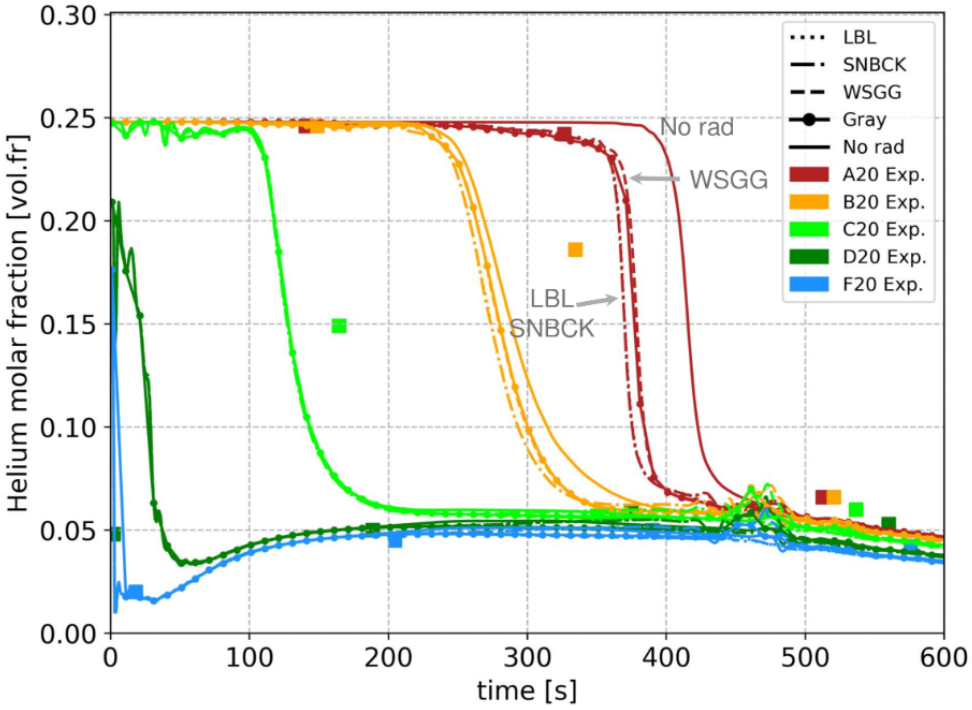

Figure 5.28: ST1_2_2 transient helium dilution process

The helium concentration predictions for the positions of $F20$, $D20$ and $C20$ sensors are overlapping with each other. Although gas radiation has no significant effect on the temperature field for the ST1_2_2 experiment, it still has an effect on the helium erosion process, especially for the $A20$ helium sensor. As shown in Fig. 5.28, there is a small concentration drop for the sensor $A20$ in the experiment, which is not related to molecular diffusion. This is because the thermal radiation can transfer heat into the stagnant fluid above the jet stagnation region where convective transport is hindered by the layer interface. Obviously, the increased slope in the concentration history is explained by means of a secondary buoyancy circulation inside the

stagnant layer. When neglecting thermal radiation, the secondary circulation at the stagnant region is not seen in the no radiation case. In comparison with the no radiation case, the radiation cases coincide with the experiment. It is concluded that the thermal radiation effect is modest if the convection effect becomes dominant. But there is an improvement for the temperature and helium concentration predictions using the Monte Carlo thermal radiation solver.

A detailed look at the velocity fields is shown in Fig. 5.29 to quantify the helium mixing effect at the top of vessel. As stated before, thermal radiation heat transfer can lead to a homogeneous density field in the ST1_2_2 experiment. The importance of thermal radiation also depends on the strength of convection in the experiment. As shown in Fig. 5.29, the velocity fields for all simulations are almost the same at 100 s. The jet velocities below the helium layer are also similar in all numerical settings; however, a larger velocity is predicted by the WSGG and Gray models at the top of PANDA vessel at 200 s. There is no flow circulation at the top of PANDA vessel in the no radiation case in Fig. 5.29. It is evident that the small density difference owing to thermal radiation at the top of PANDA vessel can evolve a secondary circulation. This is consistent with the helium erosion process in Fig. 5.28. When the hot jet reaches the top of vessel at 300 s, it has a larger horizontal velocity in the hot jet for the radiation cases than the no radiation setting (see Fig. 5.29). Since the temperature difference is modest in the ST1_2_2 experiment, it requires a long time to reach the homogeneous density field in containment flows.

The thermal radiation heat transfer between hot jet and ambient environment is also related to the dimension of facilities. In comparison with the ST1_1_2 and ST1_2_2 experiments, it is concluded that thermal radiation is not strong enough to change the turbulence mixing in containment flows. When increasing the initial momentum, the change of the density field caused by thermal radiation becomes negligible in the helium prediction. Even though it is not a dominant effect, an accurate thermal radiation solver is preferable in the hydrogen concentration prediction at boundary walls. Since the hydrogen tends to accumulate at the boundary wall owing to its density after a postulated severe accident, thermal radiation heat transfer between media and boundary walls may introduce a secondary circulation in containment flows. It is also noted that the strength of thermal radiation does not increase with increasing injection velocities. For the ST1_2_2 experiment, the simulation result is strongly related to the turbulence model, not the thermal radiation model. It is necessary to perform more test cases to demonstrate this effect. Theoretically, the thermal radiation is a function of the temperature field, total pressure, and molar fractions. Owing to the modest temperature difference, thermal radiation is only comparable with the convection and conduction heat transfer in the low injection rate experiment.

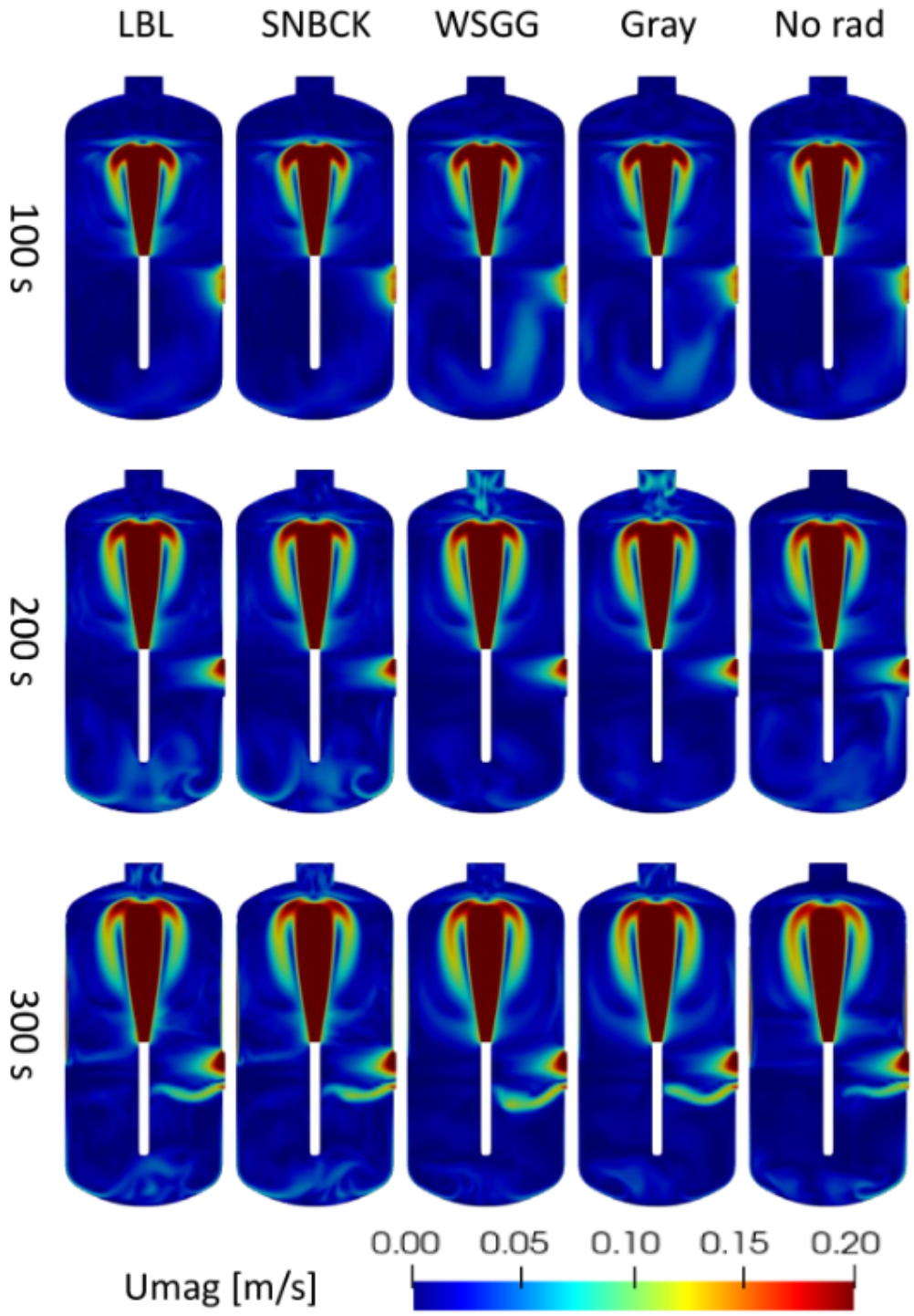

Figure 5.29: Comparison of the velocity distribution for the ST1_2_2 experiment

5.3.4 Summary of ST1 Test Series

The Monte Carlo thermal radiation solver with spectral gas properties is validated against the PANDA ST1 experiments. According to these simulation results, the numerical fluctuation of Monte Carlo simulations is remarkably reduced by applying advanced algorithms. Furthermore, the simulation including thermal radiation is significantly better than the case without thermal radiation. For different non-gray gas models, both LBL and SNBCK models are in good agreement with the experiment data. The LBL and SNBCK non-gray gas models can predict the temperature profile and the helium mixing process well. It is found that both WSGG and gray gas models overpredict the effect of thermal radiation heat transfer.

However, the coupling of Monte Carlo thermal radiation modeling and CFD simulation is a time consuming procedure. The comparisons of the heat flow rates on the boundary wall and computational times for different non-gray gas models in the ST1 test cases are given in Table 5.8. The Monte Carlo thermal radiation with

Table 5.8: Summary of different non-gray gas models for ST1_1_2 and ST1_2_2 test cases in the quasi-steady state

Exp.	Model	CPU (h)	Boundary wall radiative heat flow rate (W)	Boundary wall total heat flow rate (W)
ST1_1_2	LBL	815.04	1316.91	3356.81
	SNBCK	562.21	1303.75	3341.24
	WSGG	556.64	1599.59	2982.97
	Gray	519.94	1603.13	3557.83
	No rad	384.04	-	3785.01
ST1_2_2	LBL	949.50	1572.52	4898.73
	SNBCK	672.46	1571.25	4892.86
	WSGG	606.91	2279.35	4923.41
	Gray	609.58	2295.32	4919.45
	No rad	456.96	-	4737.02

the non-gray gas model is laborious for the technical scale applications. As shown in Table 5.8, it takes a long time for thermal radiation calculations. It is estimated that the computation time for the updating thermal radiation is about 100 times slower than one CFD time step. The thermal radiation solver is updated each second in relatively low velocity flows or buoyancy flows. For the Monte Carlo with LBL model, the simulation time is two times longer than the no radiation case. Obviously, the computation effort is highly related to the number of tracked photons within the computational domain. The investigation of parameter sensitivity in the Monte Carlo solver is of utmost importance in the future to find a balance between accuracy and efficiency. The non-gray gas model has a strong impact on the radiative heat flow rate in the quasi-steady state. According to Table 5.8, the strength

of thermal radiation is not related to the fluid velocity but only the temperature difference. Thermal radiation heat transfer is different from conduction or convection, which does not depend on the fluid velocity. Besides the vertical temperature profile, gas radiation also changes the wall heat balance and thus has an effect on wall condensations for two-phase simulations.

Due to the modest temperature difference in the ST1 experiment, the radiative source term $\nabla \cdot q_r$ is relatively small in comparison to other heat transfer modes. But thermal radiation can transfer heat over a long distance. In the stagnant region, the fluid media can be heated up by thermal radiation, while the conduction and convection heat transfer modes are relatively weak. From these two experiments, the effect of thermal radiation in the ST1_1_2 test case is more important than that in the ST1_2_2 test case. In the ST1_1_2 test case a stable thermal stratification is built below the helium layer when neglecting thermal radiation. This thermal stratification induces a negative buoyancy force, which has a strong impact on the jet momentum and thus changes the erosion process.

After performing a number of tests, a detailed explanation for the ST1_1_2 experiment is provided by the simplified energy equation. Neglecting the enthalpy transport due to inter-species diffusion and buoyancy energy source, the simplified energy equation can be written as

$$\frac{\partial(\rho h_{tot})}{\partial t} + \nabla \cdot (\rho U h_{tot}) = \underbrace{\nabla \cdot \left[(\lambda + \lambda_t)\, \nabla T\right]}_{\text{cond. + conv.}} - \nabla \cdot q_r \tag{5.6}$$

where ρ is the density; h_{tot} is the total enthalpy; U is the velocity; λ is the thermal conductivity; λ_t is the turbulent thermal conductivity; $\nabla \cdot q_r$ is the radiative source term. According to Eq. 5.6, there is a competition between thermal radiation, convection and conduction in the ST1_1_2 experiment. In order to illustrate the strength of radiation, convection and conduction, the radiative source term and $cond. + conv.$ term using the SNBCK model in the ST1_1_2 test are shown in Fig. 5.30 (600 s). In Fig. 5.30, there is a small fluctuation in the $\nabla \cdot q_r$ term owing to the statistical error from the Monte Carlo thermal radiation solver. However, the numerical fluctuation is relatively small in comparison with the $cond. + conv.$ term in the middle of Fig. 5.30. It is clear that thermal radiation can transfer energy over a long distance in comparison with other heat transfer modes. The thermal radiation source term is about 10 times smaller than the $cond. + conv.$ term in the hot jet region. Therefore, thermal radiation has only a small contribution to the heat balance near the hot jet region. But the thermal radiation heat transfer is important in the stagnant region owing to the large facility. Thermal radiation heat transfer is about five times larger than the $cond. + conv.$ term in the stagnant region (see right hand side in Fig. 5.30). Therefore, a homogeneous density field is formed when considering thermal radiation in simulations. If the injection rate is low, it has a strong effect on the buoyancy force and thereby changes the mixing process.

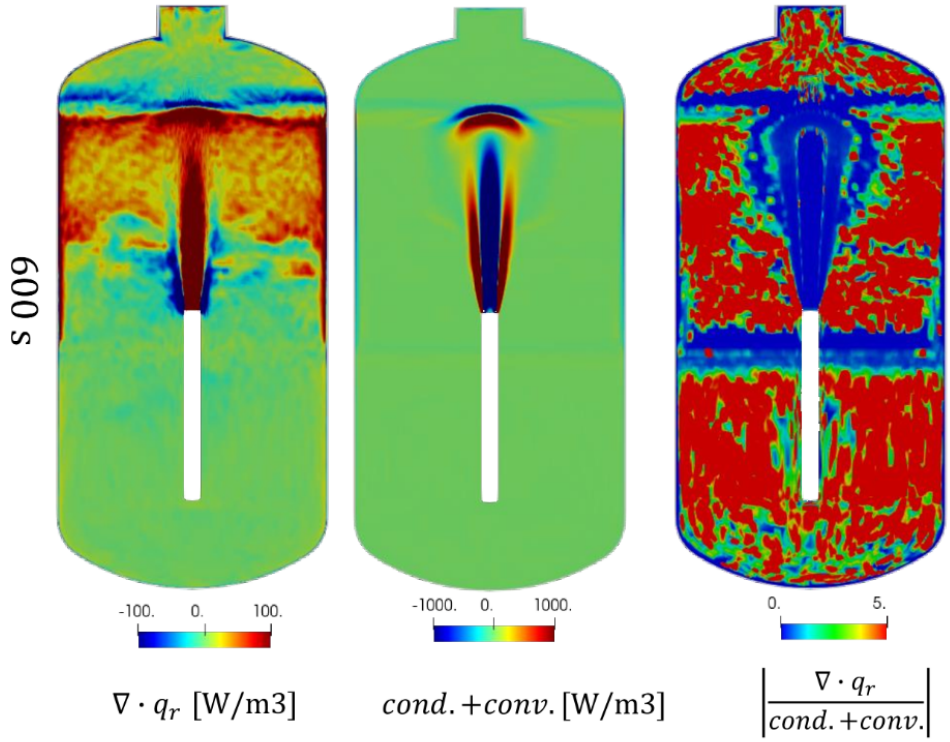

Figure 5.30: Comparison of radiative source term and $cond. + conv.$ term in the ST1_1_2 test at 600 s

Another important finding is that it may take a long time to reach a homogeneous temperature profile by thermal radiation due to the modest temperature difference. When the homogeneous temperature profile is reached, the hot steam jet in the center tends to move horizontally and it can further magnify the heat transfer between hot jet and ambient atmosphere. Obviously, the importance of thermal radiation is also related to the scale of facility, the injection direction, and the position of hot jet. If the diameter of the PANDA vessel is large enough, the thermal radiation can have a strong effect on the mixing process for the large momentum jet. It is necessary to run more simulations with different jet positions and directions to quantify the thermal radiation effect. In order to allow for a substantial improvement of thermal radiation modeling under containment conditions, dedicated experiments should be performed at a significantly large scale to reduce the near wall effect.

Chapter 6

Conclusion and Outlook

6.1 Summary and Conclusions

During a postulated severe nuclear accident, large amounts of steam, hydrogen and aerosols are released from the reactor cooling system. After the release of steam and hydrogen from the primary coolant system, containment flows are mainly driven by buoyancy forces, which are closely related to the temperature and concentration fields. Steam has a strong absorption in the infrared range, and therefore the gas radiation heat transfer may have an important role in containment flows. Nonetheless, nearly all existing CFD studies of containment flows have motivated the neglect of thermal radiation based on the relatively small thermal gradients. However, the relative impact of radiative heat transport on the flow and transport processes depends on the local strength of convective and conductive heat transfer. Therefore, if the thermal radiation has a similar significant role than the convective processes, it will affect the local gas temperature gradients, potentially induce or dampen buoyancy forces, and thereby change the hydrogen transport processes. Consequently, to enable further clarification of the effect of radiative heat transport in a containment atmosphere the objective of this thesis is to develop a reliable and efficient radiative transfer equation solver, applicable for complex 3D geometries, to formulate and assess suitable non-gray gas models for multi-component gas mixtures, and to investigate the impact of thermal radiation on the gas mixing process in buoyancy-driven flows.

As basis for the development of a suitable radiation transport solver, the reliability of existing thermal radiation solvers and non-gray gas models is investigated in Chapter 3. It is found that the fvDOM and P_1 solvers are not accurate enough for the thermal radiation analysis in large and complex 3D facilities. Addition-

ally, there is an exponential increase of computation time for the fvDOM method when applied in conjunction with non-gray gas models, making it hard to couple it with CFD. In contrary, the Monte Carlo method becomes more efficient than fvDOM when considering spectral gas properties, and it can be applied to arbitrary complex geometries. Therefore, in Chapter 4 a tailored Monte Carlo method is implemented in the *containmentFOAM* framework.

The only bottleneck of the Monte Carlo method is statistical error, which is closely linked to the number of tracked photon histories and thus the computing time. In order to reduce the statistical error while maintaining an acceptable computational cost, the following three variance reduction techniques are implemented and investigated: the global mesh method, the emission-based reciprocity method and the importance sampling method. The advanced algorithms enable the newly developed Monte Carlo solver to be applicable to technical scale applications, and the numerical fluctuation originating from the statistical error is significantly reduced. The numerical analyses proved that the Statistical Narrow band Correlated-K (SNBCK) and Line-by-Line (LBL) models are the most accurate non-gray gas models. Furthermore, a dedicated SNBCK data library is derived from the HITRAN database for accidental conditions and consequently they are not sensitive to user defined model coefficients and thus yield better predictive capabilities in applications. Compared to gray and wide band models, the computational overhead of the SNBCK model is found to be minor and does not impair the overall performance and stability, when coupled along with the Monte Carlo method to a CFD simulation. Contrary, the LBL model has proved to be more expensive, less robust and thus can preferably serve as a reference but not suggest for productive analyses.

In Chapter 5 the Monte Carlo thermal radiation solver is assessed against two experimental test series in the technical scale PANDA facility at PSI Switzerland along with different spectral gas property models. The OECD/NEA-HYMERES2 H2P2 experiments can be considered as separate effect tests for radiation modeling. They address the radiative heat transport during compression of a humid gas mixture, while convection is mostly suppressed. Both experiment and simulation confirm the general effect of radiative heat transport on the gas temperature field in a humid atmosphere, i.e., if thermal radiation is neglected the gas temperature level is significantly over predicted. Furthermore, the simulations demonstrate the overall predictive capability of the Monte Carlo method with tailored LBL and SNBCK models for steam mixtures in high and low steam concentration atmospheres. In contrast to other models, the SNBCK model is applicable without further user input to both optically thick and thin media, which are in the range of expected conditions in the containment during severe accidents. In contrast, gray and wide band models require a reliable estimate of the fluid dynamic conditions to define appropriate model coefficients and consequently reveal less consistent predictions. The

OECD/NEA-SETH2 ST1 experiments investigate the erosion of a stratified light gas layer by a turbulent vertical steam jet with different initial momentum. Due to the high steam concentrations (up to 100 vol.%), radiative heat transfer adds to the convective heat transport. The analysis confirms that radiation heat transfer affects the gas temperature field, in particular by transferring energy from the hot steam jet in the radial direction as well as into the stagnant light gas layer. Thus, it affects the local buoyancy forces and thereby changes the mixing process. If thermal radiation is neglected, the mixing time is considerably over-predicted, while it is consistently reproduced when the developed Monte Carlo approach along with the SNBCK model is employed. Again, the comparison with other gray or wide band models underlines the predictive capability of the SNBCK model.

It is concluded that thermal radiation heat transfer becomes important in large 3D geometries where it can redistribute and smoothen the internal gas temperature field. It also has an impact on the heat balance near the walls where it can enhance the wall heat transfer. Both can result in potentially safety relevant secondary effects, such as impact on gas mixing in slow buoyancy driven flows, on pressurization or on the water-steam balance. Thus, gas radiation must not be neglected in containment analyses. The Monte Carlo solver with SNBCK model, developed in this thesis, has demonstrated to be applicable for this purpose.

The advanced radiation models are applicable to complex 3D geometries, less sensitive to user input and cover a wide range of thermo-fluid dynamic conditions. During the validation runs, the computational overhead is less than 50% of the computation time of the underlying CFD analysis, while the results are significantly improved, and the overall robustness of the solver is not impaired. Considering the relative contribution of other models to the total runtime of a CFD simulation, this additional effort is rated as acceptable. Consequently, the developed method is rated to be applicable to the analysis of technical-scale applications. Building upon this work, the *containmentFOAM* package, including the developed radiation models, has been already applied to the analysis of the International Standard Problem No. 37 based on an experiment in the large-scale multi-compartmented Battelle Model Containment (600 m^3).

6.2 Outlook and Perspective

To continue the investigation of the impact of thermal radiation on containment flows and transport processes, further work should address the following issues. In the containment atmosphere an inhomogeneous multi-component mixture consisting of the IR-active species H_2O, CO_2 and CO can be present in the late phase of an accident. Obtaining a spectral gas property for the gas mixture requires fur-

ther development and investigation. In this thesis, only the non-gray gas model for steam is validated against the PANDA H2P2 and ST1 experiments. There is, however, no experimental data available for $H_2O/CO/CO_2$ mixtures for conditions relevant to containment safety analyses. Consequently, a new experimental series should be set up with detailed field measurements to enhance the characterization of the interaction of gas temperature, induced secondary flows and gas transport.

The anisotropic scattering effect on aerosol or fog also can impact the radiative heat transport under realistic containment conditions. The formation of liquid films on the containment structures can change the interaction between thermal radiation and walls. Along with the integration of corresponding models in *containmentFOAM*, these effects and interactions should be investigated to link the different models and gain insight to the phenomenology. The numerical efficiency of the radiation transport solver and non-gray gas model should be optimized along with continuous validations and applications to different geometries by identifying the lowest reasonable update frequency for the radiative source terms as well as minimum required number of photon histories. Additionally, the developed Monte Carlo solver with non-gray gas models can serve in future work as a reference to develop computationally more efficient models and to quantify the modeling error resulting from the introduced simplifications.

Acknowledgement

During the PhD study, I have received a lot of help from my supervisors, colleagues and family members to finish this research. I would like to express sincere appreciation and gratitude to all of you. First of all, I would like to thank Prof. Hans-Josef Allelein for the kind guidance throughout the thesis. Without your supervision and valuable discussion, this thesis could never be written. I would like to express my appreciation to Prof. Reinhold Kneer and Prof. Xu Cheng for reviewing the thesis and providing valuable feedback. I would also like to express my sincere gratitude to Dr. Stephan Kelm. As an excellent group leader, he was always available to discuss and gave guidance on all aspects of the PhD study. He always encouraged me to improve my skills and provided me with opportunities to meet with different experts from other countries. After attending various international meetings in the nuclear safety field, I have learned a lot and widened my eyesight in safety assessment. Thanks also for his kind support to collaborate with Dr. Chungen Yin at Aalborg University. With the help from Dr. Chungen Yin, I obtained a profound understanding about gas radiation and his valuable discussion inspired me to develop a tailored non-gray gas model for thermal radiation analysis.

I also gratefully acknowledge the OECD/NEA HYMERES-2 and SETH-2 projects, which data I used for validation. Many thanks to the project members and PANDA group in Paul Scherrer Institute in Switzerland, especially for Dr. Ralf Kapulla, Dr. Domenico Paladino, and Dr. Sidharth Paranjape. I am extremely grateful to all colleagues in Forschungszentrum Jülich, who provided kindly help to settle down. Many thanks to Dr. Andre Xhonneux, Dr. Ernst-Arndt Reinecke, Dr. Karl Verfondern, Manohar Kampili, Ruiyun Ji, Yihui Wu, Vijaya Kumar G., Allen George, Dr. Jingjing Li, Dr. Tian Zhang, Dr. Dunfu Shi, Astrid Kuhr and many others, it is a pleasure to know you. I am extremely grateful to the Chinese Scholarship Council (CSC) for the funding of the PhD position (CSC No. 201704890017) and the Helmholtz Interdisciplinary Doctoral Training in Energy and Climate Research (HITEC) for supporting the present work.

In 2017 I left everything in China and came here to earn the PhD degree. I want to thank my family and Yaqi Zhao for supporting me. Whenever I have some trouble, they always stand behind me and are a constant source of love in my life. To my father Hanqiang Liu and whole family, thank you for allowing me to pursue a PhD degree in Germany. I have to say sorry to all of you. Over the past few years, I cannot take on family responsibilities. During the COVID-19 pandemic, it was impossible for me to go back China and meet with you. Thanks for your understanding. Thanks for being with you.

Bibliography

[ABE14] Y. Abe, Y. Iizawa, Y. Terada, K. Adachi, Y. Igarashi, and et al. Detection of uranium and chemical state analysis of individual radioactive microparticles emitted from the fukushima nuclear accident using multiple synchrotron radiation x-ray analyses. Analytical chemistry, **86**:8521–8525, 2014.

[ALL08] H.J. Allelein, S. Arndt, W. Klein-Heßling, S. Schwarz, C. Spengler, and et al. Cocosys: status of development and validation of the german containment code system. Nuclear Engineering and Design, **238**(4):872–889, 2008.

[ALL10] C. Allison and J. Hohorst. Role of relap/scdapsim in nuclear safety. Science and technology of Nuclear Installations, **2010**, 2010.

[AND03] C. Andrieu, N. De Freitas, A. Doucet, and M. Jordan. An introduction to mcmc for machine learning. Machine learning, **50**(1):5–43, 2003.

[AND08] M. Andreani, K. Haller, M. Heitsch, B. Hemström, and et al. A benchmark exercise on the use of cfd codes for containment issues using best practice guidelines: A computational challenge. Nuclear Engineering and design, **238**(3):502–513, 2008.

[AND10] M. Andreani and D. Paladino. Simulation of gas mixing and transport in a multi-compartment geometry using the gothic containment code and relatively coarse meshes. Nuclear Engineering and Design, **240**(6):1506–1527, 2010.

[AND16] J. Anderson, M. Irrgang, and S. Glotzer. Scalable metropolis monte carlo for simulation of hard shapes. Computer Physics Communications, **204**:21–30, 2016.

[AND19] M. Andreani, A. Gaikwad, S. Ganju, B. Gera, S. Grigoryev, and et al. Synthesis of a cfd benchmark exercise based on a test in the panda facil-

ity addressing the stratification erosion by a vertical jet in presence of a flow obstruction. Nuclear Engineering and Design, **354**:110177, 2019.

[BAS09] S. Basu, Z. Zhang, and C. Fu. Review of near-field thermal radiation and its application to energy conversion. International Journal of Energy Research, **33**(13):1203–1232, 2009.

[BAT85] D. Bates and B. Bederson. Advances in atomic and molecular physics. Academic Press, 1985.

[BEC11] V. Becher, S. Clausen, A. Fateev, and H. Spliethoff. Validation of spectral gas radiation models under oxyfuel conditions. part a: Gas cell experiments. International Journal of Greenhouse Gas Control, **5**:S76–S99, 2011.

[BEC13] J. Becher. Validation of spectral gas radiation models under oxyfuel conditions. PhD thesis, Technische Universität München, 2013.

[BIS04] R. Bisseling. Parallel scientific computation: a structured approach using bsp and mpi. OUP Oxford, 2004.

[BOC16] R. Bocanegra, G. Jimenez, and M. Kevin Fernández-Cosials. Development of a pwr-w gothic 3d model for containment accident analysis. Annals of Nuclear Energy, **87**:547–560, 2016.

[BOE93] B. Boeck. A review of containment accidents. Nuclear engineering and design, **145**(3):279–288, 1993.

[BOL53] S. Bloom and H. Margenau. Quantum theory of spectral line broadening. Physical Review, 90(5):791, 1953.

[BOY14] W. Boyd, S. Shaner, L. Li, B. Forget, and K. Smith. The openmoc method of characteristics neutral particle transport code. Annals of Nuclear Energy, **68**:43–52, 2014.

[BUS07] P. Busch, T. Heinonen, and P. Lahti. Heisenberg's uncertainty principle. Physics Reports, **452**(6):155–176, 2007.

[CAS14] F. Cassol, R. Brittes, F. França, and O. Ezekoye. Application of the weighted-sum-of-gray-gases model for media composed of arbitrary concentrations of h2o, co2 and soot. International Journal of Heat and Mass Transfer, **79**:796–806, 2014.

[CAS15] F. Cassol, R. Brittes, F. Centeno, C. da Silva, and et al. Evaluation of the gray gas model to compute radiative transfer in non-isothermal, non-homogeneous participating medium containing co2, h2o and soot. Journal of the Brazilian Society of Mechanical Sciences and Engineering, **37**(1):163–172, 2015.

[CHA93] J. Chai, H. Lee, and S. Patankar. Ray effect and false scattering in the discrete ordinates method. Numerical Heat Transfer, Part B Fundamentals, **24**(4):373–389, 1993.

[CHA94] J. Chai, H. Lee, and S. Patankar. Finite volume method for radiation heat transfer. Journal of thermophysics and heat transfer, **8**(3):419–425, 1994.

[CHE00] X. Cheng, F.J. Erbacher, and H.J. Neitzel. Passive containment cooling by natural air convection and thermal radiation after severe accidents. Nuclear Engineering and Design, **202**(2):219 – 229, 2000.

[CHE05] Y. Chen and U. Fischer. Three-dimensional coupled monte carlo-discrete ordinates computational scheme for shielding calculations of large and complex nuclear facilities. 2005 International topical meeting on mathematics and computation, supercomputing, reactor physics and nuclear and biological applications, France SFEN, July 2005.

[CHR13] G. Chryssolouris. Laser machining: theory and practice. Springer Science & Business Media, 2013.

[CHU11] H. Chu, F. Liu, and H. Zhou. Calculations of gas thermal radiation transfer in one-dimensional planar enclosure using lbl and snb models. International Journal of Heat and Mass Transfer, **54**:4736–4745, 2011.

[CHU12] H. Chu, F. Liu, and H. Zhou. Calculations of gas radiation heat transfer in a two-dimensional rectangular enclosure using the line-by-line approach and the statistical narrow-band correlated-k model. International Journal of Thermal Sciences, **59**:66 – 74, 2012.

[CLO73] S. Clough, Y. Beers, G. Klein, and L. Rothman. Dipole moment of water from stark measurements of h2o, hdo, and d2o. The Journal of Chemical Physics, 59(5):2254–2259, 1973.

[COD94] P. D. Coddington. Analysis of random number generators using monte carlo simulation. International Journal of Modern Physics C, 5, 1994.

[COE97] P.J. Coelho and M.G. Carvalho. A conservative formulation of the discrete transfer method. Journal of Heat Transfer, **119**(1):118–128, 1997.

[COE03] P.J. Coelho, O.J. Teerling, and D. Roekaerts. Spectral radiative effects and turbulence/radiation interaction in a non-luminous turbulent jet diffusion flame. Combustion and Flame, **133**(1-2):75–91, 2003.

[COE14] P. Coelho. Advances in the discrete ordinates and finite volume methods for the solution of radiative heat transfer problems in participating media. Journal of Quantitative spectroscopy and Radiative transfer, **145**:121–146, 2014.

[CSA05] A. Császár, G. Czakó, T. Furtenbacher, and et al. On equilibrium structures of the water molecule. The Journal of chemical physics, 122(21):214305, 2005.

[CUM95] P.S. Cumber. Improvements to the discrete transfer method of calculating radiative heat transfer. International Journal of Heat and Mass Transfer, **38**(12):2251–2258, 1995.

[DEH11] A. Dehbi. Prediction of extrathoracic aerosol deposition using rans-random walk and les approaches. Aerosol Science and Technology, **45**:555–569, 2011.

[DEH19] A. Dehbi, S. Kelm, J. Kalilainen, and H. Mueller. The influence of thermal radiation on the free convection inside enclosures. Nuclear Engineering and Design, **341**:176–185, 2019.

[DEM12] R. Demarco. Modelling thermal radiation and soot formation in buoyant diffision flames. PhD thesis, Aix-Marseille, 2012.

[DOL15] W. Dols and B. Polidoro. Contam user guide and program documentation: version 3.2. National Institute of Standards and Technology, 2015.

[DOM10] L. Dombrovsky and D. Baillis. Thermal radiation in disperse systems: an engineering approach. Begell House New York, 2010.

[DON14] A. Donohoe, K.C. Armour, A.G. Pendergrass, and D.S. Battisti. Shortwave and longwave radiative contributions to global warming under increasing co2. Proceedings of the National Academy of Sciences, **111**:16700–16705, 2014.

[DOR09] J.P. Dorsselaere, C. Seropian, P. Chatelard, F. Jacq, J. Fleurot, and et al. The astec integral code for severe accident simulation. Nuclear Technology, **165**(3):293–307, 2009.

[EDW64] D. Edwards and W. Menard. Comparison of models for correlation of total band absorption. Applied Optics, **3**(5):621–625, 1964.

[EIB17] F. Eiberger. Wechselwirkung zwischen Turbulenz und Wärmestrahlung. PhD thesis, Karlsruher Institut für Technologie (KIT), 2017.

[FAR98] J. Farmer and J. Howell. Comparison of monte carlo strategies for radiative transfer in participating media. Advances in heat transfer, **31**:333–429, 1998.

[FER02] J. Ferziger, M. Perić, and R. Street. Computational methods for fluid dynamics. Springer, 3, 2002.

[FIS99] K. Fischer and T. Kanzleiter. Experiments and computational models for aerosol behaviour in the containment. Nuclear Engineering and Design, 191(1):53–67, 1999.

[FIV87] W. Fiveland. Discrete ordinate methods for radiative heat transfer in isotropically and anisotropically scattering media. Journal of Heat Transfer, **109**(3), 1987.

[FLE71] J.A. Fleck and J.D. Cummings. An implicit monte carlo scheme for calculating time and frequency dependent nonlinear radiation transport. Journal of Computational Physics, **8**(3):313–342, 1971.

[FRA07] M. Frank, A. Klar, E.W. Larsen, and S. Yasuda. Time-dependent simplified pn approximation to the equations of radiative transfer. Journal of Computational Physics, **226**:2289 – 2305, 2007.

[GAM83] R. Gamache and R. Davies. Theoretical calculations of n2-broadened half widths of h2o using quantum fourier transform theory. Appl. Opt., **22**:4013–4019, 1983.

[GAM17] R. Gamache, C. Roller, E. Lopes, I. Gordon, L. Rothman, and et al. Total internal partition sums for 166 isotopologues of 51 molecules important in planetary atmospheres: Application to hitran2016 and beyond. Journal of Quantitative Spectroscopy and Radiative Transfer, **203**:70–87, 2017.

[GAM21] R. Gamache, B. Vispoel, M. Rey, A. Nikitin, and et al. Total internal partition sums for the hitran2020 database. Journal of Quantitative Spectroscopy and Radiative Transfer, **271**:107713, 2021.

[GOL64] R. Goldstein. Measurements of infrared absorption by water vapor at temperatures to 1000 k. Journal of Quantitative Spectroscopy and Radiative Transfer, **4**:343–352, 1964.

[GOO89] R. Goody, R. West, L. Chen, and D. Crisp. The correlated-k method for radiation calculations in nonhomogeneous atmospheres. Journal of Quantitative Spectroscopy and Radiative Transfer, **42**(6):539–550, 1989.

[GOO95] R. Goody and Y. Yung. Atmospheric radiation: theoretical basis. Oxford university press, 1995.

[GOU00] V. Goutiere, F. Liu, and A. Charette. An assessment of real-gas modelling in 2d enclosures. Journal of Quantitative Spectroscopy and Radiative Transfer, **64**(3):299–326, 2000.

[GRO90] S. Grossel. An overview of equipment for containment and disposal of emergency relief system effluents. Journal of loss prevention in the process industries, **3**(1):112–124, 1990.

[GRO93] W. Grosshandler. Radcal: a narrow-band model for radiation. NIST Technical Note, **1402**, 1993.

[GRO99] W. Gropp, E. Lusk, A. Skjellum, and et al. Using mpi: portable parallel programming with the message-passing interface. MIT press, **1**, 1999.

[HAL73] G. Hale and M. Querry. Optical constants of water in the 200-nm to 200-μm wavelength region. Appl. Opt., 12(3):555–563, Mar 1973.

[HAM23] A. Hamdani, S. Soma, S. Abe, and Y. Sibamoto. Cfd analysis of thermal radiation effects on large containment cigma vessel with weighted sum of gray gases (wsgg) model. International Symposium on Zero-Carbon Energy Systems, 2023.

[HAR84] J.M. Hartmann, R. Levi Di Leon, and J. Taine. Line-by-line and narrow-band statistical model calculations for h2o. Journal of Quantitative Spectroscopy and Radiative Transfer, 32(2):119–127, 1984.

[HAS84] K. Hassmann and J.P. Hosemann. Consequences of degraded core accidents. Nuclear Engineering and Design, **80**:285–299, 1984.

[HAS07] A. Haselbacher, F.M. Najjar, and J.P. Ferry. An efficient and robust particle-localization algorithm for unstructured grids. Journal of Computational Physics, **225**(2):2198–2213, 2007.

[HEI84] W. Heitler. The quantum theory of radiation. Courier Corporation, 1984.

[HEI20] M. Heinrich and R. Schwarze. 3d-coupling of volume-of-fluid and lagrangian particle tracking for spray atomization simulation in openfoam. SoftwareX, 11:100483, 2020.

[HEN85] J. Hendricks and T. Booth. Mcnp variance reduction overview. Monte-Carlo Methods and Applications in Neutronics, Photonics and Statistical Physics: Proceedings of the Joint Los Alamos National Laboratory-Commissariat à l'Energie Atomique Meeting Held at Cadarache Castle, Provence, France, 1985.

[HER12] W. Hergert and T. Wriedt. The mie theory: basics and applications. Springer, 2012.

[HIN13] R. Hindmarsh. Nuclear disaster at fukushima daiichi. Routledge, 2013.

[HOF99] P. Hofmann. Current knowledge on core degradation phenomena, a review. Journal of nuclear materials, **270**:194–211, 1999.

[HOF00] K. A. Hoffmann and S. T. Chiang. Computational fluid dynamics volume i. Engineering education system, 2000.

[HOF02] M. Hoffert, K. Caldeira, G. Benford, D. Criswell, and et al. Advanced technology paths to global climate stability: energy for a greenhouse planet. science, **298**(5595):981–987, 2002.

[HOH86] C. Hohenemser, M. Deicher, A. Ernst, H. Hofsäss, G. Lindner, and et al. Chernobyl: an early report. Environment: Science and Policy for Sustainable Development, **28**(5):6–43, 1986.

[HOS03] S. Hostikka, K. McGrattan, A. Hamins, and et al. Numerical modeling of pool fires using les and finite volume method for radiation. Fire Safety Science, **7**:383–394, 2003.

[HOW20] J. Howell, M. Mengüç, K. Daun, and R. Siegel. Thermal radiation heat transfer. CRC press, 2020.

[HUA09] K. Huang. Introduction to statistical physics. Chapman and Hall/CRC, 2009.

[HUG63] H. Hughes. Beer's law and the optimum transmittance in absorption measurements. Applied Optics, **2**(9):937–945, 1963.

[IAE03] IAEA. Use of computational fluid dynamics codes for safety analysis of nuclear reactor systems. INTERNATIONAL ATOMIC ENERGY AGENCY, 2003.

[IAE11] IAEA. Mitigation of hydrogen hazards in severe accidents in nuclear power plants. INTERNATIONAL ATOMIC ENERGY AGENCY, 2011.

[IAE15] IAEA. The fukushima daiichi accident. INTERNATIONAL ATOMIC ENERGY AGENCY, 2015.

[ISO07] ISO. Iso 20473: 2007 optics and photonics—spectral bands. April 2007.

[JAC15] N. Jacquinet-Husson, R. Armante, N.A. Scott, A. Chédin, L. Crépeau, and et al. The 2015 edition of the geisa spectroscopic database. Journal of Molecular Spectroscopy, **327**:31–72, 2016.

[JAS96] H. Jasak. Error analysis and estimation for the finite volume method with applications to fluid flows. PhD thesis, Imperial College London, University of London, 1996.

[JI23] R. Ji, P. Wenig, S. Kelm, and M. Klein. Epistemic uncertainty in urans based cfd analysis of buoyancy driven flows—comparison of urans and les. Annals of Nuclear Energy, 181, 2023.

[JOS05] D. Joseph, M. El Hafi, R. Fournier, and B. Cuenot. Comparison of three spatial differencing schemes in discrete ordinates method using three-dimensional unstructured meshes. International journal of thermal sciences, **44**(9):851–864, 2005.

[KAM21] M. Kampili, G.V. Kumar, S. Kelm, K.A. Prakash, and H.J. Allelein. Cfd simulations of stratified layer erosion in minipanda facility using the tailored cfd solver containmentfoam. International Journal of Heat and Mass Transfer, **178**:121568, 2021.

[KAP23] R. Kapulla, X. Liu, S. Kelm, U. Doll, S. Paranjape, and D. Paladino. Importance, influence and limits of cfd radiation modeling for containment atmosphere simulations. Nuclear Engineering and Design, 411:112408, 2023.

[KEL17] S. Kelm, R. Kapulla, and H.J. Allelein. Erosion of a confined stratified layer by a vertical jet–detailed assessment of a cfd approach against the oecd/nea psi benchmark. Nuclear engineering and design, **312**:228–238, 2017.

[KEL21] S. Kelm, M. Kampili, X. Liu, A. George, D. Schumacher, and et al. The tailored cfd package containmentfoam for analysis of containment atmosphere mixing, h_2/co mitigation and aerosol transport. Fluids, **6**(3), 2021.

[KEL23] S. Kelm. Status and directions of cfd applications to containment phenomenology-a scientific perspective. Proc. OECD/NEA Computational Fluid Dynamics for Nuclear Reactor Safety (CFD4NRS-9) workshop, Texas AM University, College Station (Tx), USA, February 20-21, 2023.

[KIM90] M.H. Kim and M.L. Corradini. Modeling of condensation heat transfer in a reactor containment. Nuclear Engineering and Design, **118**:193–212, 1990.

[KIM91] T. Kim, J. Menart, and H. Lee. Nongray radiative gas analyses using the s-n discrete ordinates method. Journal of Heat Transfer, **113**(4):946–952, 1991.

[KIM01] M. Y. Kim, S. W. Baek, and J. H. Park. Unstructured finite-volume method for radiative heat transfer in a complex two-dimensional geometry with obstacles. Numerical Heat Transfer: Part B: Fundamentals, 39(6):617–635, 2001.

[KOC16] R. Kochanov, I. Gordon, L. Rothman, P. Wcisło, C. Hill, and et al. Hitran application programming interface (hapi): A comprehensive approach to working with spectroscopic data. Journal of Quantitative Spectroscopy and Radiative Transfer, **177**:15–30, 2016.

[KRA66] B. Krakow, H. Babrov, G.J. Maclay, and A. Shabott. Use of the curtis–godson approximation in calculations of radiant heating by inhomogeneous hot gases. Applied optics, **5**(11):1791–1800, 1966.

[KUL18] F. Kulacki, S. Acharya, Y. Chudnovsky, R. Cotta, R. Devireddy, and et al. Handbook of thermal science and engineering. Springer, 2018.

[KUM20] G.V. Kumar, M. Kampili, S. Kelm, K. Prakash, and H.J. Allelein. Cfd modelling of buoyancy driven flows in enclosures with relevance to nuclear reactor safety. Nuclear Engineering and Design, 365:110682, 2020.

[KUM21] G.V. Kumar, L. Cammiade, S. Kelm, K. Prakash, E. Groß, H.J. Allelein, R. Kneer, and W. Rohlfs. Implementation of a cfd model for wall condensation in the presence of non-condensable gas mixtures. Applied Thermal Engineering, 187:116546, 2021.

[LAT68] K. Lathrop. Ray effects in discrete ordinates equations. Nuclear Science and Engineering, **32**(3):357–369, 1968.

[LEE62] C. Lee. The discrete sn approximation to transport theory. Los Alamos Scientific Laboratory, 2595, 1962.

[LEH51] D. Lehmer. Mathematical methods in large-scale computing units. Annu. Comput. Lab. Harvard Univ., **26**:141–146, 1951.

[LI01] G. Li and M. F. Modest. An effective particle tracing scheme on structured/unstructured grids in hybrid finite volume/pdf monte carlo methods. Journal of Computational Physics, **173**:187–207, 2001.

[LIA22] Y. Liao, J. Li, and D. Lucas. Investigation on pool-scrubbing hydrodynamics with vof interface-capturing method. Nuclear Engineering and Design, 390:111713, 2022.

[LIO02] K.N. Liou. An introduction to atmospheric radiation. Elsevier, **84**, 2002.

[LIU97] F Liu, G Smallwood, D Snelling, and Ö Gülder. A ray-tracing method for solving the radiative transfer equation in three-dimensional participating media. Proceedings of the Combustion Institute, pages 1–17, 1997.

[LIU00] F. Liu, G. Smallwood, and Ö. Gülder. Application of the statistical narrow-band correlated-k method to low-resolution spectral intensity and radiative heat transfer calculations — effects of the quadrature scheme. International Journal of Heat and Mass Transfer, **43**(17):3119–3135, 2000.

[LIU21] X. Liu, S. Kelm, C. Yin, and H.J. Allelein. New h2o weighted sum of gray gases model for natural convection flows within large cavities. Journal of Physics: Conference Series, **2116**:012064, 2021.

[LIU22a] X. Liu, S. Kelm, M. Kampili, H.J. Allelein, R. Kapulla, D. Paladino, and S. Paranjape. Validation of a finite volume monte carlo solver for non-gray gas radiation in containemnt flows. 19th International Topical Meeting on Nuclear Reactor Thermal Hydraulics (NURETH-19), 2022.

[LIU22b] X. Liu, S. Kelm, M. Kampili, G.V. Kumar, and H.J. Allelein. Monte carlo method with snbck nongray gas model for thermal radiation in containment flows. Nuclear Engineering and Design, **390**:111689, 2022.

[LOC81] F.C. Lockwood and N.G. Shah. A new radiation solution method for incorporation in general combustion prediction procedures. Symposium (International) on Combustion, **18**(1):1405 – 1414, 1981.

[LOH90] R. Löhner and J. Ambrosiano. A vectorized particle tracer for unstructured grids. Journal of Computational Physics, **91**:22–31, 1990.

[LOU00] R. Loudon. The quantum theory of light. OUP Oxford, 2000.

[MAL10] J. Malet, E. Porcheron, and J. Vendel. Oecd international standard problem isp-47 on containment thermal-hydraulics—conclusions of the tosqan part. Nuclear Engineering and Design, **240**(10):3209–3220, 2010.

[MAL11] J. Malet, M. Bessiron, and C. Perrotin. Modelling of water sump evaporation in a cfd code for nuclear containment studies. Nuclear Engineering and Design, 241(5):1726–1735, 2011.

[MAN08] L. Mangani. Development and Validation of an Object Oriented CFD Solver for Heat Transfer and Combustion Modeling in Turbomachinery Applications. PhD thesis, Universita degli Studi di Firenze, Dipartimento di Energetica, 2008.

[MAN18] A. Mansour and E. Laurien. Numerical error analysis for three-dimensional cfd simulations in the two-room model containment thai+: Grid convergence index, wall treatment error and scalability tests. Nuclear Engineering and Design, **326**:220–233, 2018.

[MAS88] K. Masuda, T. Takashima, and Y. Takayama. Emissivity of pure and sea waters for the model sea surface in the infrared window regions. Remote Sensing of Environment, **24**:313–329, 1988.

[MCD08] R. McDermott, K. McGrattan, and S. Hostikka. Fire dynamics simulator (version 5) technical reference guide. NIST Special Publication, 1018(5), 2008.

[MCG00] K. McGrattan, H. Baum, R. Rehm, A. Hamins, G. Forney, and et al. Fire dynamics simulator–technical reference guide. National Institute of Standards and Technology, 2000.

[MCG13] K. McGrattan, S. Hostikka, R. McDermott, J. Floyd, and et al. Fire dynamics simulator technical reference guide volume 1: mathematical model. NIST special publication, 1018(1):175, 2013.

[MEL21] G. Mellau, V. Makhnev, I. Gordon, N. Zobov, J. Tennyson, and O. Polyansky. An experimentally-accurate and complete room-temperature infrared hcn line-list for the hitran database. Journal of Quantitative Spectroscopy and Radiative Transfer, **270**:107666, 2021.

[MEN99] E. Menzel. Fingerprint detection with lasers. M. Dekker New York, 1999.

[MEN12] W. Mendenhall, R. Beaver, and B.M. Beaver. Introduction to probability and statistics. Cengage Learning, 2012.

[MET49] N. Metropolis and S. Ulam. The monte carlo method. Journal of the American statistical association, **44**(247):335–341, 1949.

[MOD13] M.F. Modest. Radiative heat transfer. Academic press, 2013.

[MOR97] W. Mori. The physics of the nonlinear optics of plasmas at relativistic intensities for short-pulse lasers. IEEE Journal of Quantum Electronics, **33**:1942–1953, 1997.

[MOU16] F. Moukalled, L. Mangani, and M. Darwish. The finite volume method in computational fluid dynamics. Springer, 2016.

[MUR67] J.S. Murphy and J.E. Boggs. Collision broadening of rotational absorption lines. i. theoretical formulation. The Journal of Chemical Physics, **47**(2):691–702, 1967.

[OEC99] OECD-NEA. Soar on containment thermal-hydraulics and hydrogen distribution-prepared by an oecd/nea group of experts. Organisation for Economic Co-Operation and Development, 1999.

[OEC07a] OECD-NEA. Best practice guidelines for the use of cfd in nuclear reactor safety applications. Organisation for Economic Co-Operation and Development, 2007.

[OEC07b] OECD-NEA. International standard problem isp-47 on containment thermal hydraulics-final report. Organisation for Economic Co-Operation and Development, 2007.

[OEC08] OECD-NEA. Oecd/seth-2, panda test facility, description and geometrical specifications. Organisation for Economic Co-Operation and Development, 2008.

[OEC09a] OECD-NEA. Nuclear fuel behaviour in loss-of-coolant accident (loca) conditions. Organisation for Economic Co-Operation and Development, 2009.

[OEC09b] OECD-NEA. State of the art report on nuclear aerosols. Organisation for Economic Co-Operation and Development, 2009.

[OEC12] OECD-NEA. Oecd/seth-2 project panda and mistra experiments final summary report: Investigation of key issues for the simulation of thermal-hydraulic conditions in water reactor containment. Organisation for Economic Co-Operation and Development, 2012.

[OEC13] OECD-NEA. Oecd/seth-2 panda test st1_1_2 quick-look report. Organisation for Economic Co-Operation and Development, 2013.

[OEC14a] OECD-NEA. Containment code validation matrix. Organisation for Economic Co-Operation and Development, 2014.

[OEC14b] OECD-NEA. Status report on hydrogen management and related computer codes. Organisation for Economic Co-Operation and Development, 2014.

[OEC16] OECD-NEA. Computational fluid dynamics for nuclear reactor safety-5 (cfd4nrs-5). Organisation for Economic Co-Operation and Development, 2016.

[OEC18] OECD-NEA. Resolving complex safety relevant issues related to hydrogen release in nuclear power plant containments during a postulated severe accident. Organisation for Economic Co-Operation and Development, 2018.

[OEC21] OECD-NEA. Thermal radiation effects panda h2p2 test series and data report. Organisation for Economic Co-Operation and Development, 2021.

[OLS19] K. Olsen, C. Boone, G. Toon, F. Montmessin, A. Fedorova, O. Korablev, and A. Trokhimovskiy. Validation of the hitran2016 and geisa 2015 line lists using ace-fts solar occultation observations. Journal of Quantitative Spectroscopy and Radiative Transfer, 236, 2019.

[PAL10] D. Paladino, R. Zboray, P. Benz, and M. Andreani. Three-gas mixture plume inducing mixing and stratification in a multi-compartment containment. Nuclear Engineering and Design, **240**(2):210–220, 2010.

[PAL03] D. Paladino, M. Andreani, S. Guentay, G. Mignot, R. Kapulla, and et al. Outcomes from the euratom–rosatom ercosam samara projects on containment thermal-hydraulics for severe accident management. Nuclear engineering and design, 308:103–114, 2016.

[PAL19] L. Palluotto, N. Dumont, P. Rodrigues, O. Gicquel, and R. Vicquelin. Assessment of randomized quasi-monte carlo method efficiency in radiative heat transfer simulations. Journal of Quantitative Spectroscopy and Radiative Transfer, **236**:106570, 2019.

[PAP11] D. Papini, D. Grgić, A. Cammi, and M. Ricotti. Analysis of different containment models for iris small break loca, using gothic and relap5 codes. Nuclear Engineering and Design, 241(4):1152–1164, 2011.

[PAT18] S. V. Patankar. Numerical heat transfer and fluid flow. CRC press, 2018.

[PEN60] S. Penner and R. Landshoff. Quantitative molecular spectroscopy and gas emissivities. Physics Today, **13**(8):38–40, 1960.

[PLA14] M. Planck. The theory of heat radiation. Blakiston, 1914.

[REB95] P.H. Rebut. Iter: the first experimental fusion reactor. Fusion Engineering and Design, **30**:85–118, 1995.

[RIP90] B.D. Ripley. Thoughts on pseudorandom number generators. Journal of Computational and Applied Mathematics, **31**(1):153–163, 1990.

[RIV92] P. Rivière, A. Soufiani, and J. Taine. Correlated-k and fictitious gas methods for h2o near 2.7 μm. Journal of Quantitative Spectroscopy and Radiative Transfer, **48**(2):187–203, 1992.

[RIV95] P. Riviere, S. Langlois, A. Soufiani, and J. Taine. An approximate data base of h2o infrared lines for high temperature applications at low resolution. statistical narrow-band model parameters. Journal of Quantitative Spectroscopy and Radiative Transfer, **53**(2):221–234, 1995.

[ROM15] P. Romano, N. Horelik, B. Herman, A. Nelson, and et al. Openmc: A state-of-the-art monte carlo code for research and development. Annals of Nuclear Energy, **82**:90–97, 2015.

[ROS09] J.C. Rosa, A. Escriva, L.E. Herranz, T. Cicero, and J.L. Munoz-Cobo. Review on condensation on the containment structures. Progress in Nuclear Energy, **51**:32–66, 2009.

[ROT87] L. S. Rothman, R. R. Gamache, A. Goldman, L. R. Brown, and et al. The hitran database: 1986 edition. Appl. Opt., **26**(19):4058–4097, 1987.

[ROT05] L.S. Rothman, D. Jacquemart, A. Barbe, D. Chris Benner, M. Birk, and et al. The hitran 2004 molecular spectroscopic database. Journal of Quantitative Spectroscopy and Radiative Transfer, **96**(2):139–204, 2005.

[ROT09] L. Rothman, I. Gordon, and et al. The hitran 2008 molecular spectroscopic database. Journal of Quantitative Spectroscopy and Radiative Transfer, **110**(9-10):533–572, 2009.

[ROT10] L. Rothman, I. Gordon, R. Barber, H. Dothe, and et al. Hitemp, the high-temperature molecular spectroscopic database. Journal of Quantitative Spectroscopy and Radiative Transfer, **111**(15):2139–2150, 2010.

[SAD17] S. Šadek, D. Grgić, and Z. Šimić. Application of astec, melcor, and maap computer codes for thermal hydraulic analysis of a pwr containment equipped with the pcfv and par systems. Science and Technology of Nuclear Installations, **2017**, 2017.

[SAT10] A. Satoh. Introduction to practice of molecular simulation: molecular dynamics, monte carlo, brownian dynamics, lattice boltzmann and dissipative particle dynamics. Elsevier, 2010.

[SCH16] H. Schlichting and K. Gersten. Boundary-layer theory. springer, 2016.

[SCH20] M. Schneider, A. Froggatt, and et al. World nuclear industry status report 2020. Paris: World Nuclear Industry Status Report, 2020.

[SEH11] B. Sehgal and et al. Nuclear safety in light water reactors: severe accident phenomenology. Academic Press, 2011.

[SHA10] S. Shahedi, J. Jafari, M. Boroushaki, and F. DAuria. Development of a qualified nodalization for small-break loca transient analysis in psb-vver integral test facility by relap5 system code. Nuclear Engineering and Design, **240**(10):3309 – 3320, 2010.

[SIL19] S. Silvestri and R. Pecnik. A fast gpu monte carlo radiative heat transfer implementation for coupling with direct numerical simulation. Journal of Computational Physics: X, **3**:100032, 2019.

[SIN01] J. Singleton. Band theory and electronic properties of solids. Oxford University Press, 2, 2001.

[SMI82] T. Smith, Z. Shen, and J. Friedman. Evaluation of coefficients for the weighted sum of gray gases model. Journal of Heat Transfer, **104**(4):602–608, 1982.

[SOL01] V. Solovjov and B. Webb. An efficient method for modeling radiative transfer in multicomponent gas mixtures with soot. J. Heat Transfer, **123**(3):450–457, 2001.

[SOU91] A. Soufiani. Gas radiation spectral correlated approaches for industrial applications. Heat Transfer in Radiating and Combusting Systems: Proceedings of EUROTHERM Seminar No. 17, 8–10 October 1990, Cascais, Portugal, 1991.

[SOU97] A. Soufiani and J. Taine. High temperature gas radiative property parameters of statistical narrow-band model for h2o, co2 and co, and correlated-k model for h2o and co2. International journal of heat and mass transfer, **40**(4):987–991, 1997.

[SOU13] L. Soucasse, P. Rivière, and A. Soufiani. Monte carlo methods for radiative transfer in quasi-isothermal participating media. Journal of Quantitative Spectroscopy and Radiative Transfer, **128**:34 – 42, 2013.

[SPA97] L. Sparks. Efficient line-by-line calculation of absorption coefficients to high numerical accuracy. Journal of Quantitative Spectroscopy and Radiative Transfer, **57**(5):631 – 650, 1997.

[STA18] W.M. Stacey. Nuclear reactor physics. John Wiley & Sons, 2018.

[STR02] J. Ströhle and P.J. Coelho. On the application of the exponential wide band model to the calculation of radiative heat transfer in one- and two-dimensional enclosures. International Journal of Heat and Mass Transfer, **45**(10):2129 – 2139, 2002.

[STR07] W. Strauss. Partial differential equations: An introduction. John Wiley & Sons, 2007.

[SUN19] Y. Sun, S. Zheng, B. Jiang, J. Tang, and F. Liu. One-dimensional p1 method for gas radiation heat transfer in spherical geometry. International Journal of Heat and Mass Transfer, **145**:118777, 2019.

[TAI99] J. Taine and A. Soufiani. Gas ir radiative properties: from spectroscopic data to approximate models. 33:295–414, 1999.

[TAL75] A. Taflove and M.E. Brodwin. Numerical solution of steady-state electromagnetic scattering problems using the time-dependent maxwell's equations. IEEE transactions on microwave theory and techniques, **23**:623–630, 1975.

[TAN11] F. Tanabe. Analysis of core melt accident in fukushima daiichi-unit 1 nuclear reactor. Journal of nuclear science and technology, **48**:1135–1139, 2011.

[TAS11] S.A. Tashkun and V. Perevalov. Cdsd-4000: High-resolution, high-temperature carbon dioxide spectroscopic databank. Journal of Quantitative Spectroscopy and Radiative Transfer, **112**(9):1403–1410, 2011.

[TES02] L. Tessá, F. Dupoirieux, B. Zamuner, and J. Taine. Radiative transfer in real gases using reciprocal and forward monte carlo methods and a correlated-k approach. International Journal of Heat and Mass Transfer, **45**(13):2797 – 2814, 2002.

[TES11] L. Tessé and J. Lamet. Radiative transfer modeling developed at onera for numerical simulations of reactive flows. Aerospace Lab, 2011.

[TIE68] C. Tien. Thermal radiation properties of gases. Advances in heat transfer, **5**:253–324, 1968.

[TON79] L.S. Tong and J. Weisman. Thermal analysis of pressurized water reactors. American Nuclear Society, 1979.

[TOT86] L. Toth, A. Malinauskas, G. Eidam, and H. Burton. The three mile island accident: diagnosis and prognosis. American Chemical Society, Washington, DC, 1986.

[TRO22] J. Trosseille, A. Mongruel, L. Royon, and D. Beysens. Effective substrate emissivity during dew water condensation. International Journal of Heat and Mass Transfer, 183:122078, 2022.

[UCH64] H. Uchida, A. Oyama, and Y. Togo. Evaluation of post-incident cooling systems of light water power reactors. Tokyo University, 1964.

[UJI99] H. UJITA, N. SATOH, M. NAITOH, M. HIDAKA, N. SHIRAKAWA, and M. YAMAGISHI. Development of severe accident analysis code sampson in impact project. Journal of Nuclear Science and Technology, **36**(11):1076–1088, 1999.

[VER07] H.K. Versteeg and W. Malalasekera. An introduction to computational fluid dynamics: the finite volume method. Pearson education, 2007.

[VSI06] M. Šimečková, D. Jacquemart, L. Rothman, R. Gamache, and A. Goldman. Einstein a-coefficients and statistical weights for molecular absorption transitions in the hitran database. Journal of Quantitative Spectroscopy and Radiative Transfer, 98(1):130–155, 2006.

[WAN07] A. Wang and M.F. Modest. Spectral monte carlo models for nongray radiation analyses in inhomogeneous participating media. International Journal of Heat and Mass Transfer, **50**:3877–3889, 2007.

[WAN14] P. Wang, F. Fan, and Q. Li. Accuracy evaluation of the gray gas radiation model in cfd simulation. Case Studies in Thermal Engineering, **3**:51–58, 2014.

[WHI18] C. White, M.K. Borg, T.J. Scanlon, S.M. Longshaw, B. John, and et al. dsmcfoam+: An openfoam based direct simulation monte carlo solver. Computer Physics Communications, **224**:22 – 43, 2018.

[WIL98] D. C. Wilcox. Turbulence modeling for cfd. DCW industries La Canada, 1998.

[YIN10] C. Yin, L. Johansen, L. Rosendahl, and S. Kær. New weighted sum of gray gases model applicable to computational fluid dynamics (cfd) modeling of oxy–fuel combustion: Derivation, validation, and implementation. Energy & Fuels, **24**(12):6275–6282, 2010.

[YOU97] J. Young. Nonisothermal band model theory. Journal of Quantitative Spectroscopy and Radiative Transfer, **18**:1–28, 1977.

[ZEB82] E.L. Zebroski. The dynamics of institutional changes following the tmi accident. Progress in Nuclear Energy, **10**:249–257, 1982.

[ZHA02] H. Zhang and M.F. Modest. Evaluation of the planck-mean absorption coefficients from hitran and hitemp databases. Journal of Quantitative Spectroscopy and Radiative Transfer, **73**(6):649 – 653, 2002.

[ZHA07] Z. Zhang. Nano/microscale heat transfer. Springer, 2007.

[ZHA11] J. Zhang. Radiation Monte Carlo approcah dedicated to the coupling with LES reactive simulation. PhD thesis, Ecole Centrale Paris, July 2011.

[ZIE13] A. Ziegler and H.J. Allelein. Reaktortechnik. Springer, 2013.

[ZSC14] G. Zschaeck, T. Frank, and A. Burns. Cfd modelling and validation of wall condensation in the presence of non-condensable gases. Nuclear Engineering and Design, 279:137–146, 2014.

Appendix A

Barycentric Tracking Algorithm

In engineering simulations, the Lagrangian particle tracking along complex 3D mesh grids, which may have a large number of unsturctured and arbitrary polyhedral cells, is the most time-consuming part. The general procedure for the particle tracking algorithm is straightforward. The global search algorithm is applied to find the control volume containing this particle based on its particle position (x, y, z) [LOH90]; however, the search algorithm is inefficient in the complex mesh grid. Another efficient way is to maintain the occupied cell from the previous particle position. The next step is to determine the nearest-distance to the occupied cell surface. Finally the physical tracking information is updated after crossing the surface between two control volumes. Although applying the super-computer with the MPI library for the particle tracking, the computation time is also far from satisfactory.

In OpenFOAM, the first step of the particle tracking procedure is to decompose the polyhedral cell into a number of tetrahedrons (see Fig. A.1). If the polyhedral cell is convex, all divided tetrahedrons are within the polyhedral control volume by using this decompose algorithm. Therefore, the particle tracking among the complex polyhedral control volumes can be converted to the tracking among tetrahedral cells. In this way, the complex partial tracking in the unstructured polyhedral mesh grid becomes a general problem; however, this tetrahedral division technology undoubtedly reduces the computation efficiency. The number of tetrahedral cells can be 10 times larger than that in the original mesh grid (see Fig. A.1). The point **O** is the center of the polyhedral cell in Fig. A.1. After dividing the polyhedral cell into a number of tetrahedrons, the position of the point **P** within the tetrahedron **OABC** can be expressed in a barycentric coordinate system in the [LI01].

$$P = weight_O O + weight_A A + weight_B B + weight_C C \tag{A.1}$$

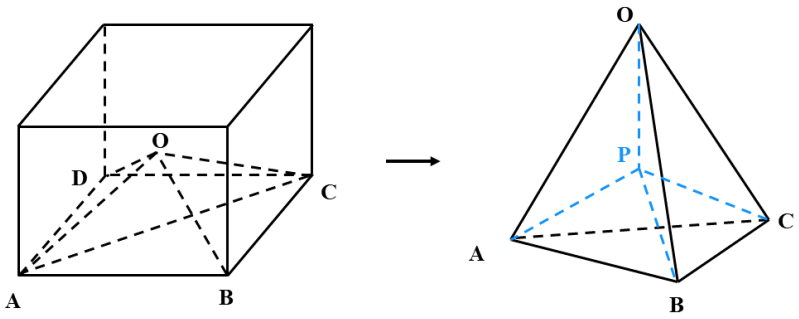

Figure A.1: Barycentric coordinate tracking algorithm

where the specific weight is

$$weight_O = \frac{V_{PABC}}{V_{OABC}} \tag{A.2}$$

$$weight_A = \frac{V_{PBCO}}{V_{OABC}} \tag{A.3}$$

$$weight_B = \frac{V_{PACO}}{V_{OABC}} \tag{A.4}$$

$$weight_C = \frac{V_{PABO}}{V_{OABC}} \tag{A.5}$$

If one of the weights is zero while others are positive, the point **P** is on the surface. The transformation matrix from the local barycentric coordinate into the global coordinate is

$$\begin{pmatrix} x_P \\ y_P \\ z_P \end{pmatrix} = \begin{pmatrix} x_O & x_A & x_B & x_C \\ y_O & y_A & y_B & y_C \\ z_O & z_A & z_B & z_C \end{pmatrix} \begin{pmatrix} weight_O \\ weight_A \\ weight_B \\ weight_C \end{pmatrix} \tag{A.6}$$

where x_P, y_P and z_P are positions for the point **P**.

Appendix B

Thermal Radiation Library Source Code

For containment flows, the following algorithm is applied owing to the fact that thermal radiation is not the dominant heat transfer mode in containment flows or natural convection flows. The following code `containmentFluidFoam.C` is a transient solver for an incompressible, variable density and multi-component turbulent flow.

```
while (pimple.run(runTime)){
    #include "rhoEqn.H"  // solve the density equation
    //update radiative source terms at N-th time steps
    radiation->correct();
    while (pimple.loop()){ //Pressure-velocity PIMPLE corrector loop
        #include "UEqn.H"  // velocity equation
        #include "YEqn.H"  // species equations
        #include "EEqn.H" // energy equation
        // --- Pressure corrector loop
        while (pimple.correct()){
            #include "pEqn.H"  // pressure equation
        }
        if (pimple.turbCorr()){  // turbulence correction
            turbulence->correct(); // turbulence equation
        }
    }
}
```

It is evident that updating thermal radiative source term at each CFD time step is computational unaffordable. As shown in the previous algorithm, the thermal radiation source term is updated at $N-th$ CFD time steps to save the computational power.

The following code `fvMCSNBCKH2OCO2Parcel.C` is the Monte Carlo thermal radiation solver.

```
void Foam::radiationModels::fvMCSNBCKH2OCO2Parcel::calculate(){
    Info<<"fvMCSNBCKH2OCO2 Monte Carlo Radiation Transport Solver"<<endl;
    UpdateLocalH2OCO2();  // update H2O and CO2 partial pressure

    GetAbsorptionCoefficientListIndex(T_, p_, ph2o_, Tlocalindex, Tweight
    , Mlocalindex, Mweight); // update absorption coefficient

    cloud_.reset(
        new MCSNBCKH2OCO2ParticleCloud<SNBCKH2OCO2Particle>
        (
            mesh_, // computational mesh
            "MCSNBCKH2OCO2ParticleCloud", // particle cloud name
            IDLList<SNBCKH2OCO2Particle>(), // particle type
            T_,     // temperature
            ph2o_,  // H2O partial pressure
            pco2_,  // CO2 partial pressure
            Tlocalindex, // temperature index
            Tweight,    // temperature weight
            Mlocalindex,  // molar fraction index
            Mweight,     // molar weight
            pSNB,        // SNBCK model
            divQr_,     // radiative source term
            qr_,       // radiative heat flux
            rndGen_,   // random generator
            cutoff_,   // cutoff energy
            mode_     // transport mode
        )
    );

    // batch loop to evaluate the statistical error
    for(label iBatch=0; iBatch<nBatch_; iBatch++){
        Info<<"  batch "<<iBatch<<": start photon sampling"<<endl;

        // sampling energy bundle
        SamplingCellFaceSource(mesh_, Tmin, Tmax, T_, ph2o_, pco2_,
    Tlocalindex, Tweight, Mlocalindex, Mweight, qr_, emission_);

        cloud_().move(cloud_(), td); // particle tracking procedure
        cloud_().clear();  // clear the system memory

        // update radiative source term and wall heat flux (batch)
        UpdateDivqrAndQr(mesh_, divQr_, qr_, emission_);

        // accumulate the simulation results
        AccumulateResults(mesh_, MCrel_, divQr_, qr_);
    }
    // update radiative source and wall heat flux (final)
    // MCrel_ is the statistical error
    FinalResults(mesh_, MCrel_, divQr_, qr_, nBatch_);
}
```